

AFIT/DS/ENG/02-02



AIRBORNE RADAR INTERFERENCE SUPPRESSION USING ADAPTIVE
THREE-DIMENSIONAL TECHNIQUES

DISSERTATION
Todd Benjamin Hale
Captain, USAF

AFIT/DS/ENG/02-02

DEPARTMENT OF THE AIR FORCE
AIR UNIVERSITY

AIR FORCE INSTITUTE OF TECHNOLOGY

Wright-Patterson Air Force Base, Ohio

APPROVED FOR PUBLIC RELEASE; DISTRIBUTION UNLIMITED.

Report Documentation Page		
Report Date Jun 02	Report Type Final	Dates Covered (from... to) Nov 00 - Jun 02
Title and Subtitle Airborne Radar Interference Suppression Using Adaptive Three-Dimensional Techniques	Contract Number	
	Grant Number	
	Program Element Number	
Author(s) Captain Todd B. Hale, USAF	Project Number	
	Task Number	
	Work Unit Number	
Performing Organization Name(s) and Address(es) Air Force Institute of Technology Graduate School of Engineering and Management (AFIT/EN) 2950 P Street, Bldg 640 WPAFB, OH 45433-7765	Performing Organization Report Number AFIT/DS/ENG/02-02	
Sponsoring/Monitoring Agency Name(s) and Address(es) AFRL/SNRT Attn: Michael C. Wicks Rome Research Site Rome, NY 13440	Sponsor/Monitor's Acronym(s)	
	Sponsor/Monitor's Report Number(s)	
Distribution/Availability Statement Approved for public release, distribution unlimited		
Supplementary Notes The original document contains color images.		
Abstract <p>This research advances adaptive interference suppression techniques for airborne radar, addressing the problem of target detection within severe interference environments characterized by high ground clutter levels, noise jammer infiltration, and strong discrete interferers. Two-dimensional (2D) Space-Time Adaptive Processing (STAP) concepts are extended into three-dimensions (3D) by casting each major 2D STAP research area into a 3D framework. The work first develops an appropriate 3D data model with provisions for range ambiguous clutter returns. Adaptive 3D development begins with two factored approaches, 3D Factored Time-Space (3D-FTS) and Elevation-Joint Domain Localized (Elev-JDL). The 3D-FTS technique exhibits greater than 15 dB improvement (over 2D-FTS) in Relative Peak Sidelobe Level (RPSL) using data from the Multi-Channel Airborne Radar Measurement (MCARM) program. The 3D adaptive development continues with optimal techniques, i.e., joint domain methods. First, the 3D Matched Filter (3D-MF) is derived followed by a 3D Adaptive Matched Filter (3D-AMF) discussion focusing on well-established practical limitations consistent with the 2D case. Finally, a 3D-JDL method is introduced and demonstrates target detection improvement of approximately 10 dB and 57 dB when compared to 2D-JDL and 2D-FTS, respectively, using an 8x8 non-uniform rectangular array and eight pulses. Proposed 3D Hybrid methods extend current state-of-the-art 2D hybrid methods. The initial 3D hybrid, a functional extension of the 2D technique, exhibits distinct performance advantages in heterogeneous clutter. The final 3D hybrid method is virtually impervious to discrete interference; an RPSL of -16.15 dB, versus 8.77 dB and 6.56 dB for the inverse 3D hybrid and 3D extension, respectively, was achieved for a typical data realization an average RPSL of -9.71 dB with standard deviation of 5.58 dB was achieved across 500 realizations.</p>		

Subject Terms radar, radar clutter, radar interference, adaptive filters, search radar	
Report Classification unclassified	Classification of this page unclassified
Classification of Abstract unclassified	Limitation of Abstract UU
Number of Pages 263	

Research sponsored in part by the Air Force Research Laboratory, Air Force Materiel Command, USAF. The United States Government is authorized to reproduce and distribute reprints notwithstanding any copyright notation thereon. The views and conclusions contained in this dissertation are those of the author and should not be interpreted as necessarily representing the official policies or endorsements, either expressed or implied, of the Air Force Research Laboratory, Department of Defense, or the United States Government.

AFIT/DS/ENG/02-02

AIRBORNE RADAR INTERFERENCE SUPPRESSION USING
ADAPTIVE THREE-DIMENSIONAL TECHNIQUES

DISSERTATION

Presented to the Faculty
Graduate School of Engineering and Management
Air Force Institute of Technology
Air University
Air Education and Training Command
In Partial Fulfillment of the Requirements for the
Degree of Doctor of Philosophy

Todd Benjamin Hale, B.S.E.E., M.S.E.E.
Captain, USAF

May 2002

APPROVED FOR PUBLIC RELEASE; DISTRIBUTION UNLIMITED.


AIRBORNE RADAR INTERFERENCE SUPPRESSION USING
ADAPTIVE THREE-DIMENSIONAL TECHNIQUES

DISSERTATION

Todd Benjamin Hale, B.S.E.E., M.S.E.E.

Captain, USAF

Approved:

 4 Jun 02
Date

Dr. Michael A. Temple
Dissertation Advisor

 4 Jun 02
Date

Dr. Mark E. Oxley
Committee Member

 30 MAY 02
Date

Maj John F. Raquet, PhD
Committee Member

 23 May 2002
Date

Dr. Michael C. Wicks
Committee Member

 30 May 2002
Date

Dr. Curtis H. Sperry
Dean's Representative

Accepted:

 5 June '02
Date

Robert A. Calico, Jr.
Dean, Graduate School of Engineering and Management

Acknowledgements

First and foremost, I owe a large debt of gratitude to Dr. Mike Temple. Our mutual inability to accept anything without question created many interesting discussions and undoubtedly aided me in this effort. Perhaps even more important, our joint interest in several non-research related pursuits helped me retain my sanity. There is definitely a point in any research effort or graduate program where you have to put all work aside and focus on other pursuits.

I would also like to thank Dr. Mike Wicks of AFRL/SNRT. Dr. Wicks' technical advice, monetary support, and general wealth of knowledge made this effort possible. His collaboration during my previous assignment to AFRL/SNRT greatly expanded my knowledge in the radar signal processing area.

Todd Benjamin Hale

Table of Contents

	Page
Acknowledgements	iv
List of Figures	ix
List of Tables	xii
List of Symbols	xiii
List of Abbreviations	xv
Abstract	xvii
 I. Introduction	 1
1.1 Multidimensional Processing	1
1.2 Contributions and Document Organization	4
1.2.1 Document Notation and Standardization	9
1.3 Research Applications	9
1.4 Research Sponsorship	12
 II. Two-Dimensional STAP	 13
2.1 Organization	14
2.2 Conceptual Overview	16
2.3 Data Model	17
2.3.1 Physical Geometry	18
2.3.2 Transmitted Waveform	19
2.3.3 Received Waveform	20
2.3.4 Formatting	21
2.3.5 Thermal Noise	23
2.3.6 Barrage Noise Jammer	24
2.3.7 Clutter	24
2.4 Homogeneity and Heterogeneity	27
2.4.1 Heterogeneity Detection	29
2.5 Interference Estimation: A Fundamental Choice	31
2.5.1 Statistical Interference Estimation	31
2.5.2 Deterministic Interference Estimation	33
2.6 Factored Methods	34
2.6.1 Factored Time-Space	35
2.7 Joint Domain Methods	36

	Page
2.7.1 Matched Filter	36
2.7.2 Adaptive Matched Filter	38
2.7.3 Joint Domain Localized	40
2.8 Hybrid Methods	42
2.8.1 Hybrid Deterministic Approach	43
2.8.2 Hybrid Statistical Approach	49
2.8.3 Numerical 2D Examples	51
2.9 Summary	54
III. Three-Dimensional Radar Model	57
3.1 Airborne Radar System	57
3.2 Transmitted Waveform	60
3.3 Received Waveform	62
3.3.1 Simplification	65
3.3.2 Down Conversion and Matched Filtering	67
3.4 Formatting Radar Returns	69
3.5 Element Patterns	71
3.6 Spatial Array Factor	72
3.6.1 Application of L'Hôpital's Rule	75
3.7 Spatial Antenna Array Pattern	77
3.8 Noise Model	80
3.9 Barrage Noise Jammer Model	81
3.10 Airborne Clutter Model	83
3.11 Consolidating Model Components	90
3.12 Summary	91
IV. Three-Dimensional Factored Methods	94
4.1 3D-FTS Using Two Element Interferometry Fused with 2D-FTS	96
4.1.1 MCARM Program	96
4.1.2 Elevation Adaptivity	97
4.1.3 2D Factored Time-Space	98
4.1.4 Test Statistic	99
4.1.5 Performance Measures	100
4.1.6 Two Element 3D-FTS Results	100
4.1.7 Target Altitude Determination	104
4.2 3D-FTS Multidimensional Mathematical Construct	105
4.2.1 Elevation Adaptivity	110
4.2.2 Doppler Filtering	114
4.2.3 Azimuth Adaptivity	114

	Page
4.2.4 Test Statistic	115
4.2.5 Results	116
4.2.6 Elevation Patterns	124
4.3 Elevation Interferometric STAP Using a Thinned Array	126
4.3.1 Results	128
4.4 Factored Elevation with Joint Domain Localized Processing	135
4.4.1 3D Elev-JDL Results	138
4.5 Range Ambiguous Interference Suppression	141
4.5.1 Geometrical Approach	141
4.5.2 Beamformed Statistical Approach	143
4.5.3 Range Ambiguous Interference Suppression Results	146
4.6 Summary	149
V. Three-Dimensional Joint Domain Methods	154
5.1 Matched Filter	155
5.1.1 Likelihood Ratio Processor	156
5.1.2 Maximum Signal-to-Interference Plus Noise Ratio Filter	158
5.1.3 Wiener Filter	160
5.2 Adaptive Matched Filter	162
5.3 Joint Domain Localized	162
5.4 3D-JDL Results	165
5.4.1 Output SINR	166
5.4.2 Detection Probability	169
5.5 Summary	169
VI. Three-Dimensional Hybrid Approach	173
6.1 3D Extension of the Original 2D Hybrid Technique	175
6.1.1 3D Deterministic Processing	176
6.1.2 Statistical Beamspace Adaptivity	184
6.1.3 3D Hybrid Results	187
6.2 Inverse 3D Hybrid Concept	191
6.2.1 Design Parameters	193
6.2.2 Inverse 3D Hybrid Results	194
6.3 Known Interferer Location	198
6.3.1 “Optimum” Results	199
6.4 Summary	203

	Page
VII. Conclusions	206
7.1 3D Data Model	206
7.2 3D Factored Approaches	209
7.3 3D Joint Approaches	211
7.4 3D Hybrid Approaches	213
7.5 Future Work	215
Appendix A. Kronecker Product	216
Appendix B. Angular Scales	218
B.1 Grating Lobes, Over Sampling, and Under Sampling .	220
Appendix C. SNR and Power Calculations	223
C.1 Target Power	223
C.1.1 Instantaneous Power, Average Power, and Total Power	224
C.2 Noise Power	226
C.3 Target SNR	227
C.4 Target SINR	227
Bibliography	229
Index	235
Author Index	242

List of Figures

Figure		Page
1.1.	Illustration showing the interference environment.	2
1.2.	Three-dimensional research progression parallels historical two-dimensional work.	4
2.1.	Adaptive weighting within a STAP radar system.	16
2.2.	Uniform linear array geometry and radar platform geometry.	19
2.3.	Side views of the clutter ring.	25
2.4.	Top view of the clutter ring.	26
2.5.	Range cell selection for homogeneous interference estimation.	28
2.6.	Large discrete interference infiltrates the range cell under test.	30
2.7.	Range cell selection for heterogeneous interference estimation.	31
2.8.	2D datacube: data available for adaptive processing over a CPI.	32
2.9.	Block diagram illustrating ideal 2D-JDL.	41
2.10.	Linear array of isotropic point sensors.	45
2.11.	2D hybrid technique block diagram.	50
2.12.	Standard JDL technique antenna pattern at target Doppler. .	53
2.13.	Standard JDL technique antenna pattern at target azimuth. .	53
2.14.	Direct data domain technique antenna pattern at target Doppler.	53
2.15.	Direct data domain technique antenna pattern at target azimuth.	53
2.16.	Hybrid technique antenna pattern at target Doppler.	53
2.17.	Hybrid technique antenna pattern at target azimuth.	53
3.1.	Planar antenna array oriented in the x - z plane.	58
3.2.	Radar platform geometry illustrates coordinate system. . . .	59
3.3.	Uniformly spaced antenna element array geometry.	59
3.4.	Ambiguous Doppler frequency illustration.	63
3.5.	Element block diagram showing received structure.	66
3.6.	3D element pattern in radar coordinates.	73
3.7.	3D element pattern in Cartesian coordinates.	73
3.8.	3D spatial array factor (W) in radar coordinates.	78
3.9.	Normalized 3D spatial array factor (W) in cartesian coordinates.	78
3.10.	Normalized 3D antenna array pattern in radar coordinates. .	79
3.11.	Normalized 3D antenna array pattern in cartesian coordinates.	79
3.12.	Top view of clutter ring geometry.	84
3.13.	Side view of clutter ring geometry.	85
4.1.	Elevation adaptivity achieves 14 dB RASL improvement. . .	102

Figure		Page
4.2.	Elevation adaptivity achieves 14 dB RASL improvement. . .	102
4.3.	Improvement surface illustrates insignificant degradation. . .	103
4.4.	Two-element interferometer elevation pattern.	106
4.5.	Proposed 3D-FTS method incorporating elevation beamforming.	109
4.6.	3D-FTS achieves 25 dB RPSL/23 dB RASL improvement. . .	118
4.7.	3D-FTS achieves 17 dB RASL improvement.	118
4.8.	Improvement surface illustrates insignificant degradation. . .	119
4.9.	3D-FTS performance degradation areas are irrelevant.	120
4.10.	3D-FTS range ambiguous detection probability.	121
4.11.	Range unambiguous detection probability for 3D-FTS.	121
4.12.	Simulated elevation pattern for the 3D-FTS technique.	125
4.13.	Full 8×8 rectangular array and thinned array configurations.	128
4.14.	P_d curves for $P_{fa} = 0.001$ <i>without</i> range ambiguous clutter. . .	131
4.15.	P_d curves for $P_{fa} = 0.001$ <i>with</i> range ambiguous clutter. . . .	131
4.16.	Output SINR curves <i>without</i> range ambiguous clutter.	133
4.17.	Output SINR curves <i>with</i> range ambiguous clutter.	133
4.18.	Elev-JDL block diagram.	137
4.19.	Output SINR of all 3D factored techniques, range unambiguous.	139
4.20.	Output SINR of all 3D factored techniques, range ambiguous.	140
4.21.	Range ambiguous interference suppression.	147
4.22.	Range ambiguous interference suppression.	148
5.1.	3D-JDL block diagram.	163
5.2.	Joint domain output SINR curves.	168
5.3.	Joint domain detection probabilities.	170
6.1.	3D original hybrid extension block diagram.	175
6.2.	Results for 3D hybrid, homogeneous data.	189
6.3.	Results for 3D hybrid, heterogeneous data.	189
6.4.	Results for 3D hybrid, heterogeneous data.	190
6.5.	3D inverse hybrid block diagram.	192
6.6.	Results for 3D inverse hybrid concept, homogeneous data. . .	196
6.7.	Results for 3D inverse hybrid concept, heterogeneous data. . .	196
6.8.	Results for 3D inverse hybrid concept, heterogeneous data. . .	197
6.9.	Known interferer location results, homogeneous data.	200
6.10.	Known interferer location results, heterogeneous data.	200
6.11.	Known interferer location results, heterogeneous data.	202
6.12.	Known interferer location results, heterogeneous data.	202

Figure		Page
7.1.	Three-dimensional research progression parallels historical two-dimensional work.	207
7.2.	Research links to publications.	208
B.1.	Sin-theta space for the MCARM array interelement distances.	222
C.1.	Receiver structure illustrating bandwidth considerations. . . .	223

List of Tables

Table		Page
1.1.	Contribution Areas.	5
1.2.	General document notation.	10
4.1.	MCARM radar parameters for acquisition 575, flight number 5.	97
4.2.	Simulated target parameters.	101
4.3.	2D-FTS vs. 3D-FTS performance summary. All units are dB.	104
4.4.	Radar simulation variables.	116
4.5.	Average 3D-FTS performance measures from Monte Carlo Analysis	123
5.1.	Radar simulation parameters.	165
A.1.	Properties of Kronecker Products	216

List of Symbols

Symbol		Page
d_x	Azimuth inter-element spacing	57
d_z	Elevation inter-element spacing	57
θ	Elevation angle	58
ϕ	Azimuth angle	58
φ	Random phase shift	60
ω_o	Carrier frequency	60
a_t	Transmitted pulse amplitude	60
$u(t)$	Pulse train envelope function	60
T_p	Pulse width	60
E_u	Pulse energy	61
E_p	Transmitted pulse energy	61
E_t	Transmitted signal energy	62
f_t	Target Doppler shift	62
v_t	Relative velocity	62
a_r	Received pulse amplitude	62
f_r	Pulse Repetition Frequency	62
$\bar{\omega}$	Normalized Doppler frequency	63
τ_t	Round trip time	63
R_t	Target range	63
$h(t)$	Filter impulse response	67
M	Number of pulses	69
N	Number of azimuth channels	69
P	Number of elevation channels	69
a	Azimuth steering vector	70
b	Temporal steering vector	70
e	Elevation steering vector	70
$f(\theta, \phi)$	Element voltage pattern	71
R_c	Range to clutter ring	84
a_e	Earth effective radius	85
h_a	Aircraft altitude	85
ψ_c	Grazing angle	85
R_u	Unambiguous range	86
N_r	Number of range ambiguities	86
K	Number of range cells for interference estimation	100

Symbol		Page
\mathbf{w}_a	Adaptive azimuth weight vector	110
\mathbf{B}	3D Doppler filter matrix	110
\mathbf{E}	Elevation weight matrix	110
\mathbf{C}_e	Artificial interference covariance	112
$\hat{\mathbf{R}}_N$	Azimuth covariance	114
\mathbf{A}	Azimuth data matrix	177
\mathbf{w}_a	Azimuth weight vector	177
\mathbf{E}	Elevation data matrix	178
\mathbf{T}	Temporal data matrix	179
$\tilde{\mathbf{A}}$	Azimuth interference matrix	180
$\tilde{\mathbf{T}}$	Temporal interference matrix	181
$\tilde{\mathbf{E}}$	Elevation interference matrix	181
G	Power gain	181
I	Residual interference	181
\mathbf{W}	LPC adaptive transform	184

List of Abbreviations

Abbreviation		Page
PRF	Pulse Repetition Frequency	1
2D	Two-Dimensional	1
STAP	Space-Time Adaptive Processing	2
D ³	Direct Data Domain	3
3D	Three-Dimensional	5
3D-FTS	Three-Dimensional Factored Time Space	5
3D-JDL	Three-Dimensional Joint Domain Localized	6
2D-FTS	2D Factored Time-Space	7
3D-MF	3D Matched Filter	8
3D-AMF	3D Adaptive Matched Filter	8
JDL	Joint Domain Localized	8
AFRL	Air Force Research Laboratory	9
AWACS	Airborne Warning and Control System	11
JSTARS	Joint Surveillance Target Attack Radar System	11
CDMA	Code Division Multiple Access	11
AFRL/SNRT	Radar Signal Processing Branch	12
PRI	Pulse Repetition Interval	17
RCS	Radar Cross Section	17
PD	Pulse Doppler	19
CPI	Coherent Processing Interval	20
JNR	Jammer-to-Noise Ratio	24
CNR	Clutter-to-Noise Ratio	26
i.i.d.	Independent and identically distributed	28
NHD	Non-Homogeneity Detector	30
DOF	Degrees of Freedom	32
SINR	Signal-to-Interference plus Noise Ratio	37
MF	Matched Filter	37
2D-AMF	Adaptive Matched Filter	38
MLE	Maximum Likelihood Estimate	38
GLRT	Generalized Likelihood Ratio Test	39
CFAR	Constant False Alarm Rate	39
2D-JDL	Joint Domain Localized	40
LPR	Localized Processing Region	41
DFT	Discrete Fourier Transform	42
GMTI	Ground Moving Target Indication	43
ICE	Interferometric Clutter Erase	48

Abbreviation		Page
FFT	Fast Fourier Transform	50
IF	Intermediate Frequency	67
TFACF	Time-Frequency Autocorrelation Function	67
MCARM	Multi-Channel Airborne Radar Measurement	94
SMI	Sample Matrix Inversion	99
RPSL	Relative Peak Sidelobe Level	100
RASL	Relative Average Sidelobe Level	100
LSMV	Linearly Constrained Minimum Variance	160
LPC	Localized Processing Cube	163
PSD	Power Spectral Density	226

Abstract

This research advances adaptive interference suppression techniques for airborne radar, addressing the problem of target detection within severe interference environments characterized by high ground clutter levels, noise jammer infiltration, and strong discrete interferers. Two-dimensional (2D) Space-Time Adaptive Processing (STAP) concepts are extended into three-dimensions (3D) by casting each major 2D STAP research area into a 3D framework. The work first develops an appropriate 3D data model with provisions for range ambiguous clutter returns. Adaptive 3D development begins with two factored approaches, 3D Factored Time-Space (3D-FTS) and Elevation-Joint Domain Localized (Elev-JDL). The 3D-FTS technique exhibits greater than 15 dB improvement (over 2D-FTS) in Relative Peak Sidelobe Level (RPSL) using data from the Multi-Channel Airborne Radar Measurement (MCARM) program. The 3D adaptive development continues with optimal techniques, i.e., joint domain methods. First, the 3D Matched Filter (3D-MF) is derived followed by a 3D Adaptive Matched Filter (3D-AMF) discussion focusing on well established practical limitations consistent with the 2D case. Finally, a 3D-JDL method is introduced and demonstrates target detection improvement of approximately 10 dB and 57 dB when compared to 2D-JDL and 2D-FTS, respectively, using an 8×8 non-uniform rectangular array and eight pulses. Proposed 3D Hybrid methods extend current state-of-the-art 2D hybrid methods. The initial 3D hybrid, a functional extension of the 2D technique, exhibits distinct performance advantages in heterogeneous clutter. The final 3D hybrid method is virtually impervious to discrete interference; an RPSL of -16.15 dB, versus 8.77 dB and 6.56 dB for the inverse 3D hybrid and 3D extension, respectively, was achieved for a given data realization. An average RPSL of -9.71 dB with standard deviation of 5.58 dB was achieved across 500 realizations.

AIRBORNE RADAR INTERFERENCE SUPPRESSION USING ADAPTIVE THREE-DIMENSIONAL TECHNIQUES

I. Introduction

The primary objective of this research effort is the advancement of adaptive interference suppression techniques for airborne radar. The problem is one of detecting targets within a severe interference environment characterized by high levels of ground clutter, jammer infiltration, and other strong sources not of interest (termed discrete interferers). Aircraft motion further complicates the detection problem due to induced velocity and dynamic ground clutter returns, causing them to occupy a wide range of Doppler frequencies. Often, platform induced clutter Doppler extends beyond the available unambiguous Doppler band as determined by the radar's Pulse Repetition Frequency (PRF). This aliasing regularly occurs for what are commonly termed low and medium PRF radars.

1.1 Multidimensional Processing

Multidimensional processing is required to solve the detection problem. Figure 1.1 shows the two-dimensional (2D) clutter Doppler distribution resulting from platform motion. Casting the problem in the framework of azimuth only beamforming, the clutter ridge projects onto the back wall as shown. The target response also projects onto the back and lies directly within the mainlobe clutter return. In this case, the target is buried in clutter and detection is difficult if not impossible. Similarly, forming a beam only in Doppler results in the interference being projected onto the left wall. In this case, the target is not only obscured by clutter but also is completely masked by noise jamming that may be present.

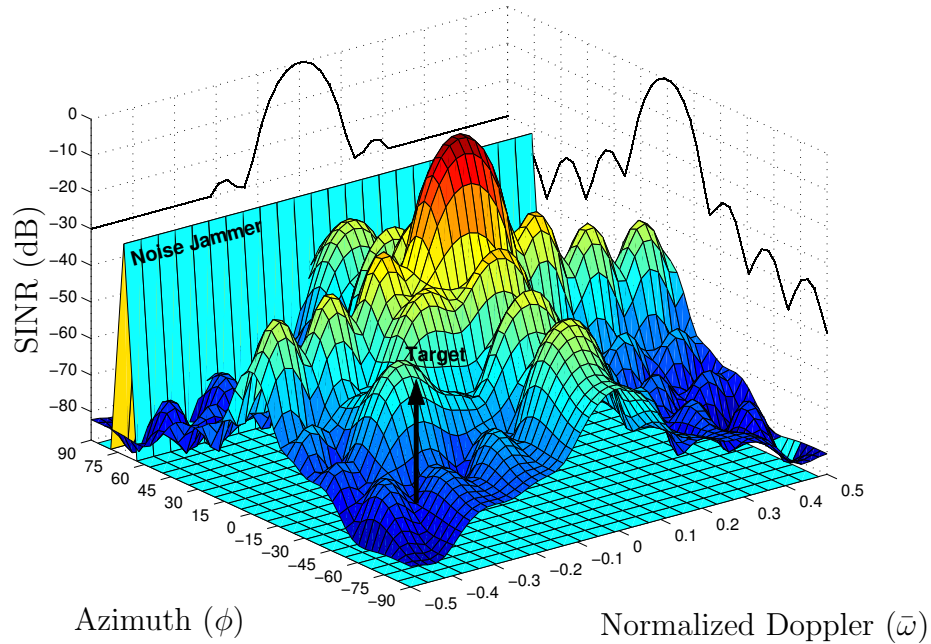


Figure 1.1: Illustration showing the 2D interference environment and the need for multidimensional processing. Clutter realization from an 8-element uniform linear array using 8 pulses.

The situation depicted in Fig. 1.1 emphasizes the need for multidimensional processing. The target is clearly detectable within the 2D azimuth-Doppler plane. The addition of height discrimination capability promises improved clutter suppression using a third dimension for adaptivity and enhancing weak target detection in a severe interference environment. Operation in hostile interference environments and the advent of stealth technology dictate the need for improved detection capability. Furthermore, today's climate of extremely small scale, surgical warfare demands technological improvements in radar target detection.

The research effort focuses toward bringing together three interference suppression methods: height discrimination, statistically adaptive methods, and direct data domain methods. To date, nearly all published research focuses on 2D Space-Time Adaptive Processing (STAP) within the azimuth-Doppler plane. This work extends 2D STAP fundamentals into the azimuth-Doppler-elevation hybercube using height

discrimination techniques. The hypercube offers greater ability to localize clutter and interference while greatly enhancing target detection capability.

In bringing together these diverse interference suppression approaches, the underlying data 2D model required fundamental changes to incorporate vertical channel responses. The physical environment served as the model foundation, paralleling that of [65]. Each environmental radar component was examined in detail, ranging from thermal noise, clutter, and barrage noise jamming to the actual target returns themselves.

Upon building an appropriate 3D data model/characterization, the next logical progression involved implementing traditional statistical STAP methods within the azimuth-Doppler-elevation space. These methods suppress correlated interference and jamming. However, statistical methods are susceptible degradation when presented with heterogeneous data, a condition discussed in Chapter II. When operating in these conditions, a different approach is needed to achieve acceptable target detection.

Direct Data Domain (D^3) methods are capable of suppressing uncorrelated interference. However, they cannot suppress correlated interference to the degree that statistical methods can. The primary advantage of D^3 approaches is reliable target detection within heterogeneous data environments.

Summarizing, statistical methods suppress correlated interference while direct data domain methods excel in suppressing uncorrelated interference. Joining these two methods into a single framework is termed *hybridization*, the newest class of 2D interference suppression methods.

Until now, all three suppression methods (D^3 , statistical, and hybrid) focused operation within the azimuth-Doppler plane. The benefits of including elevation are addressed by this work. Figure 1.2 illustrates the historical 2D research progression and the parallel development of 3D work presented here. This research merges three

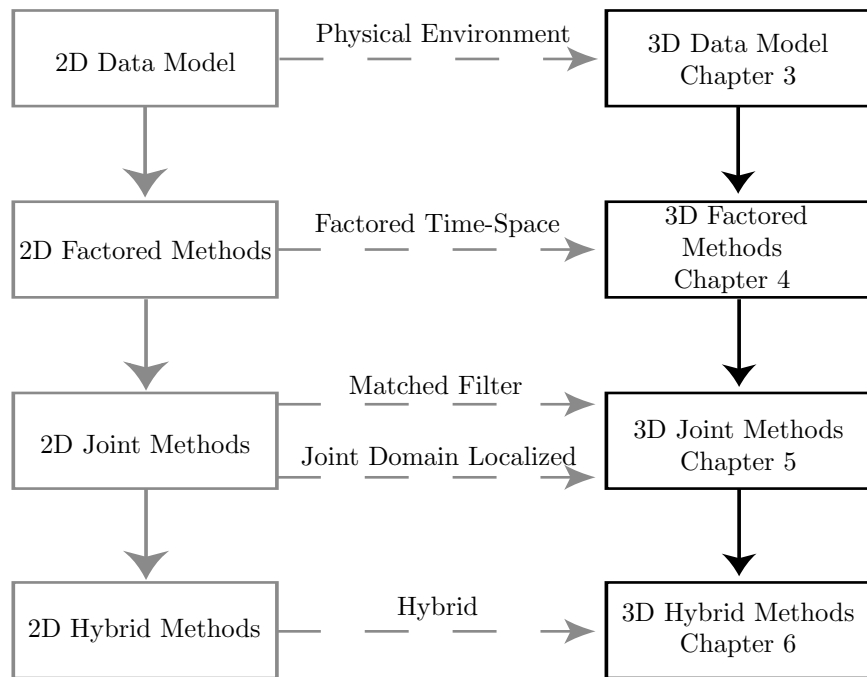


Figure 1.2: Three-dimensional research progression parallels historical two-dimensional work.

diverse interference suppression methods in a manner identical to the 2D development chain, including necessary modifications and developments required to extend target detection to the azimuth-Doppler-elevation hypercube. The work presented here offers significant contributions in each area of the 3D research chain.

1.2 Contributions and Document Organization

Figure 1.2 illustrates several diverse research contribution areas in 3D adaptive processing. The technical impact of this work is best assessed by independently examining the contribution areas which serve as a road map to this document. Table 1.1 summarizes each research contribution area, explained in detail within the designated chapter.

This document is organized in a manner paralleling Fig. 1.2. Chapter II offers relevant background material. Focus is placed on broad areas including the general premise of adaptive processing, the definition of homogeneity in relation to the

airborne radar problem, and more. These principles serve as an overview to the fundamentals of STAP versus an entire development of the 2D problem and act as a primer to what follows.

Table 1.1 Contribution Areas.

Chapter	Citation	Contribution
III	[34]	The construction of a three-dimensional (3D) airborne radar model permits simulation of realistic airborne radar data including the effects of clutter, thermal noise, jamming, and targets. The new model has no physical restriction on the number of vertical array channels and permits reliable generation of 3D data. Model performance was compared to measured data and provides identical results.
III	[32, 34, 35]	Implementation of range ambiguous clutter effects in the 3D airborne radar model. Previous 2D STAP research has typically ignored this by not accounting for or incorporating the effects of range ambiguous clutter ¹ . The impact of range ambiguous clutter is examined for each of the proposed methods.
IV	[31]	The introduction of height adaptivity through a factored approach exhibits a processing improvement on the order of 15 dB with only <i>two</i> elevation channels and measured airborne radar data. The method is termed 3D Factored Time-Space (3D-FTS).
IV	[32]	A detailed analysis of the 3D-FTS method characterizes performance gains when using a larger number of vertical channels. Improvement on the order of 25 dB is demonstrated.

¹Klemm indicates “almost all available references ignore ambiguous clutter effects” [42, page 11]

Table 1.1 (continued)

Chapter	Citation	Contribution
IV	[34]	The introduction of elevation adaptivity greatly increases the degrees of freedom, characteristically making this number significantly larger than the actual problem rank. Hence, the possibility exists to reduce computational load and cost by thinning the array to a more manageable size. Depending on the array configuration, there is little, if any, performance penalty incurred.
V	[32, 34, 35]	An optimum method is capable of placing null(s) at distinct locations within the azimuth-Doppler-elevation space. Therefore, the 3D-FTS approach is suboptimum due to its factored approach. The optimum 3D matched filter is presented as a comparison benchmark.
V	[35]	Since the 3D-FTS approach is suboptimum, the highly regarded Joint Domain Localized (JDL) method is extended from two to three dimensions. This 3D-JDL technique implements statistical adaptivity within the azimuth-Doppler-elevation beamspace. This method is shown capable of placing null(s) at distinct points within the space and approaches optimum performance.
VI		The original 2D hybrid formulation is effective at countering discrete interference sources, e.g., heterogenous data. However, there is a detection penalty paid when operating with homogeneous data. Improved 3D approaches are offered and shown capable of completely mitigating the effect of discrete interfering sources.

Table 1.1 (continued)

Chapter	Citation	Contribution
VI	[29]	Hybrid results are based on knowing the location of the interference sources. Determining these locations is not a simple task due to the computational load of scanning the entire azimuth-Doppler-elevation space and finding the local maxima. The scan resolution required can be reduced with an interpolation technique. An initial probabilistic based approach is developed.

Chapter III begins the 3D research progression of Fig. 1.2. The physical environment of an airborne radar is used to develop and characterize returns received by a rectangular array. Of particular importance is the generality of the model presented. An in-depth discussion of the previous 2D model is not provided since the 3D model developed here collapses to the 2D case. The development of the 3D data model parallels that of [65] with the necessary modifications. Although not a trivial extension, the new 3D model was designed with strong similarity to the previous 2D implementation and represents a more generic architecture.

Parallelling the 2D research efforts of Fig. 1.2, Chapter IV examines factored processing methods. The 2D Factored Time-Space (2D-FTS) approach is used as a basis for proof-of-concept. Elevation adaptivity is implemented in a factored manner, paralleling the overall approach of the original 2D-FTS method.

By definition, factored approaches are suboptimal. Suboptimal performance stems directly from the sequential (versus combined) nature of the factored approach;

effective null placement is achieved for particular locations in azimuth, Doppler, *or* elevation, but not for particular locations in azimuth, Doppler, *and* elevation. Achieving/approaching optimality requires extension to joint domain techniques, i.e., techniques operating jointly within the azimuth-Doppler-elevation space instead of individual spaces. Chapter V presents the 3D Matched Filter (3D-MF) which is the optimum adaptive processor. Unfortunately, a matched filter is exactly as its name implies, i.e., a filter that is perfectly matched to the interference scenario under consideration, thereby implying known interference statistics. Real-world application dictates estimation of interference statistics from available data. This requirement dictates the need for and development of the 3D Adaptive Matched Filter (3D-AMF) as presented in Chapter V. Chapter V provides the 3D-AMF practical limitations and offers a compromise: the extension of the highly regarded Joint Domain Localized (JDL) method [64] into the azimuth-Doppler-elevation hypercube.

The research progress to this point (through the 3D joint method block of Fig. 1.2) is directed primarily at target detection within homogeneous data. Heterogeneous data, defined in Chapter II, is commonly encountered in airborne radar scenarios. As a matter of fact, the presence of more than one target is, by definition, a heterogeneous environment. Operation within a heterogeneous environment is the primary purpose for introducing hybrid methods, the final block in Fig. 1.2. Chapter VI extends the current hybrid technique into three dimensions. Further-

more, a new variant providing substantial performance improvement over the current approach is proposed.

1.2.1 Document Notation and Standardization. This document uses standard mathematical notation common to published journals. Table 1.2 defines the notation set used.

! Key ideas and concepts are designated as shown here. These also show up in the index under the word “comments”.

1.3 Research Applications

STAP techniques have proven to be an effective means for suppressing severe, dynamic interference within two dimensions: azimuth and Doppler. Although STAP holds some promise for providing height discrimination capability, very little work has been done in this area. Practically all previous work, with the exception of some applications to circular arrays, has been performed with uniformly spaced linear arrays. Airborne radars commonly encounter severe, dynamic interference. Since a majority of airborne radars are for military applications, there is a false impression that STAP techniques only provide benefits to the military. On the contrary, military applications are merely the starting point for this area of research. Because of USAF interest in adaptive radar processing, these types of techniques commonly originate with a specific military application in mind. For example, the Air Force Research Laboratory (AFRL) funded previous research on a hybrid algorithm formulation [5,

Table 1.2: General document notation.

Example	Description	Definition
$\mathbf{x}, \boldsymbol{\chi}, \boldsymbol{\phi}$	Lower case bold letters	Vectors
$\mathbf{X}, \boldsymbol{\Xi}, \boldsymbol{\Phi}$	Upper case bold letters	Matrices
x, χ, ϕ	Lower case letters	Scalar quantities/variables
$\hat{\mathbf{R}}$	Hat above any variable	Estimated parameter or a unit vector (clear by context)
$\tilde{\mathbf{x}}$	Tilde above any variable	Transformed parameter or a complex variable (clear by context)
\mathbf{x}^H	Matrix/vector superscript H	Hermitian transpose
\mathbf{x}^T	Matrix/vector superscript T	Transpose
\mathbf{x}^*	Matrix/vector superscript *	Conjugation
$\mathbf{X}_{n,m}$	Subscripted matrix	n^{th} row, m^{th} column element
\mathbf{x}_n	Subscripted vector	n^{th} vector element, n^{th} vector, or for descriptive purposes (clear by context)
R_e, ϕ_t	Subscripted scalar	Descriptive purposes only, e.g., the “ t ” is for target and the “ e ” for elevation
$\mathcal{E}\{\cdot\}$	Calligraphic E	Expectation Operator

33] with intended applications including the Airborne Warning and Control System (AWACS) and Joint Surveillance Target Attack Radar System (JSTARS) platforms.

The civilian digital communications industry's success in making wireless communication commonplace is rapidly turning the communications spectrum into an environment of severe, dynamic interference. A typical wireless receiver in a large city environment must contend with hundreds, perhaps thousands, of transmissions. All transmissions other than the one of interest may constitute interference. This problem is currently being countered through the use of available spectral bandwidth and Code Division Multiple Access (CDMA). However, bandwidth is limited and, as the use of wireless communications increases, this interference problem will thrust its way to the communications industry forefront. STAP techniques have been applied to the communications problem and shown to offer significant performance improvements [44, 48]. The subject research offers specific, and potentially very lucrative, advantages over previous attempts at applying STAP to the digital communications problem.

This work focuses entirely on the airborne radar problem, the sponsor's primary focus. The previous communications system discussion serves as a reminder that the work is generally applicable to a broader range of detection and estimation problems.

1.4 Research Sponsorship

The Air Force Research Laboratory, Sensors Directorate, Radar Signal Processing branch (AFRL/SNRT), sponsored this research. AFRL/SNRT conducts basic research, exploratory and advanced development of low cost solutions for high performance surveillance sensors. AFRL/SNRT has been charged with responsibility for enhancing advanced target detection and tracking from long range standoff airborne, space-based and intelligence, surveillance, and reconnaissance platforms through mitigation of clutter and jamming. AFRL/SNRT solicited AFIT/ENG's support to aid in technical development, characterization, analysis, modeling, and simulation of advanced radar techniques to achieve their goals.

II. Two-Dimensional STAP

This chapter examines the role of two-dimensional (2D) Space-Time Adaptive Processing (STAP) as a precursor to the three-dimensional (3D) research presented in subsequent chapters. In broadening 2D methods to incorporate elevation interference suppression, particular emphasis has been placed on developing *general* forms of the proposed techniques. This emphasis results in 3D variants equivalent to current 2D counterparts using a single elevation channel. By taking this approach, many of the concepts and ideas successful within the azimuth-Doppler plane readily translate and remain effective in the azimuth-Doppler-elevation hypercube.

The generic 3D development approach works well for statistical techniques. For this reason, extended development of previous 2D work is not offered here. Unfortunately, the deterministic approaches do not generally offer the seamless collapse from 3D to 2D. Given this limitation, emphasis is placed on explaining the previous 2D deterministic (D^3) approaches.

In reviewing this Chapter, careful consideration should be given to how the research progression shown in Fig. 1.2 builds the overall picture. Given the research goal is advancement of interference suppression techniques with a focus on the airborne radar problem, project scope addresses three-dimensional interference suppression method development. The 3D extension requires careful analysis of nearly all facets of the 2D research progression shown in Fig. 1.2.

Two-dimensional adaptive interference suppression for airborne radar logically progressed as shown by Fig. 1.2: create a suitable data model, examine factored interference suppression approaches, examine joint domain interference suppression approaches, and, finally, given the impact of heterogeneous data, examine hybrid techniques specifically designed for operation within heterogeneous environments. After generating the model, this progression could be rephrased in very generic terms as: easy (proof-of-concept), hard (optimal in benign environments), and hardest

(optimal while operating in hostile environments). The presentation of the three-dimensional approaches in this work follows this same progression.

! The actual research time-line began with the introduction of the joint domain matched filter. However, practical considerations forced investigation of partially adaptive factored methods and finally partially adaptive joint domain methods. Given the overall viewpoint taken, it is more appropriate to introduce ideas in the order chosen.

2.1 *Organization*

Obviously, previous 2D work plays a significant role in 3D development. The 2D technology base serves as the starting block for this effort. The impact of the 2D base is discussed for each step in Fig. 1.2 with background material presented as needed.

Discussion begins with a conceptual overview of the radar adaptive processing problem in Section 2.2. The radar adaptive interference suppression concept is introduced as a general framework. Often, the details of a particular technique can be overwhelming, drowning out the overall goal. This section serves as a reminder of the overall goal.

Section 2.3 provides a review of the 2D airborne radar data model. The newly proposed 3D model presented in Chapter III is based upon this previous work [65]. The previous work is reviewed in this section with primary results reproduced for subsequent comparison to the 3D model of Chapter III.

Both the 2D and 3D data models are designed to generate homogeneous data. Although not a specific concept listed in the research chain of Fig. 1.2, the concepts of homogeneity and heterogeneity are discussed in Section 2.4 and are crucial to understanding the strengths and weaknesses of the different approaches presented throughout this research effort.

A topic which sometimes sparks hot debate in adaptive interference suppression is the choice between deterministically and statistically based interference estimation methods. Section 2.5 examines fundamental issues along with the strengths and weaknesses of each approach. Although this topic is not specifically part of this research it is inherently embedded within each block of Fig. 1.2.

The final three sections are perhaps the most important to this chapter. They establish the previous research and present the original 2D framework for comparison to the 3D framework presented in subsequent chapters. First, factored approaches are presented in Section 2.6. The section does not review every factored approach in the 2D STAP arena. Rather, a brief overview is offered along with the important concepts of the 2D Factored Time-Space method.

Section 2.7 moves away from the suboptimal factored approach and introduces joint domain techniques. The joint domain concept is explained with emphasis placed on techniques that are important to later chapters. Specifically, discussion focuses on the matched filter, adaptive matched filter, and joint domain localized methods.

Finally, Section 2.8 builds upon all concepts under consideration. The hybrid method serves a very particular purpose and is discussed at length. The original hybrid formulation is fully developed since it serves as the starting point for the work in Chapter VI. The new research not only extends the original hybrid approach to include elevation adaptivity, it also moves far beyond the original limitations by making some key observations. In developing the new hybrid methods along with the 3D extension, the previous research is fundamental.

! Because this is a literature review, the symbols established here support this chapter *only*. The discussion of the 3D work in subsequent chapters establishes the symbol set used for the entire work, not the review in this chapter.

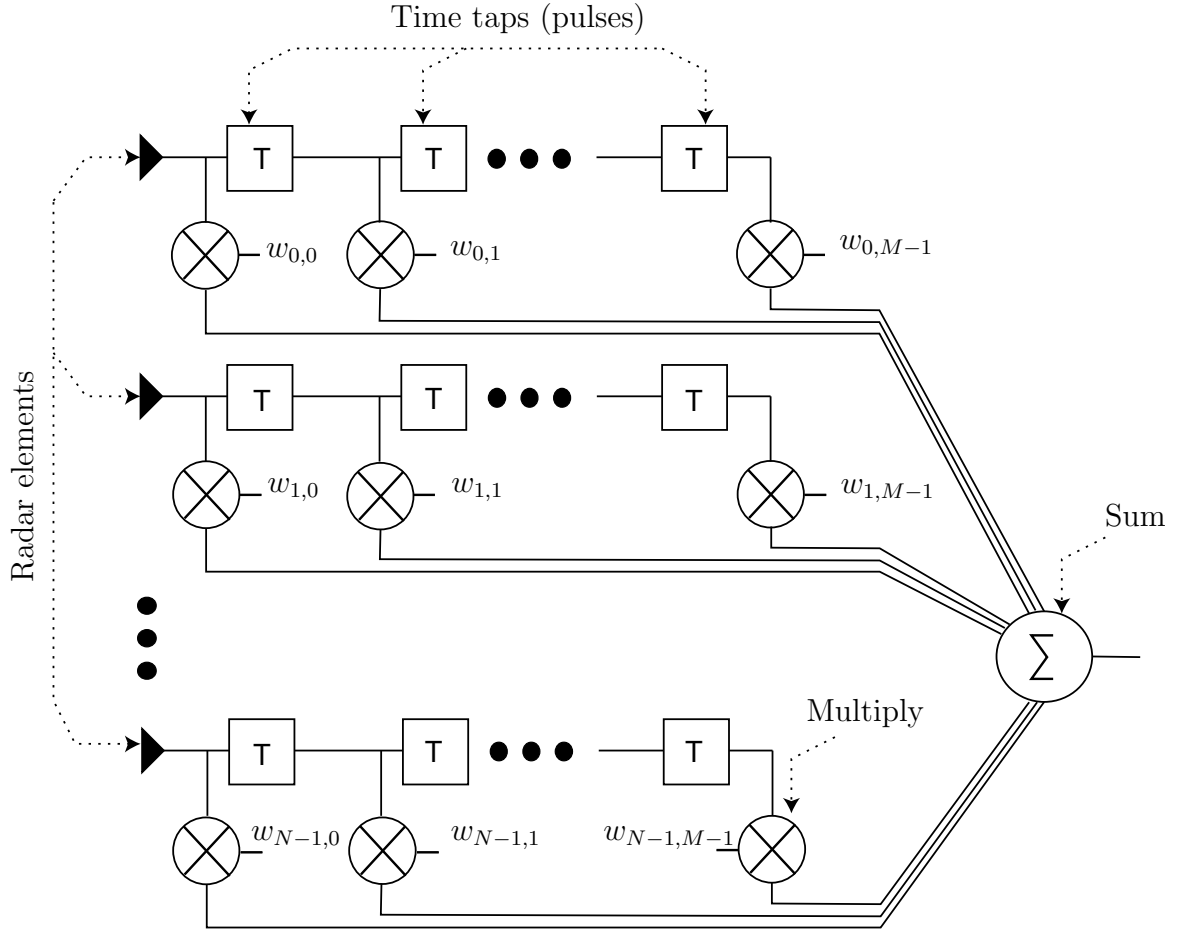


Figure 2.1: Adaptive weighting within a STAP radar system.

2.2 Conceptual Overview

STAP techniques adaptively combine data from several pulses and elements with the goal of achieving maximum interference suppression. Figure 2.1 shows a graphical, fully adaptive STAP representation. This particular method represents a distinct adaptive weight calculation ($w_{i,j}$) approach applied to returns from each element and pulse.

Historically, STAP research focuses on the linear array in an effort to simplify a complex problem. The weights, indicated by $w_{i,j}$ for all $i = 0, \dots, N - 1$ and $j = 0, \dots, M - 1$ in the figure, are calculated to give a maximum antenna response, referred to as the mainbeam, at a particular azimuth angle ϕ_t and normalized Doppler

frequency $\bar{\omega}_t$ while at the same time suppressing interference. For linear arrays, the number of horizontal antenna elements is denoted N while the number of pulses being adapted over is M . The time between pulses, or Pulse Repetition Interval (PRI) is T_r . Normalized Doppler is simply the Doppler shift f_t normalized by the Pulse Repetition Frequency (PRF) $f_r = 1/T_r$, or

$$\bar{\omega}_t = \frac{f_t}{f_r}. \quad (2.1)$$

The weights are applied through multipliers with the weighted returns summed to form a single output. This output is then applied to a thresholding scheme to determine target presence. The threshold level is determined by the desired false alarm probability P_{fa} and detection probability P_d .

All STAP approaches fall under this basic architecture. Approaches vary from fully adaptive, where every element and pulse is fully utilized, to partially adaptive approaches where only a portion of the suppression capability contained in the overall framework is used. Although many individual variants exist, each method falls into the general framework of Fig. 2.1.

2.3 Data Model

Adaptive interference suppression begins first by examining the physical environment and developing a model for the expected data. For 2D work, the model of [65], as originally proposed by [39], has served this purpose.

The 2D work first establishes an appropriate coordinate system and proceeds with a detailed examination of nuances associated with the airborne radar problem. The detailed examination begins with a mathematical transmit waveform model. Waveform transmission from a single element is characterized with associated losses due to range attenuation, variations due to target Radar Cross Section (RCS), frequency changes resulting from relative target velocity, and more. The analysis re-

sults in a mathematical expression describing the return received by a single antenna channel for a single pulse acting upon a point target/reflector.

Adaptive interference suppression implies the ability to electronically steer a radar transmit beam, thereby implying the use of a phased array antenna. From the radar return expression for a single element, single pulse, a framework is generated to encapsulate the returns from all elements in the antenna array and all pulses within a Coherent Processing Interval (CPI). Yet, at this point, only the return from a single scatterer is described. The full radar interference environment is built around the model for a single scatterer return. Ground clutter is introduced through the construction of range rings, where each particular ring is divided into individual patches (scatterers/point targets) having associated random amplitudes designed to simulate real-world clutter.

Similarly, a barrage noise jammer model is introduced along with thermal noise effects. Each component (clutter, thermal noise, barrage noise jammer, and target) characterizes the returns received in an actual airborne radar. Results using this model compare favorably to measurements taken from actual airborne radar platforms [34, 59].

The 2D model as described in [65] serves as the foundation for Chapter III. Each step is examined and reformulated to incorporate the rectangular array. Fundamental changes in the framework were required in the model, affecting the interference suppression techniques developed in Chapters IV through VI.

The original 2D model is summarized in the following subsections; this is not a complete redevelopment of Ward’s 2D work. Rather, sufficient information is introduced to highlight the differences between the 2D model and the 3D model of Chapter III.

2.3.1 Physical Geometry. In published 2D work, the radar antenna array is always assumed linear with uniformly spaced elements at a distance d apart. Each

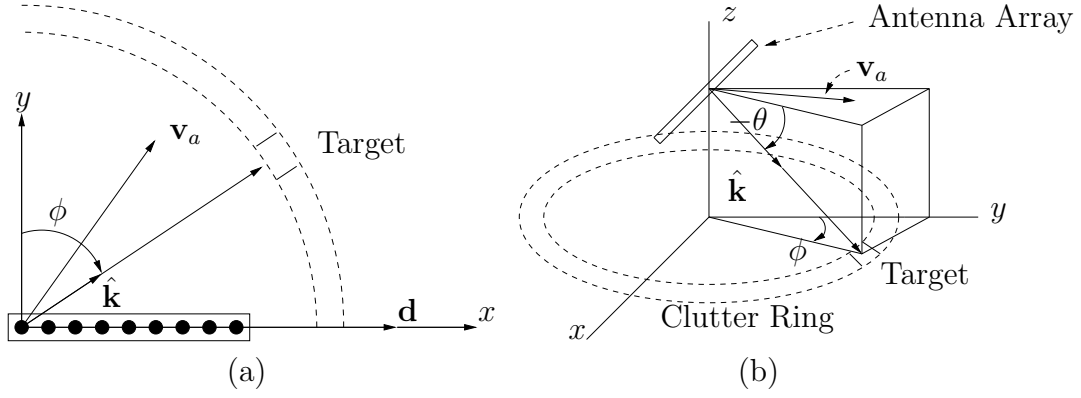


Figure 2.2: Uniform linear array geometry (a) and radar platform geometry (b).

element has a dedicated receiver for mathematical simplicity. The array orientation is along the x -axis as shown in Fig. 2.2a resulting in an element location vector $\mathbf{d} = nd\hat{\mathbf{x}}$, where $n = 0, 1, \dots, N - 1$. Consistent with Fig. 2.2b, the vector \mathbf{v}_a represents the magnitude and direction of the platform velocity. This figure also shows the corresponding radar platform geometry used by Ward [65].

The unit vector $\hat{\mathbf{k}}(\phi, \theta)$ shown in Fig. 2.2b represents the direction to a single point of interest (scatterer, target, etc.). Angular variables ϕ and θ represent the azimuth and elevation, respectively, to the point of interest. This coordinate system is related to the Cartesian coordinate system by

$$\hat{\mathbf{k}}(\phi, \theta) = \cos \theta \sin \phi \hat{\mathbf{x}} + \cos \theta \cos \phi \hat{\mathbf{y}} + \sin \theta \hat{\mathbf{z}}, \quad (2.2)$$

where $\hat{\mathbf{x}}$, $\hat{\mathbf{y}}$, and $\hat{\mathbf{z}}$ represent unit vectors along the Cartesian coordinate system $\hat{\mathbf{y}}$ and $\hat{\mathbf{z}}$ axes. The new coordinate system establishes the common frame used in airborne radar where targets are described in terms of their azimuth and elevation from the radar platform.

2.3.2 Transmitted Waveform. Given the previous physical geometry, next examine the electromagnetic properties of the radar. A Pulsed Doppler (PD) radar is assumed with target velocity information available to the processor. The sinusoidal

waveform transmitted by the radar is represented as

$$\tilde{s}(t) = a_t u(t) e^{j(2\pi f_o t + \psi)}, \quad (2.3)$$

where the complex exponential term with random phase shift ψ represents the sinusoidal carrier at frequency f_o , a_t the transmitted pulse amplitude, and $u(t)$ the envelope function. The notation used is referred to as complex envelope notation.

Envelope function $u(t)$ defines the pulse width and Pulse Repetition Interval (PRI) characteristics. Rather simplistically, a series of individual pulses is summed to form the radar transmit pulse train and defines the envelope function

$$u(t) = \sum_{m=0}^{M-1} u_p(t - mT_r). \quad (2.4)$$

The fundamental pulse $u_p(t)$ is time shifted by PRI multiples, mT_r . The finite summation of M terms represents the *Coherent Processing Interval*, or CPI. This expression implicitly defines M as the number of pulses in the CPI, allowing calculation of an adaptive dwell time.

2.3.3 Received Waveform. Continuing with Ward's 2D development, the signal received by each antenna element is the transmitted signal with a time delay τ_n from the point scatterer (target) to the n^{th} element and a Doppler shift f_t due to relative velocity v_t between the target and radar platform¹. With these definitions, the received signal at a single element is

$$\tilde{s}_n(t) = \tilde{s}(t - \tau_n) e^{j2\pi f_t(t - \tau_n)}. \quad (2.5)$$

¹The Doppler shift is assumed equal at all antenna elements.

After inserting the transmitted pulse expression, the received waveform becomes

$$\tilde{s}_n(t) = a_r u(t - \tau_n) e^{j2\pi f_o(t - \tau_n)} e^{j2\pi f_t(t - \tau_n)} e^{j\psi}, \quad (2.6)$$

where a_r represents the received pulse amplitude and incorporates atmospheric and/or Radar Cross Section (RCS) attenuation affects.

After down conversion (carrier removal) and matched filtering, the target samples at the n^{th} antenna element and m^{th} pulse, x_{nm} can be expressed as

$$x_{nm} = \alpha_t e^{j2\pi n\vartheta_t} e^{j2\pi m\bar{\omega}_t}, \quad (2.7)$$

where the complex random amplitude term α_t contains the phase and amplitude terms shown previously, i.e., $\alpha_t = a_r e^{j\psi}$. The parameter $\bar{\omega}_t$ represents the normalized Doppler frequency and ϑ_t represents spatial frequency, both defined in Section 3.3 on page 62.

2.3.4 Formatting. The received signal on a per element, per pulse basis serves as the foundation for building the rest of the model. First, create a column vector containing each antenna element sample at a particular range gate l and pulse m denoting it \mathbf{x}_m ,

$$\begin{aligned} \mathbf{x}_m &= \alpha_t e^{j2\pi m\bar{\omega}_t} \begin{bmatrix} 1 & e^{j2\pi\vartheta_t} & e^{j4\pi\vartheta_t} & \dots & e^{j2(N-1)\pi\vartheta_t} \end{bmatrix}^T \\ &= \alpha_t e^{j2\pi m\bar{\omega}_t} \mathbf{a}_t(\vartheta_t), \end{aligned} \quad (2.8)$$

where $\mathbf{a}_t(\vartheta_t)$ is the *spatial steering vector* of length N and the range gate/cell dependence has again been suppressed in the subscript. Using this notation, the incoming samples can be written as the matrix \mathbf{X} ,

$$\mathbf{X} = \begin{bmatrix} \mathbf{x}_0 & \mathbf{x}_1 & \dots & \mathbf{x}_{M-1} \end{bmatrix}, \quad (2.9)$$

where the matrix generally corresponds to the range gate/cell of interest.

Since the spatial frequency is a function of the target/scatterer elevation and azimuth angles, the spatial steering vector can be written as an explicit function of these variables,

$$\mathbf{a}_t(\theta_t, \phi_t) = \left[1 \quad e^{\frac{j2\pi d}{\lambda_o} \cos \theta_t \sin \phi_t} \quad e^{\frac{j4\pi d}{\lambda_o} \cos \theta_t \sin \phi_t} \quad \dots \quad e^{\frac{j2(N-1)\pi d}{\lambda_o} \cos \theta_t \sin \phi_t} \right]^T. \quad (2.10)$$

Similarly, the *temporal steering vector* $\mathbf{b}_t(\bar{\omega}_t)$ is defined as the vector of exponentials spanning the M pulses in the CPI,

$$\mathbf{b}_t(\bar{\omega}_t) = \left[1 \quad e^{j2\pi\bar{\omega}_t} \quad e^{j4\pi\bar{\omega}_t} \quad \dots \quad e^{j2(M-1)\pi\bar{\omega}_t} \right]^T. \quad (2.11)$$

The relationship between these two vectors forming the components of the received target sample matrix is characterized by the *Kronecker* product, denoted \otimes . See Appendix A, page 216, for a discussion of its properties. The temporal and spatial steering vector Kronecker product,

$$\mathbf{v}_t(\vartheta_t, \bar{\omega}_t) = \mathbf{b}_t(\bar{\omega}_t) \otimes \mathbf{a}_t(\vartheta_t), \quad (2.12)$$

is defined as the *space-time steering vector* \mathbf{v}_t , where the above equation emphasizes its normalized Doppler and spatial frequency dependence. Scaling this NM length vector by a random received amplitude parameter (subscripted with a t for the target or scatterer) gives

$$\boldsymbol{\chi}_t = \alpha_t \mathbf{v}_t, \quad (2.13)$$

where $\boldsymbol{\chi}_t$ is the traditional 2D *space-time snapshot* for a *single* target/scatterer. This NM length column vector $\boldsymbol{\chi}_t$ represents the target/scatterer returns received by each antenna element ($n = 0, 1, \dots, N - 1$) due to each transmitted pulse ($m = 0, 1, \dots, M - 1$) at a particular range gate/cell of interest l . Relating this Kronecker

product to the received target sample matrix \mathbf{X} illustrates it is simply the stacking (or concatenating) of the columns of \mathbf{X} end-to-end to form the column vector,

$$\boldsymbol{\chi} = \text{vec}(\mathbf{X}). \quad (2.14)$$

The $\text{vec}(\cdot)$ operator can be found in [43].

Since a single target/scatterer is not the only echo returned to the radar, an undesired component $\boldsymbol{\chi}_u$ is introduced in the model,

$$\boldsymbol{\chi} = \boldsymbol{\chi}_t + \boldsymbol{\chi}_u. \quad (2.15)$$

Undesired model components include thermal noise, barrage noise jamming, and clutter.

2.3.5 Thermal Noise. The only noise assumed present is due entirely to internally generated receiver thermal noise which is assumed white, a realistic and common assumption. Therefore, there is no correlation of the noise between pulses or antenna elements.

Let $\boldsymbol{\chi}_n$ represent the $MN \times 1$ spatial noise snapshot for each antenna element. The noise space-time covariance matrix \mathbf{R}_n is then

$$\mathbf{R}_n = \mathcal{E}\{\boldsymbol{\chi}_n \boldsymbol{\chi}_n^H\} = \sigma^2 \mathbf{I}_{MN} = \sigma^2 \mathbf{I}_M \otimes \mathbf{I}_N, \quad (2.16)$$

where \mathcal{E} is the expectation operator, \mathbf{I} is the identity matrix with dimension indicated by the subscript and σ^2 is the noise power per element, per pulse. The covariance matrix shown above serves as the thermal noise component of the overall covariance matrix \mathbf{R} .

! In certain circumstances, thermal noise plays a key role in adaptive interference suppression. Its presence within the covariance matrix ensures the matrix is invertible, a key requirement in most STAP approaches.

2.3.6 Barrage Noise Jammer. Only noise jamming originating from a long range airborne or ground based platform is considered. The jammer signal received by each antenna element is analyzed in the same manner as the target signal. Since the noise jammer is assumed uncorrelated on a pulse-to-pulse basis, but correlated on an element-by-element basis, the space-time covariance matrix when two jammers are present is determined as follows

$$\begin{aligned}
\mathbf{R}_j &= \mathcal{E} \{ \boldsymbol{\chi}_j \boldsymbol{\chi}_j^H \} \\
&= \mathbf{R}_j^{(1)} + \mathbf{R}_j^{(2)} \\
&= \mathbf{I}_m \otimes \sigma^2 \xi_j \left(\mathbf{a}_j^{(1)} \mathbf{a}_j^{(1)H} + \mathbf{a}_j^{(2)} \mathbf{a}_j^{(2)H} \right) \\
&= \mathbf{I}_m \otimes \left(\boldsymbol{\Phi}_j^{(1)} + \boldsymbol{\Phi}_j^{(2)} \right)
\end{aligned} \tag{2.17}$$

where the two $N \times N$ matrices $\boldsymbol{\Phi}_j^{(1)}$ and $\boldsymbol{\Phi}_j^{(2)}$ represent the jammer spatial covariance matrices and ξ_j is the Jammer-to-Noise Ratio (JNR). They result from taking the expected value of the received jammer signal across the elements for a particular pulse,

$$\boldsymbol{\Phi}_j^{(i)} = \mathcal{E} \{ \mathbf{x}_m \mathbf{x}_m^H \} = \sigma^2 \xi_j \mathbf{a}_j^{(i)} \mathbf{a}_j^{(i)H} \tag{2.18}$$

where $i = 1, 2$ in the two jammer case or $i = 1, \dots, J$ for J jammers. Extension to include any number of jammers is straightforward from the two jammer example just shown.

2.3.7 Clutter. Accurate clutter modeling is perhaps the most critical part of any airborne radar model. Inaccurate clutter simulation can render all results useless since clutter is the single, most defining factor in any airborne radar environment. In general, clutter may be defined as any unwanted radar echo. However, clutter in any airborne radar scenario is subject to specific correlation properties that have been the focus of debate for years. The results of the proposed 3D model compare favorably to adaptive interference suppression results based on actual air-

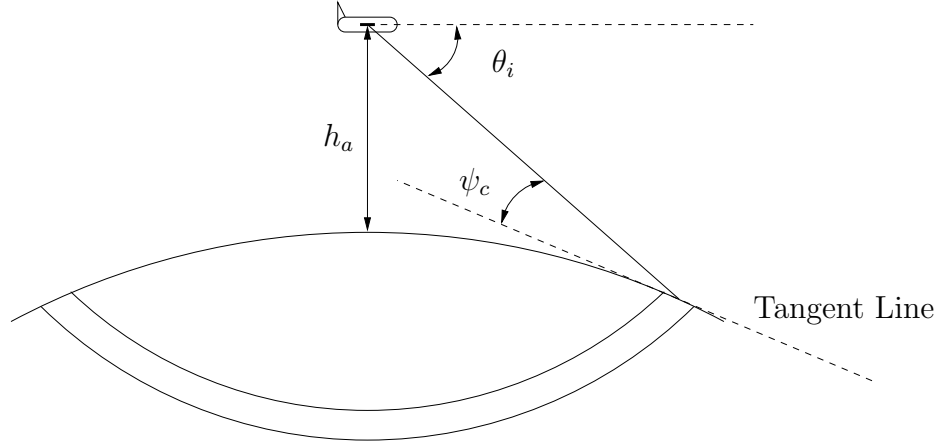


Figure 2.3: Side views of the clutter ring.

borne radar clutter measurements in the MCARM program [34,59]. Since the focus of this section is on airborne surveillance radars, ground clutter is the main concern.

The return from an individual clutter patch is identical in *form* to that of any target or other scatterer. However, several key differences beyond form play an important role in the model derivation. First, clutter is distributed in range and extends to the radar horizon. Second, assuming the Earth's surface is stationary, the only induced Doppler shift is due to the airborne platform velocity relative to the clutter patch.

Using these observations, ground clutter is analyzed using constant range rings around the aircraft. Further segmentation of the clutter ring results in clutter patches. Each patch is considered to be located at a constant range and has constant velocity with respect to the airborne platform. Figures 2.3 and 2.4 show the clutter ring for the airborne platform. A side view is shown in Fig. 2.3 and a top view of the clutter ring (with the airborne platform at the center) is shown in Fig. 2.4.

The unambiguous range (R_u) is divided into L range bins (rings of constant range) and each ring into N_c patches. Given this, the component of the space-time

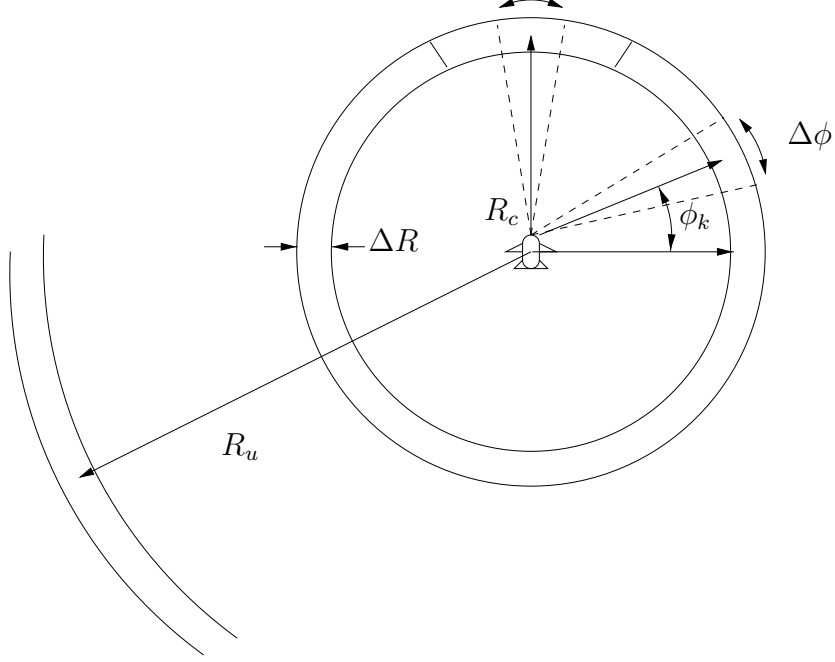


Figure 2.4: Top view of the clutter ring.

snapshot due to clutter is given by

$$\chi_c = \sum_{i=1}^{N_r} \sum_{k=1}^{N_c} \alpha_{ik} \mathbf{v}(\vartheta_{ik}, \bar{\omega}_{ik}) = \sum_{i=1}^{N_r} \sum_{k=1}^{N_c} \alpha_{ik} \mathbf{b}(\bar{\omega}_{ik}) \otimes \mathbf{a}(\vartheta_{ik}), \quad (2.19)$$

where α_{ik} denotes the random amplitude of the ik^{th} clutter patch and N_r is the number of ambiguous range rings to the radar horizon.

Due to clutter variability, returns from different patches are assumed uncorrelated as shown by

$$\mathcal{E} \{ \alpha_{ik} \alpha_{i'k'}^* \} = \sigma^2 \xi_{ik} \delta_{i-i'} \delta_{k-k'}, \quad (2.20)$$

where ξ_{ik} is the Clutter-to-Noise Ratio (CNR) for the patch. Using this fact, the clutter space-time covariance matrix \mathbf{R}_c is derived as

$$\mathbf{R}_c = \sum_{i=1}^{N_r} \sum_{k=1}^{N_c} \sigma^2 \xi_{ik} \mathbf{v}(\vartheta_{ik}, \bar{\omega}_{ik}) \mathbf{v}(\vartheta_{ik}, \bar{\omega}_{ik})^H. \quad (2.21)$$

Substituting in the 2D space-time steering vector of Eqn. (2.12) and using Kronecker product simplification properties shown in Appendix A, results in a more explicit form suitable for comparison to Chapter III results,

$$\mathbf{R}_c = \sigma^2 \sum_{i=1}^{N_r} \sum_{k=1}^{N_c} \xi_{ik} \mathbf{b}(\bar{\omega}_{ik}) \mathbf{b}(\bar{\omega}_{ik})^H \otimes \mathbf{a}(\vartheta_{ik}) \mathbf{a}(\vartheta_{ik})^H. \quad (2.22)$$

! It is important to note that, at this point in the model, range ambiguities are incorporated. However, practically all published work involving STAP ignores range ambiguities. Furthermore, the original 2D work using this 2D model ignores range ambiguities [65, page 24].

2.4 Homogeneity and Heterogeneity

The concept of homogeneity plays an important role in data generation and technique evaluation. A discussion of this concept is appropriate at this point. The 2D model as just presented involves *correlated* clutter generation distributed in range, i.e., *homogeneous* data. Actual airborne radar measurements have consistently shown the radar interference environment also contains various sources of *uncorrelated* interference [59]. Hence, real airborne radar scenarios contain *heterogeneous* interference.

! Heterogeneous data is also referred to as non-homogeneous data in the literature.

This section discusses the impact of heterogeneous interference and methods for detecting it. Target detection within range cells containing heterogeneous interference is the goal of Hybrid STAP techniques. Two-dimensional Hybrid methods are reviewed in Section 2.8 while three-dimensional advances are presented and evaluated in Chapter VI.

It is crucial to understand the Achilles heel of purely statistical approaches. Specifically, statistical techniques fail when secondary data does not accurately reflect the interference statistics in the range cell under test, e.g., in heterogeneous

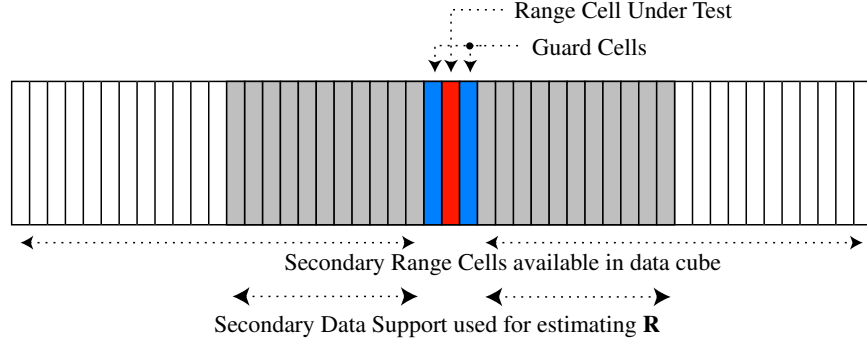


Figure 2.5: Range cell selection for homogeneous interference estimation.

data cases. As one would expect, this situation occurs when the CPI is too long, allowing the interference to change over the adaptive dwell time. However, situations commonly encountered in both airborne radar and communications systems result in heterogeneous data, independent of CPI length. This heterogeneous data occurs in many practical situations such as airborne target detection over land-sea interfaces, dense target environments, etc.

For the airborne radar problem, purely statistical STAP methods use neighboring range cells to estimate interference within the range cell under test. In a communications system, the entire data block is used to estimate the covariance matrix [44]. From the interference estimate, the STAP methods generate an adaptive interference suppression filter using the interference correlation matrix \mathbf{R} , or second-order statistics. Obviously, this approach works best when the interference statistics in neighboring range cells *accurately* reflect the interference statistics in the range cell under test; this condition is referred to as independent, identically distributed (i.i.d.) or homogeneous data.

Given i.i.d. data, the selection of neighboring range cells for interference estimation is simple. Since all data is homogeneous, a symmetric window of data of sufficient size, as shown in Fig. 2.5, is selected to support the necessary DOF for the particular approach being used. Usually, between two and four times the DOF secondary data samples are used to estimate the interference covariance matrix; two

times the DOF is Reed’s Rule [17]. The primary range cell represents the cell under test or the range cell being examined for target presence. Interference suppression within this range cell is achieved by estimating the interference using a subset of available range cells. Guard cells are introduced on either side of the range cell under test to avoid corrupting the interference estimate with possible target bleed over. Heterogeneous data is generically defined as any range cell, or cells, with interference statistics not identical to the other range cells within the datacube. The most obvious example is data including a discrete interferer or target. Other examples include abrupt terrain transitions, e.g., going from sea to land or desert to mountains. Any interference feature violating the i.i.d. definition serves as an example. The issue of corrupted interference estimates, e.g., heterogeneous data, first came to light in [15] which primarily discusses the impact of a desired signal corrupted covariance matrix estimate. The only solution offered is an increase in number of secondary data vectors to offset the impact and achieve near optimal performance. Only within the last few years has more emphasis been placed on heterogeneous data detection and working with heterogeneous data. A brief discussion of this work follows in the next subsection.

2.4.1 Heterogeneity Detection. The converse of homogeneity, heterogeneity, commonly occurs in real-world radar situations. An obvious situation is a strong aircraft sidelobe return that does not correspond to the radar look direction in either angle or Doppler, as shown in Fig. 2.6. In this case, the sidelobe return is known as a discrete interferer. When the radar is looking in a direction other than the discrete interferer location, as indicated by the mainbeam, the interference can either mask a smaller mainbeam target response or give a false target indication when a target does not exist. In a communications system, this latter problem is not characterized as a “false alarm” but rather bleed over from another conversation or data transmission. The discrete interference problem is commonly encountered with STAP techniques due to high array sidelobes. Heterogeneous data causes performance degradation be-

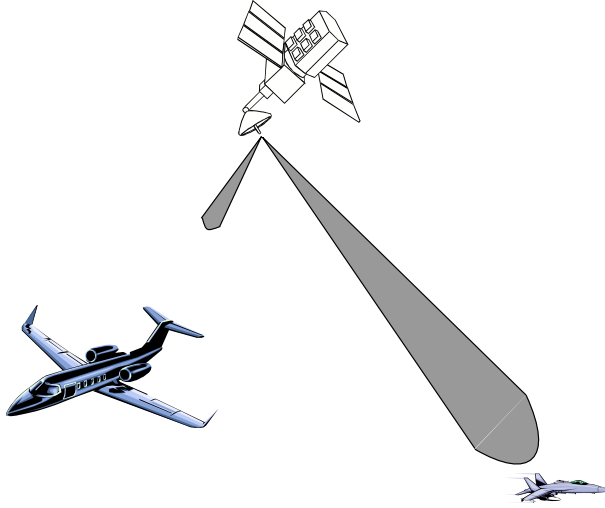


Figure 2.6: Large discrete interference infiltrates the range cell under test.

cause it perturbs the covariance matrix estimate, $\hat{\mathbf{R}}$. To minimize performance loss due to heterogeneous sample support, a Non-Homogeneity Detector (NHD) [45, 66] can be used to identify secondary data cells that do not reflect primary data, or range cell under test, statistics. These data samples are then eliminated from the correlation matrix estimation process when forming $\hat{\mathbf{R}}$ as shown in Fig. 2.7. Again, the primary range cell and guard cells are not used for interference estimation to avoid corrupting $\hat{\mathbf{R}}$. In this case, the NHD has resulted in selection of secondary range cells which are vastly different from those of Fig. 2.5. Selecting the most homogeneous range cells and excising those not reflecting the test cell statistics results in greatly improved target detection for the test cell. However, *NHDs do not address target detection within range cells identified as heterogeneous* and neighboring range cells do not possess information about the heterogeneity. Hence, statistical approaches do not suppress discrete interference in the range cell under test.

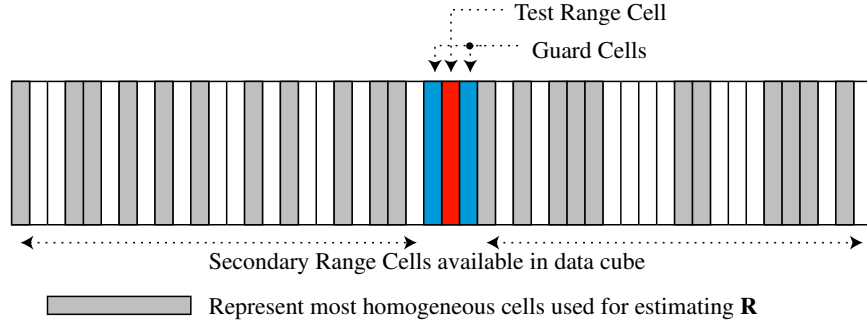


Figure 2.7: Range cell selection for heterogeneous interference estimation.

2.5 Interference Estimation: A Fundamental Choice

At this point in the development, a suitable 2D data model has been presented and a brief discussion of homogeneous data has been offered. The next step is the actual process of building an interference suppression filter, leading to a choice between deterministically and statistically based interference estimation methods. The introduction in [53] is perhaps the most interesting encapsulation of filter selection issues. Strongly slanted towards deterministic approaches, the article offers some interesting quotations from a variety of sources. Perhaps the most enticing is from [24] which states, “The assumption of randomness is an expression of ignorance.” Avoiding the more torrid debate details, this section examines the strengths and weaknesses of each approach. Although interference estimation is not specifically identified in Fig. 1.2, it is inherently embedded within each block.

2.5.1 Statistical Interference Estimation. Statistical STAP techniques enjoy considerable success because the CPI, or adaptive dwell time, is short enough such that the interference environment remains relatively stable. The adaptive dwell time merely describes how long data is collected before calculating a new set of adaptive weights. Why is this important? Within the adaptive dwell time, the method develops an interference estimate and calculates the weights required to suppress the interference. If the interference changes over the adaptivity period, the interference esti-

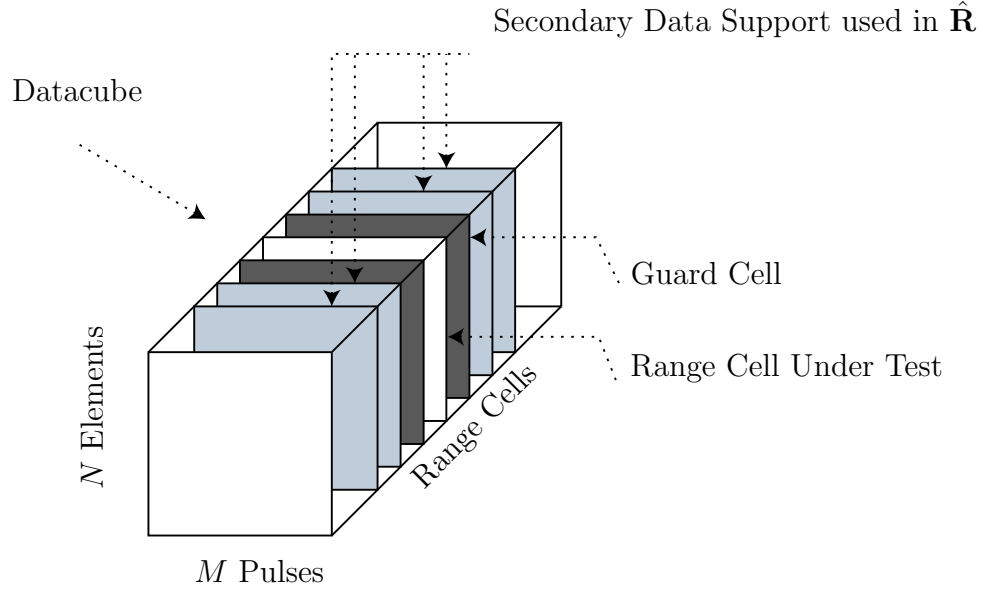


Figure 2.8: 2D datacube: data available for adaptive processing over a CPI.

mate is corrupted and the resultant filter is not properly matched to the interference environment. Most previous approaches to the interference estimation problem have taken a purely statistical viewpoint [11, 14, 17, 20, 21, 25, 26, 30, 38, 39, 41, 49, 51, 64, 65].

The purely statistical viewpoint is perhaps best understood by thinking in terms of the typical radar model. The whole purpose behind an airborne radar is to determine target presence by examining radar returns within successive range cells. Figure 2.8 shows a three-dimensional representation of the data, or returns, available to the radar within the CPI.

Each range cell contains data from all N antenna elements, the first datacube dimension. Adaptivity can be applied over all N elements or merely a subset, depending on the application and computational limitations. The second dimension is the M pulses within the CPI, or the adaptive dwell time. The number of pulses is chosen large enough to supply sufficient Degrees of Freedom (DOF) for effective interference suppression. However, choosing M too large increases the adaptive dwell time, or CPI length, to the point where the interference changes within the CPI. A

second drawback of choosing M too large is the increased computational load. The term DOF refers to the number of adaptive weights used. For example, the generic architecture of Fig. 2.1 is fully adaptive and there are NM total weights, or NM DOF. The range cells constitute the final 2D datacube dimension. The number of range cells is primarily a function of specific radar parameters such as pulse width and PRI.

From data available within the datacube, the interference within the range cell under test is estimated by averaging a large set of neighboring range cells, termed secondary data. This estimate is in the form of second-order statistics, i.e., the correlation matrix. The secondary data is assumed to be zero mean, hence the correlation matrix is synonymous with the covariance matrix. From the covariance matrix \mathbf{R} , classic statistical STAP approaches calculate an adaptive filter that suppresses interference within the range cell under test. This process is repeated for each range cell.

2.5.2 Deterministic Interference Estimation. Contrary to statistically based methods, deterministic approaches work only within the range cell under test. This approach offers one potentially huge advantage over statistical methods. The advantage is realized in heterogeneous data since discrete interference is fully characterized by the data within the range cell it occurs.

Defined succinctly, heterogeneous environments encapsulate interference scenarios where insufficient sample support exists to estimate their statistics. As such, heterogeneous environments contain correlated and uncorrelated interference. Deterministically based methods begin by co-phasing all expected target returns received on a per element, per pulse basis with no regard to interference statistical properties. Subtracting adjacent elements removes the target signal, resulting in a per element, per pulse interference snapshot. As a consequence of this approach, correlation is not accounted for and a sort of global interference suppression is offered. However, the

approach suffers in both homogeneous data and heterogeneous data environments containing significant correlated interference. These scenarios spurred research into the newest approach, the hybrid.

Most deterministic methods are factored by nature. The primary advantage offered by factored deterministic methods is the ability to suppress uncorrelated interference, the hallmark of heterogeneous data. However, these methods lack acceptable correlated interference suppression capability. The original hybrid formulation [5–7, 33] uses a factored deterministic method as a portion of the overall technique. As discussed in Chapter VI on 3D Hybrid techniques, the direct data domain approach used in the original hybrid serves as the keystone for subsequent development.

2.6 *Factored Methods*

Factored approaches represent the most simplistic interference suppression technique. Rather than work jointly, each domain is operated upon individually. For 2D factored approaches operating in the azimuth-Doppler plane, factorization translates into suppressing interference in azimuth and Doppler separately. Unfortunately, this approach suffers from a fundamental limitation – it is incapable of placing a null at a particular azimuth-Doppler location. Therefore, this interference suppression class is, by definition, suboptimal.

The value of factored techniques lies in their inherent simplicity. As Chapter IV details, the benefit of introducing elevation adaptivity is best shown by improving a method offering marginal 2D detection performance. The 2D Factored Time-Space (2D-FTS) method [65] was chosen for these reasons. Although 2D-FTS performance approaches optimal as the number of pulses within a CPI approaches infinity, it is marginal (at best) for a few pulses and azimuth channels when compared to fully adaptive joint domain methods.

2.6.1 Factored Time-Space. The fundamental architecture distinguishing factored methods is best understood by examining the simple 2D-FTS approach, which is also known as post-Doppler adaptive beamforming. The incoming sampled data is first Doppler filtered, localizing/suppressing the clutter as much as possible. This is accomplished through the matrix

$$\mathbf{B} = \mathbf{b} \otimes \mathbf{I}_N, \quad (2.23)$$

which provides Doppler filtering to the target bin given \mathbf{b} is a steering vector to the normalized Doppler of interest, e.g., under test. The Kronecker product is applied to \mathbf{b} , essentially a DFT matrix column to extract the appropriate elements of the space-time snapshot $\boldsymbol{\chi}$. Since the pulses are separated within the data structure by N samples, the identity matrix is of size N .

Given a Doppler bin of interest, an adaptive filter in azimuth is constructed based on the interference statistics within this Doppler bin. This final weight component,

$$\mathbf{w}_a = \hat{\mathbf{R}}_N^{-1} \mathbf{a}, \quad (2.24)$$

provides azimuth adaptivity. The $N \times 1$ vector is statistically based and derived from a true Wiener filter. In conjunction with previous Doppler filtering, the azimuth adaptivity completes 2D-FTS. The entire approach can be put into a single mathematical operation as

$$y = \mathbf{w}_a^H \mathbf{B}^H \boldsymbol{\chi}. \quad (2.25)$$

Obviously, the method is adaptive only within the angular (azimuth) domain since Doppler filtering is achieved with a standard transformation/steering vector. Covariance matrix estimate $\hat{\mathbf{R}}_N$ is estimated by averaging $K = 2N$ secondary data vectors oriented symmetrically about the target range cell. These secondary data vectors are taken from the Doppler filtered data, not the raw temporal samples. For K equalling twice the DOF, performance predictions are within 3 dB of optimal

(Reed's rule) [49]. The covariance estimate is simply

$$\hat{\mathbf{R}}_N = \frac{1}{K} \sum_{i=1}^{K-1} \mathbf{B}^H \boldsymbol{\chi}_i \boldsymbol{\chi}_i^H \mathbf{B}, \quad (2.26)$$

where the summation excludes the range cell under test. Output y is then applied to a threshold detection process based on desired false alarm rate.

Chapter IV illustrates the implementation of elevation adaptivity by adding another level of factorization. Drastic performance improvements are demonstrated with a detailed performance analysis of the proposed 3D-FTS technique. The role of 2D-FTS [65] is fundamental since it serves as the foundation for the proposed 3D method.

2.7 Joint Domain Methods

Joint domain approaches apply interference suppression within all available spaces. As a result, these methods are characteristically more complicated.

STAP research has traditionally focused on adaptive techniques employing statistical methods. These methods range from fully adaptive, using the entire covariance matrix, to partially adaptive. Partially adaptive methods primarily differ in how they provide dimensionality reduction. An optimal approach works jointly in all adaptive domains allowing null placement at a single location within the domain.

The proposed 3D statistical methods found in subsequent chapters uniquely collapse to the 2D case for a single vertical channel. For this reason, each statistical method presented in this section is only covered in limited detail. They are primarily presented to expose the contributions made by the proposed 3D approaches.

2.7.1 Matched Filter. The optimum filter for airborne radar applications is well known and designed to continuously maximize detection probability [17].

The work in [17] further shows this maximization is equivalent to maximizing a generalized Signal-to-Interference plus Noise Ratio (SINR).

! The equivalence of maximizing detection probability and maximizing SINR is extremely important. In many cases, the explicit development of a detection probability expression is difficult. Furthermore, generation of detection probability curves for realistic false alarm probabilities using Monte Carlo analysis can be quite time consuming. The equivalence allows comparing different techniques using SINR, a metric more easily derived and calculated.

Commonly termed the Matched Filter (MF) or the joint domain 2D-MF, the optimum filter (\mathbf{w}_{MF}) and its output are given by

$$y\mathbf{w}_{MF}^H\boldsymbol{\chi} = (\mathbf{R}^{-1}\mathbf{v})^H\boldsymbol{\chi}, \quad (2.27)$$

where \mathbf{R} is the covariance matrix of incoming space-time snapshots given by

$$\mathbf{R} = \mathcal{E}\{\boldsymbol{\chi}\boldsymbol{\chi}^H\}. \quad (2.28)$$

Of particular interest is correspondence indicating the equivalence of the likelihood ratio processor, maximum SINR filter, and Wiener filter [18]. Although actually published a few months earlier, [18] examines the results of [17] and illustrates the equivalence to previously published work. All three approaches yield the same adaptive filter for the case of a non-fluctuating target model.

! Given equivalence between the three filter approaches for the target model under consideration, the names are used interchangeably. Consistent with the literature, the filter is commonly referred to as either the MF or the Wiener filter. The same convention is used here.

The joint domain 2D-MF of Eqn. (2.27) provides a comparison benchmark for all 2D techniques since it is the optimum approach. Chapter V illustrates the 3D Matched Filter (3D-MF) based on the work of [17]. The 3D-MF provides optimum

performance and serves as the performance benchmark for techniques developed in this work.

2.7.2 Adaptive Matched Filter. The primary drawback to 2D-MF implementation is the requirement for *known* covariance. Unfortunately, interference statistics are *not* known *a priori* and must be estimated from available data. In the 2D Adaptive Matched Filter (2D-AMF) implementation [49], the known covariance matrix \mathbf{R} is replaced by the Maximum Likelihood Estimate (MLE), yielding a filter output of the form

$$y = \left(\hat{\mathbf{R}}^{-1} \mathbf{v} \right)^H \boldsymbol{\chi}. \quad (2.29)$$

This extension provides the framework necessary for implementing adaptive interference suppression in an actual airborne radar. However, the MLE introduction into the Wiener filtering processing adversely impacts performance due to the fact that it is an *estimate* rather than a known quantity.

Reed addresses the performance degradation [49] and notes the covariance matrix estimate is itself a random variable. Hence, the Wiener filter output SINR using the MLE for covariance, i.e., the AMF, is random. Reed continued the analysis and developed a performance loss expression associated with an inaccurate covariance estimate. From this analysis came the infamous Reed’s rule, “if one wishes to maintain an average loss ratio of better than one-half (less than 3 dB), at least $K = 2MN - 3 \approx 2MN$ samples of data are needed.” This rule-of-thumb established the necessary framework for adaptive interference suppression implementation in actual airborne radars. However, further complications arise in real-world applications including threshold determination issues, availability of sufficient secondary data, availability of i.i.d. (homogeneous) data, and computational load.

First, the original 2D-AMF formulation results in an output y dependent on the interference environment. The original formulation implies target presence is determined by thresholding this output. As pointed out by [41], no rule is given for

determining the threshold value. Furthermore, no predetermined threshold can be generated for a given false alarm probability because the interference environment is constantly changing. These observations led to the Generalized Likelihood Ratio Test (GLRT). The GLRT test is covariance matrix independent and attains the highly desirable Constant False Alarm Rate (CFAR) property. This test allows establishment of a predetermined threshold for a given false alarm rate. Other CFAR test statistics have been developed. In particular, the AMF CFAR test was developed independently by [51] and [21]. The GLRT and AMF CFAR represent the most commonly used in STAP literature.

Unfortunately, the CFAR test statistic developments did not relieve all the 2D-AMF restrictions. The method still requires inverting an $MN \times MN$ covariance matrix estimated using $> 2MN$ secondary data samples.

The second problem of sufficient secondary data can be sidestepped to a certain degree. Although the $2MN$ product commonly exceeds the available data in an actual airborne radar, a variety of methods can alleviate the requirement. One idea involves diagonal loading [20] while other approaches include using the actual covariance matrix structure (block Toeplitz) or developing a structured covariance estimator [13].

An even larger problem in covariance estimation occurs when using heterogeneous data. The covariance matrix MLE requires $2MN$ i.i.d., i.e., homogeneous, data samples. As research progressed, this limitation began cropping up with the first mention in [15]. The impact of using heterogeneous data and corrupted interference estimates has been previously discussed.

Finally, one major issue remains with using the 2D-AMF. The approach requires inverting a $MN \times MN$ matrix, where the space-time product MN is typically very large. The computational cost associated with the inversion typically precludes the method from real-time operation. For this reason and the ones already discussed, research efforts have migrated toward partially adaptive methods. Essentially, par-

tially adaptive methods sacrifice usable DOF to make filter implementation more feasible.

2.7.3 Joint Domain Localized. Numerous partially adaptive techniques are available for addressing the adaptive interference suppression problem, each with its own inherent advantages and disadvantages. Again, the purpose here is not to discuss each method in detail, but rather to maintain focus on work directly relevant to the 3D advances presented in subsequent chapters.

One of the most elegant joint domain partially adaptive techniques is the 2D Joint Domain Localized (2D-JDL) approach [64]. This method illustrated the advantages of working in beamspace, i.e., the radar angle-Doppler domain, rather than the space-time domain. Several advantages were highlighted. Particularly important is the ability to easily scale the covariance matrix size to reduce dimensionality and alleviate computational issues. The dimensionality reduction also provides inherent advantages for reducing susceptibility to heterogeneous data. For these reasons, the first 2D hybrid formulation [5–7, 33] used this technique for statistical adaptivity.

Conceptually, 2D-JDL is extremely simple. The method is well suited to practical implementation and, as will be shown in the hybrid discussion, provides maximum design flexibility. The 2D-JDL adaptive processing technique is encapsulated as

$$\mathbf{v}^H \mathbf{T} (\mathbf{T}^H \mathbf{R} \mathbf{T})^{-1} \mathbf{T}^H \boldsymbol{\chi} = \mathbf{w}_{2D}^H \mathbf{T}^H \boldsymbol{\chi}, \quad (2.30)$$

where interference covariance matrix \mathbf{R} is of dimension $MN \times MN$ and reflects the covariance between the planar array (spatial sampling) and temporal samples. The 2D adaptive weight vector \mathbf{w}_{2D} operates on the *transformed* data $\mathbf{T}^H \boldsymbol{\chi}$, hence the method is a joint domain or beamspace approach. Figure 2.9 illustrates the ideal 2D-JDL process.

Transformation matrix \mathbf{T} of (2.30) provides a conversion from element-time space to azimuth-Doppler space. This matrix transforms the data to a localized

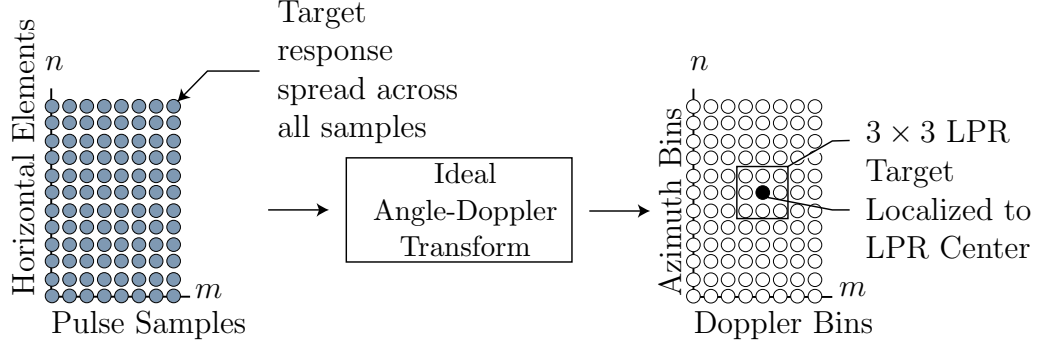


Figure 2.9: Block diagram illustrating ideal 2D-JDL. The transformation is shown only for the range cell under test, all data is transformed. Due to steering vector orthogonality (ideal case), the target is localized to the LPR center bin.

region within the transform domain, where “focused” adaptivity is implemented. The 2D transformation matrix to the Localized Processing Region (LPR) is given by,

$$\mathbf{T} = \begin{bmatrix} \mathbf{b}(\bar{\omega}_{-1}) & \mathbf{b}(\bar{\omega}_0) & \mathbf{b}(\bar{\omega}_1) \end{bmatrix} \otimes \begin{bmatrix} \mathbf{a}(\phi_{-1}, \theta_t) & \mathbf{a}(\phi_0, \theta_t) & \mathbf{a}(\phi_1, \theta_t) \end{bmatrix}. \quad (2.31)$$

The \mathbf{T} of (2.31) corresponds to a 3×3 LPR and represents the ideal transformation.

! The transformation matrix role is crucial to subsequent work. The sole purpose is transforming to beamspace, hence any method achieving this transformation is suitable. This concept is key to the idea behind hybrid techniques.

Generically, the LPR size is $\eta_a \times \eta_b$ making \mathbf{T} of dimension $MN \times \eta_a \eta_b$, where $\eta_a \leq N$ represents the size in azimuth and $\eta_b \leq M$ represents the size in Doppler. Bounding each LPR dimension ensures the interference covariance matrix across the region remains non-singular. LPR size is variable and obviously scenario dependent; interference problems of higher-order require a larger LPR to achieve results approaching the 2D-AMF. The LPR covariance matrix is found by

$$\mathbf{R}_{\text{LPR}} = \mathcal{E} \{ \mathbf{T}^H \boldsymbol{\chi} \boldsymbol{\chi}^H \mathbf{T} \}, \quad (2.32)$$

and is of dimension $\eta_a\eta_b \times \eta_a\eta_b$ corresponding to a potential $\eta_a\eta_b \leq MN$ DOF (weight vector \mathbf{w}_{2D} length). The weights (Wiener filter) are calculated using the transformed steering vector,

$$\mathbf{w}_{2D} = \mathbf{R}_{LPR}^{-1} \mathbf{T}^H \mathbf{v}. \quad (2.33)$$

The conventional Maximum Likelihood Estimator (MLE) of the interference covariance within the LPR is substituted for \mathbf{R}_{LPR} in the estimated interference case. Consistent with Reed's rule, the required secondary data support for the MLE is $2\eta_a\eta_b$ to achieve performance within 3 dB of the known covariance case [49].

Building upon the 2D-JDL work, the 3D-JDL method is developed in Chapter V. The necessary modifications are developed successively with appropriate comparisons to the original approach. Again, previous 2D work serves an intricate role in qualifying the 3D advancements.

2.8 Hybrid Methods

Hybrid methods were borne out of a basic realization. Given the ability to detect heterogeneous data, a fundamental question arose – how can targets be detected in regions declared heterogeneous? The impact of heterogeneous data on target detection within *homogeneous* locations was effectively mitigated through various techniques involving prudent secondary sample support selection. Yet, there was no answer to the question posed. Consequently, the advent of the first hybrid technique occurred [5–7, 33].

The original 2D hybrid is founded on the 2D-JDL approach, where a transformation is necessary to apply interference suppression in the azimuth-Doppler beamspace. In the original 2D-JDL formulation [64], the ideal transform is used. For simulated data, the ideal transform is a set of steering vectors or columns of the Discrete Fourier Transform (DFT) matrix. In this ideal world, a target is localized to a single azimuth-Doppler bin and the localized adaptivity region in beamspace is

easily scaled. Subsequent research [4, 6–8, 10] found that real-world antenna array effects resulted in performance degradation. A more appropriate transform was the actual measured array steering vectors, containing mutual coupling effects, array element mismatch effects, etc.

A side benefit of research on improving the transformation process was the realization that the transformation could be used for other purposes. Instead of using the transform merely as an avenue to reach the azimuth-Doppler beamspace, it could be used to simultaneously suppress uncorrelated interference. This realization represented the birth of hybrid interference suppression techniques.

The original hybrid approach has been applied to the Ground Moving Target Indication (GMTI) problem and shown to offer substantial performance gains [1–3, 9]. However, no subsequent work has been done on the original technique to improve its performance or address its limitations.

The literature devoted specifically to hybrid methods is relatively small due to the newness of the concept. Chapter VI expands on the original method through incorporation of elevation adaptivity. The first stage of the original 2D Hybrid suffers from the drawbacks of using a factored approach. Chapter VI expands the concept of hybrid processing by offering a technique with substantial processing benefits and performance improvements over the original approach. The role of the original concept is significant since it serves as the cornerstone for the improvements and complete redesign. A review of the 2D hybrid method is offered in the follow subsections.

2.8.1 Hybrid Deterministic Approach. A unique adaptive array property is its ability to steer (physically or virtually) the receive antenna mainlobe to a desired look direction while simultaneously placing deep pattern nulls in the interference direction(s). Pattern null placement in the interference direction is achieved automatically without extensive *a-priori* interference knowledge. Classic statistical

techniques achieve interference suppression using an interference covariance matrix. This matrix is typically estimated using secondary data obtained from range cells neighboring the range cell under test. Statistical techniques fail when secondary data statistics do not accurately reflect interference statistics in the range cell under test, e.g., in a heterogeneous data environment. Heterogeneous data conditions occur in many practical situations such as airborne surveillance over land-sea interfaces, dense target environments, etc.

A NHD can identify secondary data cells containing interference that does not reflect primary data statistics and minimize performance loss due to heterogeneous sample support [45, 66]. The heterogeneous data samples are then eliminated during covariance matrix estimation. However, NHDs do not support target detection within range cells identified as heterogeneous. Given neighboring range cells do not possess information about the non-homogeneity, statistical techniques cannot suppress discrete interference in the range cell under test. The following review describes an adaptive technique for countering discrete interference in the primary range cell.

The statistical technique's inability to counter heterogeneities in the range cell under test motivates research into deterministic or direct data domain techniques. These techniques only use primary range cell data, eliminating sample support problems associated with statistical approaches. This particular research field has only recently emerged with a primary focus on one-dimensional spatial adaptivity [47, 54]. This section introduces a factored two-dimensional direct data domain technique reformulated from earlier non-statistical attempts at adaptive processing. Researchers have developed a true two-dimensional direct data technique [55], perhaps superior to that presented here. However, it has its own limitations and is not discussed here because it lacks relevance to this work's primary focus.

Consider the linear array of equally spaced, isotropic point sensors shown in Fig. 2.10. Each of the N elements receives returns corresponding to M transmitted pulses per CPI. This space-time data is used to decide between target presence or

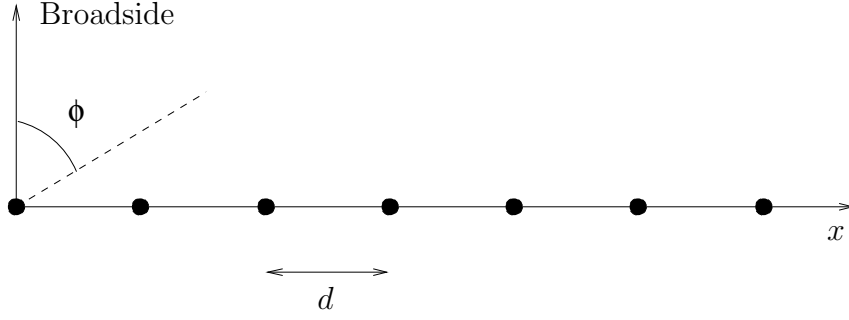


Figure 2.10: Linear array of isotropic point sensors.

absence at a given azimuth look direction $\phi = \phi_t$ and normalized Doppler frequency $\bar{\omega} = \bar{\omega}_t$. The received data for a particular range cell can be written as a $N \times M$ matrix \mathbf{X} , where $\mathbf{X}_{n,m}$ represents complex returns at the n^{th} element due to the m^{th} pulse. Data matrix \mathbf{X} is a sum of signal, external interference, and thermal noise components and essentially represents a cut of the 2D datacube in Fig. 2.8. Using the desired look direction and velocity $(\phi_t, \bar{\omega}_t)$, signal matrix \mathbf{S} can be written in the same matrix form of \mathbf{X} using the Kronecker product \otimes as follows:

$$\mathbf{S} = \xi_t \mathbf{a} \otimes \mathbf{b}^T = \xi_t \mathbf{a} \mathbf{b}^T, \quad (2.34)$$

$$\mathbf{a} = [1 \ z_a \ z_a^2 \ \dots \ z_a^{(N-1)}]^T, \quad (2.35)$$

$$\mathbf{b} = [1 \ z_b \ z_b^2 \ \dots \ z_b^{(M-1)}]^T, \quad (2.36)$$

$$z_a = e^{j \frac{2\pi}{\lambda} d \sin \phi_t}, \quad (2.37)$$

$$z_b = e^{j 2\pi \bar{\omega}_t}, \quad (2.38)$$

where ξ_t is the signal amplitude and d is the distance between two adjacent elements. Vectors \mathbf{a} and \mathbf{b} form the spatial and temporal steering vectors, respectively. It is important to note that target returns from an azimuth angle and/or velocity other than the desired look azimuth/velocity are effectively discrete interferers. Ideally, target detection should be declared only if the target return identically matches the look direction and velocity.

Equation (2.35) indicates the signal progresses by a constant phase z_a from one element to the next for each pulse. Therefore, the signal component cancels out of the $\mathbf{X}_{n,m} - z_a^{-1}\mathbf{X}_{n+1,m}$ term, leaving only interference components. Entries in the $M \times (N - 1)$ matrix \mathbf{C} , defined to be

$$\begin{bmatrix} \mathbf{X}_{0,0} - z_a^{-1}\mathbf{X}_{1,0} & \mathbf{X}_{1,0} - z_a^{-1}\mathbf{X}_{2,0} & \cdots & \mathbf{X}_{N-2,0} - z_a^{-1}\mathbf{X}_{N-1,1} \\ \mathbf{X}_{0,1} - z_a^{-1}\mathbf{X}_{1,1} & \mathbf{X}_{1,1} - z_a^{-1}\mathbf{X}_{2,1} & \cdots & \mathbf{X}_{N-2,2} - z_a^{-1}\mathbf{X}_{N-1,2} \\ \vdots & \vdots & \vdots & \vdots \\ \mathbf{X}_{0,M-1} - z_a^{-1}\mathbf{X}_{1,M-1} & \mathbf{X}_{1,M-1} - z_a^{-1}\mathbf{X}_{2,M-1} & \cdots & \mathbf{X}_{N-2,M-1} - z_a^{-1}\mathbf{X}_{N-1,M-1} \end{bmatrix} \quad (2.39)$$

are composed of interference terms only.

! The matrix \mathbf{C} is analogous to the *transpose* of its 3D extension \mathbf{A} on page 177. The convention used here matches the original development in [5–7, 33]. Unfortunately, it adds unnecessary complexity since the outer product must be expressed as $\mathbf{C}^T \mathbf{C}^*$ instead of the more conventional $\mathbf{A} \mathbf{A}^H$.

Consider the scalar expressions

$$G = \mathbf{w}_a^H \mathbf{a}_{N-1} \mathbf{a}_{N-1}^H \mathbf{w}_a, \quad (2.40)$$

$$I = \mathbf{w}_a^H \mathbf{C}^T \mathbf{C}^* \mathbf{w}_a, \quad (2.41)$$

where \mathbf{a}_{N-1} is the vector comprising the first $(N - 1)$ entries of steering vector \mathbf{a} . The term G in Eqn. (2.40) represents the power gain in the look direction due to weights \mathbf{w}_a . The I in Eqn. (2.41) represents residual interference power. Notice that matrix \mathbf{C} is defined such that the element phase progression appears across *columns* rather than the rows, forcing the transpose operation when applying the weight vector in I . The hybrid work in Chapter VI formulates a 3D version of this matrix in a manner reflecting traditional STAP techniques, removing the need for a transpose and simplifying the development. The direct data domain technique

obtains the set of weights maximizing the difference between the two terms, i.e.

$$\max_{\|\mathbf{w}_a\|_2=1} [G - \kappa^2 I] = \max_{\|\mathbf{w}_a\|_2=1} \mathbf{w}_a^H [\mathbf{a}_{N-1} \mathbf{a}_{N-1}^H - \kappa^2 \mathbf{C}^T \mathbf{C}^*] \mathbf{w}_a. \quad (2.42)$$

The constraint $\|\mathbf{w}_a\|_2 = 1$ guarantees a finite solution and the constant κ term serves as a sidelobe control parameter.

Using the Lagrange multiplier method, the weight vector maximizing $G - \kappa^2 I$ in Eqn. (2.42) is the eigenvector corresponding to the largest eigenvalue of the matrix $\mathbf{a}_{N-1} \mathbf{a}_{N-1}^H - \kappa^2 \mathbf{C}^T \mathbf{C}^*$. This weight vector constitutes the spatial adaptive weights and is length $(N - 1)$, representing a one DOF loss in the spatial domain. This loss compares favorably with other non-statistical techniques where close to one-half the DOF are lost [54].

An optimum value for κ has never been determined. Clearly, choosing $\kappa = 0$ eliminates the interference term. The adaptive weight vector then corresponds to the steering vector \mathbf{a}_{N-1} , corresponding to maximum sidelobe control at the expense of interference suppression. Conversely, if $\kappa \rightarrow \infty$ the interference term dominates to the point where the mainbeam may not be retained.

In the temporal domain, the signal progresses by the same phase z_b from one pulse to the next at each element. Therefore, the signal component cancels out in terms such as $\mathbf{X}_{n,m} - z_b^{-1} \mathbf{X}_{n,m+1}$. A formulation paralleling Eqn. (2.39) through Eqn. (2.42) can be used to obtain a $(M - 1)$ length temporal weight vector \mathbf{w}_b . The composite NM length space-time adaptive weight vector is then given by

$$\mathbf{w}(\phi_t, \bar{\omega}_t) = \begin{bmatrix} \mathbf{w}_b(\bar{\omega}_t) \\ 0 \end{bmatrix} \otimes \begin{bmatrix} \mathbf{w}_a(\phi_t) \\ 0 \end{bmatrix}. \quad (2.43)$$

The zeros appended to the spatial and temporal weight vectors represent lost DOF in space and time. Using this adaptive weight vector, the statistic used for detection

via threshold comparison at angle ϕ_t and normalized Doppler $\bar{\omega}_t$ is given by

$$\chi(\phi_t, \bar{\omega}_t) = \mathbf{w}^H \text{vec}(\mathbf{X}), \quad (2.44)$$

where $\text{vec}(\cdot)$ stacks the columns of \mathbf{X} into a length $NM \times 1$ vector [43].

The above formulation effectively side-steps the high sidelobe problems associated with previous direct data domain techniques [56] and resultant signal estimates are free of heterogeneous effects. However, direct data domain techniques in general fail to suppress correlated interference to the degree possible with statistical STAP techniques.

Unfortunately, the deterministic method as developed here has some drawbacks. The primary limitation is that it is a factored approach. Recently, a joint deterministic approach was introduced [55]. The new method still incurs a significant loss in DOF as inherent to the underlying framework used. Furthermore, the general limitation of deterministic approaches is not addressed: the method is incapable of suppressing correlated interference to the degree offered by statistical methods.

2.8.1.1 Similarity to Interferometric Clutter Erasure. The deterministic technique used in the original hybrid formulation and reviewed in Section 2.8.1, conceptually resembles a method independently developed and referred to as Interferometric Clutter Erase (ICE). The factored elevation adaptivity implemented in 3D-FTS is similar to ICE. The ICE technique is designed for ground clutter elimination/cancellation on the basis of height discrimination. As a stand-alone technique, initial research efforts using a simple ICE technique showed +10 dB of clutter suppression with two elevation channels [67]. Similarly, the research efforts of Chapter IV show +15 dB improvement using two elevation channels. Expanding the ICE technique in 3D-FTS to more elevation channels offers considerably more improvement.

Prior to the invention of ICE, the only discriminate available for discriminating airborne targets from ground clutter was motion (using Doppler and/or Space Time Adaptive Processing, STAP). The use of ICE is in addition to motion discrimination and improvements provide much greater (deeper) sub-clutter visibility/target detectability. The original ICE approach is an interferogram in its complex form, $e^{j(r_1-r_2)}$, for the purpose of co-phasing ground return signals in two interferometric channels. After the data phase in one channel is matched to the other channel, for signals reflected from the ground, signals in the two interferometer channels are subtracted, effectively cancelling ground clutter returns. However, signals reflected from targets above the ground are not cancelled since their returns are not co-phased by the interferogram phase factor [19].

Some residual clutter energy remains after co-phasing and interferometric channel subtraction. The residue results from the fact that within a given range/cross-range resolution rod, not all clutter is at exactly the same height and co-phasing is not perfect for all scattering sources. As range resolution and/or cross-range resolution improve, there is less height variation within a given resolution rod and ICE cancellation improves.

Another source of relevant literature involved a simple version of ICE, called Adaptive Clutter Erasure (ACE), which employed no Doppler beam sharpening. Simulations of this elementary version of ICE provided 10 dB of clutter cancellation in hilly terrain [67]; these favorable results foretold the great potential of ICE when used in concert with Doppler, STAP, and other clutter suppression techniques.

2.8.2 Hybrid Statistical Approach. This section presents a STAP approach achieving benefits of both direct data domain and statistical methods. The hybrid approach uses the deterministic technique as a pre-filter to suppress discrete interferers present in the range cell under test using a process illustrated in Fig. 2.11.

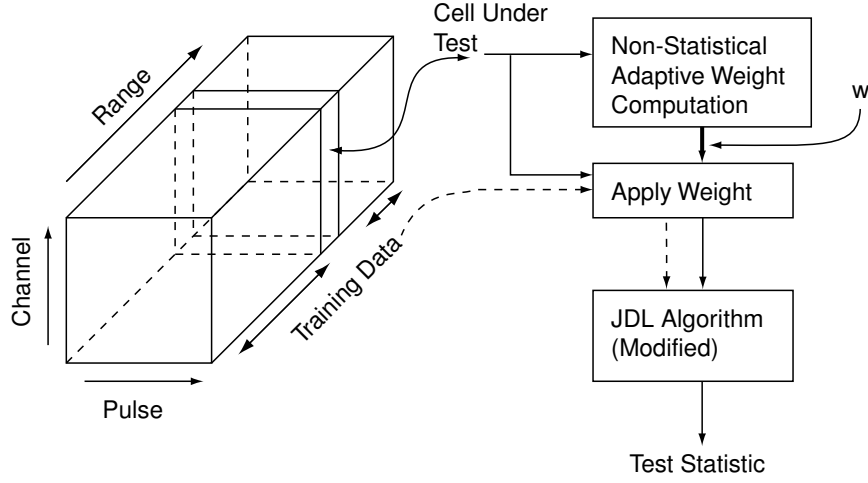


Figure 2.11: 2D hybrid technique block diagram.

The technique serves to provide an adaptive transformation between the space-time and angle-Doppler domains.

Every STAP technique estimates the signal component in the desired look direction (angle and Doppler). STAP techniques can generally be viewed as an adaptive transformation to this particular angle and Doppler. Creating a set of look angles and Doppler frequencies allows the STAP technique to perform a function similar to the Fast Fourier Transform (FFT). It must be emphasized that this transformation is non-invertible and results in some information loss. However, the information loss may be beneficial in that discrete interferers may be suppressed within the range cell under test using subsequent direct data domain processing.

The hybrid technique adaptively processes space-time data in two stages. The first stage is the direct data domain adaptive transformation detailed in Section 2.8.1. The first stage output lends itself to application of a post-Doppler, beamspace statistical technique forming the second stage adaptive processing. An enhanced 2D-JDL version [10,64] has been used as the second stage. The 2D-JDL technique suppresses interference in a LPR of the angle-Doppler domain. Figure 2.11 shows the two-stage hybrid technique block diagram.

Mathematically, the transformation to a predetermined LPR is accomplished through a matrix operator \mathbf{T} . The angle-Doppler data is given by $\tilde{\mathbf{x}} = \mathbf{T}^H \text{vec}(\mathbf{X})$. The steering vector is transformed in the same manner. A sample \mathbf{T} for a 3×3 LPR is

$$\mathbf{T} = \begin{bmatrix} \mathbf{w}_{-1,-1} & \mathbf{w}_{-1,t} & \mathbf{w}_{-1,1} & \mathbf{w}_{t,-1} & \mathbf{w}_{t,t} & \mathbf{w}_{t,1} & \mathbf{w}_{1,-1} & \mathbf{w}_{1,t} & \mathbf{w}_{1,1} \end{bmatrix}, \quad (2.45)$$

where $\mathbf{w}_{i,j}$ corresponds to a weight vector with mainbeam at ϕ_i and $\bar{\omega}_j$ and is equivalent to $\mathbf{w}(\phi_i, \bar{\omega}_j)$. For the general structure of this equation, the weight vector $\mathbf{w}_{-1,t}$ has a mainbeam corresponding to an azimuth angle ϕ one bin below the LPR center azimuth and normalized Doppler equal to the LPR center normalized Doppler. Bin size is determined by design with limitations consistent with standard sampling concepts.

Because the 2D-JDL technique only operates within a localized region of the angle-Doppler domain, fewer DOF are used and secondary data support requirements are correspondingly reduced [64]. These advantages are carried over to the hybrid technique.

2.8.3 Numerical 2D Examples. The results presented here summarize recent 2D work in analyzing and comparing 2D-JDL, direct data domain, and 2D Hybrid technologies [5–7]. The hybrid technique is tested on data generated using the 2D physical model presented by Jaffer [39] and Ward [65], and implemented by Roman and Davis [52]. Comparison of adapted beam patterns associated with JDL, the direct data domain, and the hybrid techniques illustrate the motivation for, and improved performance due to, the hybrid technique.

The adapted antenna pattern plots presented in Figs. 2.12 through 2.17 represent mean pattern values for over 200 independent realizations. Vertical bars represent the standard deviation over the 200 trials. This method was necessitated because the direct data domain technique is non-statistical and is based solely on

a single data set/realization. Operating with known covariance to obtain an ideal pattern, as in 2D-JDL or other statistical techniques, was not an option.

The simulation includes the effects of clutter, white noise, two barrage noise jammers, and a discrete interferer. The simulated linear antenna array consists of $N = 18$ elements and a CPI length of $M = 18$ pulses. Two 40 dB jammers are located at azimuth angles of 45° and -20° . The discrete interferer is simulated by injecting a 40 dB target having the same normalized Doppler as the look Doppler but at a different azimuth angle of $\phi = -51^\circ$. The look direction is set to an azimuth angle of $\phi_t = 0^\circ$ and normalized Doppler $\bar{\omega}_t = 1/3$. The 2D-JDL technique uses three angles and three Doppler frequencies centered around the look direction for a total LPR size of $N_{\text{DOF}} = 9$ DOF. The number of secondary data vectors used to estimate the covariance matrix is set to $2N_{\text{DOF}} = 18$.

Figures 2.12 and 2.13 illustrate the standard 2D-JDL antenna patterns [64] along target azimuth and Doppler. Figure 2.12 shows the technique has placed distinct nulls (approximately 60 dB below peak) in the two jammer directions. The discrete interferer does not contribute to the covariance matrix estimate and therefore is not nulled by the technique. Figure 2.13 shows a deep null at $\bar{\omega} = 0$ that effectively suppresses mainlobe clutter. The mainlobe is formed at the Doppler look direction of $\bar{\omega}_t = 1/3$.

Antenna patterns for the 2D direct data domain technique are presented in Figs. 2.14 and 2.15. It bears repeating that a direct data domain technique uses *only* data from the range cell under test for adaptation and hence does not require any secondary data. Figure 2.14 shows the direct data domain technique is effective in countering a discrete interferer in the range cell under test. The adapted angle pattern shows a distinct null (approximately 60 dB below peak) in the discrete direction of -51° . However, Figs. 2.14 and 2.15 also highlight a direct data domain technique limitation; jammer nulls are not as deep as in the case of 2D-JDL (approximately 45 dB below peak). The null near $\bar{\omega} = 0$ in the clutter spectrum is also not as deep

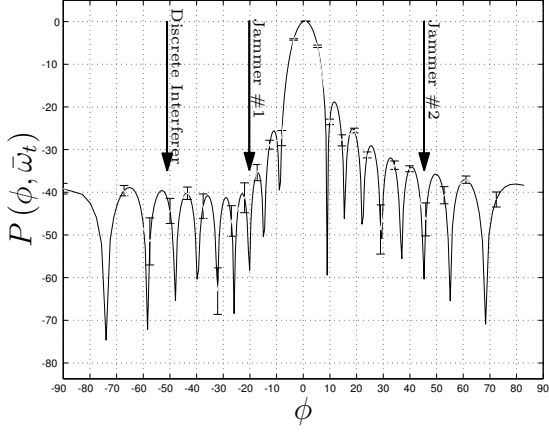


Figure 2.12: Standard JDL technique antenna pattern at target Doppler.

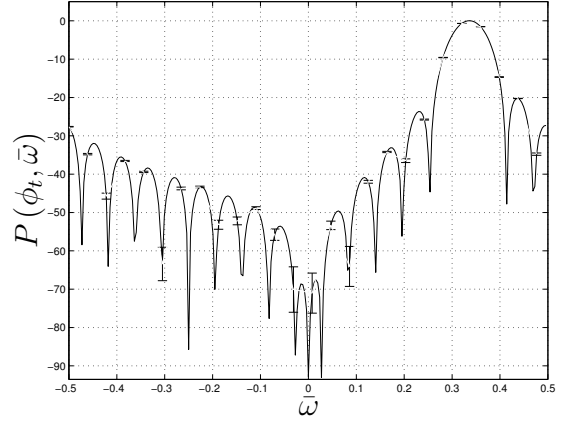


Figure 2.13: Standard JDL technique antenna pattern at target azimuth.

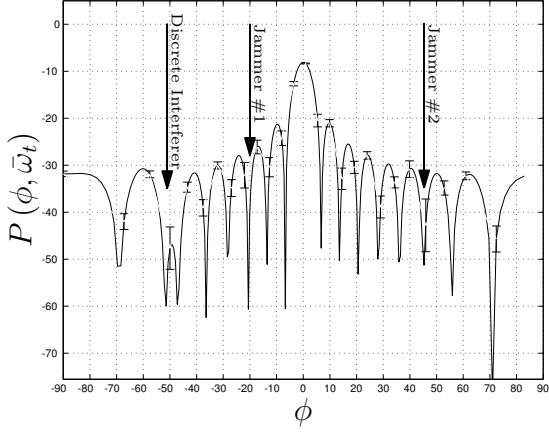


Figure 2.14: Direct data domain technique antenna pattern at target Doppler.

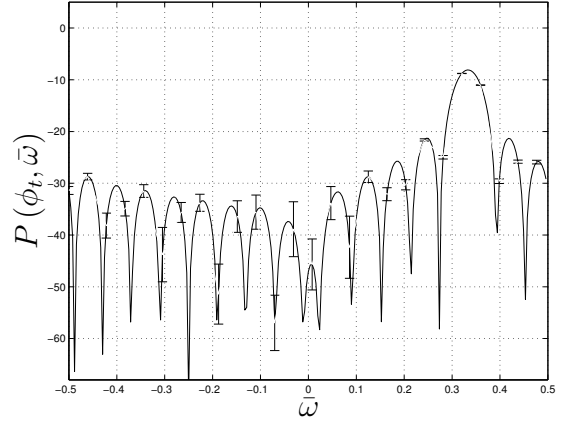


Figure 2.15: Direct data domain technique antenna pattern at target azimuth.

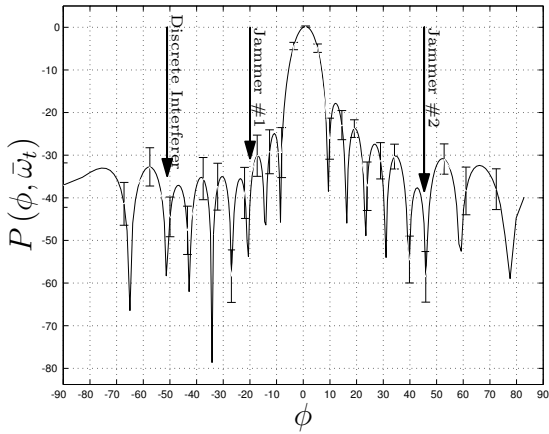


Figure 2.16: Hybrid technique antenna pattern at target Doppler.

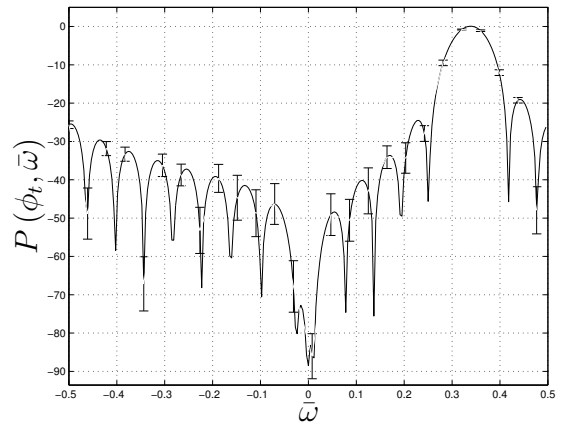


Figure 2.17: Hybrid technique antenna pattern at target azimuth.

(approximately 35 dB below peak), i.e., the mainbeam clutter is not as effectively suppressed. Also, there is a slight shift in the mainbeam clutter null, essentially making it a minimum at $\bar{\omega} = 0$ rather than the distinct null of statistical algorithms. This shift results from basing weight determination on a single data set rather than a statistical sampling.

Results presented in Fig. 2.12 through Fig. 2.15 provide the motivation for hybrid technique development. The direct data domain technique can be used as the first stage to screen out discrete interferers. A statistical technique, such as 2D-JDL, can then be used to suppress correlated interference. Figures 2.16 and 2.17 show antenna beam patterns resulting from the hybrid technique. Figure 2.16 shows the hybrid technique combines advantages of both statistical and non-statistical adaptive processing; the adapted azimuth pattern exhibits deep nulls at -51° , -20° and 45° , approximately 60 dB, 52 dB, and 58 dB below the peak, respectively. Likewise, Fig. 2.17 shows the adapted pattern has a deep null at $\bar{\omega} = 0$ resulting in effective nulling of mainbeam clutter.

2.9 Summary

This Chapter introduced the current state-of-the-art in 2D STAP techniques. In developing the literature review, attention is focused on ideas and methods relevant to 3D advances presented in subsequent chapters. The review is presented in a manner following the 2D research progression of Fig. 1.2, allowing reliable comparison of 3D advances to previously published 2D work.

Each portion of the review serves as a stepping stone into the following chapters. Section 2.2 provides a 2D STAP overview to remind the reader of the generic radar interference suppression goal and the fundamental architecture assumed with a phased array radar. The overview was purposely broad and is intended to serve as a conceptual blueprint.

Moving beyond concept into detail, Section 2.3 presented the 2D mathematical model representing actual radar returns from a uniform linear array antenna. The model incorporates significant airborne radar factors with the inclusion of receiver thermal noise, ground clutter, and barrage noise jamming. As previously mentioned, results of the 2D model, and proposed 3D model in Chapter III, compare well with measured airborne radar data.

The interference model discussion imposed certain assumptions. Based on these assumptions, the data model provides a homogeneous interference environment characterization. This concept is crucial when comparing to measured data since real airborne radars commonly encounter heterogeneous data. These ideas forced the discussion of homogeneous and heterogeneous data in Section 2.4. The two data types are compared and contrasted with a careful review of associated impacts.

Several sections are devoted to characterizing the interference environment, the first step in designing effective adaptive interference suppression techniques. Interference estimation plays a key role in building a suppression approach and leads to fundamental differences between deterministic and statistical methods. Section 2.5 examined related issues and analyzed the strengths and weaknesses of each approach.

Constructing actual interference suppression filters requires yet another fundamental choice between two primary STAP approaches: factored and joint domain. Section 2.6 defined the factored approach and examined the 2D-FTS method. The 2D-FTS approach is extended to 3D in Chapter IV, making the discussion fundamental to qualifying 3D performance.

By definition, factored approaches are suboptimal. Consequently, the 2D review progressed into a discussion of the optimal joint domain methods presented in Section 2.7. A variety of reasons force further examination of suboptimal joint domain approaches. Focus is maintained on the 2D-JDL method since it serves as a foundation to the proposed 3D-JDL method of Chapter V.

The final section provides motivation for exploration and development of the hybrid concept, an approach that reaps benefits of several contrasting approaches and melds them into a single framework. The work presented in Section 2.8 is key to Chapter VI since it represents the initial hybrid concept.

III. Three-Dimensional Radar Model

The most important factor in evaluating the performance of any interference suppression method is building an accurate data model. For this reason, this is the first step in the research chain of Fig. 1.2. As the figure shows, the 3D extensions of this work parallel the 2D development process.

This chapter addresses the extension of a common 2D radar data model used in STAP analysis to include elevation elements and their associated returns. This addition represents a significant change in the underlying framework and requires development beginning with the transmitted waveform structure. The general approach of the 3D physical model is extended from Ward [65], although it was originally offered by Jaffer [39].

3.1 Airborne Radar System

The airborne radar of interest is Pulsed Doppler (PD). The general antenna array structure can be considered as P banks of uniformly spaced N element linear arrays located along the x -axis and stacked along the z -axis as illustrated in Fig. 3.1. The elements are uniformly spaced in azimuth and elevation at inter-element distances d_x and d_z , respectively, which are not necessarily equal. An arbitrary vector describing the location of the np^{th} element is given by

$$\mathbf{d}_{np} = nd_x\hat{\mathbf{x}} + pd_z\hat{\mathbf{z}}, \quad (3.1)$$

where $n = 0, 1, \dots, N - 1$, $p = 0, 1, \dots, P - 1$, and $\hat{\mathbf{x}}$ and $\hat{\mathbf{z}}$ are unit vectors.

This work focuses on a side-looking radar with a velocity vector parallel to the positive x -axis ¹.

¹The velocity vector is allowed to deviate from this orientation for cases requiring accurate characterization of aircraft crab.

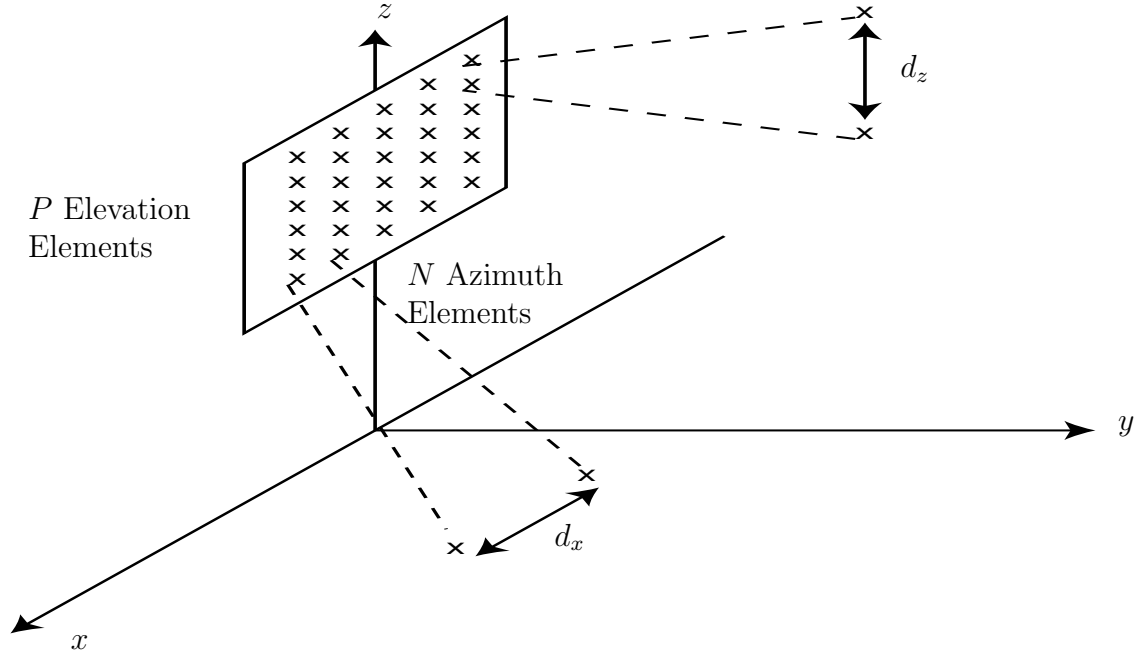


Figure 3.1: Research focuses on a planar antenna array oriented in the x - z plane.

The coordinate system of Fig. 3.2 is established for the radar using common elevation (θ) and azimuth (ϕ) angle definitions referenced to radar boresight. By convention, the radar elevation angle θ is negative when measured from radar boresight towards the ground. In the reference cartesian coordinate system², this angle is measured from the y -axis in the direction of positive z -axis, i.e., negative angles represent downward direction. Similarly, radar azimuth angle ϕ is measured from the antenna array boresight with positive angles measured from the positive y -axis towards the positive x -axis, i.e., towards the nose of the aircraft. Figure 3.3 clearly shows the azimuth angle in a two-dimensional illustration.

Conversion from radar angular coordinates (θ, ϕ) to cartesian coordinates oriented to the antenna array is given by [65]

$$\hat{\mathbf{k}}(\theta, \phi) = \cos \theta \sin \phi \hat{\mathbf{x}} + \cos \theta \cos \phi \hat{\mathbf{y}} + \sin \theta \hat{\mathbf{z}}, \quad (3.2)$$

²In the cartesian coordinate system, the origin (0,0,0) is located at the array origin.

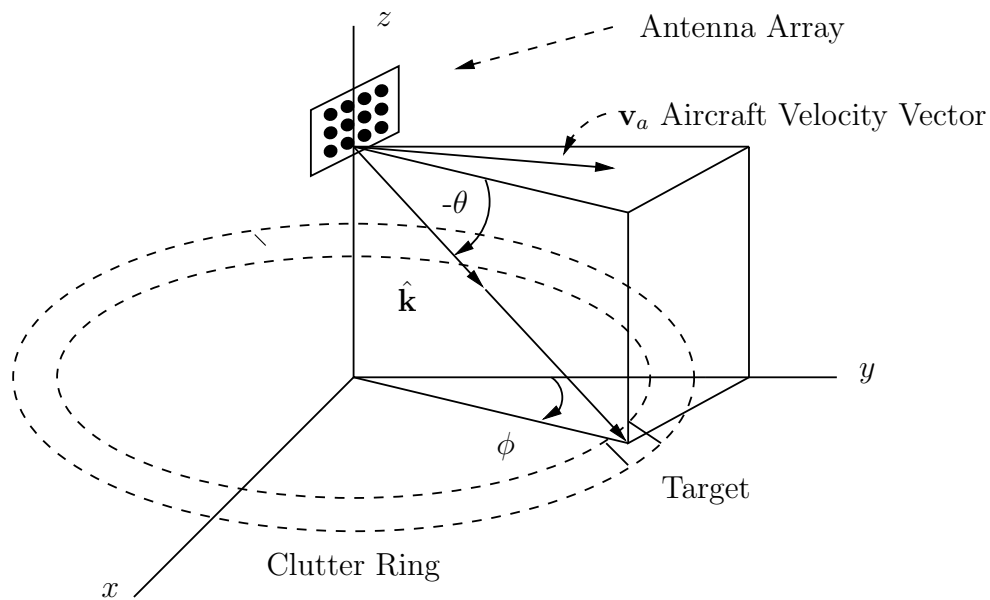


Figure 3.2: Radar platform geometry. Antenna array oriented in the x - z plane. Case where velocity vector \mathbf{v}_a is not aligned with the x -axis indicating significant crab angle.

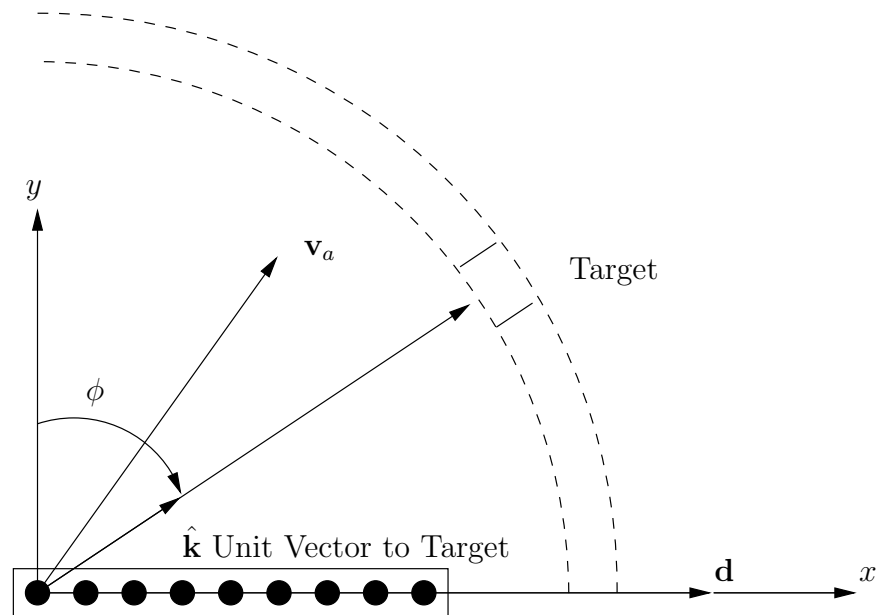


Figure 3.3: Geometry for array of uniformly spaced antenna elements. Antenna array is normal to the paper in the x - z plane with boresight extending along the y -axis.

where the *hat* (^) symbol above bold lower case variables denote unit magnitude vectors. Unit vector $\hat{\mathbf{k}}$ serves two purposes. First, it describes a unit vector in the direction of a target located at (θ, ϕ) in terms of the cartesian coordinate reference system. Second, it provides a transformation from the radar angular coordinate system to the cartesian coordinate system. Each cartesian component in Eqn. (3.2) is essentially a projection of unit vector $\hat{\mathbf{k}}$ onto the respective cartesian unit vector $\hat{\mathbf{x}}$, $\hat{\mathbf{y}}$, and $\hat{\mathbf{z}}$. The radar angular coordinate system is very similar to the spherical system, however, the angles are referenced to different axes.

3.2 Transmitted Waveform

Given the general geometric radar description of Section 3.1, the radar electromagnetic properties are next examined. Assuming a PD radar, target velocity information is available. For the purposes of this model, assume there is a receiver connected to *every* antenna element. Other assumptions will be introduced as needed in the development.

The sinusoidal transmitted radar waveform is modeled mathematically as

$$\tilde{s}(t) = a_t u(t) e^{j(\omega_o t + \varphi)}, \quad (3.3)$$

where the complex exponential and random phase shift φ represent a sinusoidal carrier at frequency ω_o , a_t is the transmitted pulse amplitude, and $u(t)$ is the real valued envelope function. The envelope function defines the pulse width T_p and Pulse Repetition Interval (PRI) characteristics. A series of individual pulses $u_p(t)$ are summed to form the radar pulse train, yielding an envelope function of the form

$$u(t) = \sum_{m=0}^{M-1} u_p(t - mT_r). \quad (3.4)$$

The fundamental pulse $u_p(t)$ is time shifted by multiples of the PRI, T_r . The summation of a finite number of M terms represents the *Coherent Processing Interval* (CPI). This expression implicitly defines M as the number of pulses in the CPI.

Care must be taken in distinguishing between the CPI and the coherent integration time. The output of any STAP method is described generically by $y = \mathbf{w}^H \boldsymbol{\chi}$, where \mathbf{w} is the adaptive weight vector and $\boldsymbol{\chi}$ is the incoming space-time snapshot (discussed later in detail). This expression implicitly indicates a coherent integration time since the inner product of the weight vector and space-time snapshot is simply the weighted sum of incoming data samples, a form of integration. For reduced dimension algorithms, this integration time may be smaller than the CPI length.

The CPI defines how much data is available to the adaptive processor, or adaptive algorithm, for forming an adapted pattern. Obviously, a smaller CPI allows rapid modifications to the antenna pattern in response to the changing environment. However, making the CPI too small can provide insufficient information about the environment interference statistics, producing poorly formed antenna patterns. Conversely, making the CPI too large can result in a slower response and possible statistical changes within the CPI. Consequently, CPI length selection is a fundamental design consideration in any STAP system.

The transmit signal amplitude a_t is defined to capture the desired pulse energy. Therefore, the fundamental pulse energy E_u is normalized to one over the PRI,

$$E_u = \int_0^{T_r} |u_p(t)|^2 dt = 1. \quad (3.5)$$

Consequently, the total energy in a single pulse E_p meets the definition for a_t ,

$$E_p = \int_0^{T_r} |\tilde{s}(t)|^2 dt = a_t^2. \quad (3.6)$$

From this expression, the waveform energy over one CPI is easily determined by integrating over the CPI length. Since the focus of STAP methods is the response and pattern after one CPI, it is customary to consider only the signal transmitted within one CPI as being the entire transmitted signal. Hence, the energy within one CPI is synonymous with the transmitted signal energy E_t ,

$$E_t = \int_0^{MT_r} |\tilde{s}(t)|^2 dt = Ma_t^2 = ME_p. \quad (3.7)$$

3.3 Received Waveform

The signal received at each antenna element is the transmitted signal (Eqn. (3.3)) with a time delay from the target to the np^{th} element, τ_{np} , and a Doppler shift³ f_t due to the target's relative velocity v_t between the target and the platform, $f_t = 2v_t/\lambda_o$,

$$\tilde{s}_{np}(t) = \tilde{s}(t - \tau_{np})e^{j2\pi f_t(t - \tau_{np})}. \quad (3.8)$$

Inserting the transmitted pulse expression of Eqn. (3.3) gives

$$\tilde{s}_{np}(t) = a_r u(t - \tau_{np}) e^{j2\pi f_o(t - \tau_{np})} e^{j2\pi f_t(t - \tau_{np})} e^{j\varphi}, \quad (3.9)$$

where a_r represents the received pulse amplitude. The a_r parameter is introduced because the atmosphere and target Radar Cross Section (RCS) attenuate the transmitted pulse amplitude. Hence, a_r is typically much less than a_t ; if a_r were large, there would be no need adaptive for processing!

If the Doppler shift is greater than the Pulse Repetition Frequency (PRF), e.g., $f_t > f_r$, then the target velocity is ambiguous due to aliasing, commonly referred to as Doppler foldover and illustrated in Fig. 3.4. Once the target Doppler shift has increased past the first PRF line at f_r , the radar can no longer unambiguously

³The Doppler shift is assumed equal at all antenna elements.

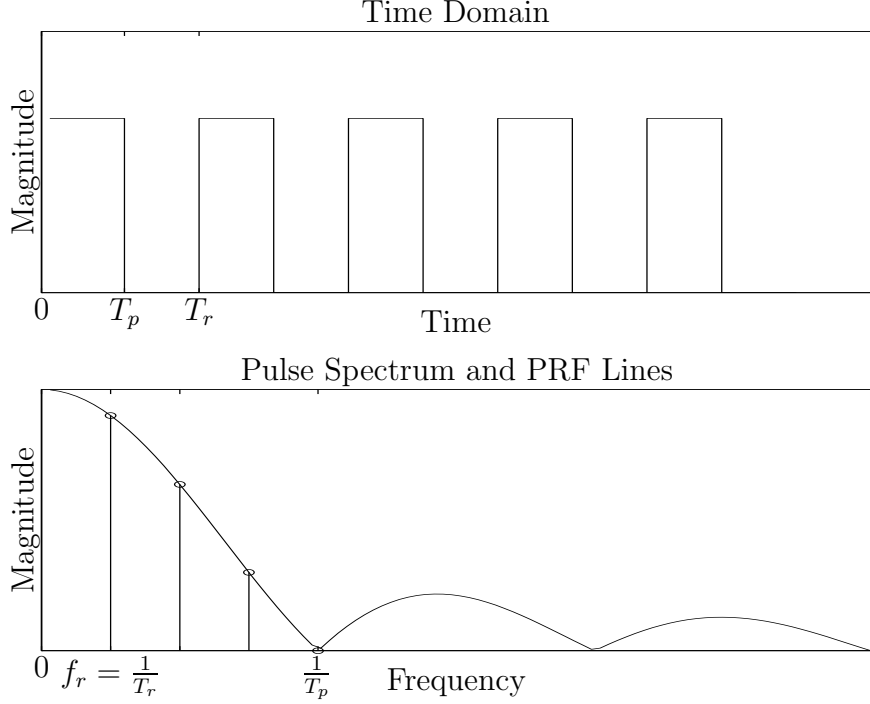


Figure 3.4: Time domain and frequency domain plots of the transmitted pulse illustrating ambiguous Doppler frequency.

determine target velocity. For this reason, target Doppler frequency is normalized by the PRF,

$$\bar{\omega}_t = \frac{f_t}{f_r} = f_t T_r. \quad (3.10)$$

Using the normalized Doppler frequency $\bar{\omega}$, a quick glance determines if the Doppler shift is unambiguous ($\bar{\omega} < 1$) or ambiguous ($\bar{\omega} > 1$).

Total signal delay (τ_{np}) to the np^{th} element equals the sum of the delay from the np^{th} element to a reference element (first element to receive the return signal) τ'_{np} and a delay equal to the round trip time to the target τ_t ,

$$\tau_{np} = \tau_t + \tau'_{np}. \quad (3.11)$$

Considering the physical geometry of the scenario, τ_{np} is a function of target elevation angle θ_t , azimuth angle ϕ_t , and range R_t . The round trip time to the target (τ_t) is

a function of the propagation velocity c and range R_t ,

$$\tau_t = \frac{2R_t}{c}. \quad (3.12)$$

The differential delay from the reference element to the np^{th} element (τ'_{np}) equals the physical separation distance divided by c . The physical separation distance is merely the projection of a unit vector in the direction of the target onto a vector describing the location of the np^{th} element. These operations result in

$$\tau'_{np} = -\frac{\hat{\mathbf{k}}(\theta_t, \phi_t) \cdot \mathbf{d}_{np}}{c}, \quad (3.13)$$

where the *center dot* (\cdot) represents the vector dot product, equivalent to the inner product. Substituting from Eqn. (3.2) and Eqn. (3.1) and simplifying gives the differential delay from the reference element to the np^{th} element as

$$\tau'_{np} = -\frac{(\cos \theta_t \sin \phi_t \hat{\mathbf{x}} + \cos \theta_t \cos \phi_t \hat{\mathbf{y}} + \sin \theta_t \hat{\mathbf{z}}) \cdot (nd_x \hat{\mathbf{x}} + pd_z \hat{\mathbf{z}})}{c} \quad (3.14)$$

$$= \frac{-nd_x \cos \theta_t \sin \phi_t - pd_z \sin \theta_t}{c}. \quad (3.15)$$

Note that for a single row of elements ($P = 1$) $d_z = 0$ and the expression collapses to that derived in previous 2D work for a uniformly spaced linear array. Correspondingly, the *phase delay* from the reference element to the np^{th} element is calculated as

$$-\omega_o \tau'_{np} = 2\pi f_o \left(\frac{nd_x \cos \theta_t \sin \phi_t + pd_z \sin \theta_t}{c} \right). \quad (3.16)$$

For simplicity, define the target spatial frequency as

$$\vartheta_t = \frac{\hat{\mathbf{k}}(\theta_t, \phi_t) \cdot \mathbf{d}_{np}}{\lambda_o} \quad (3.17)$$

The element location vector \mathbf{d}_{np} lies in the np^{th} element direction as shown in Fig. 3.3 and originally introduced in Eqn. (3.1). Repeated here, this vector is

$$\mathbf{d}_{np} = nd_x \hat{\mathbf{x}} + pd_z \hat{\mathbf{z}}, \quad (3.18)$$

where d_x and d_z are the inter-element distances for the azimuth and elevation elements, respectively, $n = 0, 1, \dots, N - 1$, and $p = 0, 1, \dots, P - 1$. Using this, the target spatial frequency becomes

$$\vartheta_t = \frac{nd_x \cos \theta_t \sin \phi_t + pd_z \sin \theta_t}{\lambda_o}. \quad (3.19)$$

To simplify subsequent developments, ϑ_t is broken into two components given by

$$\vartheta_x = \frac{d_x \cos \theta_t \sin \phi_t}{\lambda_o} \quad (3.20)$$

$$\vartheta_z = \frac{d_z \sin \theta_t}{\lambda_o}. \quad (3.21)$$

These components represent the x -axis and z -axis spatial frequencies, respectively. Notice that both quantities are unitless. Substituting back into the phase delay term of Eqn. (3.16) yields

$$-\omega_o \tau'_{np} = 2\pi (n\vartheta_x + p\vartheta_z). \quad (3.22)$$

3.3.1 Simplification. Using expressions and definitions developed in Section 3.3, the received signal of Eqn. (3.9) can be simplified into a framework easier to analyze. Since each antenna element is assumed to have its own receiver and matched filter, the following derivation follows the block diagram shown in Fig. 3.5.

First, substitute the np^{th} element delay into the received signal expression,

$$\tilde{s}_{np}(t) = a_r u(t - \tau_t - \tau'_{np}) e^{j2\pi(f_o + f_t)(t - \tau_t - \tau'_{np})} e^{j\varphi}. \quad (3.23)$$

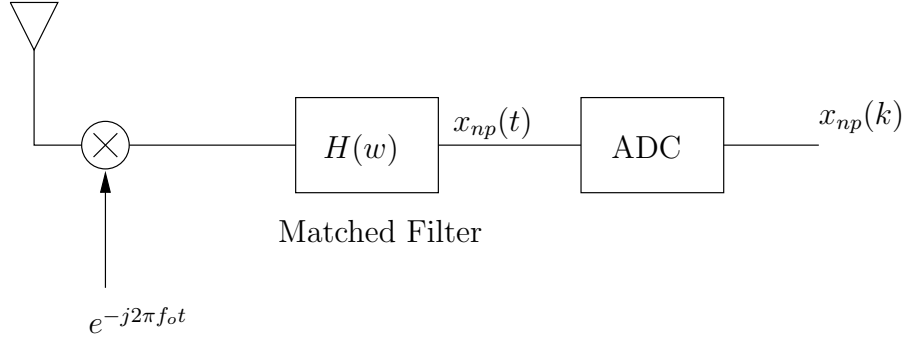


Figure 3.5: Antenna array element receiver block diagram. ADC is an analog to digital converter.

Since the delay from the reference element to the element of interest τ'_{np} is much smaller than the pulse width, it can be ignored in the waveform envelope function $u(t)$,

$$\tilde{s}_{np}(t) = a_r u(t - \tau_t) e^{j2\pi(f_o+f_t)t} e^{-j2\pi(f_o+f_t)\tau_t} e^{-j2\pi(f_o+f_t)\tau'_{np}} e^{j\varphi}. \quad (3.24)$$

Now take a closer look at the third exponential term, which incorporates the phase delay, and write it in terms of spatial frequencies using Eqn. (3.22),

$$e^{-j2\pi f_o \tau'_{np}} = e^{-j\omega_o \tau'_{np}} = e^{j2\pi(n\vartheta_x + p\vartheta_z)}. \quad (3.25)$$

Substituting this expression back into $\tilde{s}_{np}(t)$ of Eqn. (3.23) results in

$$\tilde{s}_{np}(t) = a_r u(t - \tau_t) e^{j2\pi(f_o+f_t)t} e^{-j2\pi(f_o+f_t)\tau_t} e^{-j2\pi f_t \tau'_{np}} e^{j2\pi(n\vartheta_x + p\vartheta_z)} e^{j\varphi}. \quad (3.26)$$

A final observation is in order to permit further simplification. The second and third exponential terms of Eqn. (3.26) are not a function of time, hence they are constant expressions for a given $\tilde{s}_{np}(t)$. Therefore, they can be accounted for in the random phase term without loss of generality. This final simplification gives the following received signal,

$$\boxed{\tilde{s}_{np}(t) = a_r u(t - \tau_t) e^{j2\pi(f_o+f_t)t} e^{j2\pi(n\vartheta_x + p\vartheta_z)} e^{j\varphi}.} \quad (3.27)$$

At this point, this signal is applied to the receiver processing chain shown in Fig.3.5. The first step is down conversion and matched filtering.

3.3.2 Down Conversion and Matched Filtering. As Fig. 3.5 illustrates, the received signal is down converted using a complex exponential. This operation translates the received signal down to an Intermediate Frequency (IF) assumed as baseband for this development,

$$\tilde{s}_{np}(t) = a_r u(t - \tau_t) e^{j2\pi f_t t} e^{j2\pi(n\vartheta_x + p\vartheta_z)} e^{j\varphi}. \quad (3.28)$$

The next receiver step is matched filtering, thereby introducing a form of the Time-Frequency Autocorrelation Function (TFACF). The TFACF is defined in [22, 46, 68] and its form is highlighted as it naturally appears in the development. The matched filter output is simply the convolution of the filter impulse response with the received signal,

$$x_{np}(t) = \int_{-\infty}^{\infty} \tilde{s}_{np}(\tau) h(t - \tau) d\tau, \quad (3.29)$$

where $\tilde{s}_{np}(t)$ represents the received signal at the np^{th} antenna element, as derived in this chapter, and $h(t)$ is the matched filter impulse response. The radar match filters the received signal on a pulse-by-pulse basis. Therefore, the filter impulse response is

$$h(t) = u_p^*(-t). \quad (3.30)$$

Derivation of the matched filter output follows. First, substituting from Eqns. (3.28) and (3.30) and simplifying,

$$x_{np}(t) = \int_{-\infty}^{\infty} a_r u(\tau - \tau_t) e^{j2\pi f_t \tau} e^{j2\pi(n\vartheta_x + p\vartheta_z)} e^{j\varphi} u_p^*(t - \tau) d\tau \quad (3.31)$$

$$= a_r e^{j2\pi(n\vartheta_x + p\vartheta_z)} e^{j\varphi} \int_{-\infty}^{\infty} \sum_{m=0}^{M-1} u_p(\tau - \tau_t - mT_r) u_p^*(t - \tau) e^{j2\pi f_t \tau} d\tau. \quad (3.32)$$

In an effort to simplify further, a change of variables is performed within the integral. First, let $\beta = \tau - \tau_t - mT_r$ which implicitly redefines τ in the integral as $\tau = \beta + \tau_t + mT_r$ with $d\beta/d\tau = 1$. The change of variables and some minor rearranging results in

$$x_{np}(t) = a_r e^{j2\pi(n\vartheta_x + p\vartheta_z)} e^{j\varphi} e^{j2\pi f_t \tau_t} \sum_{m=0}^{M-1} e^{j2\pi f_t m T_r} \int_{-\infty}^{\infty} u_p(\beta) u_p^*(\beta + \tau_t + mT_r - t) e^{j2\pi f_t \beta} d\beta. \quad (3.33)$$

There are two very important realizations evident at this point in the derivation. First, the exponential after the summation represents normalized Doppler frequency since $f_t T_r = \bar{\omega}_t$. Second, the integral term is the TFACF for a single transmitted pulse within the pulse train of M pulses; the magnitude of the TFACF squared is the radar ambiguity function [58]. The value of this TFACF is dependent on the Doppler tolerance of the waveform, however, some easy generalizations can be made to further reduce the expression into a more manageable form.

First, interest is focused on the *range cell under test* (a target is assumed present at this point). The target range cell corresponds to a range delay t equal to $\tau_t + mT_r$ for the m^{th} pulse. Furthermore, assume the waveform is relatively tolerant to Doppler shift for the velocities of interest. This assumption may not be valid for spaceborne platforms. Given these realizations, the TFACF of the transmitted pulse equals one because of the unit energy constraint placed earlier in the development (all the received signal energy is captured in the a_r term). Mathematically, this statement is equivalent to

$$\int_{-\infty}^{\infty} u_p(\beta) u_p^*(\beta) e^{j2\pi f_t \beta} d\beta \approx \int_{-\infty}^{\infty} u_p(\beta) u_p^*(\beta) d\beta = 1. \quad (3.34)$$

Given these observations, the scalar received signal for a scatterer/target given a particular range and the np^{th} element is

$$x_{np} = a_r e^{j\varphi} e^{j2\pi(n\vartheta_x + p\vartheta_z)} \sum_{m=0}^{M-1} e^{j2\pi m\bar{\omega}_t}, \quad (3.35)$$

where the constant phase term $e^{j2\pi f_t \tau_t}$ is incorporated into the random phase $e^{j\varphi}$. Equation (3.35) actually represents a form of coherent integration due to summing across the M pulses within the CPI. The adaptive processing framework to be established will include this coherent integration. Therefore, only the return from the m^{th} pulse is considered and given by

$$\boxed{x_{mnp} = \alpha_t e^{j2\pi(n\vartheta_x + p\vartheta_z)} e^{j2\pi m\bar{\omega}_t}}, \quad (3.36)$$

where the return amplitude a_r and random phase $e^{j\varphi}$ have been combined into a single complex amplitude term (α_t) corresponding to the scatterer/target. This expression represents the signal response after transmission, reflection from an arbitrary scatterer/target at a particular range cell, down conversion, and matched filtering.

3.4 Formatting Radar Returns

Equation (3.36) is in a format describing the signal response at each element of the planar array for each pulse within a CPI. The next step is to arrange the returns for all elements and pulses into a format suitable for linear algebra operations.

The adaptive processor has $MNPL$ returns available to it, one for each of the M pulses, N azimuth elements, P elevation elements, and L range gates. Equation (3.36) includes a range gate dependence since the return corresponds to a range delay of τ_t . To gain a suitable format for the incoming set of radar returns, first

define the vector

$$\mathbf{x}_{mp} = \alpha_t e^{j2\pi m \bar{\omega}_t} e^{j2\pi p \vartheta_z} \begin{bmatrix} 1 & e^{j2\pi \vartheta_x} & \dots & e^{j2\pi(N-1)\vartheta_x} \end{bmatrix}^T \quad (3.37)$$

containing all returns from the N azimuth elements. Now define the column vector of Eqn. (3.37) as a spatial (azimuth) steering vector \mathbf{a} ,

$$\mathbf{a}(\vartheta_x) = \begin{bmatrix} 1 & e^{j2\pi \vartheta_x} & \dots & e^{j2\pi(N-1)\vartheta_x} \end{bmatrix}^T. \quad (3.38)$$

For consistency with previous work in 2D STAP, the previous convention is used to define a temporal steering vector \mathbf{b} ,

$$\mathbf{b}(\bar{\omega}_t) = \begin{bmatrix} 1 & e^{j2\pi \bar{\omega}_t} & \dots & e^{j2\pi(M-1)\bar{\omega}_t} \end{bmatrix}^T. \quad (3.39)$$

At this point, the algebraic structure is consistent with previous 2D STAP work. However, more data is now available to the adaptive processor through the introduction of elevation elements. To incorporate this data into the new 3D structure, spatial steering vector \mathbf{e} is introduced to account for returns from the elevation elements,

$$\mathbf{e}(\vartheta_z) = \begin{bmatrix} 1 & e^{j2\pi \vartheta_z} & \dots & e^{j2\pi(P-1)\vartheta_z} \end{bmatrix}^T. \quad (3.40)$$

Using these definitions, a single column vector containing all returns is constructed. First, the vector containing N returns for all azimuth elements at the p^{th} elevation row and m^{th} pulse is given as

$$\mathbf{x}_{mp} = \alpha_t e^{j2\pi m \bar{\omega}_t} e^{j2\pi p \vartheta_z} \mathbf{a}(\vartheta_x). \quad (3.41)$$

Using the Kronecker product, write the NM returns from p^{th} elevation row as

$$\mathbf{x}_p = \alpha_t e^{j2\pi p \vartheta_z} \mathbf{b}(\bar{\omega}_t) \otimes \mathbf{a}(\vartheta_x). \quad (3.42)$$

The Kronecker product and its properties are defined in Appendix A. Notice from the definition of z -axis spatial frequency in Eqn. (3.21) that if there are only one elevation element ($P = 1$) the expression collapses to the space-time snapshot definition given in [65] and reviewed in Eqn. (2.13). The final operation uses the Kronecker product once again to obtain a single 3D space-time snapshot $\boldsymbol{\chi}_t$ at the l^{th} range cell given by

$$\boxed{\boldsymbol{\chi}_t = \alpha_t \mathbf{e}(\vartheta_z) \otimes \mathbf{b}(\bar{\omega}_t) \otimes \mathbf{a}(\vartheta_x)}, \quad (3.43)$$

where the 3D steering vector is

$$\mathbf{e}(\vartheta_z) \otimes \mathbf{b}(\bar{\omega}_t) \otimes \mathbf{a}(\vartheta_x). \quad (3.44)$$

The structure of Eqn. (3.44) is consistent with the 2D space-time steering vector of Eqn. (2.12).

The role of steering vectors as transformations in STAP is explained in Appendix B. These vectors are analogous to the discrete Fourier transform. Also, concepts of over- and under-sampling are explained in terms of sin-theta space with an emphasis on grating lobe characteristics.

3.5 Element Patterns

The next step logically continues with the development and establishment of models for clutter, jamming, and noise. However, a couple of key elements are necessary for building these models, including element patterns and the array pattern.

For this work, the antenna array elements are assumed identical, i.e., each element has identical voltage and power patterns denoted by $f(\theta, \phi)$ and $g(\theta, \phi) = |f(\theta, \phi)|^2$, respectively.

When extending to 3D to include elevation elements, the element pattern must now reflect both elevation and azimuth dependence. Although previous work did propose using element and array patterns to incorporate elevation functionality, the elevation dependence is typically assumed away or neglected. For this work, full elevation and azimuth antenna patterns are implemented for proper attenuation of range ambiguous clutter. A simple cosine pattern in both elevation and azimuth is used with a backlobe attenuation factor. Previous work [65] used a cosine pattern in azimuth only, treating the elevation pattern as unity. The 3D element pattern is given by

$$f(\theta, \phi) = \begin{cases} \cos \theta \cos \phi & -90^\circ \geq \phi, \theta \geq 90^\circ \\ b_e \cos \theta \cos \phi & 90^\circ \geq \phi, \theta \geq 270^\circ. \end{cases} \quad (3.45)$$

The azimuth (ϕ) and elevation (θ) angles are in *radar* coordinates. The factor b_e is the element backlobe weighting factor and is chosen in this work to provide a backlobe level that is 30 dB lower than the mainlobe. Figure 3.6 shows the 3D element pattern in radar coordinates as a function of azimuth and elevation. Figure 3.7 shows the identical response transformed to cartesian coordinates.

3.6 Spatial Array Factor

Derivation of the spatial antenna array pattern is fairly simple using the two spatial steering vector expression. Care is taken here to distinguish this as the spatial array pattern since the final STAP adapted pattern includes temporal adaptivity as well. The development of the spatial array factor is primarily important for generating models of the clutter and jamming environment which do not require generation of the temporal array factor. At this point, no temporal processing is applied; only spatial processing to form a transmit beam in a given azimuth and elevation direction.

The (θ, ϕ) dependence embedded in ϑ_x and ϑ_z explicitly defines the element-by-element weighting necessary to steer the array response to the desired azimuth

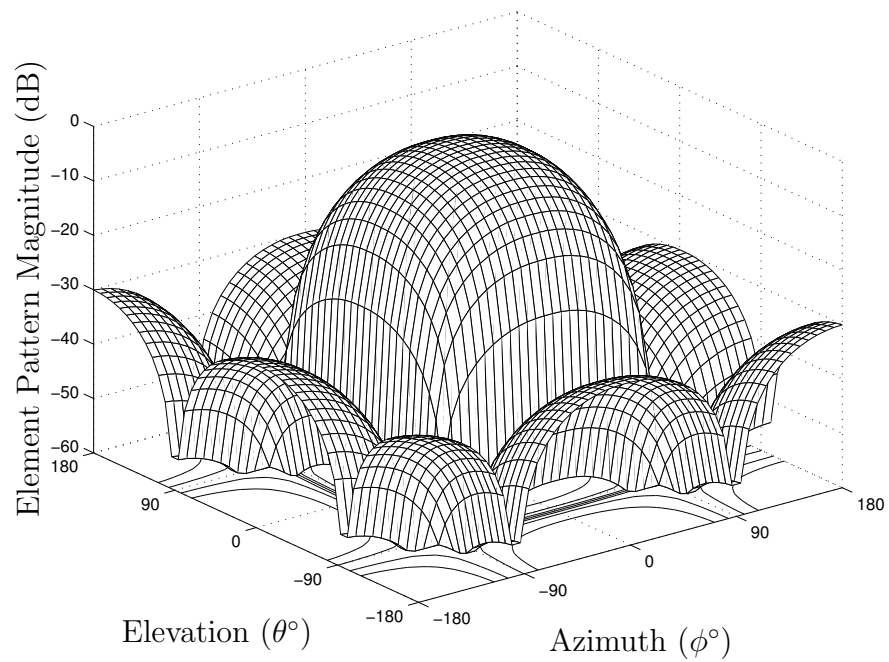


Figure 3.6: 3D element pattern in radar coordinates.

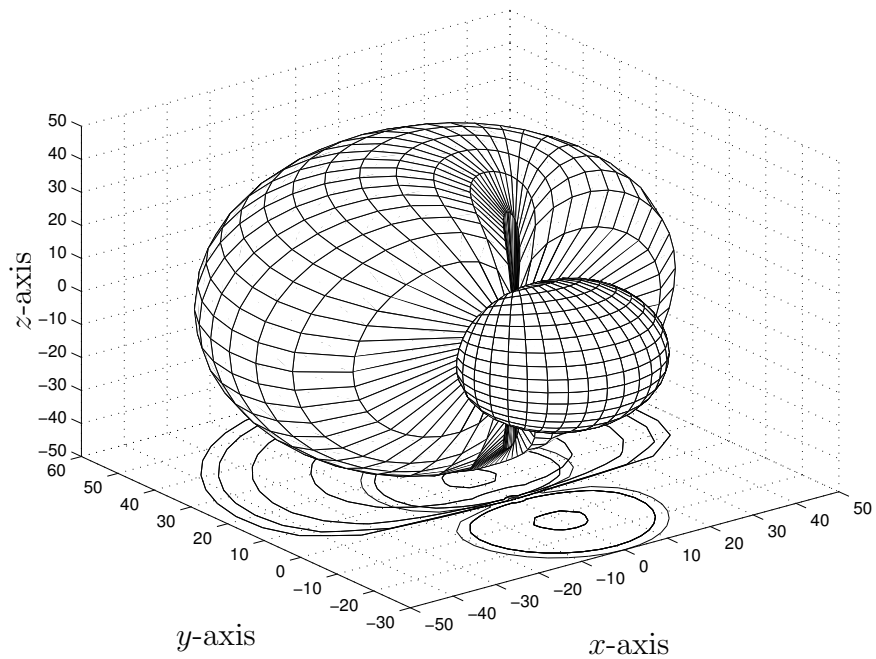


Figure 3.7: 3D element pattern in Cartesian coordinates.

and elevation angle. As such, the spatial array factor is merely the sum of all the weights over the array,

$$W(\theta, \phi) = [\mathbf{e}(\vartheta_z) \otimes \mathbf{a}(\vartheta_x)]^T \mathbf{1}. \quad (3.46)$$

A more conventional notation equivalent to the above expression and matching literature [12, 61] is

$$W(\theta, \phi) = \sum_{p=0}^{P-1} \sum_{n=0}^{N-1} e^{j2\pi p\vartheta_z} e^{j2\pi n\vartheta_x}. \quad (3.47)$$

Again, the goal is to simplify this expression into something more manageable and intuitive. First, use an expression for the partial sum of a geometric series for finite N and P . Obviously, there is a finite number of elements so this requirement is not overly restrictive. One such sum is found in [50] and generally defined as

$$\sum_{l=0}^n a^l = \frac{1 - a^{n+1}}{1 - a}, \quad (3.48)$$

where $a \neq 1$. Applying the simplification to Eqn. (3.47) results in

$$W(\theta, \phi) = \left(\frac{1 - e^{j2\pi P\vartheta_z}}{1 - e^{j2\pi\vartheta_z}} \right) \left(\frac{1 - e^{j2\pi N\vartheta_x}}{1 - e^{j2\pi\vartheta_x}} \right). \quad (3.49)$$

This expression can be further simplified by factoring the complex exponentials as

$$W(\theta, \phi) = \frac{e^{j\pi P\vartheta_z}}{e^{j\pi\vartheta_z}} \left(\frac{e^{-j\pi P\vartheta_z} - e^{j\pi P\vartheta_z}}{e^{-j\pi\vartheta_z} - e^{j\pi\vartheta_z}} \right) \frac{e^{j\pi N\vartheta_x}}{e^{j\pi\vartheta_x}} \left(\frac{e^{-j\pi N\vartheta_x} - e^{j\pi N\vartheta_x}}{e^{-j\pi\vartheta_x} - e^{j\pi\vartheta_x}} \right). \quad (3.50)$$

Gathering like terms and recognizing the components in the form of Euler's equation yields

$$W(\theta, \phi) = e^{j\pi(P-1)\vartheta_z} e^{j\pi(N-1)\vartheta_x} \frac{\sin(\pi P\vartheta_z)}{\sin(\pi\vartheta_z)} \frac{\sin(\pi N\vartheta_x)}{\sin(\pi\vartheta_x)}. \quad (3.51)$$

At this point, it is convenient to substitute in ϑ_x and ϑ_z from Eqn. (3.20) and Eqn. (3.21), respectively. This final substitution highlights the azimuth and elevation

angle dependence in the array pattern,

$$W(\theta, \phi) = e^{j\frac{\pi d_z}{\lambda_o}(P-1)\sin\theta} e^{j\frac{\pi d_x}{\lambda_o}(N-1)\cos\theta\sin\phi} \times \frac{\sin\left(\frac{\pi d_z}{\lambda_o}P\sin\theta\right)}{\sin\left(\frac{\pi d_z}{\lambda_o}\sin\theta\right)} \frac{\sin\left(\frac{\pi d_x}{\lambda_o}N\cos\theta\sin\phi\right)}{\sin\left(\frac{\pi d_x}{\lambda_o}\cos\theta\sin\phi\right)}. \quad (3.52)$$

3.6.1 Application of L'Hôpital's Rule. For certain values of θ and ϕ , the array pattern becomes indeterminate. By applying L'Hôpital's rule, the appropriate array response can be determined in these directions. First examine the case when $\phi = 0$. The array pattern is now an indeterminate 0/0 form. Next, apply L'Hôpital's rule by taking the derivative of the numerator and denominator and evaluate the expression.

To simplify this seemingly arduous task, write the array pattern as

$$W(\theta, \phi) = \frac{ABCD}{EF}, \quad (3.53)$$

where

$$A = e^{j\frac{\pi d_z}{\lambda_o}(P-1)\sin\theta} \quad (3.54)$$

$$B = e^{j\frac{\pi d_x}{\lambda_o}(N-1)\cos\theta\sin\phi} \quad (3.55)$$

$$C = \sin\left(\frac{\pi d_z}{\lambda_o}P\sin\theta\right) \quad (3.56)$$

$$D = \sin\left(\frac{\pi d_x}{\lambda_o}N\cos\theta\sin\phi\right) \quad (3.57)$$

$$E = \sin\left(\frac{\pi d_z}{\lambda_o}\sin\theta\right) \quad (3.58)$$

$$F = \sin\left(\frac{\pi d_x}{\lambda_o}\cos\theta\sin\phi\right). \quad (3.59)$$

Taking the derivative of the numerator with respect to ϕ results in

$$\frac{d(ABCD)}{d\phi} = \frac{dA}{d\phi}BCD + A\frac{dB}{d\phi}CD + AB\frac{dC}{d\phi}D + ABC\frac{dD}{d\phi}. \quad (3.60)$$

Before proceeding, evaluate A , B , C , and D at $\phi = 0$,

$$A(\phi = 0) = e^{j\frac{\pi d_z}{\lambda_o}(P-1)\sin\theta} \quad (3.61)$$

$$B(\phi = 0) = 1 \quad (3.62)$$

$$C(\phi = 0) = \sin\left(\frac{\pi d_z}{\lambda_o}P\sin\theta\right) \quad (3.63)$$

$$D(\phi = 0) = 0. \quad (3.64)$$

Clearly, the only non-zero term from the numerator derivative of Eqn. (3.60) is the last one since $D = 0$ at $\phi = 0$. The non-zero derivative term is

$$\frac{dD}{d\phi} = \cos\left(\frac{\pi d_x}{\lambda_o}N\cos\theta\sin\phi\right)\frac{\pi d_x}{\lambda_o}N\cos\theta\cos\phi. \quad (3.65)$$

Evaluating this derivative at $\phi = 0$ results in

$$\left.\frac{dD}{d\phi}\right|_{\phi=0} = \frac{\pi d_x}{\lambda_o}N\cos\theta. \quad (3.66)$$

Constructing the non-zero term for the numerative derivative evaluated at $\phi = 0$ results in

$$e^{j\frac{\pi d_z}{\lambda_o}(P-1)\sin\theta}\sin\left(\frac{\pi d_z}{\lambda_o}P\sin\theta\right)\frac{\pi d_x}{\lambda_o}N\cos\theta. \quad (3.67)$$

Now apply the same process to the denominator. Following the same method, the derivative of the denominator evaluated at $\phi = 0$ becomes

$$E\left.\frac{dF}{d\phi}\right|_{\phi=0} = \sin\left(\frac{\pi d_z}{\lambda_o}P\sin\theta\right)\frac{\pi d_x}{\lambda_o}\cos\theta. \quad (3.68)$$

Taking the ratio of numerator and denominator terms gives the solution for the array pattern response at $\phi = 0$,

$$W(\theta, 0) = N e^{j \frac{\pi d_z}{\lambda_o} (P-1) \sin \theta} \frac{\sin \left(\frac{\pi d_z}{\lambda_o} P \sin \theta \right)}{\sin \left(\frac{\pi d_z}{\lambda_o} \sin \theta \right)}. \quad (3.69)$$

The same process is used to find the array pattern response at $\theta = 0$ and is given by

$$W(0, \phi) = P e^{j \frac{\pi d_x}{\lambda_o} (N-1) \sin \phi} \frac{\sin \left(\frac{\pi d_x}{\lambda_o} N \sin \phi \right)}{\sin \left(\frac{\pi d_x}{\lambda_o} \sin \phi \right)}. \quad (3.70)$$

The array response at $W(0, 0)$ is found using the same method, and was determined to be

$$W(0, 0) = NP. \quad (3.71)$$

The normalized 3D spatial array factor is plotted in Fig. 3.8 for radar coordinates. A different visualization is obtained after using rectangular coordinates as shown in Fig. 3.9. The latter figure shows contour lines on the bottom floor of the three-dimensional plot corresponding to cuts in the array pattern. As plotted, the array pattern does not have any backlobe attenuation applied. Therefore, the pattern is symmetrical and has a grating lobe at 180° in both azimuth and elevation.

3.7 Spatial Antenna Array Pattern

The spatial antenna pattern is the spatial array factor scaled by the element pattern, given the identical element assumption. The spatial antenna array pattern is simply given by

$$G(\theta, \phi) = W(\theta, \phi) |f(\theta, \phi)|^2. \quad (3.72)$$

Planar array pattern plots for an 8×8 element array (including element pattern effects) are shown in Figs. 3.10 and 3.11.

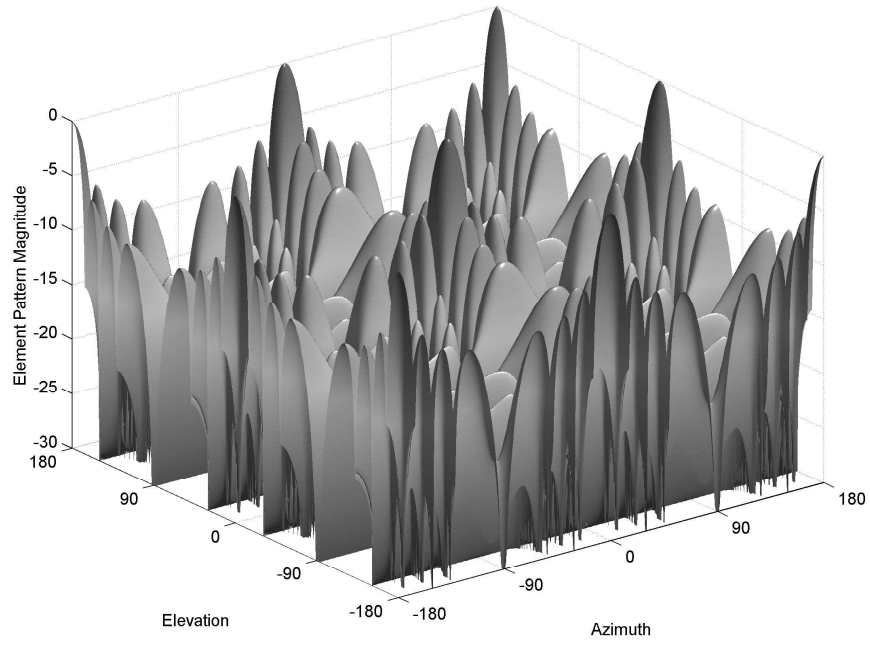


Figure 3.8: Normalized 3D spatial array factor (W) in radar coordinates for an 8×8 element array (no backlobe attenuation).

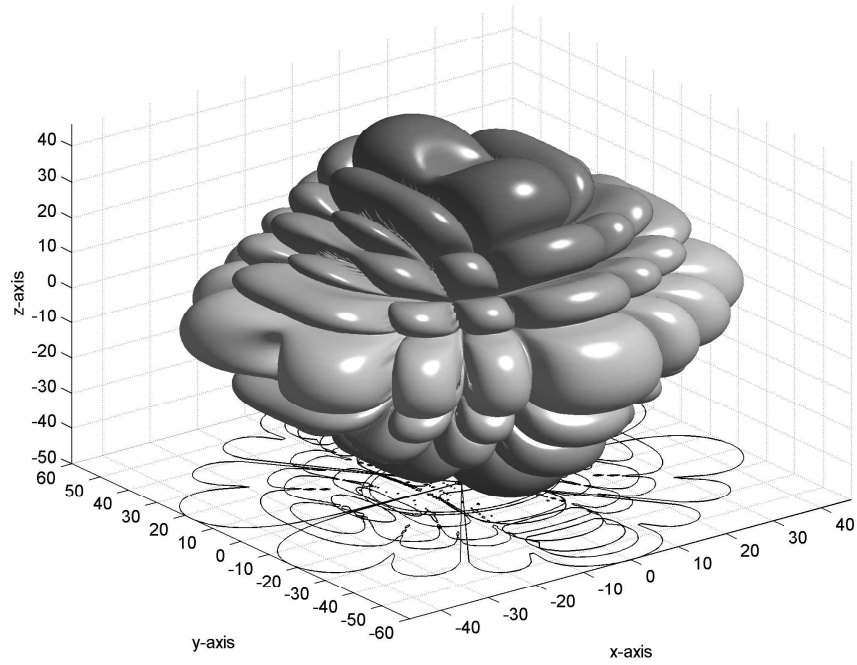


Figure 3.9: Normalized 3D spatial array factor (W) in cartesian coordinates for an 8×8 element array (no backlobe attenuation).

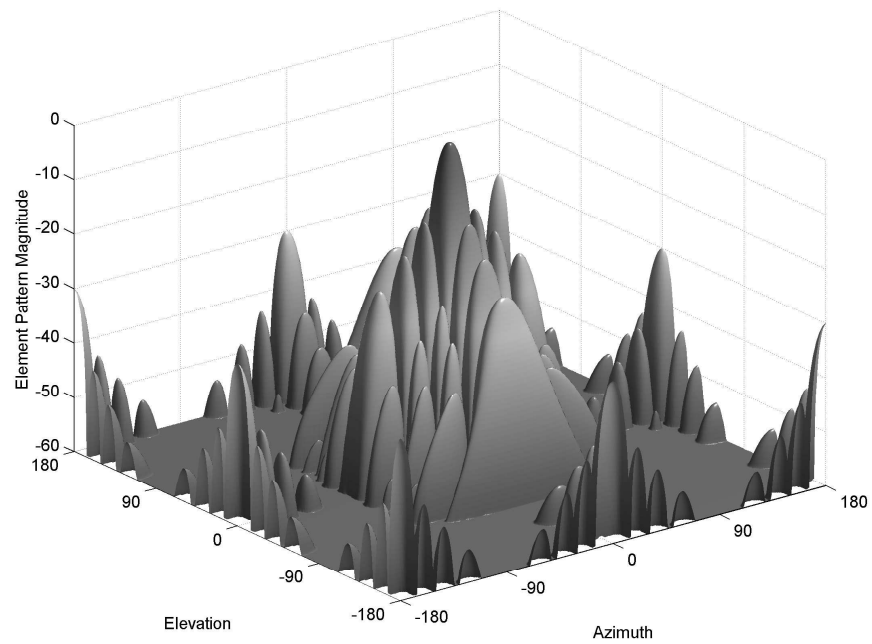


Figure 3.10: Normalized 3D antenna array pattern for an 8×8 element array in radar coordinates.

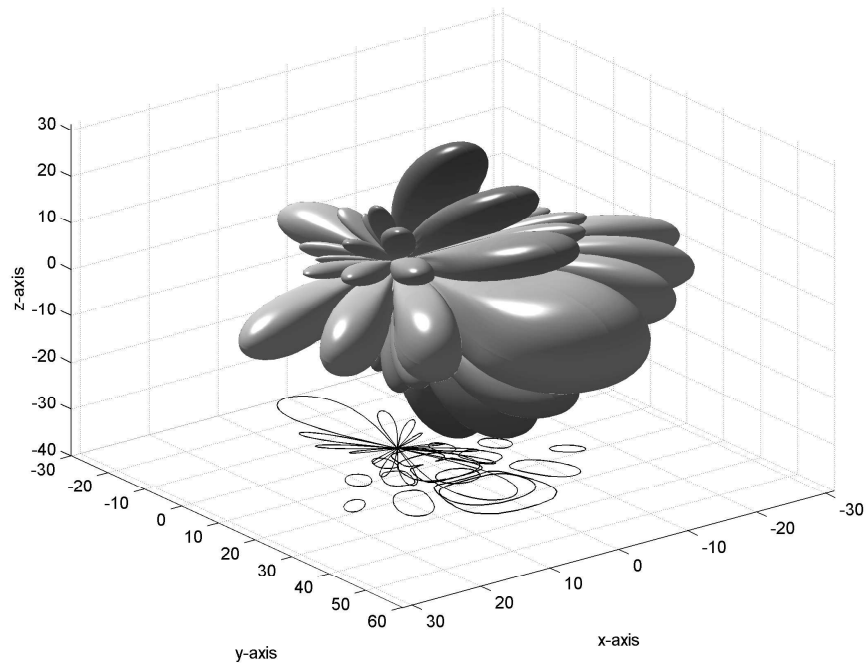


Figure 3.11: Normalized 3D antenna array pattern for an 8×8 element array in cartesian coordinates.

3.8 Noise Model

For the 3D noise model component, only internally generated receiver noise is assumed present. Given every array element has its own receiver, there is noise present at all times. Furthermore, assuming a separate receiver for each channel dictates the noise is mutually uncorrelated on an element-by-element basis. Given noise sample y_{nmp} on the n^{th} azimuth element, p^{th} elevation element, and m^{th} pulse, the expected value of the noise across pulses is

$$\mathcal{E} \{ y_{n_i m p_j} y_{n_k m p_l}^* \} = \sigma^2 \delta_{n_i - n_k} \delta_{p_j - p_l}, \quad (3.73)$$

where $\delta_{n_i - n_k}$ is a Kronecker delta function defined in Eqn. (3.74) and σ^2 is the noise power per element, per pulse. It is convenient to define $\sigma^2 = 1$, however this quantity can also be calculated from the noise power spectral density and the radar bandwidth as $N_o B$. The Kronecker delta is defined as

$$\delta_{n_i - n_k} = \begin{cases} 1 & i = k \\ 0 & \text{otherwise.} \end{cases} \quad (3.74)$$

The noise is mutually uncorrelated temporally as well. This assumption is valid for a PRF much less than the waveform bandwidth, given the bandwidth is also much less than the carrier/transmit frequency, i.e., $f_r \ll B \ll f_o$. For an airborne radar scenario, this is a reasonable assumption. Therefore, the expected value of two pulse samples is very similar to that of two different elements,

$$\mathcal{E} \{ y_{nm_j p} y_{nm_k p}^* \} = \sigma^2 \delta_{m_j - m_k}. \quad (3.75)$$

Given these correlation properties for the noise model, the correlation properties of the incoming noise signal can be determined. A received noise signal is characterized in the same form as any other target signal and its development is the

same data model of this chapter. Given this point, the noise space-time snapshot $\boldsymbol{\chi}_n$ is used and the structure of its correlation matrix determined by taking the expected value of its outer product,

$$\mathbf{R}_n = \mathcal{E} \{ \boldsymbol{\chi}_n \boldsymbol{\chi}_n^H \}. \quad (3.76)$$

Using the form of Eqn. (3.43) and substituting yields

$$\mathbf{R}_n = \mathcal{E} \left\{ [\mathbf{e}(\vartheta_z) \otimes \mathbf{b}(\bar{\omega}_t) \otimes \mathbf{a}(\vartheta_x)] [\mathbf{e}(\vartheta_z) \otimes \mathbf{b}(\bar{\omega}_t) \otimes \mathbf{a}(\vartheta_x)]^H \right\}. \quad (3.77)$$

Application of Eqn. (A.2) in Appendix A simplifies the expression to

$$\mathbf{R}_n = \mathcal{E} \left\{ \mathbf{e}(\vartheta_z) \mathbf{e}^H(\vartheta_z) \otimes \mathbf{b}(\bar{\omega}_t) \mathbf{b}^H(\bar{\omega}_t) \otimes \mathbf{a}(\vartheta_x) \mathbf{a}^H(\vartheta_x) \right\}. \quad (3.78)$$

Furthermore, using the fact the noise samples are mutually uncorrelated on a pulse-by-pulse and element-by-element basis allows for the following simplification,

$$\mathbf{R}_n = \sigma^2 \mathbf{I}_P \otimes \mathbf{I}_M \otimes \mathbf{I}_N. \quad (3.79)$$

The Kronecker product of these three identity matrices is simply another identity matrix of size $MNP \times MNP$. Hence, the noise covariance matrix simply becomes

$$\boxed{\mathbf{R}_n = \sigma^2 \mathbf{I}_{MNP}}. \quad (3.80)$$

! Thermal noise plays a key role in adaptive interference suppression. Its presence within the covariance matrix ensures the matrix is invertible, a key requirement in most STAP approaches.

3.9 Barrage Noise Jammer Model

The jamming model only includes barrage noise jamming. The jamming signal remains correlated across the array although there is decorrelation from pulse-to-

pulse. The received jammer power spectral density at one element is derived from the one-way radar equation

$$J_o = \frac{S_j g(\phi, \theta) \lambda_o^2}{(4\pi)^2 R_j^2 L_r}, \quad (3.81)$$

where L_r represents the receiver losses and S_j the jammer effective radiated power spectral density. Hence, the jammer to noise ratio (JNR) at one element is

$$\xi_j = \frac{J_o}{N_o}, \quad (3.82)$$

where N_o is the receiver noise power spectral density. The jamming model is developed consistent with [65] and begins by first considering the spatial snapshot for the m^{th} PRI. However, the model is now extended to include elevation elements and the 3D mathematical framework must accommodate these elements. This accommodation results in the m^{th} spatial snapshot being written as

$$\mathbf{x}_m = \alpha_m \mathbf{e}(\vartheta_z) \otimes \mathbf{a}(\vartheta_x), \quad (3.83)$$

where \mathbf{e} and \mathbf{a} are in terms of the jammer's azimuth angle ϕ and elevation angle θ . The parameter α_m represents the jammer amplitude on the m^{th} pulse. By writing the signal in this manner, i.e., as a spatial snapshot, it is relatively easy to include the temporal decorrelation. The received jammer amplitudes on a pulse-by-pulse basis are considered random and can be written as a vector of random amplitudes,

$$\boldsymbol{\alpha} = [\alpha_0 \quad \alpha_1 \quad \cdots \quad \alpha_{M-1}]^T. \quad (3.84)$$

Since there is no temporal correlation, the space-time snapshot for a jammer can be written as

$$\boldsymbol{\chi}_j = \mathbf{e}(\vartheta_z) \otimes \boldsymbol{\alpha}_j \otimes \mathbf{a}(\vartheta_x). \quad (3.85)$$

Finding the expected covariance matrix of the jammer space-time snapshot involves first examining the cross correlation characteristics of individual jammer amplitudes. Assuming the jammer signal is stationary over a CPI permits drawing the general conclusion that

$$\mathcal{E} \{ \alpha_{m_k} \alpha_{m_l}^* \} = \sigma^2 \xi_j \delta_{m_k - m_l} \quad (3.86)$$

which holds for all m_k and m_l . As before, σ^2 represents the noise power per element per pulse and is equal to $N_o B$. Extending the above equation to accommodate the previously defined vector of received jammer amplitudes on each pulse gives

$$\mathcal{E} \{ \boldsymbol{\alpha}_j \boldsymbol{\alpha}_j^H \} = \sigma^2 \xi_j \mathbf{I}_M. \quad (3.87)$$

Using these facts, the jammer covariance matrix is found as

$$\mathbf{R}_j = \mathcal{E} \{ \boldsymbol{\chi}_j \boldsymbol{\chi}_j^H \} \quad (3.88)$$

$$= \mathcal{E} \left\{ [\mathbf{e}(\vartheta_z) \otimes \boldsymbol{\alpha}_j \otimes \mathbf{a}(\vartheta_x)] [\mathbf{e}(\vartheta_z) \otimes \boldsymbol{\alpha}_j \otimes \mathbf{a}(\vartheta_x)]^H \right\} \quad (3.89)$$

$$= \boxed{\sigma^2 \xi_j \mathbf{e}(\vartheta_z) \mathbf{e}^H(\vartheta_z) \otimes \mathbf{I}_M \otimes \mathbf{a}(\vartheta_x) \mathbf{a}^H(\vartheta_x)}. \quad (3.90)$$

The final simplification uses Eqn. (A.2) from Appendix A. The $M \times M$ identity matrix accounts for the uncorrelated temporal characteristics of the jammer signal. The spatial correlation across the array retains the other two terms in the covariance structure.

3.10 Airborne Clutter Model

The airborne clutter model is considerably more complicated than the previous two models. Clutter models represent one of the most contentious topics in the radar arena. This dissertation work not only establishes a 3D clutter model but also strives to confirm all performance results obtained using the model with actual measured

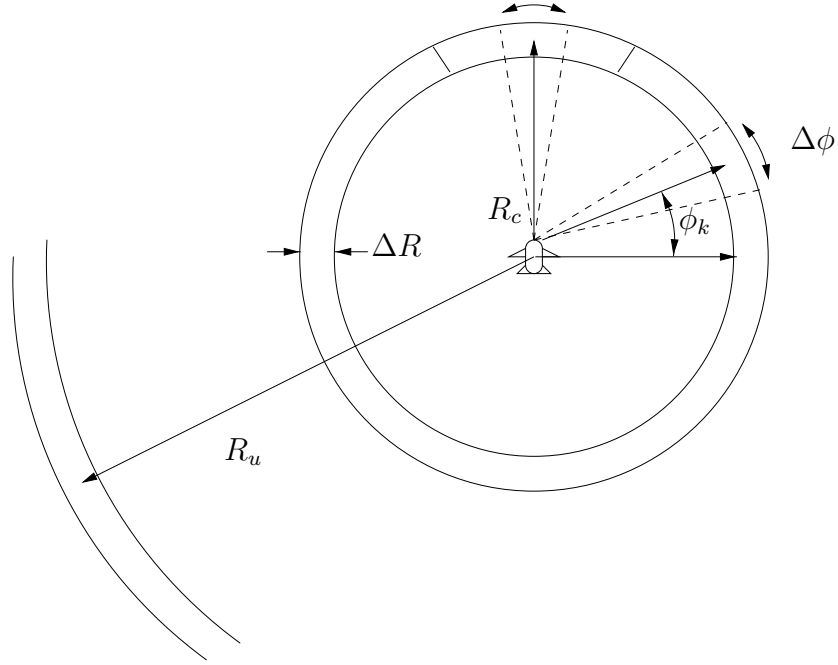


Figure 3.12: Top view of clutter ring geometry.

airborne radar data. Measured data is obtained from the MCARM program [59] and is discussed in detail in Section 4.1.1. The basic clutter model presented here represents an extension to one developed in [65] which has been generally accepted within the radar adaptive processing community.

Model development begins by first confining the primary source of clutter to the Earth's surface, e.g., ground or sea clutter. The effects of sky clutter are considered small when compared to the ground and are neglected in the model. The earth is spherically modeled using a $4/3$ effective radius.

The airborne radar can be interpreted as only viewing a single range cell at a time. Given this view, the range cell is defined by a circular region around the aircraft where the radius represents the range and is also called the clutter ring. Figure 3.12 shows the clutter ring at a range R_c . Figure 3.13 shows the same clutter ring when viewed from the side illustrating the elevation angle and grazing angle ψ_c .

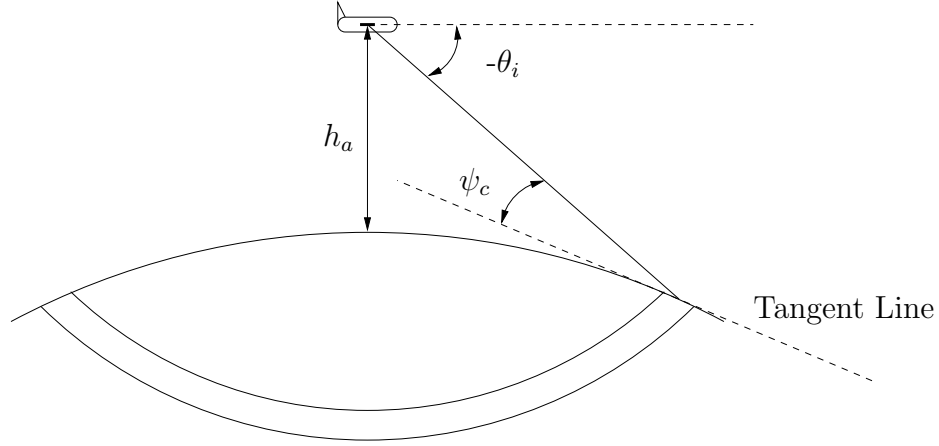


Figure 3.13: Side view of clutter ring geometry.

The clutter model establishes a single clutter patch of angular extent $\Delta\phi$ located distance R_c from the radar. The clutter ring is made up of N_c clutter patches around the aircraft. A simplistic viewpoint of the model is to describe each patch and then simply add them up to form the clutter returns for that range cell.

Each clutter patch is described in terms of its elevation and azimuth angles along with the range relationship to the radar. Furthermore, the reflectivity of the patch is incorporated through its radar cross section. Begin by first describing the elevation angle to a clutter patch (θ_c) at range R_c . This angle is determined geometrically using the law of cosines, i.e.,

$$\theta_c = -\sin^{-1} \left[\frac{R_c^2 + h_a(h_a + 2a_e)}{2R_c(a_e + h_a)} \right], \quad (3.91)$$

where the negative is a result of the previous definition of positive elevation angles upward, a_e is the effective radius of the earth and h_a is the aircraft altitude. The effective radius of the earth (a_e) uses the 4/3 radius model and hence $a_e = 4r_e/3$.

The grazing angle ψ_c is important to the actual modeling of the clutter itself. A constant gamma model is later used to characterize clutter reflectivity. The constant gamma reflectivity model depends solely on ψ_c for a particular terrain type. The grazing angle represents the angle between a line tangential to the earth's surface at

the clutter patch and a line extended from the airborne radar to the patch, e.g.,

$$\psi_c = -\sin^{-1} \left(\frac{R_c^2 - h_a(h_a + 2a_e)}{2R_c a_e} \right). \quad (3.92)$$

Ambiguous range returns are also modeled. Therefore, the next step is to determine range to the horizon. If the horizon range is greater than the unambiguous range of the radar, R_u , the ambiguous clutter rings must be incorporated. Since the grazing angle is the angle between the line tangential to the clutter patch and a line from the radar to the patch, the horizon range is simply the point at which $\psi_c = 0$. Using this realization, the horizon range is easily found as

$$R_h = \sqrt{h_a^2 + 2h_a a_e}. \quad (3.93)$$

The unambiguous range is simply $R_u = cT_r/2$ where T_r is the PRI. The number of range ambiguities N_r is simply the floor function (round down) operating on R_h/R_u or

$$N_r = \left\lfloor \frac{R_h}{R_u} \right\rfloor. \quad (3.94)$$

The next step is determining the spatial frequency of an individual clutter patch. Let's examine the ik^{th} patch. The spatial frequency (ϑ_{ik}) is the projection of a vector to the ik^{th} patch onto a vector to the np^{th} element of the array divided by the wavelength, i.e.,

$$\vartheta_{ik} = \frac{\hat{\mathbf{k}}(\theta_i, \phi_k) \cdot \mathbf{d}}{\lambda_o}. \quad (3.95)$$

Substituting definitions of Eqn. (3.2) and Eqn. (3.1) into Eqn. (3.95) yields

$$\vartheta_{ik} = \frac{nd_x \cos \theta_i \sin \phi_k + pd_z \sin \theta_i}{\lambda_o}. \quad (3.96)$$

Using the previously defined ϑ_x and ϑ_z of Eqn. (3.20) and Eqn. (3.21), respectively, results in

$$\vartheta_{ik} = n\vartheta_x + p\vartheta_z. \quad (3.97)$$

Equation (3.97) represents the spatial frequency of the ik^{th} clutter patch.

To this point, only one component is missing to write the space-time snapshot to the ik^{th} clutter patch: the normalized Doppler frequency. The Doppler frequency of this individual patch is proportional to the projection of the vector to the patch onto the velocity vector of the platform,

$$f_c(\theta_i, \phi_k) = \frac{2\hat{\mathbf{k}}(\theta_i, \phi_k) \cdot \mathbf{v}_a}{\lambda_o}. \quad (3.98)$$

Assuming no platform crab angle, the velocity vector is simply $v_a\hat{\mathbf{x}}$. Therefore, the Doppler frequency of the ik^{th} clutter patch is

$$f_c(\theta_i, \phi_k) = \frac{2 \cos \theta_i \sin \phi_k}{\lambda_o}. \quad (3.99)$$

The normalized Doppler frequency is obtained by dividing by the PRF, $\bar{\omega}_{ik} = f_c(\theta_i, \phi_k) / f_r$.

! A critical realization is evident from Eqn. (3.99). The clutter Doppler frequency is azimuth (ϕ_k) *and* range (θ_i) dependent. When speaking of mainbeam clutter, the array transmit beam is formed at boresight, perpendicular to the aircraft velocity vector, and maximum clutter response occurs at $\phi = 0$ (unless surface RCS characteristics result in higher sidelobe returns). Since $\sin \phi = 0$ in this case, the maximum clutter response occurs at 0 Hz and is not range dependent. This conclusion also neglects beamwidth effects since range independence is *only* true for clutter lying exactly along the $\phi = 0$ line.

Also, if the mainbeam is no longer perpendicular to the aircraft velocity vector (aircraft crab) the maximum clutter response again becomes a function of range, e.g., $\cos \theta$. Steering the mainbeam from boresight (on transmit) also introduces range functionality. Individual clutter patches, i.e., sidelobe clutter

returns, retain range dependence regardless of array attitude with respect to the velocity vector.

Using normalized Doppler and spatial frequency, the 3D space-time snapshot corresponding to clutter patches around a range ring at range R_c can be written as

$$\mathbf{x}_c = \sum_{i=1}^{N_c} \sum_{k=1}^{N_r} \alpha_{ik} \mathbf{e}(\vartheta_z) \otimes \mathbf{b}(\bar{\omega}_{ik}) \otimes \mathbf{a}(\vartheta_x). \quad (3.100)$$

Spatial frequencies ϑ_z and ϑ_x are a function of clutter patch elevation and azimuth angles.

The next step involves determining the form of the random clutter patch amplitude α_{ik} . First, begin by finding the effective RCS of the clutter patch. Given ground reflectivity (per unit area) at this patch, $\sigma_o(\theta_i, \phi_k)$, the effective RCS is this reflectivity multiplied by the patch area [58, 65]

$$\sigma_{ik} = \sigma_o(\theta_i, \phi_k) R_i \Delta\phi \Delta R \sec \psi_i. \quad (3.101)$$

The area reflectivity is also known as *sigma zero* in other literature and represents an RCS density. This form is commonly used because of the distributed nature of clutter. The area of the clutter patch depends on the grazing angle and range to the patch. Hence, the effective patch RCS depends on which range ambiguity is being calculated and there is a dependence on the ambiguous range R_i . If the PRI and horizon range result in no range ambiguities, then $R_i = R_c$ and there is only one clutter patch to deal with at a particular azimuth. The angular extent of the patch, $\Delta\phi$, is simply $2\pi/N_c$. The term ΔR is the range resolution of the radar and is equal to $c/(2B)$. Using a constant gamma model for clutter [58], the area reflectivity is defined as

$$\sigma_o(\theta_i, \phi_k) = \gamma \sin \psi_i. \quad (3.102)$$

The clutter patch RCS now allows use of the radar equation to define an element Clutter-to-Noise Ratio (CNR). The CNR at a single element is

$$\xi_{ik} = \frac{P_t G_t(\theta_i, \phi_k) g(\theta_i, \phi_k) \lambda_o^2 \sigma_{ik}}{(4\pi)^3 N_o B L_s R_i^4}. \quad (3.103)$$

The term $G_t(\theta_i, \phi_k)$ represents the antenna array pattern on transmit and was shown in Fig. 3.11. The receive power pattern is $g(\theta_i, \phi_k)$ and is simply the magnitude of the voltage pattern $f(\theta_i, \phi_k)$ squared. Using the CNR definition, the random clutter amplitudes must satisfy

$$\mathcal{E} \{ \alpha_{ik} \alpha_{ik}^* \} = \sigma^2 \xi_{ik}, \quad (3.104)$$

where σ^2 is the noise power per element, hence this quantity is the clutter power per element. However, returns from different clutter patches are uncorrelated. Therefore,

$$\mathcal{E} \{ \alpha_{ik} \alpha_{jl}^* \} = \sigma^2 \xi_{ik} \delta_{i-j} \delta_{k-l}. \quad (3.105)$$

With these expected values, the covariance matrix for the clutter can be found. The operation is simple and as before involves taking the expected value of the space-time snapshot outer product corresponding to the clutter for a particular range cell. This definition begins as

$$\mathbf{R}_c = \mathcal{E} \{ \boldsymbol{\chi}_c \boldsymbol{\chi}_c^H \} \quad (3.106)$$

$$= \mathcal{E} \left\{ \sum_{i=1}^{N_c} \sum_{k=1}^{N_r} \alpha_{ik} \mathbf{e}(\vartheta_z) \otimes \mathbf{b}(\bar{\omega}_{ik}) \otimes \mathbf{a}(\vartheta_x) \left[\sum_{j=1}^{N_c} \sum_{l=1}^{N_r} \alpha_{jl} \mathbf{e}(\vartheta_z) \otimes \mathbf{b}(\bar{\omega}_{jl}) \otimes \mathbf{a}(\vartheta_x) \right]^H \right\}, \quad (3.107)$$

where the reader is reminded of the embedded dependence on θ_i and ϕ_k within ϑ_x and ϑ_z . Using expected value properties previously defined (in particular, the lack

of correlation from patch to patch), allows the simplification to

$$\mathbf{R}_c = \sigma^2 \sum_{i=1}^{N_c} \sum_{k=1}^{N_r} \xi_{ik} \mathbf{e}(\vartheta_z) \mathbf{e}^H(\vartheta_z) \otimes \mathbf{b}(\bar{\omega}_{ik}) \mathbf{b}^H(\bar{\omega}_{ik}) \otimes \mathbf{a}(\vartheta_x) \mathbf{a}^H(\vartheta_x). \quad (3.108)$$

This is the form of the clutter covariance matrix for a given range cell. Obviously this development only applies for range cells corresponding to ranges greater than the aircraft altitude. A range less than the platform altitude will not include ground clutter!

! The clutter model presented in this section incorporates range ambiguous clutter returns. Unlike previous 2D work, these ambiguous returns *are* used in the performance evaluations shown in the following chapters. Depending on the number of range ambiguities, i.e, the radar PRI, significant performance degradation is incurred as a direct result. The impact is fully characterized in the following work by comparing results both with and without range ambiguous clutter.

3.11 Consolidating Model Components

The final step involves consolidating the components developed in previous sections. Each component has been derived independently and some explanation is warranted on joining them. Consider two different scenarios: target present and no target present. In the target present scenario, a single space-time snapshot is composed of the target return, clutter returns, thermal noise, and barrage noise jammer returns. Using the notation established in this chapter, a composite space-time snapshot for this case is described by

$$\boldsymbol{\chi} = \boldsymbol{\chi}_t + \boldsymbol{\chi}_c + \boldsymbol{\chi}_n + \boldsymbol{\chi}_j \quad (3.109)$$

and is commonly called the H_1 hypothesis (target present).

The null hypothesis H_0 (no target present) is characterized by a space-time snapshot containing only clutter returns, thermal noise, and barrage noise jammer

returns. The H_0 composite space-time snapshot is described by

$$\boldsymbol{\chi} = \boldsymbol{\chi}_c + \boldsymbol{\chi}_n + \boldsymbol{\chi}_j. \quad (3.110)$$

Using these two equations, 3D model data can be generated on a snapshot-by-snapshot basis. Although this approach is the most accurate, it is also the most time consuming and sometimes overwhelms computer resources.

An alternate approach involves coloring whitened data using covariance matrix \mathbf{R} . The covariance matrix describing the entire process is composed of each individual component. This result, for H_0 , is seen by

$$\mathbf{R} \equiv \mathcal{E} \{ \boldsymbol{\chi} \boldsymbol{\chi}^H \} \quad (3.111)$$

$$= \mathbf{R}_c + \mathbf{R}_n + \mathbf{R}_j. \quad (3.112)$$

The cross correlation terms are identically zero because clutter, thermal noise, and any barrage noise jammer are all statistically independent.

3.12 Summary

Establishing an accurate data model is crucial in the research and evaluation of interference suppression methods. This chapter establishes a 3D model based on the physical characteristics of the airborne radar. Comparisons to actual measured airborne radar data in the following chapters show the model produces accurate and reliable results.

Based on previous 2D work, the proposed 3D model offers several extensions. First, returns from elevation channels have been incorporated into the vector framework. Extension to a 2D planar array forced the use of array element patterns as a function of azimuth and elevation, now explicitly included in the model. Elevation

functionality within the individual element patterns represents an important factor when attempting to compare with actual measured data.

Each facet of the airborne radar problem is addressed in detail. A coordinate system common to airborne radar platforms serves to describe returns from the entire sphere surrounding the radar. Using this coordinate system, the transmit signal is examined within a mathematical framework suitable for subsequent analysis. This mathematical foundation allows characterization of the return signal on a per pulse, per element basis. Working at the per pulse, per element level, a vectorized format was developed allowing statistical characterization of clutter, jamming, and thermal noise components present in actual airborne radar scenarios.

A fairly important aspect of the 3D data model involves range ambiguous returns. Although the original 2D model has range ambiguous return capability, *all reported results based on the model, including the original work [65], do not account for nor include range ambiguous clutter effects*. This work not only provides for these returns within the 3D model, but also presents results for cases including range ambiguous clutter. Range ambiguous clutter has a significant impact for medium and high-PRF radars as shown throughout this work. Elevation adaptivity serves to alleviate the associated performance loss.

From the 3D data model framework, expressions for the space-time steering vector, covariance matrix, and related processing elements were developed. These individual components serve as the building blocks for the subsequent 3D adaptive methods. The 3D model is purposely constructed in a manner providing generality. An in-depth discussion of the original 2D model was not provided since the 3D model effectively collapses to the 2D case.

As presented in this chapter, the 3D model is designed to produce *homogeneous* data. When examining most interference suppression methods, this approach is sufficient and desirable. However, the goal behind the hybrid research in Chapter VI is operation within *heterogeneous* interference.

Simulating heterogeneous interference is not difficult. For this work, the data model of this chapter is used for clutter, noise, and jamming. The resulting homogeneous data is then corrupted using the target model. As discussed in Section 2.4, the introduction of a target return different from the radar look direction generates a basic heterogeneous data case termed a discrete interferer.

IV. Three-Dimensional Factored Methods

This research effort's primary objective is the advancement of adaptive interference suppression techniques for airborne radar. The problem is one of detecting targets within a severe interference environment characterized by high levels of ground clutter, jammer infiltration, and other strong sources not of interest (termed discrete interferers). Each of these individual interference factors were addressed in the 3D data model of Chapter III. The next step in the research chain of Fig. 1.2 considers development of 3D factored interference suppression approaches. The validity of elevation based interference suppression is examined in this chapter.

Radar Space-Time Adaptive Processing (STAP) techniques have classically focused on azimuth-Doppler adaptivity while placing minimal emphasis on elevation. Elevation beamforming offers significant clutter suppression improvement, allowing further suppression of interference sources having identical Doppler and azimuth. This chapter incorporates elevation adaptivity through an interferometric approach, greatly improving clutter suppression while providing an often overlooked target height discrimination capability.

The first section provides a proof-of-concept for 3D-FTS, a simple two-element interferometer fused with the 2D-FTS method reviewed in Section 2.6. The idea involves a basic implementation of the ICE concept discussed in Section 2.8.1.1 followed by 2D-FTS.

Since the Multi-Channel Airborne Radar Measurement (MCARM) program used a planar array with two vertical channels, constraining the 3D proof-of-concept to two vertical elements allows a critical comparison. This comparison is between results based on the 3D data model developed in Chapter III and those based on measured data. Validity of the 3D data model is key to the 3D performance improvement claims made throughout the remainder of this document. Obviously, this

first design serves a key role in validating not only the 3D data model but also the overall 3D interference suppression concept.

Based on original 3D-FTS success, the second major topic of this chapter moves forward with a mathematical construct encapsulating a multi-stage processing framework capable of operating with any number of elements or pulses. The multi-stage 3D framework clearly extends traditional 2D-FTS into the azimuth-Doppler-elevation hypercube. The proposed concept is validated using results based on simulated airborne radar data. Target detection improvement on the order of 25 dB, when compared to standard 2D-FTS processing, is demonstrated for an 8×8 non-uniform rectangular array. Elevation pattern data is provided to illustrate achievable null width/depth capabilities. This data also indicates target height discrimination is inherently provided and warrants further development.

The improvements gained by 3D-FTS, when compared to 2D-FTS for the array and CPI sizes considered, suggest other possible benefits may be realized. One possible benefit involves a previous assumption: reducing array size typically implies a reduction in performance. An array thinning analysis is provided in Section 4.3 and shows how performance reduction can be avoided in a typical radar environment. The result occurs because, in 3D STAP, more DOF are available than necessary to suppress the interference. Hence, an array can be thinned and maintain equivalent performance.

The final factored approach considered in this work is 3D-JDL. The 3D-FTS development repeatedly reminds the reader that *any* 2D STAP technique can follow elevation adaptivity. For this final method, 2D-FTS is replaced by the joint domain 2D-JDL method reviewed in Section 2.7. Obviously, 2D-JDL offers much better performance than 2D-FTS within the azimuth-Doppler plane due to the joint approach. This baseline improvement allows 3D-JDL to outperform 3D-FTS in terms of output SINR and, equivalently, detection probability.

The last section of this chapter discusses range ambiguous interference suppression. Two distinct alternatives are developed for the elevation beamforming stage of processing. Each approach seeks to suppress range ambiguous interference in a different manner. The first approach offers elevation null placement based on the physical geometry of the airborne radar in relation to the spherical Earth model. This model is identical to the one used in Chapter III. The second approach proposes elevation null placement based on a statistical technique. In effect, an elevation only interference covariance matrix is generated and used to formulate the elevation weights. Each technique is compared with results reported for each factored method developed in this chapter.

4.1 3D-FTS Using Two Element Interferometry Fused with 2D-FTS

This section presents interferometric 3D-FTS [31, 32, 34], a two channel vertical beamformer operating in conjunction with 2D-FTS STAP. Reported results use measured airborne radar data from the Multi-Channel Airborne Radar Measurement (MCARM) program [59]. These results illustrate consistent performance improvements approaching 15 dB. The improvements from this two element vertical interferometer implementation mirror reported Adaptive Clutter Erasure (ACE) [67] results. Although comparable to the elevation interference suppression approach of 3D-FTS, ACE is a one-dimensional interference suppression method and is *not* comparable to the *overall* 3D-FTS approach developed here.

4.1.1 MCARM Program. The MCARM program is an airborne radar testbed for the exploration of adaptive interference suppression methods, including STAP. All algorithm investigation is done off-line; no real-time processing was implemented on the platform. Hence, the primary goal of the program was multi-channel clutter data collection from an airborne platform.

Table 4.1: MCARM radar parameters for acquisition 575, flight number 5.

Parameter	Value
Aircraft Altitude	3073 m
Transmit Frequency, f	1.24 GHz
Pulse Repetition Frequency (PRF), f_{PRF}	1984 Hz
Transmit Azimuth Angle, ϕ_{xmit}	-0.895°
Transmit Elevation Angle, θ_{xmit}	0°
Elevation Channel Spacing, d_z	0.1407 m
Azimuth Channel Spacing, d_x	0.1092 m
Azimuth Channels, N	11
Elevation Channels, P	2
Pulses per Coherent Processing Interval, M	128
Range Cells per Inter-Pulse Period, L	630

A BAC 1-11 served as the test platform for the L-band radar. Table 4.1 shows the pertinent parameters for the data acquisition used here. All angles are referenced to the array normal where $+\phi_{\text{xmit}}$ points towards the nose of the aircraft and $+\theta_{\text{xmit}}$ points upwards. The antenna array was located on the port (left) side of the MCARM aircraft, indicating the expected mainbeam clutter Doppler frequency is negative for $\phi_{\text{xmit}} = -0.895^\circ$. Furthermore, there is a constant down tilt of 5° on the antenna array in conjunction with aircraft roll. Aircraft orientation for this acquisition was -7.3° crab angle (positive is clockwise when looking down on the aircraft), 4.1° pitch (positive is nose up), and a -0.1° roll (positive is right wing down).

4.1.2 Elevation Adaptivity. Elevation adaptivity is incorporated using a simple two-channel interferometer, e.g., beamformer. The two channel restriction at this point is a direct result of the MCARM aircraft configuration, not a consequence of technical limitations, thereby allowing the use of measured airborne radar data.

As shown in Section 4.2, the results presented here can be improved as the elevation DOF increase, i.e., number of elevation channels P increases.

The elevation beamformer is implemented with the goal of ground clutter suppression. Steering an elevation null in the ground direction for each range cell accomplishes this goal. Therefore, the elevation weights (inter-channel phase delays) vary on a range cell basis. Steering the elevation null to the ground location is a simple trigonometric or beamforming problem. The appropriate vertical weighting for nulling ground clutter is

$$\begin{bmatrix} 1 & -\exp\left(j2\pi\frac{fd_z}{c}\sin\theta_g\right) \end{bmatrix}^T, \quad (4.1)$$

where c is the speed of light, and θ_g is the elevation angle to the ground, referenced to the array normal, for a particular range cell.

The entire elevation beamforming process can be thought of as co-phasing the ground clutter returns for each range cell. Ideally, ground clutter returns are cancelled leaving moving and airborne targets. A direct benefit of applying interferometric ground clutter suppression is that target amplitude is now proportional to height as a function of the vertical beamformer pattern. The overall elevation concept is similar to ICE and the implementation in ACE.

4.1.3 2D Factored Time-Space. As Section 2.6 showed, the 2D Factored Time-Space (2D-FTS) technique is effectively post-Doppler adaptive beamforming.

The data is first Doppler filtered and then adaptive weighting is calculated for each Doppler cell across the azimuth channels. Hence, the 2D-FTS technique is only spatially adaptive. However, the method is recognized as one of the simplest STAP algorithms and commonly used as a benchmark for developmental comparison.

The FTS implementation used here implements the Doppler filter without windowing, e.g., beam sharpening. A variety of windows/tapers can be applied to the Doppler filter forcing a significant reduction in sidelobe level, all at the expense of mainbeam widening [36]. Results may be further improved over those reported here by varying target Doppler location with respect to mainbeam clutter.

4.1.4 Test Statistic. The results presented use the Constant False Alarm Rate (CFAR) test statistic for unknown/estimated covariance given by [21],

$$\rho = \frac{\left| \mathbf{a}(\phi)^H \hat{\mathbf{R}}_N^{-1} \tilde{\mathbf{x}} \right|^2}{\mathbf{a}(\phi)^H \hat{\mathbf{R}}_N^{-1} \mathbf{a}(\phi)}, \quad (4.2)$$

where $\hat{\mathbf{R}}_N$ is the $N \times N$ covariance matrix estimated for the range cell and Doppler bin of interest, $\mathbf{a}(\phi)$ is a $N \times 1$ spatial steering vector oriented towards the azimuth angle of interest [65], and $\tilde{\mathbf{x}}$ is the $N \times 1$ azimuth channel data for the elevation angle and Doppler bin of interest. The test statistic is also known as the modified Sample Matrix Inversion (SMI) test for estimated covariance. The SMI test statistic is identical to the Adaptive Matched Filter (AMF) test [51] and both exhibit embedded CFAR characteristics.

Using the test statistic of Eqn. (4.2), the false alarm probability P_{FA} can be shown to be dependent only on the integers N and K , the number of range cells used in the covariance matrix estimate. Therefore, the test is CFAR [21]. Any improvement in the test statistic translates into direct improvement in output Signal-to-Interference plus Noise Ratio (SINR) and detection probability P_{D} . The CFAR claim is made given the sum of the outer product of each data vector used in the covariance estimate,

$$K\hat{\mathbf{R}}_N = \sum_{i=1}^K \tilde{\mathbf{x}}_i \tilde{\mathbf{x}}_i^H, \quad (4.3)$$

is complex Wishart distributed. The quantity is assumed complex Wishart distributed after the elevation beamforming operation and the test statistic remains CFAR. This assumption is valid given the elevation beamforming operation does not change the distribution of the incoming data.

4.1.5 Performance Measures. Tabular results are presented given two performance measures; Relative Peak Sidelobe Level (RPSL) and Relative Average Sidelobe Level (RASL). Both metrics are defined relative to the *target peak* response. RPSL refers to the difference (in dB) between the target and next highest peak response. RASL refers to the average difference (in dB) between the target and sidelobe peak responses.

4.1.6 Two Element 3D-FTS Results. For comparison purposes, a simulated target was injected into the measured data set using parameters given in Table 4.2.

Table 4.2: Simulated target parameters.

Parameter	Value
ϕ_t	-0.895°
θ_t	45°
Altitude	4923 m
Doppler	496 Hz
Range Cell	300
Range	71.95 km

The target azimuth angle ϕ_t matches the radar transmit azimuth for this data acquisition. The target elevation angle θ_t was chosen to ensure the target is in the elevation pattern mainbeam; the resulting target altitude is shown in the table.

Figure 4.1 shows the results of 2D-FTS (dashed line) using only the upper azimuth channels of the MCARM array compared to 3D-FTS (solid line) using the elevation beamforming fused with 2D-FTS. The figure shows the normalized AMF test statistic at the target Doppler bin along a set of range cells neighboring the target location. RPSL, the separation between target and next highest peak responses, improved by 14.71 dB and RASL improved by 13.71 dB.

Similarly, Fig. 4.2 shows the normalized AMF test statistic at the target range cell across all $M = 128$ Doppler bins. RPSL improved by 13.82 dB when using the elevation ground clutter suppression in conjunction with FTS and RASL improved by 16.62 dB.

Because the test is CFAR, these results translate directly to improvement in output SINR and a corresponding improvement in P_D for a constant P_{FA} (constant

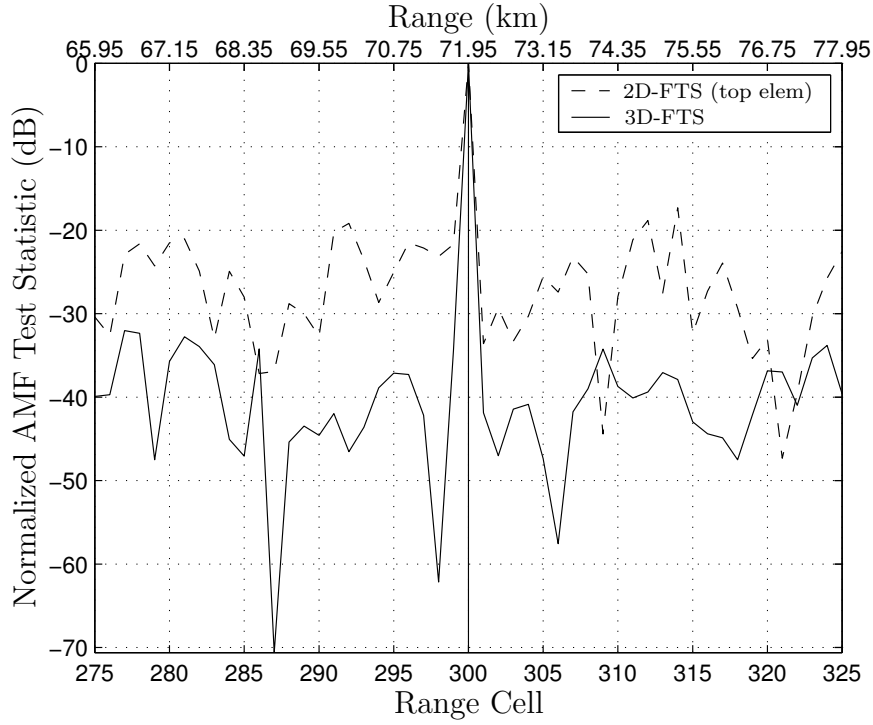


Figure 4.1: Interferometric elevation ground clutter suppression achieves almost 14 dB improvement in spurious range returns at target Doppler bin.

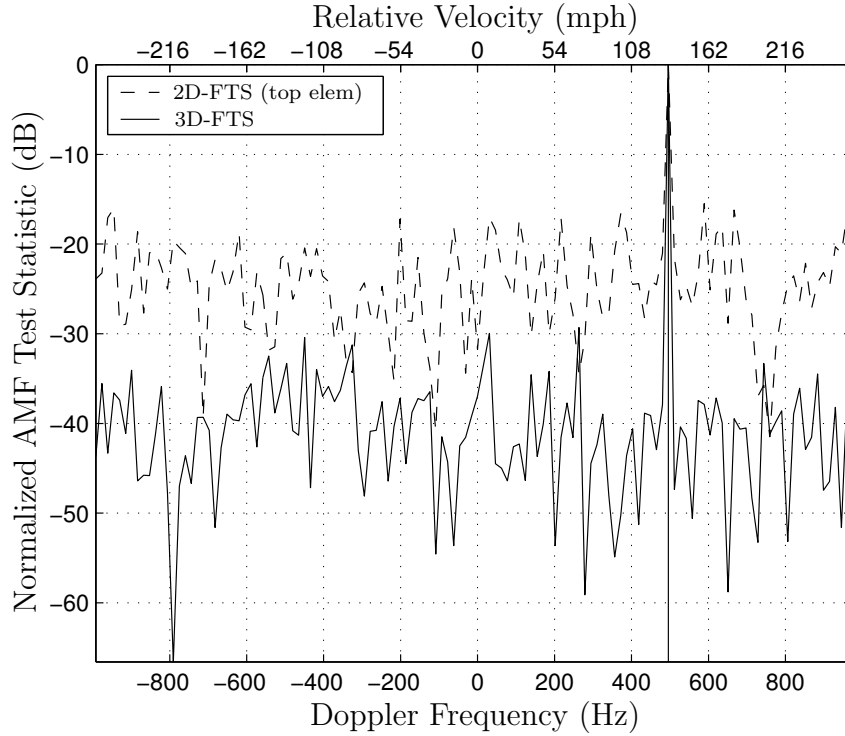


Figure 4.2: Interferometric elevation ground clutter suppression achieves almost 14 dB improvement in spurious Doppler returns at target range cell.

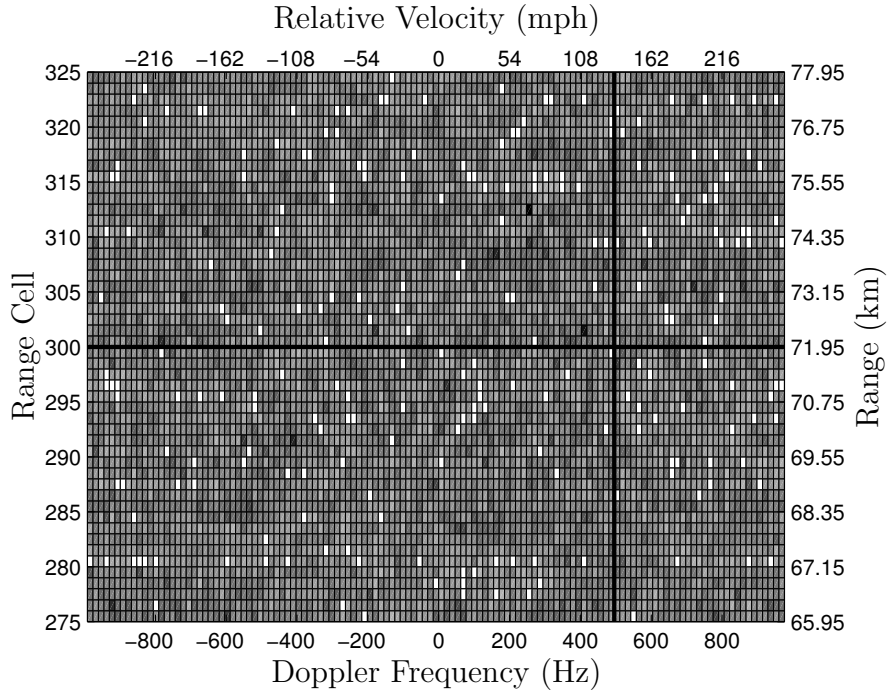


Figure 4.3: An improvement surface shows performance degradation only in the white Range-doppler bins when using the elevation beamformer.

decision threshold). Therefore, a significant performance improvement results when applying elevation interferometry to suppress ground clutter returns.

Figure 4.3 represents an improvement surface generated from data used for Figs. 4.1 and 4.2. The surface is generated by subtracting the test statistic (in dB) for elevation beamforming with 2D-FTS (3D-FTS) from the test statistic generated for standard 2D-FTS, where both are normalized by the peak target response. The intersecting solid lines in the figure correspond to the target location and represent 0 dB improvement by definition (given the data is normalized prior to subtraction). The pure white portions of the surface represent degradation of the output test statistic when using elevation beamforming with 2D-FTS (3D-FTS).

Table 4.3: 2D-FTS vs. 3D-FTS performance summary. All units are dB.

	Range Cut (Fig. 4.1)		Doppler Cut (Fig. 4.2)		Surface (Fig. 4.3)	
	RPSL	RASL	RPSL	RASL	RPSL	RASL
2D-FTS	-17.31	-27.75	-15.48	-25.00	-10.76	-26.85
3D-FTS	-32.01	-41.46	-29.30	-41.62	-25.01	-40.68
Improvement	14.71	13.71	13.82	16.62	14.25	13.83

A visual scan of the surface clearly reveals very little degradation over the entire range-Doppler surface under consideration. Furthermore, analysis of the white regions revealed only a small amount of degradation actually occurs. Specifically, the white areas merely represent areas of deep nulls in the 2D-FTS approach that increased slightly when using interferometric 3D-FTS; these areas still represent nulls and not false target detections. For example, consider the white area along the target range cell line (300) at a Doppler of approximately 750 Hz. Close examination of Fig. 4.2 at this point shows a degradation of approximately 5 dB, yet the response at this Doppler bin is still 34 dB below the target peak response.

Table 4.3 summarizes results in terms of the RPSL and RASL performance metrics previously introduced. Obviously, using elevation interferometry in conjunction with 2D-FTS STAP provides significant performance improvements in target detection capability. A much higher P_D can be obtained for the same P_{FA} setting.

4.1.7 Target Altitude Determination. As mentioned previously, joining elevation beamforming with 2D-FTS imparts a pattern specific relationship between

target altitude and test statistic magnitude. If this relationship is present, target elevation angle variation should allow indirect plotting of the elevation beamforming pattern.

Figure 4.4 shows the result of this experiment. The solid curve is the analytical elevation interferometric pattern. The dashed curve is the result of measuring the separation between the target peak and next highest peak with the target located at the elevation angle θ depicted in the figure, for elevation interferometry in conjunction with 2D-FTS. As surmised, the output response is now directly related to target altitude.

! The positive $\theta = 2^\circ$ (as referenced to the array normal) for the elevation interferometric null in the direction of the ground clutter is a result of the constant 5° down tilt of the MCARM antenna array and the small aircraft roll angle in this acquisition. When referenced to a fixed coordinate system, the null is actually pointed towards the ground.

4.2 3D-FTS Multidimensional Mathematical Construct

Target detection improvement within the azimuth-Doppler plane has been clearly demonstrated using STAP, with limited work addressing the benefits of elevation adaptivity. A previous contribution [42] introduced the concept of using elevation processing to suppress range ambiguous interference. However, no results were provided and the realization that little published work even addressed elevation adaptivity was offered [42].

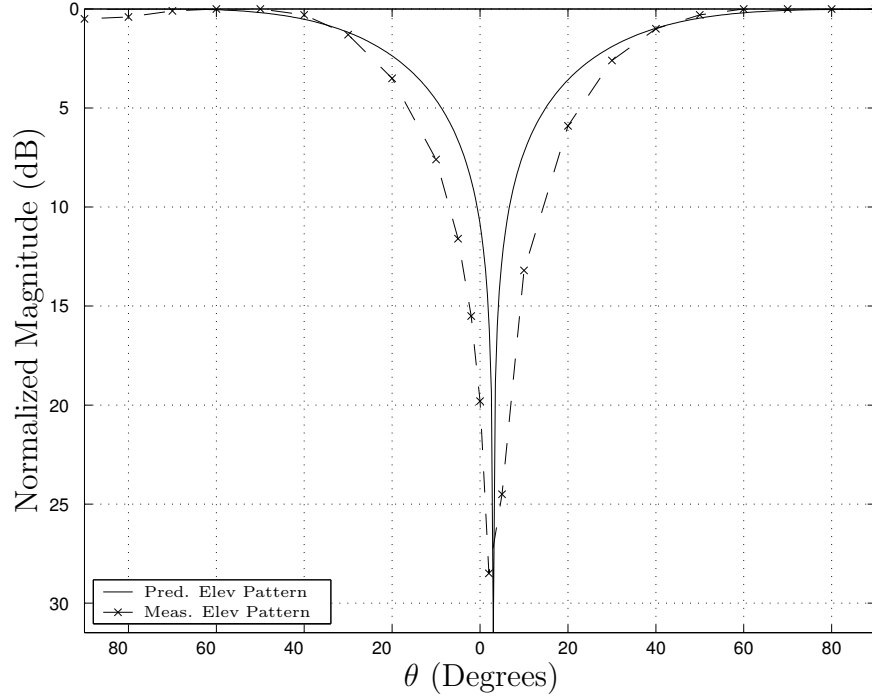


Figure 4.4: Elevation pattern plotted by measuring difference between target range cell peak and next highest range peak. This figure indicates amplitude is now proportional to target altitude.

The interferometric 3D-FTS approach and analysis presented to this point [31] represents a significant improvement over conventional 2D-FTS. Although the elevation interferometer can be followed by any adaptive processing method, 2D-FTS was chosen merely for simplicity to provide baseline results. Specific results for the data acquisition (real airborne radar measurements) promise performance improvements approaching 15 dB for a two channel vertical interferometer. This improvement compares favorably with previously reported results for ACE [67]. Furthermore, the results presented in Section 4.1.6 are independent of the particular data acquisition. The proposed interferometric 3D-FTS technique was performed on all freely

releasable MCARM data acquisitions and shown to offer similar improvement over 2D-FTS.

Anticipated performance improvement increases as the number of vertical channels is increased. Furthermore, increasing the number of vertical channels offers greatly improved target altitude resolution and narrows the ground clutter null. Narrowing the ground clutter null alleviates involuntary low-altitude target suppression. Ideally, the ground clutter null should only cover the elevation extent required to suppress the desired range ring. This observation suggests an optimum number of vertical antenna channels, although it will be a function of target range and therefore impractical.

The primary problem with using the MCARM data is the limitation to two vertical channels. Within this constraint, the primary purpose of Section 4.1 was achieved, i.e., demonstrating that 3D interference suppression offers significant performance gains. The next step involves generalizing the elevation interferometric approach beyond the two channel limitation, as provided in this section.

! Due to the MCARM two vertical channel limitation, measured data is no longer useful in evaluating the proposed 3D methods and the 3D data model of Chapter III becomes crucial. For preliminary validation, the work of Section 4.1 was duplicated with simulated 2D and 3D data from the 3D model and compared with MCARM data; nearly identical results were obtained.

Using simulated data generated from the 3D physical radar environment model, this section extends previous 3D-FTS results by improving interferometric elevation

processing and demonstrating capabilities for larger vertical DOF than available in the MCARM radar. Extremely deep and relatively wide clutter nulls are achieved while maintaining an elevation mainbeam in the target direction. Detection improvement approaching 25 dB, when compared to standard 2D-FTS processing, is demonstrated for an 8×8 rectangular array using a Coherent Processing Interval (CPI) of eight pulses. Furthermore, target height information as a function of scan angle is inherently available with resolution dependent on the number of elevation channels.

The overall 3D concept proposed here is consistent with Section 4.1 and reduces to the factored approach detailed in Fig. 4.5. Array element data is first filtered using elevation beamforming. The goal is clutter suppression while avoiding target nulling. This filtering is adaptive on a range cell basis with the clutter null centered at the clutter elevation angle. Doppler filtering follows and the final stage is statistical adaptive processing. The final two filtering stages represent traditional 2D-FTS. The goal is to show significant performance improvements using (1) the relatively simple 2D-FTS STAP technique having marginal stand-alone detection capability and (2) smaller array/CPI sizes generally thought to provide insufficient suppression. However, any STAP technique can follow the interferometric elevation processing with expected performance improvements over those presented here, as shown in Section 4.4.

! The purpose of this work is *not* to provide an adequate implementation of 2D-FTS on the ULA. Conversely, marginal 2D-FTS performance is

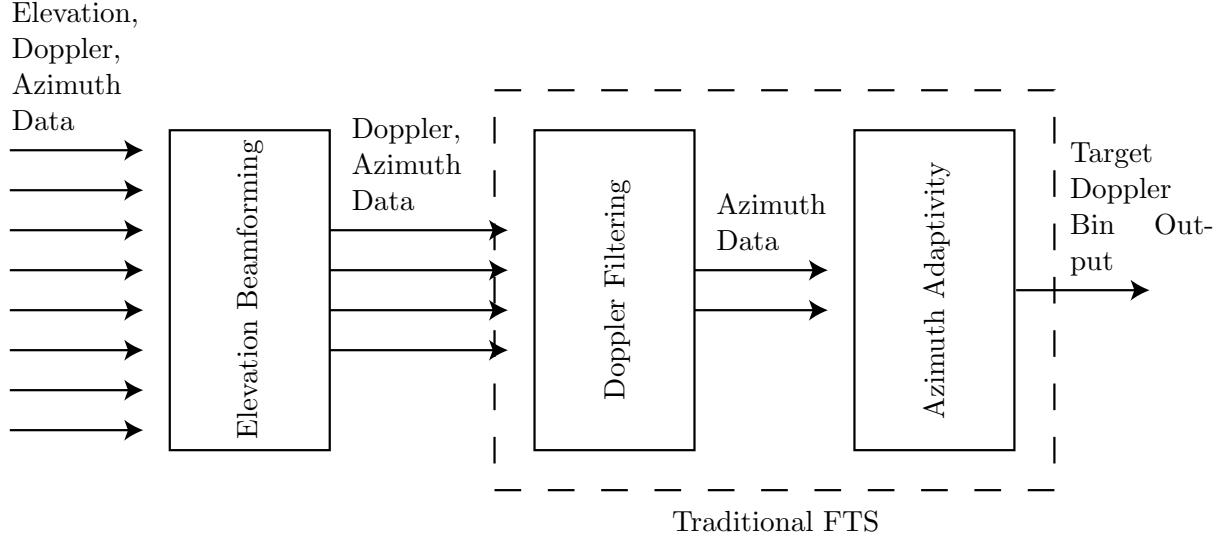


Figure 4.5: Proposed 3D-FTS technique incorporating elevation beamforming.

desired to show the *drastic* improvements gained through the introduction of elevation based interference suppression with 3D-FTS. These improvements are shown for array/CPI sizes characteristically considered unacceptable.

Because the proposed 3D-FTS method attempts to suppress interference over an entire range ring, it is suboptimum. An optimum processor is capable of placing nulls at point(s) in the three-dimensional space, i.e., at a particular azimuth angle, Doppler frequency, and elevation angle. Achieving optimum processing capability is the subject of Chapter V.

The proposed adaptive processing method can be represented by expanding the traditional 2D structure of the incoming space-time snapshot \mathbf{x} to incorporate array elevation data. This expansion yields the space-time steering vector of Eqn. (3.44) on page 71,

$$\mathbf{e} \otimes \mathbf{b} \otimes \mathbf{a}, \quad (4.4)$$

where \mathbf{e} and \mathbf{a} represent the elevation ($P \times 1$) and azimuth ($N \times 1$) steering vectors, and \mathbf{b} is the Doppler ($M \times 1$) steering vector. This formulation drives the form of $\boldsymbol{\chi}$, yielding a $PMN \times 1$ vector. Using this structure, the proposed 3D-FTS interference suppression technique is easily encapsulated as

$$(\mathbf{E}\mathbf{B}\mathbf{w}_a)^H \boldsymbol{\chi} = \mathbf{w}^H \boldsymbol{\chi}, \quad (4.5)$$

where \mathbf{w}_a , \mathbf{B} , and \mathbf{E} are defined in the following subsections. This mathematical construct casts a three-dimensional problem into a one-dimensional, vectorized framework. Although a more compact format may exist, the framework presented here offers strong similarity to existing STAP architectures.

4.2.1 Elevation Adaptivity. Each weight vector component is derived sequentially in a factored approach. First, elevation adaptivity is applied in Eqn. (4.5) through

$$\mathbf{E} = \mathbf{w}_e \otimes \mathbf{I}_{MN}, \quad (4.6)$$

a $PMN \times MN$ matrix with \mathbf{I}_{MN} an $MN \times MN$ identity matrix and \mathbf{w}_e , a $P \times 1$ elevation weight vector (described below). The Kronecker product with the identity matrix is a direct result of the incoming data format. The goal is elevation beamforming with the set of weights contained in \mathbf{w}_e , yet the operation is a $P \times 1$ weight vector filtering an incoming space-time snapshot $\boldsymbol{\chi}$ of dimension $PMN \times 1$. After elevation beamforming, the data vector should contain only MN elements. Exam-

ining the structure of the space-time snapshot shows the mathematical form of this operation to be

$$\mathbf{E}^H \boldsymbol{\chi} = (\mathbf{w}_e \otimes \mathbf{I}_{MN})^H \boldsymbol{\chi}. \quad (4.7)$$

The Kronecker product provides a compact, succinct notation that is easy to read and understand within the overall framework of the defined data structure. The identity matrix role is seen by simply expanding $\mathbf{w}_e \otimes \mathbf{I}_{MN}$ into

$$\begin{bmatrix} \mathbf{w}_{e,0} \\ \mathbf{w}_{e,1} \\ \vdots \\ \mathbf{w}_{e,P-1} \end{bmatrix} \otimes \begin{bmatrix} 1 & 0 & \cdots & 0 \\ 0 & 1 & \cdots & 0 \\ & \vdots & \ddots & \\ 0 & 0 & \cdots & 1 \end{bmatrix} = \begin{bmatrix} \mathbf{w}_{e,0} & 0 & \cdots & 0 \\ 0 & \mathbf{w}_{e,0} & \cdots & 0 \\ & \vdots & \ddots & \\ 0 & 0 & \cdots & \mathbf{w}_{e,0} \\ \mathbf{w}_{e,1} & 0 & \cdots & 0 \\ 0 & \mathbf{w}_{e,1} & \cdots & 0 \\ & \vdots & \ddots & \\ 0 & 0 & \cdots & \mathbf{w}_{e,1} \\ & \vdots & \ddots & \\ \mathbf{w}_{e,P-1} & 0 & \cdots & 0 \\ 0 & \mathbf{w}_{e,P-1} & \cdots & 0 \\ & \vdots & \ddots & \\ 0 & 0 & \cdots & \mathbf{w}_{e,P-1} \end{bmatrix}. \quad (4.8)$$

From Eqn. (4.8), it is clear how this method (after the Hermitian operation in the weight application) extracts the correct elements of the incoming space-time snapshot for elevation beamforming. For this portion of the processing, the identity matrix has dimension MN since each set of vertical channel/array samples is separated by MN samples.

The range cell under test (range ring) defines an elevation angle from array boresight to the ground. Elevation weights \mathbf{w}_e are chosen to suppress clutter at this angle while simultaneously focusing a beam towards the target's elevation location. Clutter suppression in elevation reduces interference, allowing improved performance of partially adaptive methods in azimuth and Doppler. Using an operation paralleling Wiener filter theory, \mathbf{w}_e and \mathbf{C}_e (an artificially generated interference covariance matrix designed to place null(s) at the unambiguous clutter ring) are calculated from the filter look direction angle θ and the angle to the clutter ring θ_c under consideration

$$\mathbf{w}_e = \mathbf{C}_e^{-1} \mathbf{e}(\theta) \quad (4.9)$$

where

$$\mathbf{C}_e = \frac{1}{J} \sum_{i=1}^{J-1} \mathbf{e}(\theta_i) \mathbf{e}(\theta_i)^H + \sigma^2 \mathbf{I}_P \quad (4.10)$$

$$\theta_i = \alpha_i \theta_c \text{ where } \alpha_i \in \mathfrak{R}. \quad (4.11)$$

The role of steering vector $\mathbf{e}(\theta)$ is mainbeam/target preservation. The projection of matrix \mathbf{C}_e^{-1} onto the steering vector results in strong clutter nulls at locations described by θ_c , given the look direction θ does not lie within the range of θ_i used in Eqn. (4.10). For simulations presented later in this chapter, \mathbf{C}_e contains $J = 3$ significant clutter sources with the clutter elevation angle bracketed, i.e., $\theta_i = \{0.95\theta_c, \theta_c, 1.05\theta_c\}$. These angles and the degree of separation between them act as a null width control parameter.

One design consideration, or optimization, is of interest at this point. It may be beneficial to vary the clutter null width based on the range to the clutter source/ring. For shorter ranges, the angular extent of the range ring is considerably more than at longer ranges. In this case, optimization may be possible by merely choosing an appropriate balance of J and angular separation in θ_i (a constant of 0.05 in this development) to fully cover the range ring angular extent.

! A second point of considerable importance involves range ambiguous data. At this point in the development of 3D-FTS, the elevation beamformer does *not* attempt to null range ambiguous clutter returns. This choice was made to keep the initial concept simple, although it ignores potentially significant performance improvements gained by suppressing range ambiguous interference. The elevation beamforming extension for range ambiguous clutter suppression is presented in Section 4.5 where the modified matrix \mathbf{C}_e in Eqn. (4.20) is easily substituted for Eqn. (4.10).

The final term of Eqn. (4.10), $\sigma^2 \mathbf{I}_P$, injects noise into the process ensuring \mathbf{C}_e is full rank and invertible. Here, σ^2 was set equal to the noise power spectral density multiplied by the receiver bandwidth. Eqn. (4.9) projects \mathbf{C}_e^{-1} onto an

elevation steering vector, ensuring the target is not nulled in the clutter suppression process. Sidelobe levels are of little concern, since the range gating process effectively constrains harmful clutter to a small angular extent in elevation.

4.2.2 Doppler Filtering. Consistent with conventional 2D-FTS processing, the second weight vector component in Eqn. (4.5),

$$\mathbf{B} = \mathbf{b} \otimes \mathbf{I}_N, \quad (4.12)$$

provides non-adaptive Doppler filtering to the target bin. A Kronecker product is applied to a DFT matrix column, essentially the temporal steering vector of Eqn. (3.39). Again, the Kronecker product extracts the appropriate elements of the elevation beamformed space-time snapshot $\mathbf{E}^H \boldsymbol{\chi}$. Since pulses are separated within the data structure by N samples, the identity matrix dimension is N .

4.2.3 Azimuth Adaptivity. The final weight vector component in Eqn. (4.5) provides azimuth adaptivity and is given by

$$\mathbf{w}_a = \hat{\mathbf{R}}_N^{-1} \mathbf{a}, \quad (4.13)$$

where $\hat{\mathbf{R}}_N$ is the $(N \times N)$ covariance matrix estimate and \mathbf{a} is an $(N \times 1)$ azimuth steering vector. This $(N \times 1)$ weight vector \mathbf{w}_a is statistically based and derived from a true Wiener filter. In conjunction with the previous Doppler filtering step,

this operation completes the 2D-FTS portion of the processing. This method is only adaptive within the angular domain since the Doppler filtering is done with the standard transformation/steering vector. Covariance matrix estimate $\hat{\mathbf{R}}_N$ is estimated by averaging $K = 2N$ secondary data vectors oriented symmetrically about the target range cell. These secondary data vectors are taken from the Doppler filtered data, not the raw temporal samples. For K equal to twice the degrees of freedom, performance predictions are within 3 dB of optimal for this stage of processing (Reed's rule) [49]. For standard 2D-FTS, $\hat{\mathbf{R}}_N$ is given by [65]

$$\hat{\mathbf{R}}_N = \frac{1}{K} \sum_{i=1}^{K-1} \mathbf{B}^H \boldsymbol{\chi}_i \boldsymbol{\chi}_i^H \mathbf{B} = \mathbf{B}^H \hat{\mathbf{R}} \mathbf{B}. \quad (4.14)$$

However, an additional level of factored processing has been introduced by the proposed method. Thus, the new covariance estimate must reflect the additional transformation on the incoming data vector and is given by

$$\hat{\mathbf{R}}_N = \frac{1}{K} \sum_{i=1}^{K-1} \mathbf{B}^H \mathbf{E}_i^H \boldsymbol{\chi}_i \boldsymbol{\chi}_i^H \mathbf{E}_i \mathbf{B}. \quad (4.15)$$

4.2.4 Test Statistic. Results presented use the modified Sample Matrix Inversion (SMI) test [21] for estimated covariance shown in Eqn. (4.2). The SMI test statistic is identical to the Adaptive Matched Filter (AMF) test [51] and both exhibit embedded CFAR. Therefore, any improvement directly improves output Signal-to-Interference plus Noise Ratio (SINR) and detection probability (P_d). The CFAR

Table 4.4: Radar simulation variables.

Parameter	Value
Aircraft Altitude	9 km
Transmit Frequency	1.24 GHz
Pulse Repetition Frequency (PRF)	1984 Hz
Pulse Width	50 μ sec
Az (d_x) & El (d_z) Channel Spacing	0.1092 m/0.1407 m
Az (N) & El (P) Channels	8/8
Pulses per CPI (M)	8

claim is valid for the SMI test provided $K\hat{\mathbf{R}}_N$ is complex Wishart distributed [21], assumed true after elevation beamforming.

4.2.5 Results. Radar data was simulated using the 3D data model of Chapter III and simulation parameters consistent with the MCARM array (Table 4.4). For this work, the radar parameters of Table 4.4 result in range ambiguous data consisting of the unambiguous clutter response plus the clutter response from four range ambiguous regions. For initial validation, 2D and 3D work of [31] was duplicated using simulated data and compared with MCARM results; simulated data results were identical. For comparing the proposed 3D-FTS technique with a conventional 2D-FTS approach, a simulated target was injected into range cell 80 (36.8 km) with 496 Hz Doppler shift at an azimuth angle of 0° and elevation angle of 45° . Reported results correspond to an 8×8 planar array (side-looking) using a CPI of eight pulses (resulting in eight Doppler bins).

Figures 4.6 and 4.7 present normalized CFAR test statistic results for 2D-FTS (dashed line) using an azimuth array with the proposed 3D-FTS technique (solid line) incorporating elevation adaptivity. Received SINR (per element, per pulse)¹ was set to -53.0 dB, making the target virtually undetectable by standard 2D-FTS processing. As illustrated in the range profile (at the target Doppler) of Fig. 4.6, the target's RPSL across range improved by 24.5 dB to -27.0 dB and RASL across range improved by 23.2 dB to -36.6 dB. Figure 4.7 offers a similar comparison of the two output measures across Doppler in the target range cell. Here, the target's Doppler RPSL and RASL improved by 20 dB and 17 dB, respectively.

The improvement surface of Fig. 4.8 illustrates points where the method degrades performance over standard 2D-FTS (using a linear array). The surface was generated by subtracting the proposed 3D-FTS CFAR test statistic (in dB) from the standard 2D-FTS CFAR test statistic (in dB) with both normalized by the target peak response (not necessarily the highest peak in the test statistic surface). The dashed intersecting lines correspond to the target location and represent 0 dB improvement (by definition given the data was normalized prior to subtraction). The black regions of the surface represent output CFAR test statistic degradation when using the proposed 3D-FTS method. White areas represent varying levels of improvement.

¹See Appendix C for a discussion of received SINR calculations.

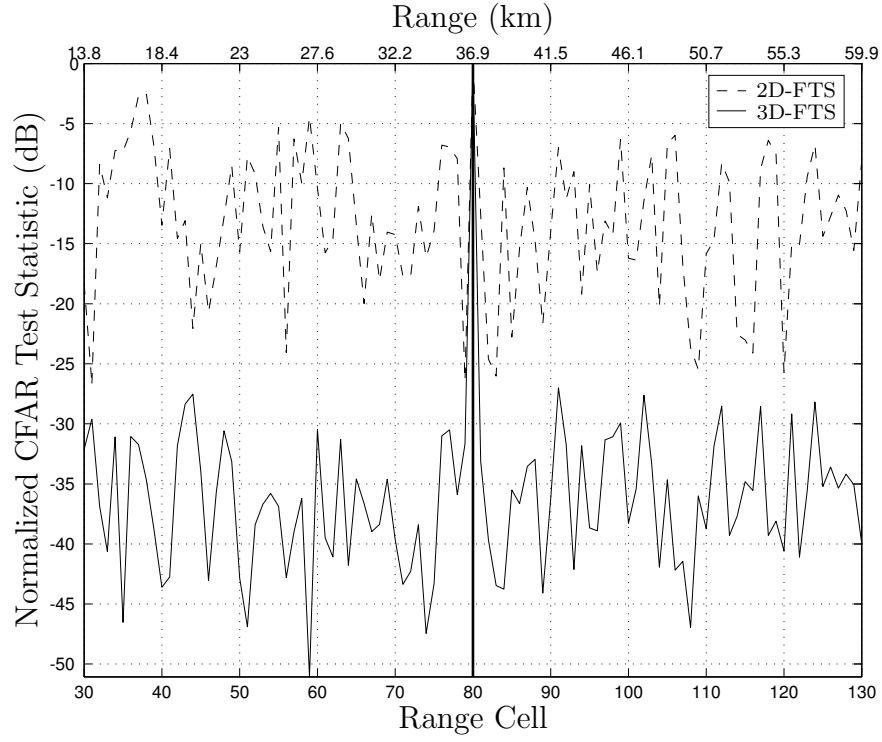


Figure 4.6: 3D-FTS (with four times the number of vertical elements used for Figs. 4.1 and 4.2) achieves almost 25 dB RPSL and 23 dB RASL improvement in spurious range responses.

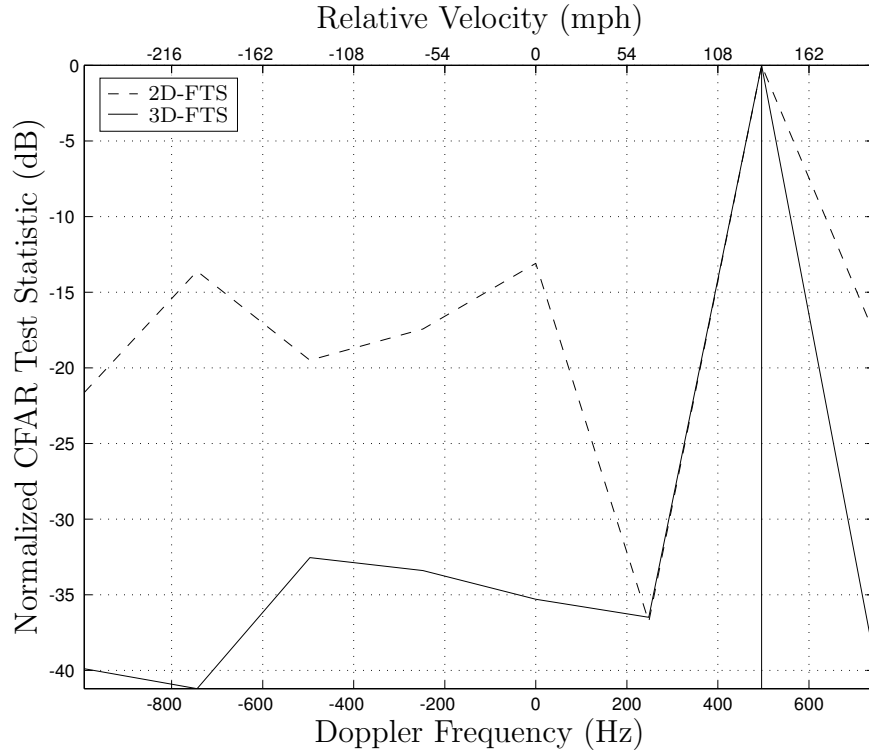


Figure 4.7: 3D-FTS achieves almost 20 dB RPSL and 17 dB RASL improvement in spurious Doppler responses.

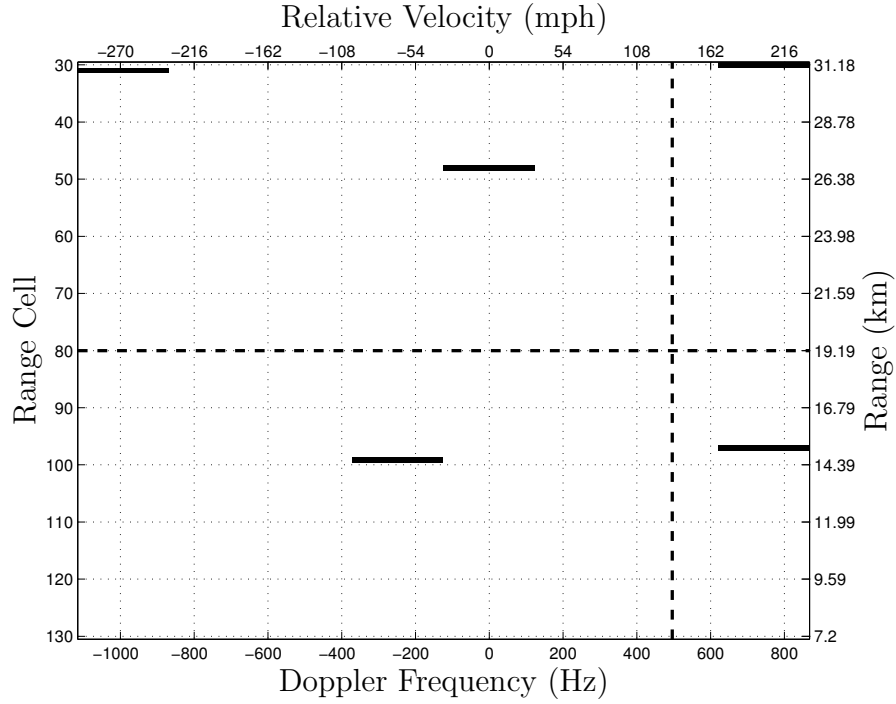


Figure 4.8: Range-Doppler improvement surface shows performance degradation only in the black bins when using 3D-FTS.

Figure 4.8 clearly shows minimal degradation over the entire range-Doppler surface under consideration. Furthermore, the small amount of indicated degradation (only five range-Doppler regions) is proven inconsequential upon closer examination, i.e., the black regions merely represent areas of deep nulls in the 2D-FTS approach that increased slightly when using 3D-FTS. These areas still represent considerable nulls and not false target detections. For example, consider the black pixel in the upper right-hand corner (range cell 30 and Doppler bin containing 800 Hz). A Doppler cut of Fig. 4.8 at this range cell, shown in Fig. 4.9, shows a degradation of approximately 8 dB near 800 Hz yet the 3D-FTS test statistic remains 27 dB below the target peak response.

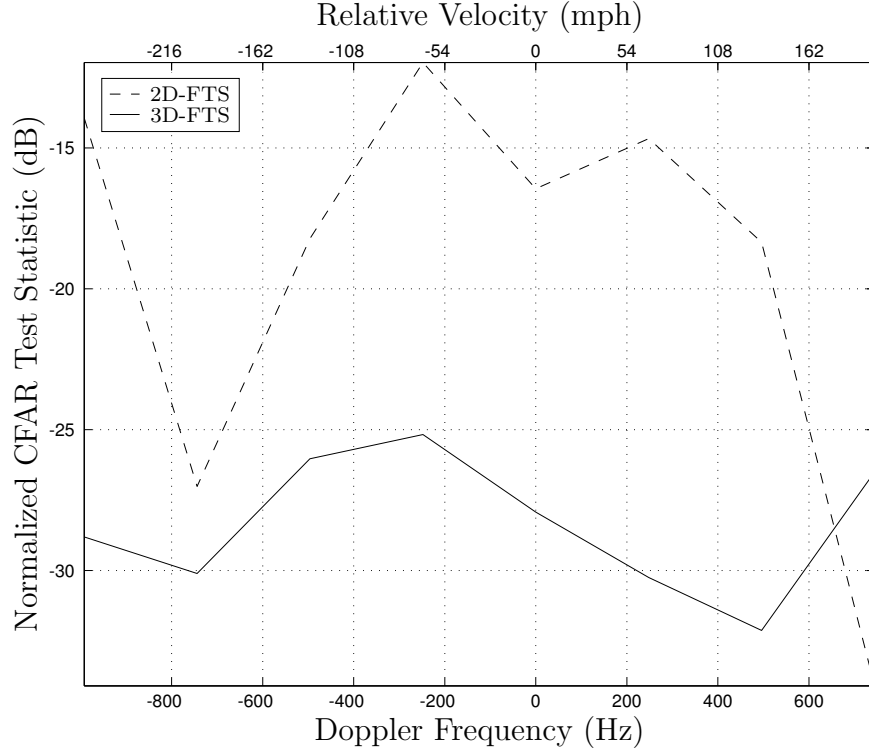


Figure 4.9: Doppler profile shows 3D-FTS performance degradation is inconsequential near 800 Hz. Although the statistic is 8 dB higher, it remains 27 dB below the target peak.

Figure 4.10 compares the proposed 3D-FTS method to 2D-FTS using a detection probability (P_d) metric at a constant false alarm probability (P_{fa}) of 10^{-4} . The proposed method exhibits ≈ 30 dB improvement in SINR for constant P_d , consistent with previous CFAR test statistic improvements.

All results presented thus far include range ambiguous interference. As observed by Klemm [42], researchers seldom address the range ambiguous interference case. For completeness, range ambiguous clutter was removed from the data and further comparisons made with the two-dimensional fully Adaptive Matched Filter (2D-AMF) of Section 2.7. Results are presented in Fig. 4.11. Using $K = 2MN$

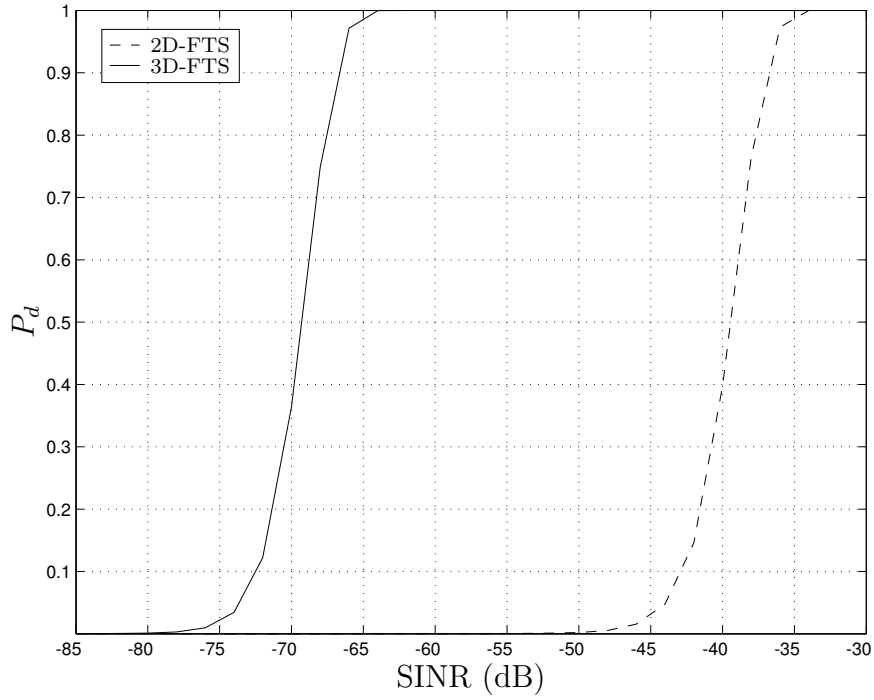


Figure 4.10: 3D-FTS detection probability (P_d) vs. SINR (per element, per pulse) *with* range ambiguous clutter and false alarm probability (P_{fa}) of 10^{-4} .

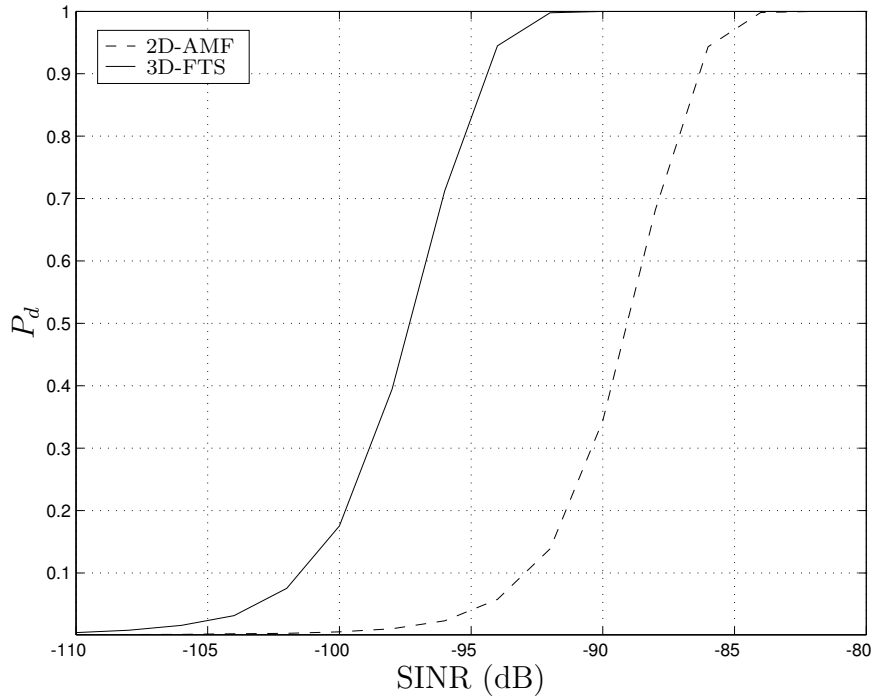


Figure 4.11: 3D-FTS detection probability (P_d) versus SINR (per element, per pulse) *without* range ambiguous clutter and false alarm probability (P_{fa}) of 10^{-3} .

secondary data samples for the 2D-AMF, the unambiguous data results show the proposed technique offers significant detection improvement, as evidenced by Fig. 4.11. Each curve in Figs. 4.10 and 4.11 is the result of a Monte Carlo simulation for 100,000 and 10,000 realizations, respectively. For each ambiguous and unambiguous case considered, identical realizations were used to determine P_{fa} and P_d for each algorithm shown. This approach removes any data dependencies within the results and represents the most consistent detection analysis approach. For each case, P_{fa} was held constant allowing a side-by-side comparison of the data shown. Although higher than practical, a P_{fa} of 10^{-3} was used in Fig. 4.11 primarily for illustrative purposes and permits reliable comparative analysis within computational constraints.

For clarification, the proposed 3D-FTS technique shows improved performance over the AMF operating on a two-dimensional data set, i.e., over a *linear* array with constant pulse sampling. The 3D method developed here operates over a two-dimensional *rectangular* array with constant pulse sampling. Therefore, the idea that a matched filter provides optimum performance over an Additive White Gaussian Noise (AWGN) channel has not been violated. Development of the three-dimensional matched filter framework is reserved for Chapter V.

As stated before, the MCARM program only provides data for two vertical channels ($P = 2$). Therefore, the only practical validation technique for the proposed multidimensional processing technique ($P > 2$) is a Monte Carlo analysis of

Table 4.5: Average (\pm standard deviation) 3D-FTS performance measures using Monte Carlo analysis. All measurements in dB.

Range Cut (Fig. 4.6)		Doppler Cut (Fig. 4.7)		Surface (Fig. 4.8)	
RPSL	RASL	RPSL	RASL	RPSL	RASL
2D-FTS					
-2.6 ± 2.8	-15.5 ± 2.3	-9.6 ± 3.2	-15.7 ± 3.3	-0.1 ± 2.7	-15.1 ± 2.3
3D-FTS					
-25.8 ± 2.6	-38.1 ± 1.6	-30.9 ± 3.0	-37.5 ± 2.7	-22.4 ± 2.5	-37.5 ± 1.5
Improvement					
23.2 ± 4.0	22.6 ± 2.8	21.3 ± 4.4	21.8 ± 4.2	22.29 ± 3.7	22.3 ± 2.8

the RPSL and RASL performance measures. The physical model used for data generation demonstrated reliable results for comparison with MCARM two channel vertical data. Table 4.5 summarizes results for the RASL/RPSL Monte Carlo analysis. The tabulated statistics imply that the results presented are statistically significant. The proposed 3D-FTS method consistently offered an average of 22.3 dB RPSL improvement (directly impacting P_{fa}) with a standard deviation of 3.7 dB (just over 10%). Likewise, an average of 22.3 dB RASL improvement was achieved. These findings illustrate the significant performance gains realized through the introduction of elevation adaptivity.

The data in Table 4.5 also illustrates a previously mentioned point regarding 2D-FTS. By examining the 2D-FTS surface RPSL measurements for the target, one sees an average of only -0.1 dB of separation in the test statistic between the

target and next highest peak. Thus, the detection threshold would have to be set relatively close to spurious non-target responses to detect the relatively small target response, likely resulting in unacceptable P_{fa} . However, the proposed method offers 22.3 dB average separation, allowing realistic threshold values and acceptable P_d/P_{fa} performance. These concepts are reinforced by inspection of the P_d data presented in Fig. 4.10.

4.2.6 Elevation Patterns. The simulated elevation pattern (45° main-beam), shown in Fig. 4.12, illustrates the achievable depth and width of vertical clutter nulls. Given a spherical earth model and radar parameters of Table 4.4, the ground location angle to the clutter ring corresponding to the target range cell is approximately -14° . The figure clearly shows the deep clutter null suppressing returns from this clutter ring. Note that the indicated suppression level of nearly 110 dB is primarily attributable to computational capability and is likely not realizable in practical systems. This figure provides simulated and calculated elevation patterns for comparison. As indicated, grating lobes encroach upon the angular extent of the array; this result is merely a consequence of under sampling along the vertical array axis. Because of the range gating process, the *only* source of unambiguous interfering clutter occurs in the clutter ring located at -14° . This condition strictly applies to the simulated data case since the earth surface is not truly spherical in real-world applications due to terrain variations.

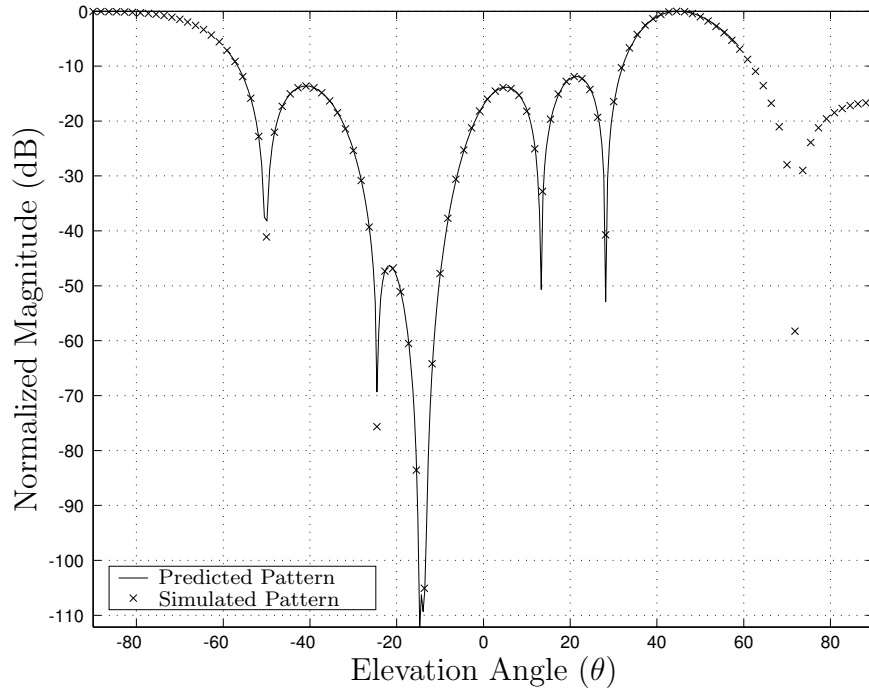


Figure 4.12: Simulated elevation pattern for the 8×8 array with mainbeam formed to 45° . The pattern was calculated by moving a constant amplitude target through the elevation extent of the array.

Figure 4.12 validates the pattern calculation methodology and shows the algorithm is performing as predicted. Similar plots can be generated for Doppler and azimuth dimensions. However, these are not of primary concern to this development. For example, the Doppler filtering operation is a simple non-adaptive filter. As such, its pattern exhibits the typical -13 dB sidelobe pattern commonly found in textbooks. (The only distinguishing characteristic is its shifting to the target Doppler bin.) Similarly, the factored approach taken in this development allows the azimuth pattern to be generated independently of the other two dimensions. The focus of this development was on the proposed 3D-FTS hybrid approach and achieving enhanced

clutter suppression through elevation processing; the idiosyncracies of basic 2D-FTS processing were not addressed.

4.3 Elevation Interferometric STAP Using a Thinned Array

The creation of the 3D-FTS technique in the previous section and the significant performance gains due to elevation based interference suppression suggest new possibilities. Generally, the idea of thinning an array coincides with performance degradation. Yet, addition of the third dimension for interference suppression gives much greater localization capability, both for targets and interference. This realization leads to the possibility that thinning an array does not necessarily result in performance degradation. This section evaluates this possibility and shows the hypothesis is true, with remaining elements playing a critical role in performance [34].

The research applies Space-Time Adaptive Processing (STAP) techniques to a pseudo-circular array generated by selectively thinning a rectangular array. The 3D-FTS approach of Section 4.2 is used. Results show the thinned 16-element pseudo-circular array offers significant detection performance improvement over the baseline 2D-FTS technique operating on a linear array, i.e., an 8-element horizontal linear array. Results are demonstrated for cases with and without range ambiguous clutter. This performance level is achieved using a factor of M less sample support than required for full adaptivity where M represents the number of pulses within a coherent processing interval.

As discussed in Chapter II, most STAP research focuses on applying adaptive processing techniques to a Uniform Linear Array (ULA). Recently, research emphasis has begun to shift away from the traditional ULA architecture and is moving towards applications involving STAP on alternate array configurations. In particular, STAP methods have been applied to a non-linear set of sensors oriented in an arc [69, 70] corresponding to an experimental, circular, electronically scanned array being fabricated by Raytheon. The research in [69, 70] highlights complications arising from the non-linear array configuration, namely, clutter ridge locus movement as a function of range. Other research efforts acknowledge this problem and offer remedies for subsequent performance degradation resulting from violating the range i.i.d. assumption for these atypical non-linear/planar arrays [16]. Also of interest is the work presented in [42], where nonlinear array configurations are discussed in some detail with all results presented for the known covariance, range unambiguous, case.

Previous STAP work on arc arrays typically focused on the case where the array and target were within the sample plane [69, 70]. The new work presented here does not propose to take advantage of unique benefits offered by the circular array when used in this manner, e.g., the lack of mainbeam degradation due to beam steering. Rather, this work focuses on improving the well-researched detection capabilities of the conventional ULA by incorporating a planar array. Figure 4.13 illustrates the three array configurations considered for this research. Configuration

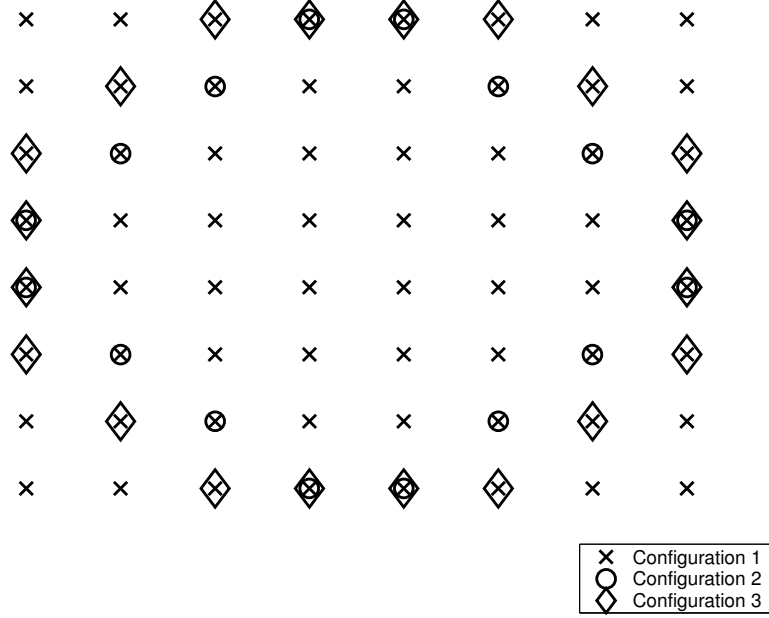


Figure 4.13: Full 8×8 rectangular array and thinned array configurations.

1 represents the baseline rectangular array and directly relates to previous work in [31, 32]. Configurations 2 and 3 correspond to two distinct “thinned” arrays with elements chosen to achieve the largest possible horizontal and vertical element displacement across the array while minimizing the total number of active elements.

4.3.1 Results. Results are presented with detection probability (P_d) curves for a fixed false alarm probability (P_{fa}) using estimated covariance and Monte Carlo analysis, necessary because a closed-form P_d expression has not been developed for the technique. The P_d metric may be considered the ultimate qualifier of radar signal processing performance, where all engineering effort is focused towards the goal of enhanced target detection. However, other factors must be taken into considera-

tion when comparing processing techniques in this manner. For example, a specific P_d curve represents target detection capability in a given direction (at a particular azimuth/elevation angle) at a particular Doppler frequency. The question then becomes, “How well can we detect targets at other locations having different Doppler frequencies?” To avoid generating countless P_d curves and spending undue time on analysis, an output SINR metric (for known covariance) is provided in an attempt to better characterize overall array and STAP performance.

Radar data was simulated using the physical environment model of Chapter III and simulation parameters consistent with the MCARM aircraft array [59] (Table 4.4). In this work, the radar parameters of Table 4.4 result in ambiguous data consisting of the unambiguous clutter response plus the clutter response from four range ambiguous regions. For each P_d curve generation, 10,000 realizations were processed. A single known covariance matrix provides clutter statistics located at a single range cell/elevation angle. For each realization, a target with a particular input SINR (per element, per pulse) was injected. The target was placed at an azimuth of 0° , elevation of 45° , and normalized Doppler of 0.25 for a Doppler of $0.25f_{PRF} = 496$ Hz.

! Although clutter Doppler varies with elevation angle, e.g., range, the realizations were formed on a block basis (using a single desired covariance matrix to color white data) rather than on a snapshot-by-snapshot basis. This approximation is valid when using small secondary data set sizes and is commonly employed in STAP analysis. A limited P_d analysis using data generated on a snapshot-by-snapshot basis verified the approximate results.

Figure 4.14 shows P_d results for each array configuration (see Fig. 4.13) and three baseline techniques, namely, the two-dimensional Adaptive Matched Filter (2D-AMF) corresponding to fully adaptive STAP, the two-dimensional FTS (2D-FTS) (traditional) method, and the 3D-FTS technique for the full array. Detection thresholds were set such that all methods exhibited a constant P_{fa} of 0.001. To avoid any effects of data dependency, each technique was evaluated using the same data.

As previously reported in [31, 32] and Sections 4.1-4.2, the 3D-FTS technique offers a significant performance improvement when operating over the full rectangular array. As Fig. 4.14 illustrates, detection performance equivalent to 2D-FTS can be obtained with approximately 55 dB less SINR (per element, per pulse). These results are somewhat misleading in that they neglect the effects of range ambiguous clutter. Figure 4.15 incorporates range ambiguous clutter effects. Substantial improvement is still demonstrated as 3D-FTS offers detection equivalence at > 30 dB less SINR. This result is expected since there is not only a significant increase in available DOF (16 versus 8), but the planar array also provides resolution capability in both elevation and azimuth, greatly increasing its ability to suppress ground clutter. Since the elevation weights ignore range ambiguities, the results in range ambiguous clutter can be further improved as previously noted.

The solid line with a circular marker in Fig. 4.14 denotes detection capability of 3D-FTS applied to a thinned array (configuration 3 of Fig. 4.13). As expected, performance decreases relative to that obtained from 3D-FTS over the full array (solid

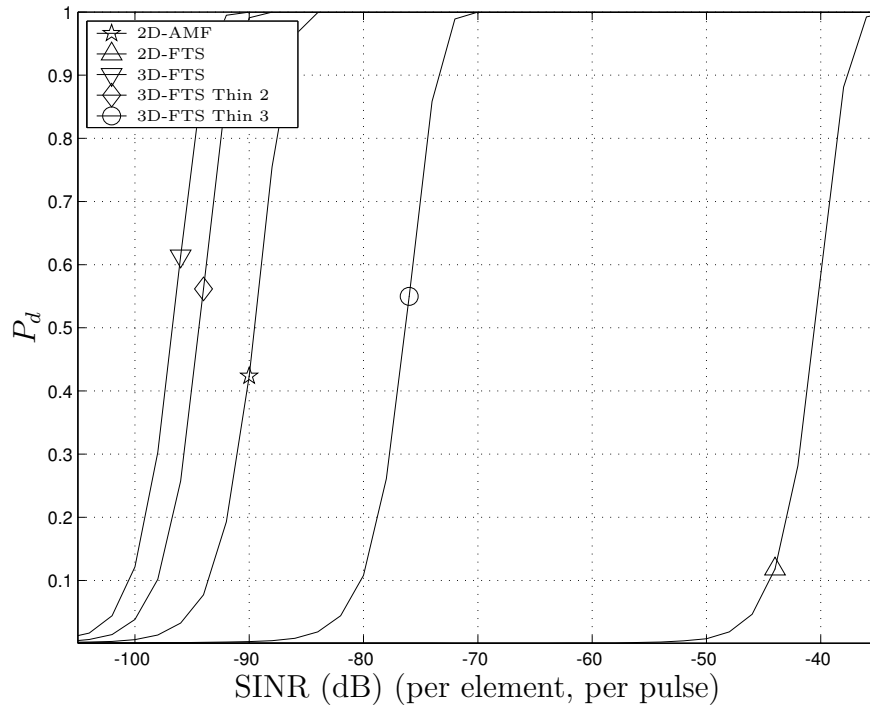


Figure 4.14: P_d curves for $P_{fa} = 0.001$ *without* range ambiguous clutter for 10,000 realizations.

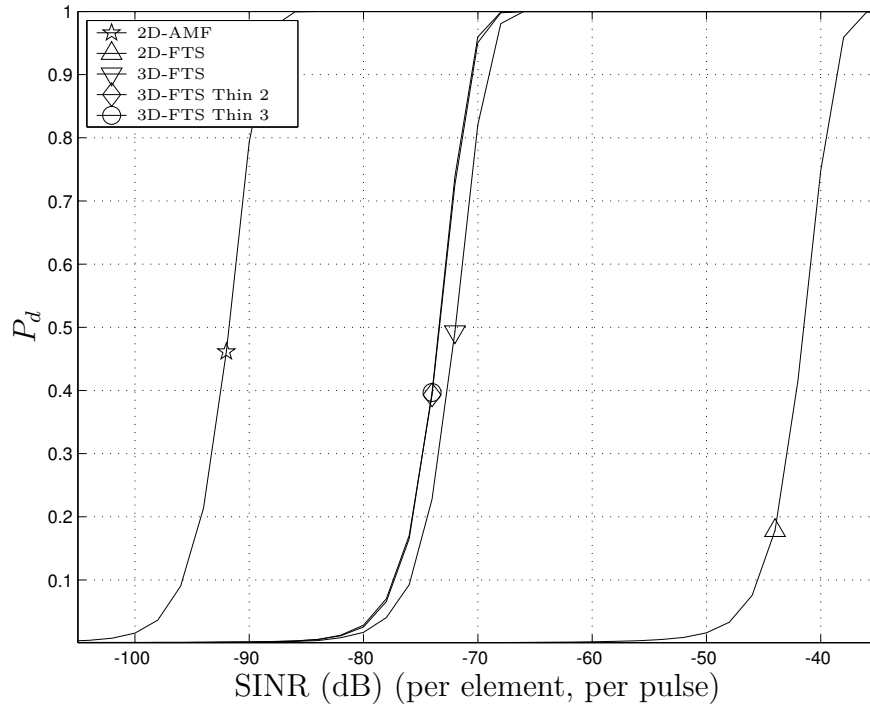


Figure 4.15: P_d curves for $P_{fa} = 0.001$ *with* range ambiguous clutter for 10,000 realizations.

line with inverted triangles). Of particular interest here, is the curve corresponding to 3D-FTS operating on thinned array configuration 2 (solid line with diamonds). In this case, detection performance is consistent with the that of full array operation. Very little penalty is incurred as a result of the missing elements. Again, this data is void of range ambiguous clutter effects.

Figure 4.15 presents range ambiguous clutter results. As expected, 3D-FTS performance over the full array degrades from the previous case. This degradation is entirely due to the 3D-FTS formulation and, as mentioned previously, could be mitigated by incorporating the suppression of range ambiguous interference rings in the 3D-FTS development.

Figures 4.16 and 4.17 present output SINR results (the P_d results are a function of *input* SINR per element, per pulse) for the two cases of neglecting and including range ambiguous clutter. The SINR curves are generated using *known* covariance, hence there is no estimation loss. As expected (due to the equivalence of output SINR maximization and detection probability maximization), these curves mirror results of the P_d analysis in terms of their locations relative to each other.

4.3.1.1 Performance Bound. Of particular interest in Figs. 4.16 and 4.17 is the introduction of an upper performance bound. The 2D Matched Filter (2D-MF) response (solid line with star), see Section 2.7, represents the bound for 2D STAP in colored noise. The case where the data is only corrupted by unit variance noise (identity covariance matrix, i.e., white noise) results in a constant bound given

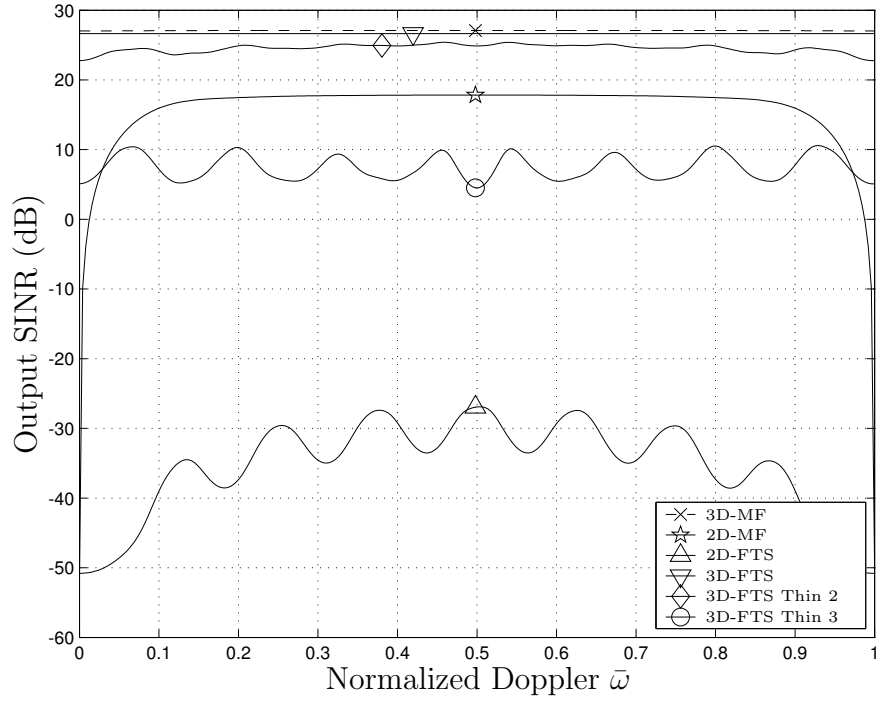


Figure 4.16: Output SINR curves using known covariance *without* range ambiguous clutter.

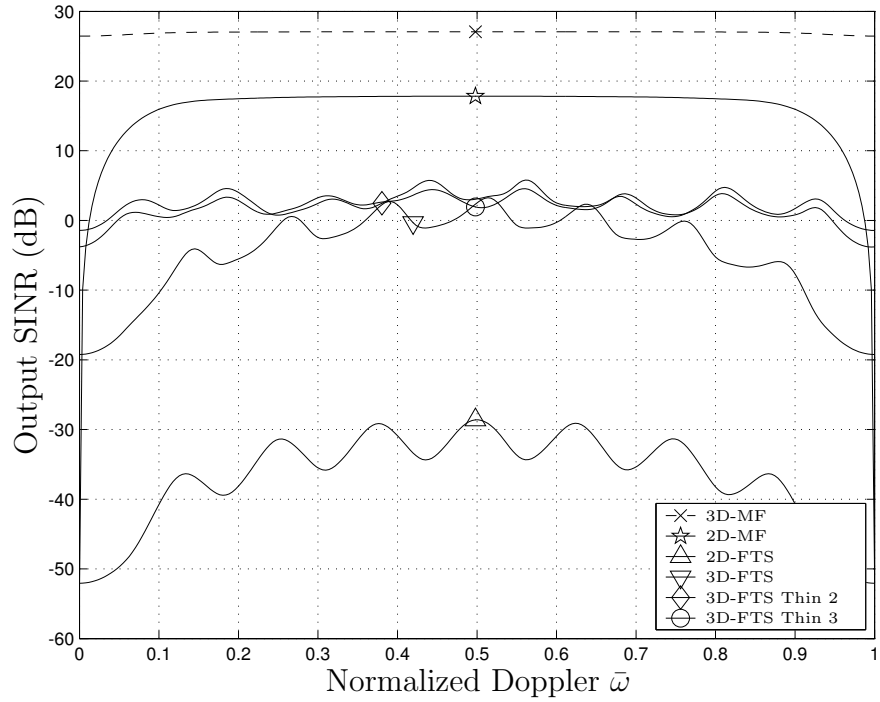


Figure 4.17: Output SINR curves using known covariance *with* range ambiguous clutter.

by

$$\text{SINR}_{\text{Max}}^{2\text{D}} = 10 \log_{10} MN. \quad (4.16)$$

The 3D Matched Filter (3D-MF) (dashed line), see Chapter V, also exists and serves as the 3D-FTS bound. This bound, for *noise only* interference, is given by

$$\text{SINR}_{\text{Max}}^{3\text{D}} = 10 \log_{10} MNP. \quad (4.17)$$

For parameters used in this work, the 3D bound is 27.09 dB. These bounds both assume a unit amplitude target. Neglecting range ambiguous clutter (Fig. 4.16), the 3D-FTS technique is within 0.44 dB of this bound. The impact of range ambiguous clutter is significant, as performance drops to a peak output SINR of approximately 3 dB in Fig. 4.17; 24 dB less than the bound. Again, the proposed method can be greatly improved by modifying the first stage of the 3D-FTS formulation. The proposed modification is reserved for Section 4.5.

Approaching the 3D-MF bound in severe interference environments requires all available DOF, e.g., the 3D-AMF, a difficult if not impossible task. The 3D-AMF requires $2MNP$ secondary data snapshots for covariance estimation, an amount almost certainly unavailable for most practical values of M , N , and P . Furthermore, the extension to a planar array implies the clutter Doppler is now a function of range, thereby violating the i.i.d. assumption required for secondary data snapshots.

! The use of constant N in Eqns. (4.16) and (4.17) corresponds to the comparison used in this work. Specifically, the comparison drawn between 2D

and 3D approaches, as presented in this document, constrains the number of azimuth channels N and the number of pulses M . This constraint puts the two methods on an equal footing in terms of azimuth and Doppler resolution. The 3D approach gains the added elevation processing advantage. Reported results give an improvement due to the extension to 3D, bounded to be no *less* than $10\log_{10} P$. Improvement is no *less* than this bound because 2D methods typically cannot approach maximum output SINR in severe interference environments. Conversely, the robust nature of 3D methods allows them to approach maximum output SINR. Hence, the difference between the two approaches is a *minimum* of $10\log_{10} P$ dB.

A portion of the improvement could be attributed to the increase in total DOF, depending on the interference scenario. In light of this argument, future work could constrain the total DOF. The new $\text{SINR}_{\text{Max}}^{2\text{D}}$ would be $10\log_{10} MN_1$ with $\text{SINR}_{\text{Max}}^{3\text{D}} = 10\log_{10} MN_2P$. The equal DOF requirement is expressed as $MN_1 = MN_2P$ and defines the relationship $N_1 = N_2P$. From these maximum output SINR expressions, a minimum improvement due to the 3D extension would be $N_2P/N_1 = 1$. Hence, there would be no improvement in the ideal white noise limited case. However, simulations with $\mathbf{R} \neq \mathbf{I}$ (as shown in this work) would indicate significant improvement.

4.4 Factored Elevation with Joint Domain Localized Processing

One of the more robust STAP techniques is the 2D Joint Domain Localized (2D-JDL) method [64], previously introduced in Section 2.7. Since adaptivity is implemented in the azimuth-Doppler domain, the method is a beamspace approach. Of particular interest is the analytical simplicity of the ideal target model when transformed to the azimuth-Doppler domain. Given ideal conditions, a target is projected into a single azimuth-Doppler bin inherently allowing adaptivity within a small localized region. Using a small localized adaptivity region offers several benefits. First, fewer DOF are needed, resulting in computational efficiency (when compared to methods such as the 2D-AMF). Second, required sample support is

drastically reduced in response to fewer DOF. This reduction in sample support makes 2D-JDL performance less susceptible to heterogeneous clutter effects. For these reasons, a three-dimensional variant of 2D-JDL appeared enticing for research and was pursued next.

As mentioned in the progressive development of 3D-FTS, any adaptive processing technique can follow the elevation beamforming in a factored approach. This section develops a second factored approach, termed Elev-JDL. Obviously, the approach remains suboptimum due to the inherent general limitations of factored approaches. Chapter V explores 3D-JDL, a technique approaching optimality.

The overall approach to Elev-JDL is factored since elevation beamforming is followed by 2D-JDL. A crucial distinction from 3D-FTS is that post beamforming processing is *joint domain*, i.e., 2D-JDL. Therefore, Elev-JDL melds both factored and joint domain approaches. Unfortunately, the technique remains suboptimal since it can place nulls at particular points within the azimuth-Doppler plane but *not* at particular points within the azimuth-Doppler-elevation hypercube.

The Elev-JDL concept is shown in Fig. 4.18. Array element data is first filtered using elevation beamforming, essentially suppressing an entire range ring (covering all azimuth extent and all Doppler shifts). The goal is clutter suppression while avoiding target nulling. This filtering is adaptive on a range cell basis with the clutter null centered at the clutter elevation angle in each (ambiguous and unambiguous)

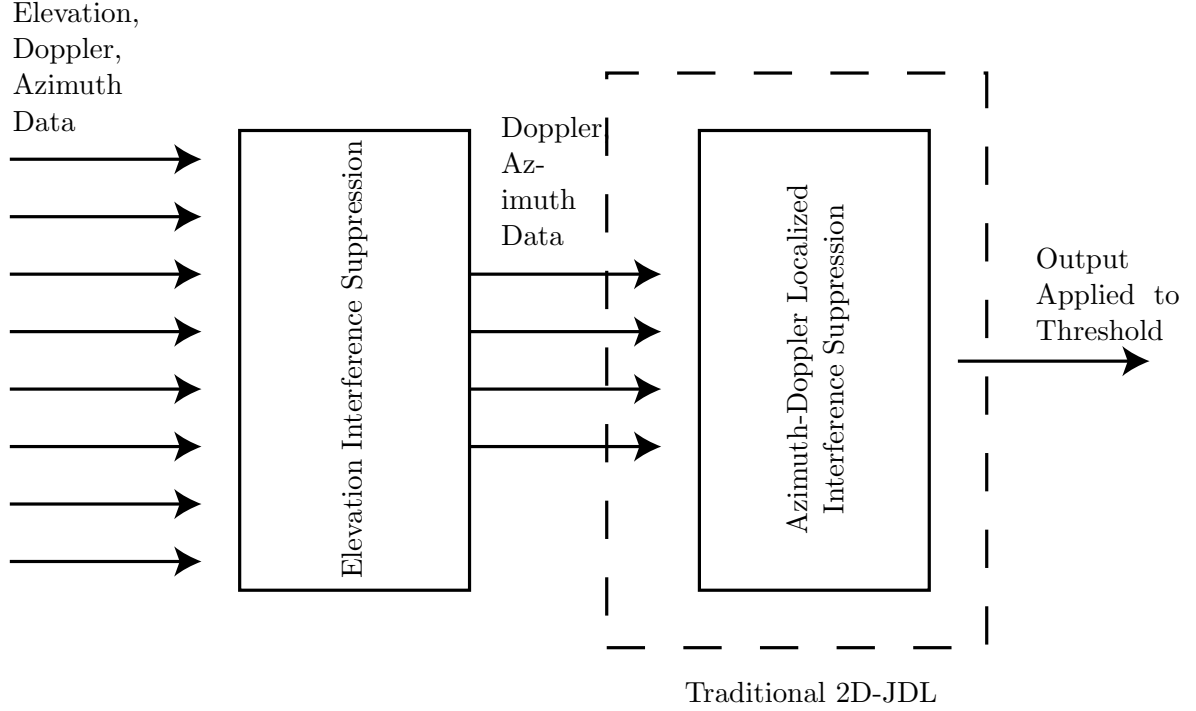


Figure 4.18: Elev-JDL block diagram.

range ring. Contrary to the original 3D-FTS approach [31,32], subsequent azimuth-Doppler interference suppression is achieved using 2D-JDL.

The proposed Elev-JDL technique is encapsulated as

$$(\mathbf{E}\mathbf{T}\mathbf{w}_{2D})^H \boldsymbol{\chi} = \mathbf{w}^H \boldsymbol{\chi}, \quad (4.18)$$

where \mathbf{T} and \mathbf{w}_{2D} are the 2D-JDL components of Eqns. (2.31) and (2.33) and \mathbf{E} is defined in Eqn. (4.21). Transformation operator \mathbf{T} represents the conversion from element-time-elevation space to azimuth-Doppler-elevation space. This operator transforms the data to a localized region within the transform domain, where “focused” adaptivity is implemented. This operator is identical to the one used in 2D-JDL, shown in Eqn. (2.31). However, the formulation here differs slightly in that

the adaptive weights contained in \mathbf{w}_{2D} are calculated for the azimuth-Doppler space region corresponding to the beamformed elevation angle from the first stage. The difference is primarily conceptual since the actual adaptive weight calculations are identical to that of the original 2D-JDL formulation described in Section 2.7.

4.4.1 3D Elev-JDL Results. The 3D Elev-JDL method is evaluated using the same interference scenario found in the 3D-FTS evaluation, including an 8×8 planar array and $M = 8$ pulses. Table 4.1 contains the radar parameters specifically chosen to match the MCARM radar. Again, the radar data was simulated using the 3D model developed in Chapter III. Range ambiguous interference effects are characterized by offering results both with and without these returns. As before, the radar parameters result in ambiguous data consisting of the unambiguous clutter response plus the clutter response from four range ambiguous regions.

Figure 4.19 shows output SINR results for each factored technique developed in this chapter. For comparison, the 2D-MF filter is offered along with the 2D counterparts for each factored method. The 2D-MF serves as the 2D performance bound for this interference scenario, i.e., specific colored noise case. Given a noise only interference scenario, the constant 2D performance bound is $10 \log_{10}(MN) = 18.06$ dB regardless of azimuth angle, elevation angle, or normalized Doppler. The impact of mainbeam location, e.g., look direction, is evident only in the colored interference case. The equivalent constant 3D performance bound, i.e., *white* noise

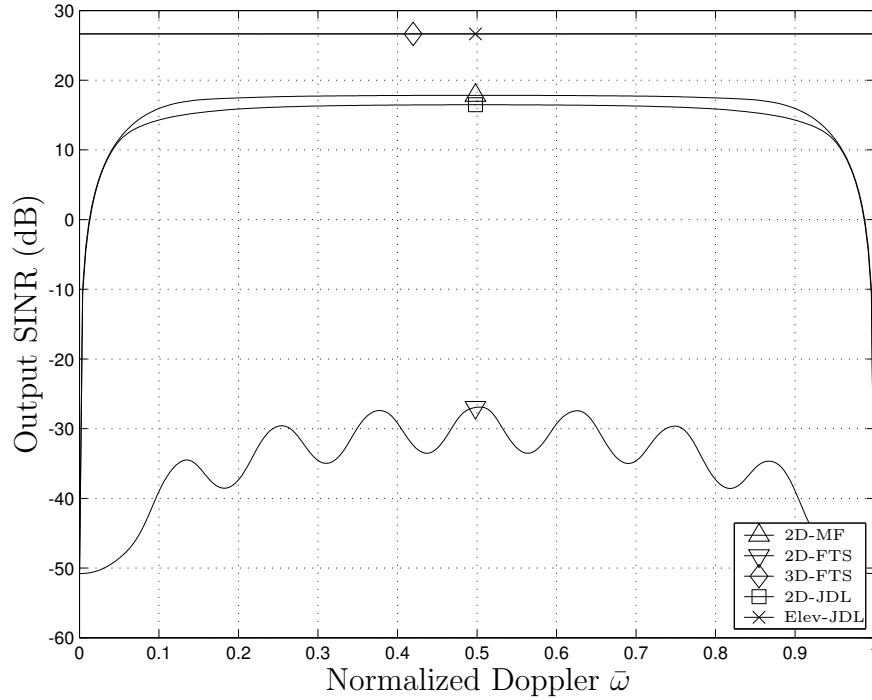


Figure 4.19: Output SINR comparison, using known covariance *without* range ambiguous clutter, for all proposed 3D factored techniques.

case, is $10 \log_{10}(MNP) = 27.09$ dB. The 3D-MF is developed in Chapter V with presentation of results reserved for that chapter.

Neglecting range ambiguous interference, the output SINR results for 3D-FTS and Elev-JDL shown in Fig. 4.19 are nearly equivalent. Both techniques outperform the 2D-MF by > 9 dB. As mentioned previously, this result does not violate a performance bound. The two proposed factored approaches are 3D and constrained the 3D performance bound. The two approaches produce 26.65 dB output SINR, or 0.44 dB below the 3D performance limit of 27.09 dB.

Figure 4.20 reports output SINR results when using range ambiguous clutter data. Clearly, the impact is significant for 3D-FTS as evidenced by the more than

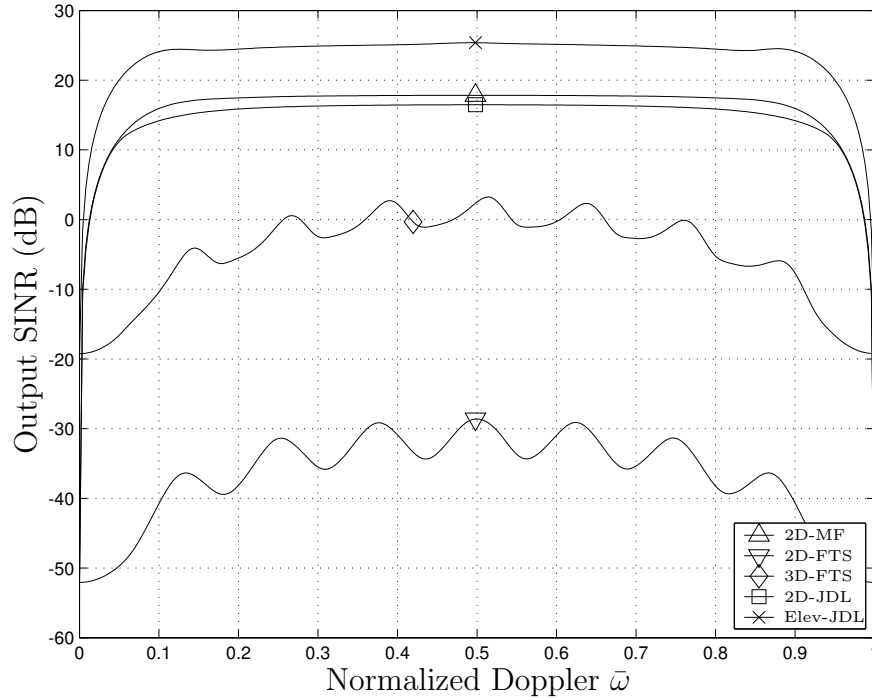


Figure 4.20: Output SINR comparison, using known covariance *with* range ambiguous clutter, for all proposed 3D factored techniques illustrates Elev-JDL offers robust performance.

20 dB of degradation in performance. However, Elev-JDL appears extremely robust and exhibits virtually no performance degradation. Since both factored approaches use an identical elevation null formation method (neglecting range ambiguous clutter suppression), the Elev-JDL robustness is clearly due entirely to the elegant 2D-JDL method. These results indicate that a true 3D-JDL method is highly desirable and such a technique would likely produce output SINR results surpassing that of Elev-JDL. Research into 3D-JDL is presented in Chapter V.

As a reminder, the results presented to this point merely characterize range ambiguous clutter impact on each technique of this chapter. The elevation beamforming

method, as developed thus far, does *not* attempt to suppress range ambiguities. The following section addresses this issue.

4.5 *Range Ambiguous Interference Suppression*

The original 3D-FTS formulations [31, 32] offer elevation adaptivity specifically designed to suppress interference *only* within the primary range ring; range ambiguous interference effects are ignored. Incorporating range ambiguous interference suppression into the original concept is relatively straightforward and required for fair comparison to the joint domain methods of Chapter V. This requirement is forced by the inherent ability of joint domain methods to suppress range ambiguous clutter in elevation.

Two approaches are presented. The first technique is based entirely on aircraft geometry relative to the spherical Earth model. Ground clutter elevation angles are calculated based on this geometry and used to form elevation nulls. The second approach is more suited for real-world application, i.e., the Earth's surface does not obey a strict spherical model. The second approach requires estimation of an elevation-only covariance matrix.

4.5.1 Geometrical Approach. Consistent with the original elevation beamforming method,

$$\mathbf{w}_e = \mathbf{C}_e^{-1} \mathbf{e}(\theta), \quad (4.19)$$

where elevation weights \mathbf{w}_e are chosen to suppress clutter in the appropriate range ring while maintaining a beam in the target direction and thereby adaptive on a range cell basis. Using an operation paralleling Wiener filter theory, \mathbf{w}_e and \mathbf{C}_e (an artificially generated interference covariance matrix designed to place null(s) at the unambiguous clutter ring) are calculated from the filter look direction angle θ and the angle to the clutter ring θ_c under consideration. This work modifies the original \mathbf{C}_e of Eqn. (4.10) to allow range ambiguous interference suppression,

$$\mathbf{C}_e = \frac{1}{J} \sum_{k=1}^{\eta_r} \sum_{i=1}^J \frac{1}{k} \mathbf{e}(\theta_{ik}) \mathbf{e}(\theta_{ik})^H + \sigma^2 \mathbf{I}_P, \quad (4.20)$$

where η_r represents the total number of range rings; five for the parameters of Tables 4.4 and 4.1. This formulation collapses to the original approach if $\eta_r = 1$. The k^{-1} attenuation factor serves to embed a natural emphasis on the unambiguous range ring, the largest interference source when considering range attenuation. Elevation angles θ_{ik} are defined as $\alpha_i (\theta_c)_k$, where $(\theta_c)_k$ represents the angle to the k^{th} clutter ring and $\alpha_i \in \Re$. For this work $i = 3$ and $\alpha = \{0.95 \ 1.00 \ 1.05\}$, forcing the elevation null width to correspond to the range ring angular extent.

Elevation adaptivity is the achieved through

$$\mathbf{E} = \mathbf{w}_e \otimes \mathbf{I}_{MN}, \quad (4.21)$$

a $PMN \times MN$ matrix with \mathbf{I}_{MN} an $MN \times MN$ identity matrix and \mathbf{w}_e the $P \times 1$ elevation weight vector. As before, the Kronecker product with the identity matrix is required for consistency with the incoming data format.

A geometrical approach may experience degradation when operating in real-world scenarios. This degradation occurs as the environment deviates from the spherical Earth model used to formulate elevation null locations. Furthermore, aircraft orientation must be incorporated into the $(\theta_c)_k$ calculations.

4.5.2 Beamformed Statistical Approach. A more robust approach involves estimating an elevation covariance matrix. This technique completely removes any dependence on the spherical Earth model since it adapts to the current data set.

The elevation covariance matrix, replacing the artificial covariance matrix \mathbf{C}_e , first requires beamforming the data in azimuth and Doppler. These two beamforming operations are performed separately, i.e., in a factored manner. The approach taken here first constructs a $NMP \times MP$ azimuth beamforming matrix \mathcal{A} using the non-adaptive azimuth steering vector,

$$\mathcal{A} = \mathbf{I}_{MP} \otimes \mathbf{a}, \quad (4.22)$$

where \mathbf{I}_{MP} is an $MP \times MP$ identity matrix. The identity matrix ensures the non-adaptive beamforming vector \mathbf{a} is applied to the appropriate space-time snapshot χ elements. The structure of χ motivates the operation's form. The output of

the operation, $\mathcal{A}^H \chi$, is a $MP \times 1$ vector representing the M pulse returns and P elevation element returns at the azimuth angle ϕ contained in \mathbf{a} .

The non-adaptive Doppler beamforming concept is identical, with the necessary modifications for application to the azimuth beamformed space-time snapshot. Construct the $MP \times P$ matrix

$$\mathcal{B} = \mathbf{I}_P \otimes \mathbf{b}, \quad (4.23)$$

where \mathbf{I}_P is a $P \times P$ identity matrix and \mathbf{b} is the non-adaptive temporal steering vector. The symbol \mathcal{B} is used to distinguish this matrix from \mathbf{B} , used previously for an identical operation in concept, e.g., Doppler beamforming, but very different in structure. The output of this beamforming operation, $\mathcal{B}^H \mathcal{A}^H \chi$, is a $P \times 1$ vector representing the P elevation element returns at the azimuth angle ϕ contained in \mathbf{a} and the normalized Doppler frequency $\bar{\omega}$ contained in \mathbf{b} . Notice the matrix product $\mathcal{A}\mathcal{B}$ is equivalent to

$$\mathcal{A}\mathcal{B} = \mathbf{I}_P \otimes (\mathbf{b} \otimes \mathbf{a}). \quad (4.24)$$

The covariance matrix is found in the usual manner by examining the outer product expected value,

$$\mathbf{R}_P = \mathcal{E} \{ \mathcal{B}^H \mathcal{A}^H \chi \chi^H \mathcal{A} \mathcal{B} \}. \quad (4.25)$$

Obviously, for the case of known covariance this simplifies to

$$\mathbf{R}_P = \mathcal{B}^H \mathcal{A}^H \mathbf{R} \mathcal{A} \mathcal{B}. \quad (4.26)$$

The elevation weight vector is then calculated using the same method as before,

$$\mathbf{w}_e = \mathbf{R}_P^{-1} \mathbf{e}. \quad (4.27)$$

This weight vector is then cast into the matrix form \mathbf{E} shown in Eqn. (4.21).

Several variants of this approach are possible. The non-adaptive beamforming could be replaced with some adaptive approach, although the utility of such a modification is limited. The reason is buried amid the actual purpose of the beamforming operations in the technique. One must remember that the ultimate goal is an elevation interference covariance matrix reflecting *only* the sources negatively impacting output SINR, and, ultimately, detection probability. In other words, some interference sources will be suppressed in the subsequent azimuth and Doppler processing. Hence, valuable elevation DOF should not be applied to those sources. Unfortunately, elevation nulling is the first step in the factored approach and there is no mechanism available to gather this information. The choice of elevation weights directly impacts the following azimuth and Doppler adaptive weight calculations. In terms of factored methods, the only compromise might be an iterative method

driving towards some optimum solution. However, joint domain methods alleviate this limitation entirely, effectively negating any real need for research in this area.

4.5.3 Range Ambiguous Interference Suppression Results. The improvement due to range ambiguous interference suppression is clearly seen through output SINR analysis. Reported results correspond to known covariance, incorporating range ambiguous returns, using the standard array configuration of this work. In particular, this configuration corresponds to an 8×8 planar array with $M = 8$ pulses. Table 4.1 contains specific radar parameters such as pulse width, PRI, transmit frequency, etc. Figures 4.21 and 4.22 offer output SINR results for each range ambiguous suppression method developed in this chapter: no suppression, geometric approach, and beamformed statistical approach. The first figure provides comparison data for all three methods. However, the scale required to show output SINR for all three methods hides some important details. Fig. 4.22 compares only the geometric and beamformed statistical techniques, allowing more appropriate scaling and a discussion of these finer details.

Obviously, suppressing range ambiguous interference using either approach offers significant performance gains. For example, Fig. 4.21 illustrates a ≈ 22 dB output SINR improvement for 3D-FTS when using the geometric approach. Once again, Elev-JDL robustness is apparent by its high output SINR when using *no* range ambiguous interference suppression. However, even this technique experiences some degradation as the look direction approaches mainbeam clutter, i.e., zero normal-

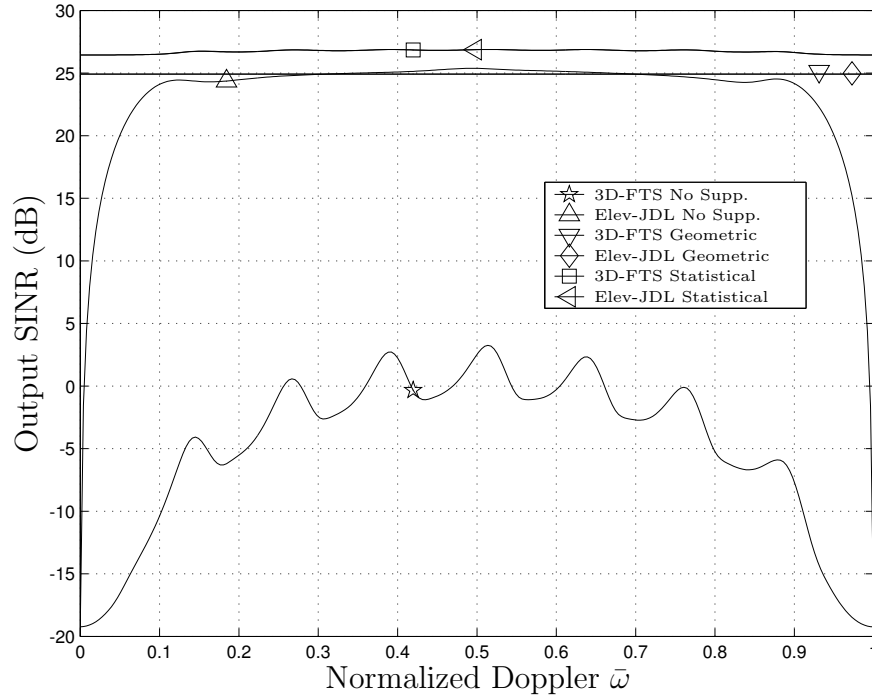


Figure 4.21: Range ambiguous interference suppression, measured by output SINR, comparing all three approaches: no range ambiguity suppression, geometric method, and beamformed statistical method.

ized Doppler (aliases to one). Introduction of the geometric suppression approach removes this degradation.

Improvement gained by using the beamformed statistical approach, as compared to the geometric method, is relatively small. Figure 4.22 is a plot of these two techniques using an expanded y -axis scale. At peak output SINR, ≈ 2 dB improvement is evident. Hence, the beamformed statistical method results in ≈ 24 dB output SINR improvement when compared to no range ambiguous interference suppression.

The flat line apparent in the two geometric applications, 3D-FTS and Elev-JDL, indicates that practically all the interference is suppressed by the elevation

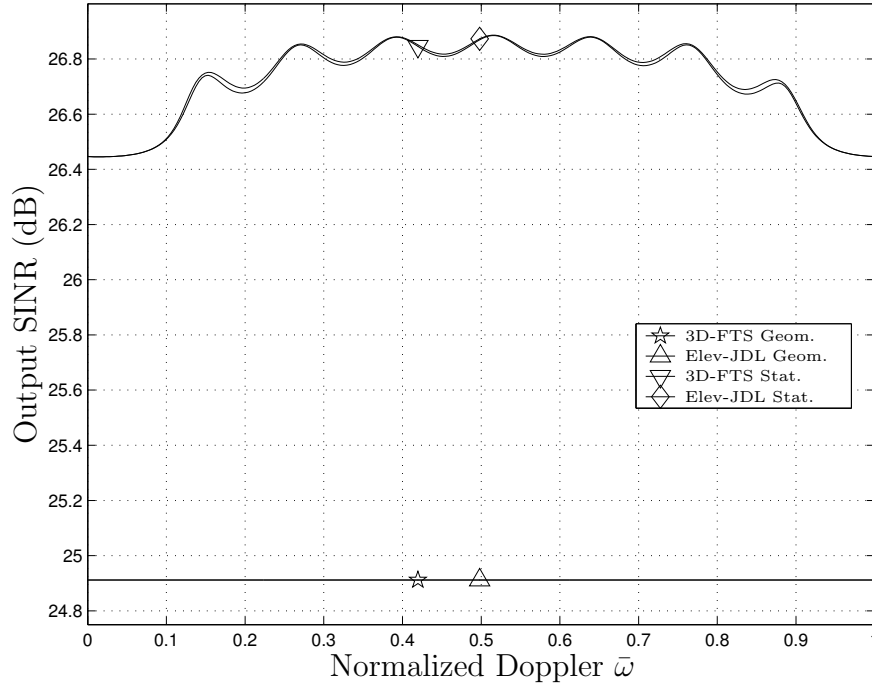


Figure 4.22: Range ambiguous interference suppression, measured by output SINR, comparing two approaches: geometric method and beamformed statistical method.

nulls. In the geometric method, elevation weights do not change as the look direction scans across normalized Doppler when generating output SINR curves. On the contrary, the beamformed statistical approach results in a new adaptive elevation weight set each time mainbeam changes, whether the look direction changes in azimuth, elevation, and/or normalized Doppler. Hence, the statistical technique offers improved elevation null location and corresponding output SINR improvement.

The results presented here use simulated covariance matrices. The data model of Chapter III uses the spherical Earth model that also serves as the geometrical approach foundation. Hence, the beamformed statistical approach matches this data and produces results with relatively small improvement over the geometrical ap-

proach. If real-world data utilizing more than two vertical channels were available, a comparative analysis of the two approaches would show the beamformed statistical method is more robust and the geometric approach would degrade.

4.6 Summary

Classic 2D STAP technique limitations include large computational load and large secondary data sets. Community response has focused on developing computationally efficient reduced dimension algorithms, from which 2D-FTS evolved. Although 2D-FTS provides the desired reduction in DOF, a performance penalty is incurred.

The work presented in this chapter develops and characterizes a new class of factored 3D adaptive processing algorithms. In general, these techniques offer distinct advantages over 2D methods through elevation based clutter suppression.

For a 3D proof-of-concept, elevation interferometry was fused with 2D-FTS to provide clutter suppression. Results based on actual airborne radar data indicate the proposed technique is very effective while providing little increase in computational intensity. The initial 3D proof-of-concept was limited to two elevation channels for comparison and validation with available measured data.

The full 3D-FTS method has no such limitations on the number of elevation channels. Through standard beamforming techniques, an elevation null was formed in the direction of ground clutter based on radar platform geometry and a spherical

Earth model. For the 8×8 rectangular array considered, 3D-FTS demonstrated significant performance improvements over 2D-FTS using the ULA (single row of the rectangular array). Further enhancement was possible through range ambiguous clutter suppression, given the framework presented in the first iteration ignored range ambiguous clutter. An elevation null was formed *only* for the single unambiguous clutter elevation angle. The modification is straightforward with two different approaches presented in Section 4.5.

The 3D-FTS method [31, 32, 34], operating within the azimuth-Doppler-elevation hypercube, effectively mitigates the performance penalty associated with reduced dimensionality by adding elevation processing without increasing secondary data support. Improved performance over a two-dimensional *fully* adaptive algorithm operating within the azimuth-Doppler plane was demonstrated for the range unambiguous clutter case; secondary data support *remains the same as 2D-FTS*. Furthermore, target height discrimination is inherently provided through elevation beamforming. However, extension into the elevation domain dictates the establishment of a new upper performance bound, i.e., the performance provided by a three-dimensional fully adaptive processor. This new performance bound is fully addressed in Chapter V.

The results presented approach fully adaptive 2D STAP performance (operating on a ULA) using a much smaller training interval. In fact, the training interval is reduced by a factor of M . Fully adaptive STAP could be directly applied to the

8×8 rectangular array considered. However, even if results could be obtained, they would likely be inferior to the 3D-FTS results presented here for one primary reason: extending STAP into the azimuth-Doppler-elevation hypercube provides the ability to resolve responses in both elevation and azimuth. As discussed in [16, 69, 70], this two-dimensional angle resolution capability “greatly complicates” the clutter Doppler situation since clutter Doppler is now range (elevation angle) dependent and the fundamental i.i.d. assumption is violated. Therefore, estimating interference statistics in range requires smaller training intervals where the clutter essentially satisfies the i.i.d. requirement in an approximate sense. However, extension to fully adaptive 3D-STAP results in a corresponding DOF increase and training interval size (dictated by the sample support requirement). Therefore, satisfying both is impossible and no realistic compromise exists. The development of the 3D-MF, and consequently the 3D-AMF, is addressed in Chapter V.

The factored 3D-FTS approach not only offers easy application of STAP processing to a rectangular array, but also operates effectively on a thinned array of quasi-circular elements. As included in the proposed method, elevation adaptivity fosters other concepts for providing potentially significant performance improvements. Heterogeneous clutter has long been the nemesis of many STAP techniques, given the inherent inability to obtain accurate interference estimates. Heterogeneous clutter effects can perhaps be diminished through elevation processing since interference over an entire range ring can be reduced. There is also potential for im-

proved jammer suppression and enhanced performance in environments containing hot clutter regions, given the localized (angular) nature of such interference and the ability to form elevation nulls. This leads directly to the hybrid concepts proposed in Chapter VI.

The final factored method developed in this chapter was Elev-JDL. Even without range ambiguous interference suppression, the technique offered excellent performance on data containing range ambiguous clutter. The robustness of the joint domain 2D-JDL method was evident in the results. These results indicate a true 3D joint JDL method, 3D-JDL, is highly desirable and would likely produce output SINR surpassing that of Elev-JDL. Research in the 3D-JDL area is presented in Chapter V.

To conclude the factored 3D development, and allow fair comparison to the 3D joint domain methods of Chapter V, two range ambiguous interference suppression techniques were considered. The first technique is based entirely on the physical geometry of the radar platform and the spherical Earth model. The second technique implements a statistical method for elevation null placement. Due to the unavailability of measured data for more than two vertical channels, performance was evaluated using the simulated data based on the 3D model of Chapter III. Although the model compares *very* well to actual measured airborne radar data, it *is* based upon a spherical Earth model. Hence, the results of both elevation null placement techniques were nearly identical (within 2 dB). In actual airborne radars, the Earth does not strictly

follow a spherical model and the geometric approach will likely suffer performance degradation while the statistical approach remains relatively robust.

V. Three-Dimensional Joint Domain Methods

Radar Space-Time Adaptive Processing (STAP) techniques have classically focused on azimuth-Doppler adaptivity while placing minimal emphasis on elevation. Elevation adaptivity offers significant clutter suppression improvement, allowing further suppression of interference sources having identical Doppler and azimuth as the expected target.

The previous chapter incorporated elevation adaptivity using factored approaches, greatly improving clutter suppression performance. Conversely, this chapter focuses on joint domain techniques. First, the three dimensional matched filter is derived using three different approaches. As in the 2D case, the three approaches generate identical filters (within a scale factor), showing equivalence.

Unfortunately, the interference encountered in actual airborne radar scenarios is not known *a priori*. This fact forces construction of adaptive methods for estimated covariance. The most obvious approach is the Adaptive Matched Filter (AMF), where the estimated covariance matrix is substituted into the matched filter. This approach generates well known practical limitations even in the 2D case. As expected, the extension to 3D further compounds these limitations.

The desire to generate a practical 3D adaptive interference suppression method motivates this research. The subject of this research, and subsequently the main goal of this chapter, involves one of the more robust 2D STAP techniques: the 2D Joint Domain Localized (2D-JDL) method [64]. This method is a beamspace approach with adaptivity implemented in the azimuth-Doppler domain. Of particular interest is the analytical simplicity of the ideal target model when transformed to the azimuth-Doppler domain. Given ideal conditions, a target is projected into a single azimuth-Doppler bin, inherently allowing adaptivity within a small localized region. Using a small localized adaptivity region offers several benefits. First, fewer Degrees Of Freedom (DOF) are needed, directly resulting in tremendous computational ef-

iciency (when compared to methods such as the AMF). Second, required sample support can be drastically reduced in response to fewer DOF. This reduction in sample support makes 2D-JDL performance less susceptible to heterogeneous data effects. For these reasons, a three-dimensional variant of 2D-JDL is an enticing subject for research.

This chapter implements a true 3D Joint Domain Localized (3D-JDL) adaptive processor within the azimuth-Doppler-elevation space [35]. The proposed concepts are validated using results based on simulated range ambiguous airborne radar data. Target detection improvement on the order of 10 dB (as compared to standard 2D-JDL processing) is demonstrated for the 3D-JDL approach using an 8×8 non-uniform rectangular array.

This research extends previous work of Chapter IV and [31,32] by removing the inherent limitations of a factored approach; interference suppression using a factored approach is suboptimal at best. By design, the factored method suppresses an entire range ring in elevation and lacks the ability to place null(s) at specific locations in azimuth, Doppler, *and* elevation. Although a 3D-AMF is capable of achieving near optimal performance, it is impractical for several reasons. Hence, a 3D-JDL development is offered and shown capable of placing nulls at distinct locations in the azimuth-Doppler-elevation space.

5.1 *Matched Filter*

A discussion of 3D joint domain methods necessarily begins with the optimum filter. As mentioned in Chapter II, the optimum 2D filter can be found using three different methods. Equivalence of the likelihood ratio processor, maximum SNR filter, and Wiener filter for the 2D case is well established [18]. Development of three optimum filters for the 3D case is presented in the following subsections. As in the original 2D development, equivalence of each approach is shown.

! Each of the 3D approaches result in a filter for *known* mean and covariance. In general, this condition is not the case. However, the resultant filter performance serves as a bound for comparing partially adaptive techniques with known interference statistics.

5.1.1 Likelihood Ratio Processor. Detecting a signal embedded in interference can be accomplished using hypothesis testing. As discussed in [37], two criteria are of interest for hypothesis testing: the Neyman-Pearson and Baye's criteria. The Neyman-Pearson test is particularly interesting for the radar problem because it involves maximizing detection probability subject to a false alarm probability constraint. Regardless, both tests are based on generating a test statistic, called the likelihood ratio, which is subsequently compared to a threshold. As further noted [37], simple binary hypothesis testing (target present or no target present) results in two cases. The first case occurs when the interference (noise) is both white and Gaussian; the likelihood ratio test yields a matched filter. Conversely, colored Gaussian interference, with known mean and correlation matrix, yields a whitening filter followed by a matched filter.

The likelihood ratio is formed from the hypothesis test. Consider the two hypotheses,

$$H_0 : \boldsymbol{\chi} = \boldsymbol{\chi}_n + \boldsymbol{\chi}_c + \boldsymbol{\chi}_j \quad (5.1)$$

$$H_1 : \boldsymbol{\chi} = \mathbf{v} + \boldsymbol{\chi}_n + \boldsymbol{\chi}_c + \boldsymbol{\chi}_j, \quad (5.2)$$

where the null hypothesis H_0 corresponds to interference only (noise, clutter, jammer) while the hypothesis H_1 includes the target return (\mathbf{v}) plus interference. Under the model of Chapter III, the interference is assumed Gaussian with zero mean and covariance matrix \mathbf{R} . Therefore, the joint probability density functions for the two

hypotheses are (complex valued $\boldsymbol{\chi}$) [40]

$$p_{H_0}(\boldsymbol{\chi}) = \frac{1}{\pi^{NMP} \det(\mathbf{R})} \exp(-\boldsymbol{\chi}^H \mathbf{R}^{-1} \boldsymbol{\chi}) \quad (5.3)$$

$$p_{H_1}(\boldsymbol{\chi}) = \frac{1}{\pi^{NMP} \det(\mathbf{R})} \exp\left[-(\boldsymbol{\chi} - \mathbf{v})^H \mathbf{R}^{-1} (\boldsymbol{\chi} - \mathbf{v})\right], \quad (5.4)$$

where NMP represent the length of the space-time snapshot $\boldsymbol{\chi}$ and target space-time steering vector \mathbf{v} , and is also the dimension of the $NMP \times NMP$ covariance matrix \mathbf{R} .

The *likelihood ratio* is defined as the ratio of the two probability density functions,

$$l(\boldsymbol{\chi}) = \frac{p_{H_1}}{p_{H_0}}. \quad (5.5)$$

Substituting in Eqns. (5.3) and (5.4) and taking the natural log produces the *log likelihood ratio*

$$L(\boldsymbol{\chi}) = \ln[l(\boldsymbol{\chi})] = \mathbf{v}^H \mathbf{R}^{-1} \mathbf{v} - |\mathbf{v}^H \mathbf{R}^{-1} \boldsymbol{\chi}|^2. \quad (5.6)$$

Since l is compared to some threshold α ,

$$l(\boldsymbol{\chi}) \underset{H_0}{\overset{H_1}{\gtrless}} \alpha, \quad (5.7)$$

then the natural log of l is an equivalent operation and L can be also compared to the threshold,

$$L(\boldsymbol{\chi}) \underset{H_0}{\overset{H_1}{\gtrless}} \ln \alpha. \quad (5.8)$$

In a similar fashion, the scalar terms can also be folded into the threshold

$$\mathbf{v}^H \mathbf{R}^{-1} \mathbf{v} - |\mathbf{v}^H \mathbf{R}^{-1} \boldsymbol{\chi}|^2 \underset{H_0}{\overset{H_1}{\gtrless}} \ln \alpha \quad (5.9)$$

$$|\mathbf{v}^H \mathbf{R}^{-1} \boldsymbol{\chi}|^2 \underset{H_0}{\overset{H_1}{\gtrless}} \mathbf{v}^H \mathbf{R}^{-1} \mathbf{v} - \ln \alpha. \quad (5.10)$$

Defining a new threshold β yields

$$|\mathbf{v}^H \mathbf{R}^{-1} \boldsymbol{\chi}|^2 \underset{H_0}{\overset{H_1}{\geq}} \beta, \quad (5.11)$$

where the weight vector is clearly evident from the expected form $\mathbf{w}^H \boldsymbol{\chi}$, i.e.,

$$|\mathbf{w}^H \boldsymbol{\chi}|^2 = |\mathbf{v}^H \mathbf{R}^{-1} \boldsymbol{\chi}|^2 \quad (5.12)$$

or, more explicitly, the “infamous”

$$\boxed{\mathbf{w} = \mathbf{R}^{-1} \mathbf{v}.} \quad (5.13)$$

As predicted by [37], the likelihood ratio test results in a filter \mathbf{w} consisting of two components: a whitening filter represented by \mathbf{R}^{-1} and a matched filter \mathbf{v} . The matched filter is “matched in the sense that its impulse response equals the time-reversed version of the known signal” [37]. To conform with common literature, the *entire* filter \mathbf{w} of Eqn. (5.13) is referred to as the matched filter in this work.

Clearly, the 3D version of the matched filter is identical to its 2D counterpart shown in Eqn. (2.27). This result is expected since the 3D data model does nothing to change the data distribution. The radar returns are still modeled as Gaussian distributed with a covariance matrix \mathbf{R} . The 3D extension to incorporate elevation merely changes the form of \mathbf{R} .

5.1.2 Maximum Signal-to-Interference Plus Noise Ratio Filter. Mirroring the original 2D equivalence proof in [18], the next approach is to solve for the optimum filter by maximizing SINR. The 3D proof is relatively straightforward. First, assume an optimum weight vector \mathbf{w}_o exists and evaluate the SINR

$$\text{SINR} = \frac{\mathcal{E} \left\{ |\mathbf{w}_o^H \mathbf{v}|^2 \right\}}{\mathcal{E} \left\{ |\mathbf{w}_o^H (\boldsymbol{\chi}_n + \boldsymbol{\chi}_c + \boldsymbol{\chi}_j)|^2 \right\}}. \quad (5.14)$$

The numerator represents the output power resulting from the optimum weight vector operating on the target return. The denominator represents the output power resulting from the optimum weight vector operating on the interference sources. The target model in this work is not random, hence the expected value operator in the numerator has no effect. Using this fact and simplifying the denominator term results in

$$\text{SINR} = \frac{|\mathbf{w}_o^H \mathbf{v}|^2}{\mathbf{w}_o^H \mathbf{R} \mathbf{w}_o}. \quad (5.15)$$

Determining the appropriate contents of \mathbf{w}_o is somewhat challenging, although no more so than the likelihood ratio processor. This approach used is identical to the 2D variant of [18]. First, expand the terms into

$$\text{SINR} = \frac{\mathbf{w}_o^H \mathbf{R}^{\frac{1}{2}} \mathbf{R}^{-\frac{1}{2}} \mathbf{v} \mathbf{v}^H \mathbf{R}^{-\frac{1}{2}} \mathbf{R}^{\frac{1}{2}} \mathbf{w}_o}{\mathbf{w}_o^H \mathbf{R}^{\frac{1}{2}} \mathbf{R}^{\frac{1}{2}} \mathbf{w}_o}. \quad (5.16)$$

Now define the unit vector,

$$\mathbf{u} = \frac{\mathbf{R}^{\frac{1}{2}} \mathbf{w}_o}{\left\| \mathbf{R}^{\frac{1}{2}} \mathbf{w}_o \right\|}, \quad (5.17)$$

where $\| \cdot \|$ represents the Euclidean norm, e.g., Frobenius norm [27]. Substituting back into the SINR expression results in

$$\text{SINR} = \left| \mathbf{u}^H \mathbf{R}^{-\frac{1}{2}} \mathbf{v} \right|^2. \quad (5.18)$$

Since \mathbf{u} is a unit vector, this expression is maximized by choosing \mathbf{u} such that it lies directly on the whitened target signal return, or

$$\mathbf{u} \propto \mathbf{R}^{-\frac{1}{2}} \mathbf{v}. \quad (5.19)$$

Using this result in Eqn. (5.17) allows a solution for the weight vector producing the maximum SINR,

$$\mathbf{w}_o \propto \mathbf{R}^{-1} \mathbf{v} \left(\mathbf{w}_o^H \mathbf{R} \mathbf{w}_o \right)^{\frac{1}{2}}. \quad (5.20)$$

The last term in this equation is merely a scalar. Therefore, the resultant optimum weight vector \mathbf{w}_o is equivalent to the likelihood ratio processor of Eqn. (5.13),

$$\boxed{\mathbf{w} \propto \mathbf{R}^{-1} \mathbf{v}.} \quad (5.21)$$

5.1.3 Wiener Filter. Since the class of linear optimum discrete-time filters all reduce to the Wiener-Hopf equations, they are collectively known as Wiener Filters [37]. This section derives the Linearly Constrained Minimum Variance (LSMV) beamformer and shows equivalence to the maximum SINR filter and likelihood ratio processor.

The LSMV beamformer derivation is academic. The filter output power given a weight vector \mathbf{w}_o is

$$\mathcal{E} \left\{ |\mathbf{w}_o^H \boldsymbol{\chi}|^2 \right\} = \mathbf{w}_o^H \mathbf{R} \mathbf{w}_o. \quad (5.22)$$

The object is to minimize this output variance subject to a linear constraint. For the radar problem, a realistic constraint is mainbeam power in the target direction,

$$\mathbf{w}_o^H \mathbf{v} = g, \quad (5.23)$$

where g is a complex parameter typically set to unity. Using the method of Lagrange Multipliers [63, page 693], the Lagrangian cost function to be minimized is

$$Q = \mathbf{w}_o^H \mathbf{R} \mathbf{w}_o + \lambda (g - \mathbf{w}_o^H \mathbf{v}) + \lambda^* (g^* - \mathbf{v}^H \mathbf{w}_o), \quad (5.24)$$

where λ is the complex Lagrange multiplier. Continuing with the constrained optimization method, the optimum weight vector \mathbf{w}_o minimizing Q is derived as follows,

$$\nabla_{\mathbf{w}_o^*} Q = \mathbf{R} \mathbf{w}_o - \lambda \mathbf{v} = \mathbf{0} \quad (5.25)$$

$$\mathbf{w}_o = \lambda \mathbf{R}^{-1} \mathbf{v}, \quad (5.26)$$

where $\mathbf{0}$ is the zero vector and $\nabla_{\mathbf{w}_o^*}$ is the gradient with respect to \mathbf{w}_o^* . Although not important to the derivation here, the scalar λ is found by using the constraint and substituting back into the optimum weight vector expression of Eqn. (5.26) to get

$$\lambda = \frac{g}{\mathbf{v}^H \mathbf{R}^{-1} \mathbf{v}} \quad (5.27)$$

$$\mathbf{w}_o = \frac{g \mathbf{R}^{-1} \mathbf{v}}{\mathbf{v}^H \mathbf{R}^{-1} \mathbf{v}}. \quad (5.28)$$

As expected, the LSMV filter is equivalent to those found for minimum SINR and maximum likelihood, or

$$\boxed{\mathbf{w}_o \propto \mathbf{R}^{-1} \mathbf{v}.} \quad (5.29)$$

The normalization factor (denominator) in Eqn. (5.28) results in a form very similar to the CFAR test statistic of [21,51]. Substituting the optimum weight vector into the output power expression results in

$$\mathcal{E} \left\{ |\mathbf{w}_o^H \boldsymbol{\chi}|^2 \right\} = \frac{|g|^2}{\mathbf{v}^H \mathbf{R}^{-1} \mathbf{v}}. \quad (5.30)$$

Clearly, the filter output power, if used as a test statistic, is dependent on the actual noise power present and the test is *not* CFAR. However, this dependence is easily removed by redefining the weight vector as

$$\mathbf{w} = \frac{g \mathbf{R}^{-1} \mathbf{v}}{\sqrt{\mathbf{v}^H \mathbf{R}^{-1} \mathbf{v}}}. \quad (5.31)$$

Using this weight vector, the output power becomes independent of the interference and the test statistic is CFAR [21,51].

5.2 Adaptive Matched Filter

The 3D Adaptive Matched Filter (3D-AMF) is introduced here for comparison to 2D. As shown, the filter is impractical for actual implementation for a variety of reasons.

The 3D-AMF essentially results in replacing the known covariance \mathbf{R} in the 3D-MF with its maximum likelihood estimate $\hat{\mathbf{R}}$. The utility of this adaptive filter is limited for practical reasons. First, consider the dimensionality of \mathbf{R} in the case of 3D data. Since \mathbf{R} is of dimension $NMP \times NMP$, $2MNP$ secondary data samples are required to achieve output results within 3 dB of the 3D-MF, analogous to Reed's Rule for the 2D-AMF [49]. In practical airborne radar systems, there simply is not enough secondary data to meet this requirement; the 2D-AMF has been all but discarded for this very reason. Furthermore, computational considerations when inverting a matrix of this size can become prohibitive for real-time operation.

Even if the large number of secondary data was available, the i.i.d. requirement is almost certainly violated. Since secondary data is obtained from the range dimension, the terrain characteristics spanning $2NMP$ range cells would vary widely except in unusual circumstances.

Given the variety of practical limitations, the 3D-AMF technique is largely ignored for this work. Alternatively, focus is placed on more practical methods.

5.3 Joint Domain Localized

The 3D-JDL adaptive processing approach mirrors that of the original 2D-JDL formulation [64] but includes the required elevation extension. The proposed adaptive processing technique, termed 3D-JDL, is encapsulated as

$$\mathbf{v}^H \mathbf{T} (\mathbf{T}^H \mathbf{R} \mathbf{T})^{-1} \mathbf{T}^H \boldsymbol{\chi} = \mathbf{w}_{3D}^H \mathbf{T}^H \boldsymbol{\chi}, \quad (5.32)$$

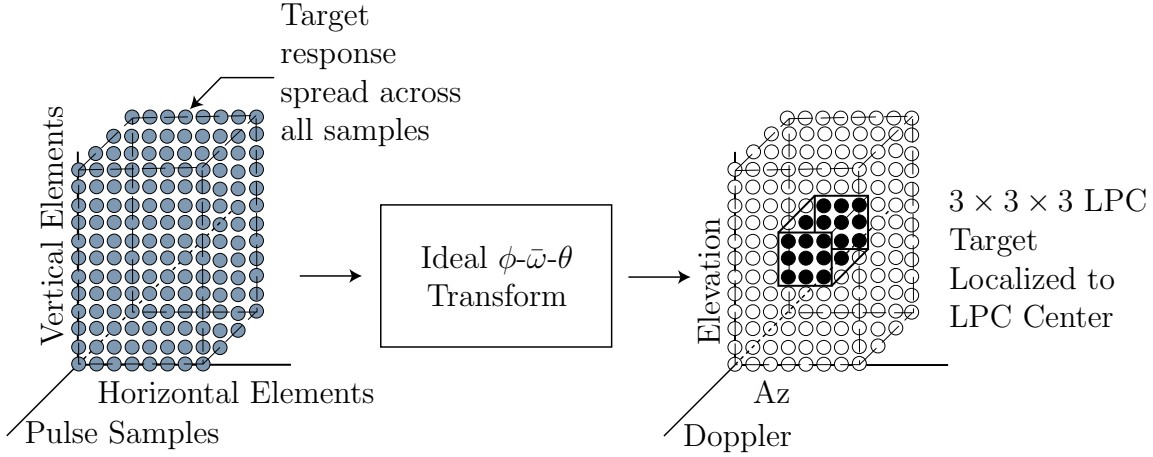


Figure 5.1: Ideal 3D-JDL block diagram. The transformation is shown only for the range cell under test, all data is transformed. Due to steering vector orthogonality (ideal case), the target is localized to the LPC center bin.

where interference covariance matrix \mathbf{R} is of dimension $NMP \times NMP$ and reflects the covariance between the planar array (spatial sampling) and temporal samples. The 3D adaptive weight vector \mathbf{w}_{3D} operates on the *transformed* data $\mathbf{T}^H \boldsymbol{\chi}$, hence the method is a joint domain or beamspace approach. A diagram of the proposed method is presented in Fig. 5.1. Superficially, the mathematical form of Eqn. (5.32) is identical to the 2D concept of [64]. The fundamental difference is embedded within the matrices themselves.

Transformation operator \mathbf{T} of Eqn. (5.33) provides conversion from element-time space to azimuth-Doppler-elevation space. This operator transforms the data to a localized region within the transform domain, where “focused” adaptivity is implemented. The 3D transformation matrix is similar to the 2-D implementation with adjustments made to generate a Localized Processing Cube (LPC), similar to the Localized Processing Region (LPR) of the 2D-JDL case,

$$\begin{aligned} \mathbf{T} = & \begin{bmatrix} \mathbf{e}(\theta_{-1}) & \mathbf{e}(\theta_0) & \mathbf{e}(\theta_1) \end{bmatrix} \\ & \otimes \begin{bmatrix} \mathbf{b}(\bar{\omega}_{-1}) & \mathbf{b}(\bar{\omega}_0) & \mathbf{b}(\bar{\omega}_1) \end{bmatrix} \\ & \otimes \begin{bmatrix} \mathbf{a}(\phi_{-1}, \theta_t) & \mathbf{a}(\phi_0, \theta_t) & \mathbf{a}(\phi_1, \theta_t) \end{bmatrix}. \quad (5.33) \end{aligned}$$

The \mathbf{T} of Eqn. (5.33) corresponds to a $3 \times 3 \times 3$ LPC. Generically, the LPC size is $\eta_a \times \eta_b \times \eta_e$ making \mathbf{T} of dimension $NMP \times \eta_a \eta_b \eta_e$, where $\eta_a \leq N$ represents the size in azimuth, $\eta_b \leq M$ represents the size in Doppler, and $\eta_e \leq P$ represents the size in elevation. Bounding each LPC dimension ensures the interference covariance matrix across the cube remains nonsingular. The bounds also ensure a level of generality, i.e., the 3D identically model collapses to conventional 2D-JDL when $P = 1$. LPC size is variable and scenario dependent; interference problems of higher-order require a larger LPC to achieve results approaching the 3D-AMF.

! The 3D-AMF, albeit approaching practical impossibility, provides an upper performance bound in the estimated interference case given homogeneous space-time snapshots. Although the P_d analysis does not include 3D-AMF results due to computational limitations, output SINR results do include the 3D-MF since known covariance removes the practical limitations.

The LPC covariance matrix is found by

$$\mathbf{R}_{\text{LPC}} = \mathcal{E} \{ \mathbf{T}^H \boldsymbol{\chi} \boldsymbol{\chi}^H \mathbf{T} \}, \quad (5.34)$$

and is of dimension $\eta_a \eta_b \eta_e \times \eta_a \eta_b \eta_e$ corresponding to a potential $\eta_a \eta_b \eta_e \leq NMP$ DOF (weight vector $\mathbf{w}_{3\text{D}}$ length). The weights (Wiener filter) are calculated using the transformed steering vector,

$$\mathbf{w}_{3\text{D}} = \mathbf{R}_{\text{LPC}}^{-1} \mathbf{T}^H \mathbf{v}. \quad (5.35)$$

The 3D method identically collapses to 2D-JDL in the $P = 1$ case resulting in,

$$\mathbf{w}_{2\text{D}} = \mathbf{R}_{\text{LPC}}^{-1} \mathbf{T}^H (\mathbf{a} \otimes \mathbf{b}), \quad (5.36)$$

where \mathbf{T} and \mathbf{R}_{LPC} correspond to the $P = 1$ case. The conventional Maximum Likelihood Estimator (MLE) of the interference covariance ($\hat{\mathbf{R}}_{\text{LPC}}$) within the LPC

Table 5.1: Radar simulation parameters.

Parameter	Value
Aircraft Altitude	9 km
Transmit Frequency	1.24 GHz
Pulse Repetition Frequency (PRF)	1984 Hz
Pulse Width	50 μ sec
Az (d_x) & El (d_z) Channel Spacing	0.1092 m/0.1407 m
Az (N) & El (P) Channels	8/8
Pulses per CPI (M)	8

is substituted for \mathbf{R}_{LPC} in the estimated interference case. Required secondary data support for the MLE is $2\eta_a\eta_b\eta_e$, to achieve performance within 3 dB of known covariance [49].

5.4 3D-JDL Results

Radar data was simulated using the 3D model described in Section III. For comparing the proposed techniques, a simulated target with 496 Hz Doppler shift at an azimuth angle of 0° and elevation angle of 45° was used. Reported results correspond to an 8×8 planar array (side-looking) using a CPI of eight pulses (resulting in eight Doppler bins) with parameters given in Table 5.1, identical to Table 4.4, to allow comparison of results between factored and joint approaches.

Performance results are characterized using two metrics: 1) output SINR and 2) detection probability (P_d). Output SINR represents detection capability for known interference statistics and unity target amplitude (amplitude variation merely scales the results). Consistent with [65], the SINR metric is plotted versus normalized Doppler. The P_d metric is essentially the ultimate characterization metric for a radar system. The P_d results are presented for fixed false alarm rate (allowing side-by-side

comparison) as a function of *input* SINR per element, per pulse. These results were obtained using Monte Carlo simulation (estimated interference statistics) where the number of realizations is equal to $10P_{fa}^{-1}$. For $P_{fa} = 0.01$, the simulations used 1,000 realizations.

5.4.1 Output SINR. Figure 5.2 presents output SINR versus normalized Doppler for the techniques considered. This figure introduces upper performance bounds (dashed lines) based on dimensionality. The 2D Matched Filter (2D-MF) represents the bound for conventional 2D STAP *operating in colored noise*. Hence, 2D-MF output is scenario, i.e., colored noise realization, dependent. Given data only corrupted by unit variance noise (identity covariance matrix), the constant 2D STAP bound is [65]

$$\text{SINR}_{\text{Max}}^{2\text{D}} = 10 \log_{10} MN. \quad (5.37)$$

The 3D Matched Filter (3D-MF) operating in unit variance white noise serves as the constant upper bound for the proposed Elev-JDL and 3D-JDL techniques. This bound is given by

$$\text{SINR}_{\text{Max}}^{3\text{D}} = 10 \log_{10} MNP. \quad (5.38)$$

For parameters of this work, the constant 3D bound of Eqn. (5.38) is 27.09 dB. Results for the 3D-MF (dashed line with star) operating in the colored noise of this scenario are shown in the figure. Achieving 3D-MF performance in severe interference environments requires all available DOF. The 3D-AMF requires $2MNP$ secondary

data snapshots for covariance estimation, an amount most likely unavailable for practical values of M , N , and P . Furthermore, extension to include planar arrays dictates clutter Doppler is a function of range, thereby violating the i.i.d. assumption required for secondary data snapshots.

! The use of constant N in Eqns. (5.37) and (5.38) corresponds to the comparison used in this work. Specifically, the comparison drawn between 2D and 3D approaches, as presented in this document, constrains the number of azimuth channels N and the number of pulses M . This constraint puts the two methods on an equal footing in terms of azimuth and Doppler resolution. The 3D approach gains the added elevation processing advantage. Reported results give an improvement due to the extension to 3D, bounded to be no *less* than $10\log_{10} P$. Improvement is no *less* than this bound because 2D methods typically cannot approach maximum output SINR in severe interference environments. Conversely, the robust nature of 3D methods allows them to approach maximum output SINR. Hence, the difference between the two approaches is a *minimum* of $10\log_{10} P$ dB.

A portion of the improvement could be attributed to the increase in total DOF, depending on the interference scenario. In light of this argument, future work could constrain the total DOF. The new $\text{SINR}_{\text{Max}}^{2\text{D}}$ would be $10\log_{10} MN_1$ with $\text{SINR}_{\text{Max}}^{3\text{D}} = 10\log_{10} MN_2P$. The equal DOF requirement is expressed as $MN_1 = MN_2P$ and defines the relationship $N_1 = N_2P$. From these maximum output SINR expressions, a minimum improvement due to the 3D extension would be $N_2P/N_1 = 1$. Hence, there would be no improvement in the ideal white noise limited case. However, simulations with $\mathbf{R} \neq \mathbf{I}$ (as shown in this work) would indicate significant improvement.

As expected, 2D-JDL performance (solid line with box) approaches $\text{SINR}_{\text{Max}}^{2\text{D}}$ for the clutter environment under consideration. Compared to 2D-JDL, the proposed Elev-JDL factored approach offers substantial improvement in output SINR, almost 8.5 dB, while the proposed 3D-JDL method (solid line with circle) offers 10.25 dB improvement. Of particular interest is the lack of blind speeds for the Elev-JDL factored approach. By suppressing entire rings of ambiguous interference,

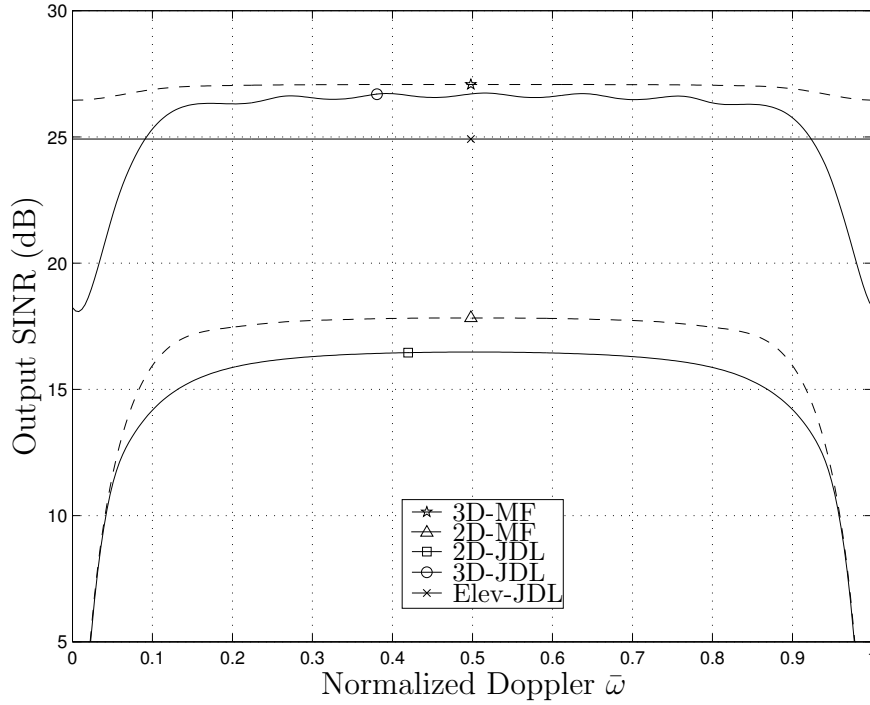


Figure 5.2: Output SINR curves using known covariance for range ambiguous clutter. Dashed lines represent corresponding upper bounds.

the factored method offers better suppression than the 3D-JDL approach as the look direction approaches mainbeam Doppler ($\bar{\omega} \rightarrow 0$). Although blind speeds are mitigated, they are not entirely removed. As the look direction, or potential target, approaches mainbeam clutter in all three dimensions (azimuth, Doppler, and elevation), all methods suffer degradation since there is no remaining dimension to discern a target. Obviously, this worst case scenario is more likely to occur in the 2-D case since the target only has to approach mainbeam clutter in azimuth and Doppler.

The 3D-JDL performance can be further improved by increasing the LPC size, set to $3 \times 3 \times 3$ for results presented here. Of particular interest, the 3D-JDL technique makes better use of available DOF. As the target moves away from mainbeam

clutter in Doppler, 3D-JDL performance edges out the factored approach due to more optimal null placement. Blind speeds could be completely mitigated, as in the factored approach, given a larger LPC and more DOF.

5.4.2 Detection Probability. Detection probability (P_d) results should be consistent with output SINR results since the two metrics are interrelated. Comparison of Fig. 5.2 with the P_d results of Fig. 5.3 shows this is the case. False alarm probability (P_{fa}) is held constant at 0.01 for each technique, using 1,000 realizations for the Monte Carlo analysis. Interference statistics estimation was accomplished using the appropriate MLE for \mathbf{R} for each technique according to Reed's Rule [49].

Figure 5.2 output SINR results at $\bar{\omega} = 496/1984 = 0.25$ provide expected relative detection performance, under the case of *known* interference statistics, for each technique. As Fig. 5.3 illustrates, the detection results under the case of *estimated* interference statistics follow these performance expectations. The bottom axis of the figure corresponds to *input* SINR per element, per pulse. For the given target location of $\phi = 0$, $\theta = 45$, and $\bar{\omega} = 0.25$, 3D-JDL offers the best detection performance.

5.5 Summary

The proposed three-dimensional methods offer significant detection performance improvement over current two-dimensional adaptive techniques for airborne radar. Including work from the previous chapter, two proposed 3D STAP classes were

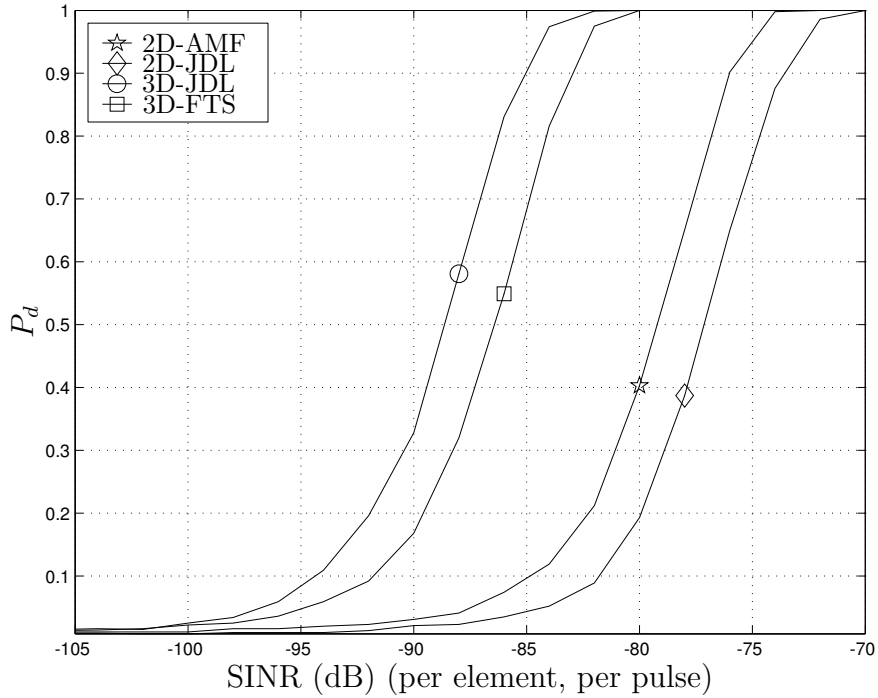


Figure 5.3: Detection probability for $P_{fa} = 0.01$, 1,000 realizations. Elev-JDL uses the proposed elevation beamforming approach suppressing range ambiguous interference.

considered, including 1) suboptimal factored methods offering improved interference rejection by placing nulls in elevation (suppressing entire range rings) and 2) optimal joint domain methods offering improved interference rejection by placing nulls at particular locations in elevation, azimuth, and Doppler. This chapter focused on joint domain techniques.

Three joint domain methods were presented. First, the 3D-MF offers optimal performance in the case of known interference statistics. Unfortunately, the airborne radar interference statistics are not known *a priori*. This limitation led to the introduction of the 3D-AMF, essentially the 3D-MF with estimated second-order

interference statistics. A variety of practical limitations preclude the use of this filter for real-time operation in actual airborne radar scenarios.

The main goal of this chapter involved development of a proposed 3D-JDL technique. This technique is a locally adaptive approach operating in beamspace with performance approaching optimal – optimal performance is defined as that of the matched filter. The 3D-JDL results speak for themselves: excellent target detection capability was demonstrated with small sample support requirements and limited computational load. The small sample support requirement translates to an inherent resistance to heterogeneous data, a generic benefit of joint domain localized concepts.

The factored techniques of previous chapters, 3D-FTS and Elev-JDL, offer a brute force approach to addressing the interference problem. Since range ambiguous ground clutter serves as the most significant problem in airborne radar, Section 4.5 offered a modified elevation approach mitigating its impact by attempting to suppress all ground clutter using elevation null(s). As mentioned there, this modified approach was required to permit fair comparison to the joint domain methods presented in this chapter. The 3D factored techniques require no increase in sample support over their 2D counterparts, since the elevation filter calculation is based entirely on physical parameters. Furthermore, the proposed 3D factored approaches incur little increase in computational burden.

The more optimal approach is 3D-JDL, the locally adaptive beamspace method in all three dimensions. This method approaches optimality because it maintains the capability to place null(s) at distinct locations in azimuth, Doppler, and elevation. As a consequence of incorporating elevation adaptivity, there is only a marginal increase in required sample support.

VI. Three-Dimensional Hybrid Approach

At this point in the research, the 3D research chain of Fig. 1.2 is nearly complete. Chapter III constructed the 3D data model, Chapter IV developed a variety of suboptimal factored approaches to the 3D interference suppression problem, and Chapter V developed optimal joint domain approaches including a partially adaptive 3D-JDL method. All work presented to this point focused on homogeneous data. This chapter addresses target detection within heterogeneous data.

Hybrid methods were borne out of a basic realization, namely, a fundamental question was raised given the ability to detect heterogeneous data. The impact of heterogeneous data on target detection within *homogeneous* locations was effectively mitigated through various techniques of secondary sample support selection. Yet, there was no answer on how to detect targets within locations deemed *heterogeneous*. Consequently, the the first hybrid technique was invented [5–7, 33].

The original 2D hybrid method presented in Section 2.8 is founded on the 2D-JDL approach where a transformation is necessary to apply interference suppression in the azimuth-Doppler beamspace. In the original 2D-JDL formulation [64], the ideal transform is used. For simulated data, the ideal transform is a set of steering vectors or DFT matrix columns. In this ideal world, a target is localized to a single azimuth-Doppler bin and the localized adaptivity region in beamspace is easily scaled. Subsequent research [4, 6–8, 10] determined that real-world antenna array effects resulted in performance degradation. A more appropriate transform was the actual measured array steering vectors, containing mutual coupling effects, array element mismatch effects, etc.

A side benefit of improving the transformation was the realization that this transformation could be used for other purposes. Instead of using the transform to merely reach the azimuth-Doppler beamspace, the transform could be used to simul-

taneously provide uncorrelated interference suppression. This realization spawned the birth of hybrid interference suppression techniques.

The literature devoted specifically to hybrid methods is limited primarily due to the newness of the concept. This chapter builds on the original 2D method through an elevation adaptivity extension.

The original 2D method suffers from several drawbacks. First, the general limitations of a factored approach for deterministic adaptivity are suboptimal. A joint deterministic method would be more suitable. Second, the order of processing is a perceived drawback. A solution to this perceived drawback is offered in Section 6.2, namely the inverse hybrid method. Finally, an inherent differencing operation between two adjacent elements incurs inadvertent suppression of interferers *within the interference estimate*. A solution for this final problem is offered in Section 6.3 for the case of known interferer location.

One proposed method, termed the inverse hybrid, essentially reverses the processing order of the original 2D hybrid technique. A perceived drawback of the original 2D approach involves the inability of deterministic techniques to distinguish between correlated and uncorrelated (discrete) interference. Since the original 2D approach first implements deterministic adaptivity, the potential exists to expend valuable DOF suppressing correlated interference. Such interference is better suppressed in the statistical processing stage. By reversing the processing order, correlated interference is first removed, effectively freeing the following deterministically adaptive stage for residual discrete interferer suppression. The actual development of such an approach is much more complicated than the concept and is addressed fully.

Finally, a concept having substantial processing benefits and performance improvement over the original approach is offered. Given known interferer location, a null is easily placed. Excellent results in homogeneous data can be obtained with practically flawless operation in heterogeneous data. Clearly, interferer location is not

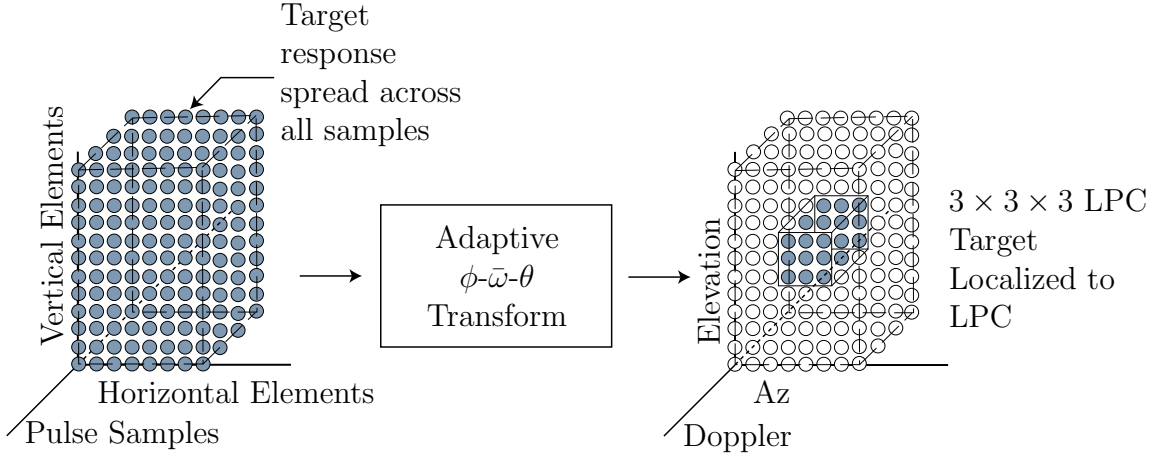


Figure 6.1: 3D original hybrid extension block diagram. The transformation is shown only for the range cell under test, all data is transformed.

known *a priori*. However, the concept is sound and techniques capable of accurately locating discrete interference sources can be developed. The design considerations for such approaches are considered in limited detail with full development reserved for future research.

6.1 3D Extension of the Original 2D Hybrid Technique

The 3D hybrid concept mirrors the original 2D hybrid approach. The work in this section represents a non-trivial extension into the azimuth-Doppler-elevation space rather than a complete redesign. Figure 6.1 is a block diagram illustrating the proposed extension. As in the original 2D work, the general processing flow is identical to the joint domain localized concept. The incoming space-time data is adaptively transformed to the azimuth-Doppler-elevation space (the original 2D work uses only the azimuth-Doppler space) where localized statistical adaptivity is implemented.

The 3D extension differs from the original 2D method in two primary ways. First, the adaptive transform is three-dimensional and remains non-stochastic (deterministic). The factored nature of the adaptive transform is preserved. Hence, the azimuth and Doppler portions of the 3D method are *conceptually* identical to their 2D counterparts. However, the elevation technique is new. Second, the localized sta-

tistical adaptivity within the beamspace now operates across all three dimensions, as compared to two dimensions in the original 2D hybrid. Each facet of the 3D hybrid extension is developed in the following subsections.

6.1.1 3D Deterministic Processing. Statistical techniques fail to counter heterogeneities in the range cell under test, motivating deterministic or direct data domain technique research. These techniques use only primary range cell (range cell under test) data, eliminating sample support problems associated with statistical approaches. This research field has recently emerged with a focus on one-dimensional spatial adaptivity [47, 54]. This section builds upon the factored 2D direct data domain technique that reformulated earlier non-statistical (deterministic) attempts at adaptive processing. Other researchers have developed a true two-dimensional direct data technique [55], perhaps superior to the original concept. However, it too has limitations and is not discussed here because it lacks relevance to this work’s primary focus.

The original 2D direct data formulation worked on a factored premise, meaning the weights for temporal adaptivity were calculated independently from the weights for azimuth adaptivity. Furthermore, when calculating temporal adaptive weights, the *spatial* samples serve to build the required system of equations. The converse is true when calculating spatial adaptive weights. This premise stands for the 3D extension, however, the framework becomes much more complicated due to the third dimension.

The following discussion is designed to work within the space-time snapshot framework defined in Chapter III. Because of this choice, the method requires two new mathematical definitions similar to MATLAB[®] functional commands. The approach taken here keeps the overall structure similar to previous methods and, hopefully, allows the reader to concentrate on the approach rather than the mathematics.

First, consider the construction of the azimuth *data* matrix \mathbf{A} used to construct the $N \times 1$ azimuth weight vector \mathbf{w}_a . To create this matrix, the following definition is introduced.

Definition (reshape operator). *Given the vector χ of dimension $NMP \times 1$, let $\text{reshape}(\chi, N, M, P)$ define the operation taking N elements column wise from χ to form an $N \times M \times P$ multidimensional array. The number of elements in the output array must equal the total number of elements in χ . This operation is equivalent to*

$$\begin{aligned}\mathbf{Y} &= \text{reshape}(\chi, N, M \cdot P) \\ \mathbf{Y}_{i,j} &= \chi_{i+jN},\end{aligned}\tag{6.1}$$

where $i = 0, 1, \dots, N - 1$ and $j = 0, 1, \dots, MP - 1$. The small dot (\cdot) indicates a product operation, typically implied but included here to avoid confusion. The reshape operation is equivalent in both name and function to the MATLAB[®] reshape command.

Using the range cell under test data, construct azimuth data matrix \mathbf{A} using the elevation and temporal dimensions as independent samples. This operation is accomplished through

$$\mathbf{A} = \text{reshape}(\chi, N, M \cdot P),\tag{6.2}$$

resulting in the $N \times MP$ matrix.

! Notice the form of \mathbf{A} is *not* the same as in the original 2D hybrid approach. This form is designed to give the common form for the complex outer product. See page 46 for clarification and comparison to the original 2D method.

Similarly, elevation data matrix \mathbf{E} is composed using the temporal and azimuth dimensions as independent samples. The $P \times NM$ matrix \mathbf{E} is found from

$$\mathbf{E} = [\text{reshape}(\boldsymbol{\chi}, N \cdot M, P)]^T. \quad (6.3)$$

Unfortunately, temporal data matrix generation is much more difficult for the 3D extension. Since there is no multidimensional mathematical framework available, the notation used here garners concepts established by MATLAB[®]. Constructing the temporal data matrix first requires changing the shape of the snapshot being tested for target presence into a $N \times M \times P$ matrix,

$$\boldsymbol{\Xi} = \text{reshape}(\boldsymbol{\chi}, N, M, P). \quad (6.4)$$

The next step requires a multidimensional transpose definition.

Definition (permute operator). Let $\text{permute}(\mathbf{X}, \mathbf{z})$ represent the multidimensional transpose of the three-dimensional array \mathbf{X} , where the elements of \mathbf{z} represent the desired output dimension order, i.e., $\mathbf{z} = [z_1 \ z_2 \ z_3]$ is a row vector such that $z_i = \{1, 2, 3\}$. Define the three-dimensional $N \times M \times P$ array \mathbf{X} as

$$\begin{aligned} \mathbf{X}_0 &= \begin{bmatrix} \mathbf{x}_{0,0} & \mathbf{x}_{1,0} & \cdots & \mathbf{x}_{N-1,0} \end{bmatrix}^T \\ \mathbf{X}_1 &= \begin{bmatrix} \mathbf{x}_{0,1} & \mathbf{x}_{1,1} & \cdots & \mathbf{x}_{N-1,1} \end{bmatrix}^T \\ &\vdots \\ \mathbf{X}_{P-1} &= \begin{bmatrix} \mathbf{x}_{0,P-1} & \mathbf{x}_{1,P-1} & \cdots & \mathbf{x}_{N-1,P-1} \end{bmatrix}^T, \end{aligned} \quad (6.5)$$

where $\mathbf{x}_{i,j}^T$ is the $M \times 1$ vector corresponding to the i^{th} row, $i = 0, 1, \dots, N-1$, and the j^{th} matrix (third dimension), $j = 0, 1, \dots, P-1$. Given the desired dimension

order vector of

$$\mathbf{z} = \begin{bmatrix} 2 & 1 & 3 \end{bmatrix}, \quad (6.6)$$

the permutation of the $N \times M \times P$ matrix \mathbf{X} is $\text{permute}(\mathbf{X}, \mathbf{z})$, or

$$\begin{aligned} \mathbf{X}_0 &= \begin{bmatrix} \mathbf{x}_{0,0} & \mathbf{x}_{1,0} & \cdots & \mathbf{x}_{N-1,0} \end{bmatrix} \\ \mathbf{X}_1 &= \begin{bmatrix} \mathbf{x}_{0,1} & \mathbf{x}_{1,1} & \cdots & \mathbf{x}_{N-1,1} \end{bmatrix} \\ &\vdots \\ \mathbf{X}_{P-1} &= \begin{bmatrix} \mathbf{x}_{0,P-1} & \mathbf{x}_{1,P-1} & \cdots & \mathbf{x}_{N-1,P-1} \end{bmatrix}. \end{aligned} \quad (6.7)$$

Hence, the output of this operation is the $M \times N \times P$ matrix where the original matrix \mathbf{X} dimensions have been reordered. As expected for a generalized transpose, the operation for standard two-dimensional matrices collapses to the common transpose operator. The operation is equivalent in both name and function to the MATLAB[®] `permute` command.

Rearrange the space-time snapshot using the `permute` operator,

$$\text{permute}(\mathbf{\Xi}, \mathbf{z}), \quad (6.8)$$

and the same dimension order in \mathbf{z} as used in the definition. The `reshape` operator then transforms the samples into the desired $M \times NP$ temporal data matrix \mathbf{T} ,

$$\mathbf{T} = \text{reshape}(\text{permute}(\mathbf{\Xi}, \mathbf{z}), M, N \cdot P). \quad (6.9)$$

Again, the premise behind each interference matrix is identical - one dimension is adapted across while the other two dimensions provide independent sampling.

Azimuth weights are calculated using the azimuth data matrix \mathbf{A} of Eqn. (6.2). Adjacent elements of \mathbf{A} are co-phased, precluding signal cancellation and forming

the azimuth *interference* matrix. The phase delay between returns from adjacent azimuth elements is given by

$$z_a = e^{j2\pi \frac{d_x}{\lambda} \sin \phi \cos \theta}, \quad (6.10)$$

where ϕ and θ correspond to the desired mainbeam azimuth and elevation angles, respectively. Using this phase delay, the individual azimuth element returns are co-phased using

$$\tilde{\mathbf{A}}_{i,j} = \mathbf{A}_{i,j} - z_a^* \mathbf{A}_{i+1,j}, \quad (6.11)$$

where $i = 0, 1, \dots, N - 2$ and $j = 0, 1, \dots, MP - 1$. This operation is simply the difference between adjacent elements with an appropriate phase term to ensure the desired signal is completely cancelled and only interference remains. Note, this differencing operation results in a loss of one DOF in the azimuth adaptive weight vector. Essentially, this DOF is used to ensure the desired signal component is not corrupted.

The $N - 1 \times MP$ matrix $\tilde{\mathbf{A}}$ can also be expressed using strict matrix notation as

$$\tilde{\mathbf{A}} = \mathbf{A}_1 - z_a^* \mathbf{A}_2 \quad (6.12)$$

with the matrix partitions \mathbf{A}_1 and \mathbf{A}_2 obtained from

$$\mathbf{A} = \begin{bmatrix} \mathbf{A}_1 \\ \mathbf{A}_2 \end{bmatrix} = \begin{bmatrix} \boldsymbol{\alpha}^T \\ \mathbf{A}_2 \end{bmatrix}, \quad (6.13)$$

where α is a scalar placeholder and $\boldsymbol{\alpha}$ is a $N \times 1$ vector placeholder representing the samples in the original \mathbf{A} matrix.

Temporal and elevation weights are calculated in the same manner as the azimuth weights. The difference lies only in the sample-to-sample phase progression and the steering vectors used. For example, the temporal weights are calculated

using

$$z_b = e^{j2\pi\bar{\omega}}. \quad (6.14)$$

This term co-phases the samples using matrix partitions, exactly as before, i.e.,

$$\tilde{\mathbf{T}}_{i,j} = \mathbf{T}_{i,j} - z_b^* \mathbf{T}_{i+1,j}, \quad (6.15)$$

where $i = 0, 1, \dots, M-2$ and $j = 0, 1, \dots, NP-1$. The weight vectors are calculated using either of the following two techniques with appropriate substitution for $\tilde{\mathbf{T}}$ or $\tilde{\mathbf{E}}$ and \mathbf{b}_{M-1} or \mathbf{e}_{P-1} .

! To this point, the development mirrors the original 2D hybrid formulation in concept. Note, the differencing operation is essentially a two element beamforming operation where a null is placed on the desired signal to avoid nulling it in subsequent processing. However, the act of placing this null has consequences in that discrete interferers lying close to the desired signal will *not* be cancelled. The differencing null effectively removes them from the subsequent calculations. This consequence is a limitation of the current hybrid approach and is inherent in either the constrained difference maximization or maximum SINR adaptive weights that follow.

6.1.1.1 Constrained Difference Maximization. Following the original 2D hybrid technique, consider the scalar expressions

$$G = |\mathbf{w}_a^H \mathbf{a}_{N-1}|^2, \quad (6.16)$$

$$I = \left\| \mathbf{w}_a^H \tilde{\mathbf{A}} \right\|^2, \quad (6.17)$$

where \mathbf{a}_{N-1} is the vector comprising the first $(N-1)$ elements of steering vector \mathbf{a} and $\|\cdot\|$ represents the Frobenius norm. The G term in Eqn. (6.16) represents the power gain in the look direction due to weights \mathbf{w}_a , e.g., signal power. The I term in Eqn. (6.17) represents residual interference power. The previous 2D direct data domain technique obtains the adaptive weights maximizing the difference between

the two terms, i.e.

$$\max_{\|\mathbf{w}_a\|^2=1} (G - \kappa^2 I) = \max_{\|\mathbf{w}_a\|^2=1} \mathbf{w}_a^H \left(\mathbf{a}_{N-1} \mathbf{a}_{N-1}^H - \kappa^2 \tilde{\mathbf{A}} \tilde{\mathbf{A}}^H \right) \mathbf{w}_a. \quad (6.18)$$

The constraint $\|\mathbf{w}_a\|^2 = 1$ guarantees a finite solution. The κ^2 term serves as a sidelobe control parameter. Using the Lagrange multiplier method, the weight vector maximizing Eqn. (6.18) is the eigenvector corresponding to the largest eigenvalue of the matrix

$$\mathbf{a}_{N-1} \mathbf{a}_{N-1}^H - \kappa^2 \tilde{\mathbf{A}} \tilde{\mathbf{A}}^H. \quad (6.19)$$

This weight vector constitutes the azimuth adaptive weights and is length $(N - 1)$, representing a one DOF loss in the spatial domain. As in the original 2D approach, this loss compares favorably with other non-statistical techniques where close to one-half the DOF are lost [54].

! The previous statement can be misleading. The DOF loss due to this approach is one in *each* dimension. Hence, the *total* DOF loss is

$$(P - 1) [(M - 1) + N] + MN$$

for $P \neq 1$.

6.1.1.2 SINR Maximization. An alternate approach to the original constrained maximization formulation involves maximizing the SINR. The technique is identical to the 3D-MF development of Section 5.1.2. The SINR can be constructed using the G and I terms previously defined,

$$\text{SINR} = \frac{G}{I} = \frac{|\mathbf{w}_a^H \mathbf{a}_{N-1}|^2}{\left\| \mathbf{w}_a^H \tilde{\mathbf{A}} \right\|^2}. \quad (6.20)$$

Next, expand the numerator and denominator into

$$\text{SINR} = \frac{\mathbf{w}_a^H \left(\tilde{\mathbf{A}} \tilde{\mathbf{A}}^H \right)^{\frac{1}{2}} \left(\tilde{\mathbf{A}} \tilde{\mathbf{A}}^H \right)^{-\frac{1}{2}} \mathbf{a}_{N-1} \mathbf{a}_{N-1}^H \left(\tilde{\mathbf{A}} \tilde{\mathbf{A}}^H \right)^{-\frac{1}{2}} \left(\tilde{\mathbf{A}} \tilde{\mathbf{A}}^H \right)^{\frac{1}{2}} \mathbf{w}_a}{\mathbf{w}_a^H \left(\tilde{\mathbf{A}} \tilde{\mathbf{A}}^H \right)^{\frac{1}{2}} \left(\tilde{\mathbf{A}} \tilde{\mathbf{A}}^H \right)^{\frac{1}{2}} \mathbf{w}_a}. \quad (6.21)$$

Define the unit vector \mathbf{u} as

$$\mathbf{u} = \frac{\left(\tilde{\mathbf{A}} \tilde{\mathbf{A}}^H \right)^{\frac{1}{2}} \mathbf{w}_a}{\left\| \left(\tilde{\mathbf{A}} \tilde{\mathbf{A}}^H \right)^{\frac{1}{2}} \mathbf{w}_a \right\|}. \quad (6.22)$$

SINR maximization is now easily seen by substituting \mathbf{u} into Eqn. (6.21),

$$\text{SINR} = \left| \mathbf{u}^H \left(\tilde{\mathbf{A}} \tilde{\mathbf{A}}^H \right)^{-\frac{1}{2}} \mathbf{a}_{N-1} \right|^2. \quad (6.23)$$

For maximum SINR, the unit vector lies parallel to $\left(\tilde{\mathbf{A}} \tilde{\mathbf{A}}^H \right)^{-\frac{1}{2}} \mathbf{a}_{N-1}$, hence

$$\mathbf{u} \propto \left(\tilde{\mathbf{A}} \tilde{\mathbf{A}}^H \right)^{-\frac{1}{2}} \mathbf{a}_{N-1}. \quad (6.24)$$

The azimuth weight vector \mathbf{w}_a ignoring scale factors is then

$$\mathbf{w}_a \propto \left(\tilde{\mathbf{A}} \tilde{\mathbf{A}}^H \right)^{-1} \mathbf{a}_{N-1}. \quad (6.25)$$

Similarly, the temporal (\mathbf{w}_b) and elevation (\mathbf{w}_e) adaptive weight sets, after making the appropriate substitutions in the above development, are given by

$$\mathbf{w}_b \propto \left(\tilde{\mathbf{T}} \tilde{\mathbf{T}}^H \right)^{-1} \mathbf{b}_{M-1} \quad (6.26)$$

$$\mathbf{w}_e \propto \left(\tilde{\mathbf{E}} \tilde{\mathbf{E}}^H \right)^{-1} \mathbf{e}_{P-1}. \quad (6.27)$$

6.1.1.3 Full Weight Vector. Whether using the constrained optimization approach or the SINR maximization method, the full weight vector is constructed in a manner identical to a space-time steering vector, e.g., using the Kronecker product. The primary difference involves appending a zero to the end of each weight vector, accommodating the single DOF loss as a result of the initial differencing operation. Hence, the weight vector forming a beam to a single azimuth, elevation, and Doppler location while placing nulls in the direction of discrete interferers is given by

$$\mathbf{w} = \begin{bmatrix} \mathbf{w}_e \\ 0 \end{bmatrix} \otimes \begin{bmatrix} \mathbf{w}_b \\ 0 \end{bmatrix} \otimes \begin{bmatrix} \mathbf{w}_a \\ 0 \end{bmatrix}. \quad (6.28)$$

From this equation, the previous statement regarding the total DOF lost due to the approach is clearer. One DOF is sacrificed in *each* dimension. Hence, the *total* DOF loss is $(P - 1)[(M - 1) + N] + MN$ for $P \neq 1$.

6.1.2 Statistical Beam-space Adaptivity. The non-statistical (deterministic) adaptive transform results in a complex output at a particular azimuth, Doppler, and elevation location. Repeated iterations of the deterministic approach, where each is steered to a different look direction, forms a LPC suitable for statistical beam-space adaptivity. In this manner, the *overall* approach of the hybrid technique is identical to JDL. The most significant difference involves replacing the conventional, non-adaptive discrete Fourier transform with repeated applications of the deterministic method. In this manner, the technique inherently suppresses discrete interferers.

Mathematically, this repeated operation of the deterministic approach can be represented by a transformation to the predetermined LPC. Consider the matrix operator \mathbf{W} . The azimuth-Doppler-elevation data is given by $\tilde{\mathbf{x}} = \mathbf{W}^H \mathbf{x}$. The steering vector is transformed in the same manner. An example of \mathbf{W} for a $3 \times 3 \times 3$

LPC is

$$\mathbf{W} = \begin{bmatrix} \begin{bmatrix} \mathbf{w}_{-1,-1,-1}^T \\ \mathbf{w}_{-1,-1,t}^T \\ \mathbf{w}_{-1,-1,1}^T \\ \mathbf{w}_{-1,t,-1}^T \\ \mathbf{w}_{-1,t,t}^T \\ \mathbf{w}_{-1,t,1}^T \\ \mathbf{w}_{-1,1,-1}^T \\ \mathbf{w}_{-1,1,t}^T \\ \mathbf{w}_{-1,1,1}^T \end{bmatrix}^T & \begin{bmatrix} \mathbf{w}_{t,-1,-1}^T \\ \mathbf{w}_{t,-1,t}^T \\ \mathbf{w}_{t,-1,1}^T \\ \mathbf{w}_{t,t,-1}^T \\ \mathbf{w}_{t,t,t}^T \\ \mathbf{w}_{t,t,1}^T \\ \mathbf{w}_{t,1,-1}^T \\ \mathbf{w}_{t,1,t}^T \\ \mathbf{w}_{t,1,1}^T \end{bmatrix}^T & \begin{bmatrix} \mathbf{w}_{1,-1,-1}^T \\ \mathbf{w}_{1,-1,t}^T \\ \mathbf{w}_{1,-1,1}^T \\ \mathbf{w}_{1,t,-1}^T \\ \mathbf{w}_{1,t,t}^T \\ \mathbf{w}_{1,t,1}^T \\ \mathbf{w}_{1,1,-1}^T \\ \mathbf{w}_{1,1,t}^T \\ \mathbf{w}_{1,1,1}^T \end{bmatrix}^T \end{bmatrix}, \quad (6.29)$$

where $\mathbf{w}_{i,j,k}$ corresponds to a weight vector with mainbeam at ϕ_i , $\bar{\omega}_j$, and θ_k . For the general architecture reflected by this equation, the weight vector $\mathbf{w}_{-1,t,1}$ has a mainbeam corresponding to an azimuth angle ϕ one bin below the LPC center azimuth, normalized Doppler equaling the LPC center normalized Doppler (the mainbeam look direction or “target” location), and elevation angle θ equal to one bin above the LPC center elevation. Bin size is determined by design with limits consistent with standard sampling concepts. Obviously, the $3 \times 3 \times 3$ LPC results in 27 iterations of the deterministic approach. In general, for a $\eta_e \times \eta_b \times \eta_a$ size LPC, there are $\eta_e \eta_b \eta_a$ iterations necessary to populate the LPC, e.g., beamspace, for statistical adaptivity.

! The azimuth-Doppler-elevation data as given by $\tilde{\chi} = \mathbf{W}^H \chi$ is in vector form, corresponding to the column vector framework established in Chapter III. Hence, the $\eta_e \eta_b \eta_a \times 1$ vector $\tilde{\chi}$ is arranged such that the first η_a elements contain azimuth samples corresponding to the first normalized Doppler bin and first elevation bin. The second set of η_a elements correspond to azimuth samples from the *second* normalized Doppler bin and first elevation bin. The η_b^{th} set of η_a elements are the azimuth samples corresponding to the η_b^{th} normalized Doppler bin and first elevation bin. Finally, the $\eta_b + 1$ set of η_a elements are azimuth samples for the first normalized Doppler bin and *second* elevation bin. The pattern continues in this man-

ner. The data could be rearranged into a three-dimensional data cube using reshape ($\tilde{\mathbf{X}}, \eta_a, \eta_b, \eta_e$).

The locally adaptive weight vector is then calculated in a manner identical to 3D-JDL. Since the first stage consists of a deterministic technique, it no longer makes sense to generate an expression with known covariance. This point becomes clear when constructing the locally adaptive weight vector \mathbf{w}_{LPC} . First, consider the data within the LPC,

$$\tilde{\mathbf{X}} = \mathbf{W}^H \mathbf{X}, \quad (6.30)$$

where the *tilde* (\sim) denotes beamspace, e.g., the LPC. Now examine the second-order statistics,

$$\mathbf{R}_{LPC} = \mathcal{E} \{ \tilde{\mathbf{X}} \tilde{\mathbf{X}}^H \} = \mathcal{E} \{ \mathbf{W}^H \mathbf{X} \mathbf{X}^H \mathbf{W} \}. \quad (6.31)$$

The weight vector is then calculated exactly as before,

$$\mathbf{w}_{LPC} = \mathbf{R}_{LPC}^{-1} \mathbf{W}^H \mathbf{v}, \quad (6.32)$$

where the inner product between the adaptive transformation \mathbf{W} and \mathbf{v} is the steering vector *within* the beamspace LPC. The reason a formulation in terms of known covariance is no longer suitable is apparent when examining \mathbf{R}_{LPC} of Eqn. (6.31). *The transformation \mathbf{W} is random*, hence, the expected value operator does not distribute across this term. Since \mathbf{W} is realization dependent (as a result of this specific approach), there is no way to determine \mathbf{R}_{LPC} other than by estimation. Therefore, all results are reported using either Monte Carlo analysis or the RPSL/RASL measures of previous chapters. The weight vector is given by

$$\mathbf{w}_{LPC} = \hat{\mathbf{R}}_{LPC}^{-1} \mathbf{W}^H \mathbf{v}. \quad (6.33)$$

The LPC covariance estimate is given by the MLE

$$\hat{\mathbf{R}}_{LPC} = \sum_{i=1}^K \tilde{\mathbf{x}}_i \tilde{\mathbf{x}}_i^H = \sum_{i=1}^K \mathbf{W}_i^H \mathbf{x}_i \mathbf{x}_i^H \mathbf{W}_i, \quad (6.34)$$

where the number of secondary data vectors K is twice the LPR size, i.e., $2\eta_e\eta_b\eta_a$. This expression highlights the range/sample dependence of the deterministic first stage.

6.1.3 3D Hybrid Results. Results are characterized using simulation parameters consistent with previous chapters. Homogeneous data is generated using the 3D model of Chapter III and a target added within the designated range cell corresponding to the radar look direction. Heterogeneous data is simulated using the same data and target; the radar mainbeam is formed in a direction differing from the true target location, essentially turning the “target” into a discrete interferer. This case corresponds to a “no target present” scenario. In this manner, target detection capability is evaluated using the homogeneous data. Interferer rejection capability is evaluated using the heterogeneous data.

The true target (discrete interferer for the heterogeneous case) is generated at 25° azimuth, 10° elevation, 0.25 normalized Doppler, and range cell 80. For the homogeneous data test, the radar look direction matches the true target and allows detection capability characterization. The radar look direction is moved to 65° in azimuth, a difference of 40° from the interferer location for the heterogeneous test. Ideally, *no* response should occur in this case since the radar is not “looking” at the interferer.

Figure 6.2 is a plot of the normalized output test statistic versus range cell for the *homogeneous* data case. As mentioned in the previous chapter, 3D-JDL offers excellent detection capability as evidenced by the strong response at range cell 80. The RPSL is nearly 43.5 dB, indicating superb detection probability at this target

amplitude and SNR. The 3D hybrid extension also offers good response at the range cell under test, although some penalty is incurred as a result of the deterministic processing of the first stage. The indicated RPSL for the 3D hybrid extension is appropriately 30 dB, 13.5 dB poorer than 3D-JDL.

The real benefit of hybrid methods is evident in Fig. 6.3, where the normalized output test statistic is plotted versus range for the *heterogeneous* test case. In this case, the methods should *not* have any response at range cell 80, the interferer location. The 3D-JDL method does suppress the interferer to an extent as evidenced by an 18 dB RPSL; greatly reduced from the 43.5 dB when the radar was looking directly at the target/interferer. However, the response is significant enough to yield a high false alarm rate. Conversely, the 3D hybrid extension results in an RPSL of -5 dB, well below surrounding ground clutter returns and indicating superb false alarm characteristics when operating in heterogeneous data.

! Good performance in homogeneous data results in positive RPSL values, the standard up to this point in the research. However, good performance in heterogeneous data results in *negative* RPSL values. Negative RPSL indicates there is *minimal response* to the discrete interferer and is the desired condition. The results in heterogeneous data measure the ability to suppress discrete interference and do *not* indicate target detection capability.

At this point, results for the 3D extension to the original 2D hybrid seem excellent. However, *some important limitations have been buried as a result of the scenario*. The differencing operation used to co-phase the returns effectively avoids desired signal cancellation. However, the approach does incur a rather significant penalty. The differencing operation equates to a two-element beamforming operation, effectively creating a virtual null¹ in the direction of the desired signal. Unfortunately, a two-element beamformer produces a very wide null that not only removes

¹The term virtual is used here since the nulling operation is performed in data processing rather than through physical beam steering.

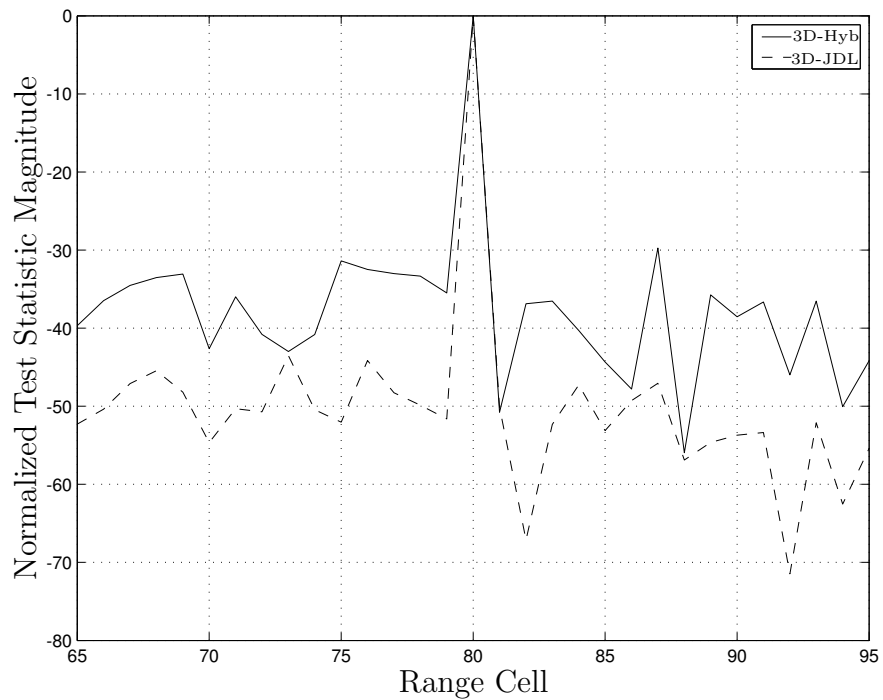


Figure 6.2: Results for the 3D hybrid in *homogeneous* data.

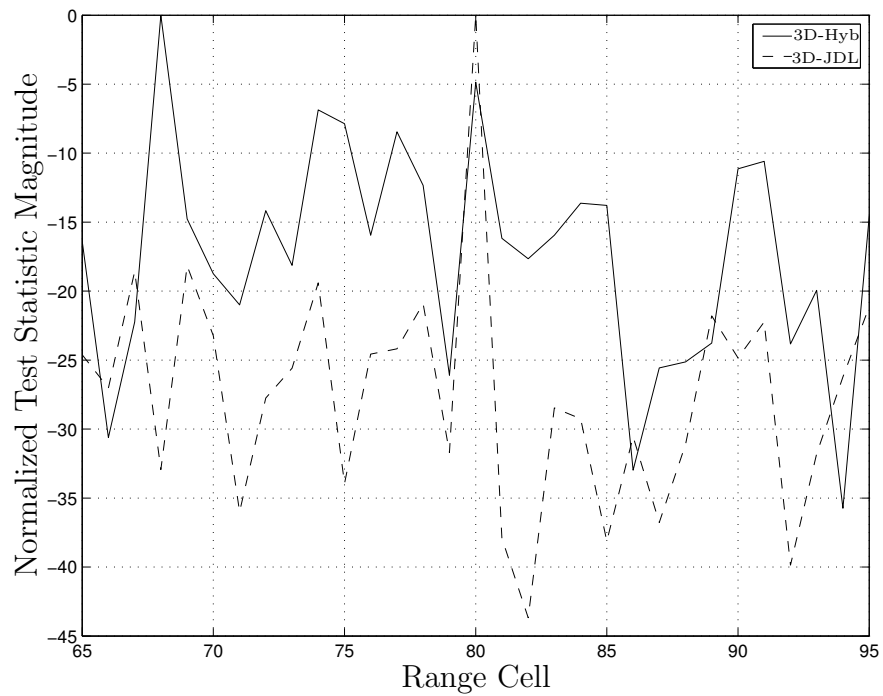


Figure 6.3: Results for the 3D hybrid in *heterogeneous* data.

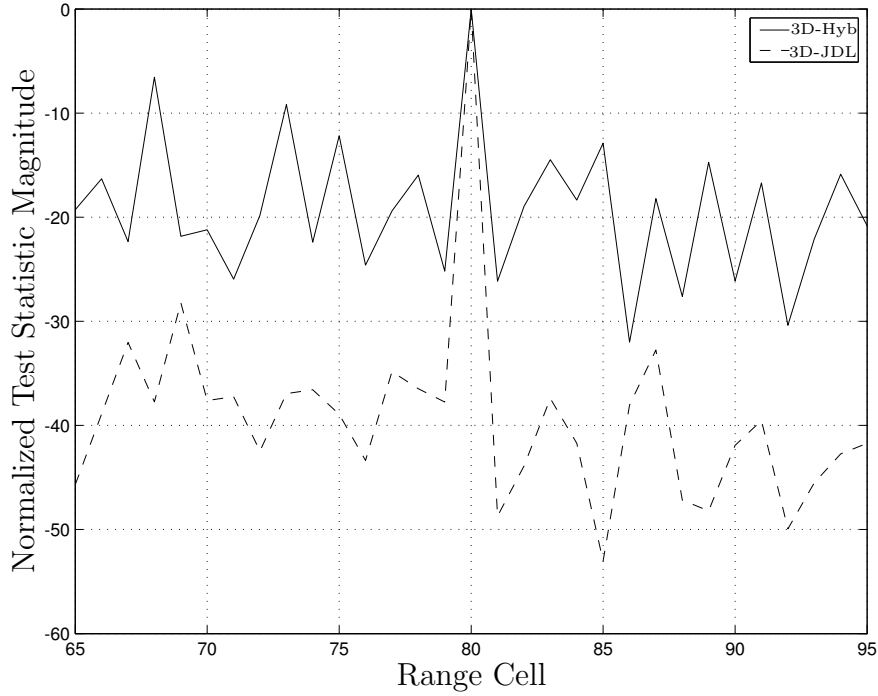


Figure 6.4: Results for the 3D hybrid in heterogeneous data. Look direction is now at 45° azimuth instead of 65° .

the desired signal from the interference estimate but also removes a significant portion of the interference. Therefore, *as the look direction converges on interferer location, the method becomes incapable of suppressing the interferer(s).*

Figure 6.4 illustrates this concept. The 3D hybrid method is applied to the same data set as used in the previous two figures. The *only* exception is that the radar look direction is now at 45° azimuth. Since the target is located at 25° azimuth (look direction is matched to the interferer in elevation and normalized Doppler, but not azimuth), the scenario remains heterogeneous. In this case, the interferer is 20° away from the look direction and there should be *no* response indicating target presence at range cell 80. Unfortunately, the initial co-phasing operation resulted in significant suppression of the interferer and effectively removed it from the interference estimation used in the deterministic processing. As indicated in Fig. 6.4, the 3D original hybrid extension produces a 6.56 dB RPSL response at the discrete interferer range cell, falsely indicating target presence.

6.2 Inverse 3D Hybrid Concept

One drawback of the original hybrid formulation involves a fundamental design issue. Deterministic techniques offer inferior correlated interference suppression, when compared to statistical interference suppression methods. Therefore, discrete interferer suppression would likely be improved if correlated interference were suppressed *first*. This order is the exact *opposite* of the original 2D hybrid technique and the proposed 3D extension of Section 6.1.

Two conflicting observations dominate the fundamental design issue. First, the deterministic processing stage goal is discrete interferer removal. Hence, this goal could be achieved by suppressing statistical interference first. Second, the statistical processing stage goal is correlated interference removal. Achieving this goal is impeded if discrete interferers are present in secondary data. Based on the second observation, it seemed reasonable that discrete interferers should be suppressed first. The realization resulted in the birth of the original 2D hybrid formulation.

Discrete interferer effects on statistical processing methods can be alleviated using a Non-Homogeneity Detector (NHD) [7] to remove offending secondary data samples from interference estimation. Unfortunately, no method has been developed to alleviate correlated interference effects on deterministic processing methods. Deterministic methods attempt to suppress *all* interference sources and lack the ability to discern correlated interference (subject to later suppression by the statistical approach) from discrete interferers. For this reason, a logical hierarchy is to:

1. Detect heterogeneous secondary data samples using an NHD.
2. Excise heterogeneous secondary data samples from interference estimates.
3. Apply a statistical method for correlated interference suppression.
4. Finally, apply a deterministic method for discrete interferer suppression.

Unfortunately, actual technique development is never quite as simple as concept visualization. The most significant limitation is implicit in the above processing

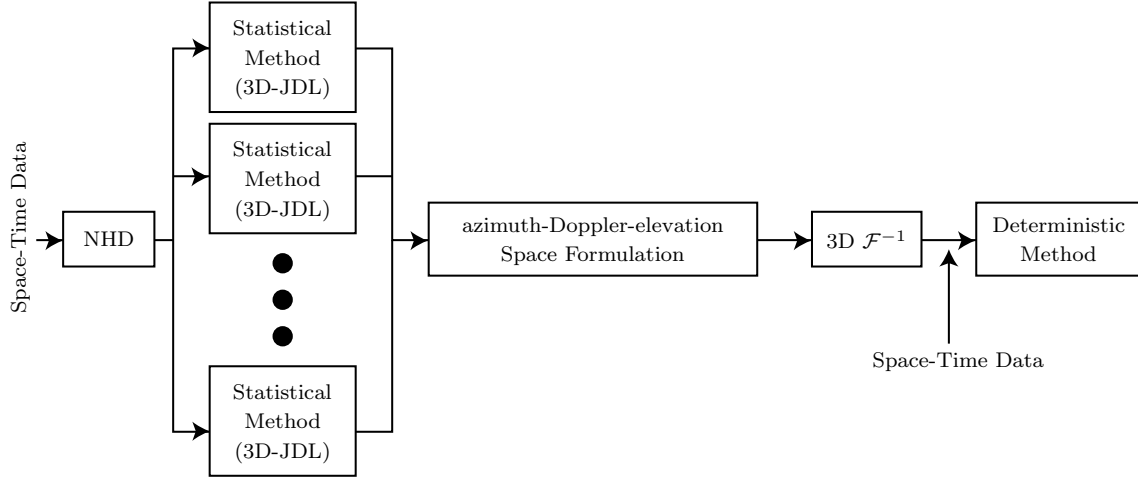


Figure 6.5: Proposed 3D hybrid concept maximizing discrete interferer suppression, where $3D \mathcal{F}^{-1}$ represents the 3D inverse discrete Fourier transform.

hierarchy. The output of the statistical method, or any method, is a complex number representing the return for a single azimuth, Doppler, and elevation position. Although statistical methods operating in beamspace exist, deterministic methods typically operate in the space-time domain.

One straightforward solution is to use original 2D hybrid concepts. Simply apply a *statistical* method repetitively, building the entire azimuth-Doppler-elevation space. In this manner, the technique serves as an adaptive transform analogous to the non-adaptive Fourier transform. A three-dimensional inverse discrete Fourier transform can be used to transform back to space-time data, allowing deterministic interference suppression. Figure 6.5 is a block diagram of this concept.

Although any statistical technique can be used, 3D-JDL is indicated since it offers advantages in scalability, computation time, and robustness. The size of the azimuth-Doppler-elevation space dictates how many times 3D-JDL is run given each instance of 3D-JDL results in a single azimuth-Doppler-elevation bin. If the desired space is $N \times M \times P$, then NMP 3D-JDL iterations are required. This choice results in identical dimensionality between the final and original space-time data sets. Scaling the azimuth-Doppler-elevation space down results in fewer available

DOF for deterministic processing. Increasing azimuth-Doppler-elevation space size is equivalent to zero padding the original data set, giving higher beamspace resolution, and resulting in more available DOF for deterministic processing at the expense of increased computational load.

A new mathematical framework is not necessary for this development. Following the block diagram in Fig. 6.5, the first step fills the azimuth-Doppler-elevation space and uses an repetitive 3D-JDL operation. The mathematical framework for 3D-JDL is provided in Section 5.3.

The next step is an inverse three-dimensional discrete Fourier transform. The multidimensional discrete Fourier transform is developed and presented in [23]. The block diagram uses the notation $3D \mathcal{F}^{-1}$ to denote this transform. This operation results in space-time data, identical in form to the original space-time data set. The only difference between the two is the suppression of correlated interference.

The final operation is implementation of a deterministic approach for suppressing discrete interference. The method of Section 6.1 is used. A standard space-time steering vector is used in this final stage, with no provisions implemented for possible warping in the two previous stages.

6.2.1 Design Parameters. The inverse hybrid concept involves several design considerations, each involving a tradeoff between performance and computational load. Perhaps the most critical design criteria is the size of the azimuth-Doppler-elevation space. For this work, dimensionality was set to $N \times M \times P$. However, distinct advantages and disadvantages arise by making this space either larger or smaller.

Using smaller dimensionality results in tremendous computational load savings since fewer 3D-JDL iterations are required. The penalty is beamspace resolution loss and fewer DOF available for deterministic processing in the final adaptivity stage. The resolution loss could be alleviated to a certain extent through zero padding the

inverse discrete Fourier transform, although the impact of zero padding on the final adaptivity stage has not been explored.

Conversely, using larger dimensionality makes significantly more DOF available for the final stage. However, populating the beamspace becomes computationally prohibitive for real-time operation. Increased dimensionality results in exponential increases in computational load.

Perhaps the most important consideration involves *actual locations* of the azimuth-Doppler-elevation bins used to populate the beamspace. Intuitively, the desired signal location (the location under test) should become one of the bins. However, this choice places an additional constraint on beamspace dimensionality. If the desired signal location does not lie on a standard sampling interval of the $N \times M \times P$ space, the space must be increased until one of the points coincides with the desired signal location. This stipulation occurs because the discrete Fourier transform is based on uniform sampling. Unfortunately, this can lead to larger dimensionality and larger computational load.

Rather than attempt to balance all these tradeoffs, this work offers a proof-of-concept technique using a single azimuth-Doppler-elevation dimensionality equal to the original data set sizes, i.e, $N \times M \times P$. As shown in the following results, performance with this choice is acceptable.

6.2.2 Inverse 3D Hybrid Results. Results are characterized using the 3D data simulation parameters from previous chapters, allowing side-by-side comparison of the two proposed hybrid methods. A point of importance for this inverse hybrid technique is the choice of beamspace bin locations. As already mentioned, beamspace dimensionality is chosen as $N \times M \times P$, where $N = 8$, $M = 8$, and $P = 8$. Unfortunately, the target does *not* fall in directly into one of the bins. Consider the azimuth dimension, for example. The uniform sampling requirements forces the azimuth bins to occur at -90° , -67.5° , -45° , -22.5° , 0° , 22.5° , 45° , and

67.5° (90° aliases to -90). As before, the target is placed at $\phi_t = 25^\circ$ which results in a slight mismatch with the uniform sampling locations. Now consider the elevation dimension. Since the number of elevation channels is also eight, the elevation bins occur at the same intervals as the azimuth bins. Consistent with previous chapters, the target is located at $\theta_t = 10^\circ$ which results in a minimum mismatch of 10° with the uniform sampling locations. The normalized Doppler uniform sampling results in a bin exactly at the target normalized Doppler of 0.25, although this fact is of little consequence since there is a mismatch in the other two dimensions. The effects of mismatch between target and beamspace uniform sampling grids are not addressed here. Rather, the intent is to highlight the proposed technique's design considerations and illustrate nominal capabilities.

Figure 6.6 is a plot of the normalized output test statistic versus range cell for *homogeneous* data. The 3D-JDL performance (used here for reference) was introduced in Figs. 6.2 through 6.4. Fig. 6.6 illustrates the 3D inverse hybrid concept offers acceptable homogeneous data performance with 18.7 dB RPSL, although not quite as good as the 3D original hybrid extension (30 dB RPSL).

As before, the real benefit of hybrid methods is revealed by analyzing Fig. 6.7. Again, the methods should *not* offer any significant response at range cell 80, the interferer location. Previously, the 3D hybrid extension resulted in an RPSL of -5 dB, well below surrounding ground clutter returns. The proposed 3D inverse hybrid method offers comparable results with -4.8 dB RPSL. Clearly, both 3D hybrid approaches offer superb false alarm characteristics when operating in heterogeneous data.

Once again, results of the proposed 3D inverse hybrid technique's appear excellent. However, *some important limitations have been buried as a result of the scenario*. Using the same deterministic adaptivity approach has introduced the same performance penalty resulting from the differencing operation used to co-phase the returns and avoid signal cancellation. As discussed in Section 6.1, the differencing

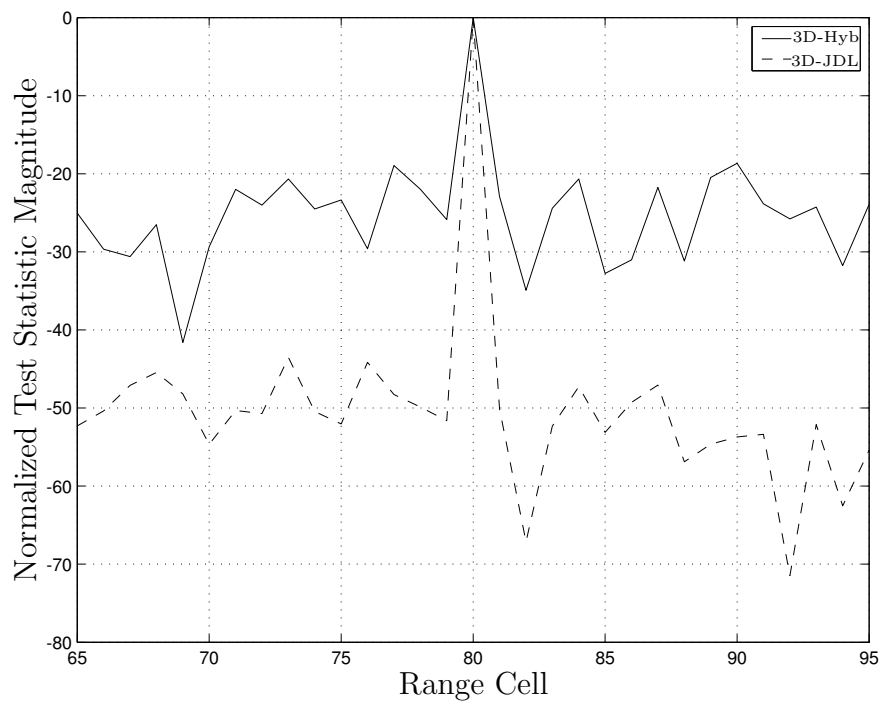


Figure 6.6: Results for the 3D inverse hybrid concept in *homogeneous* data.

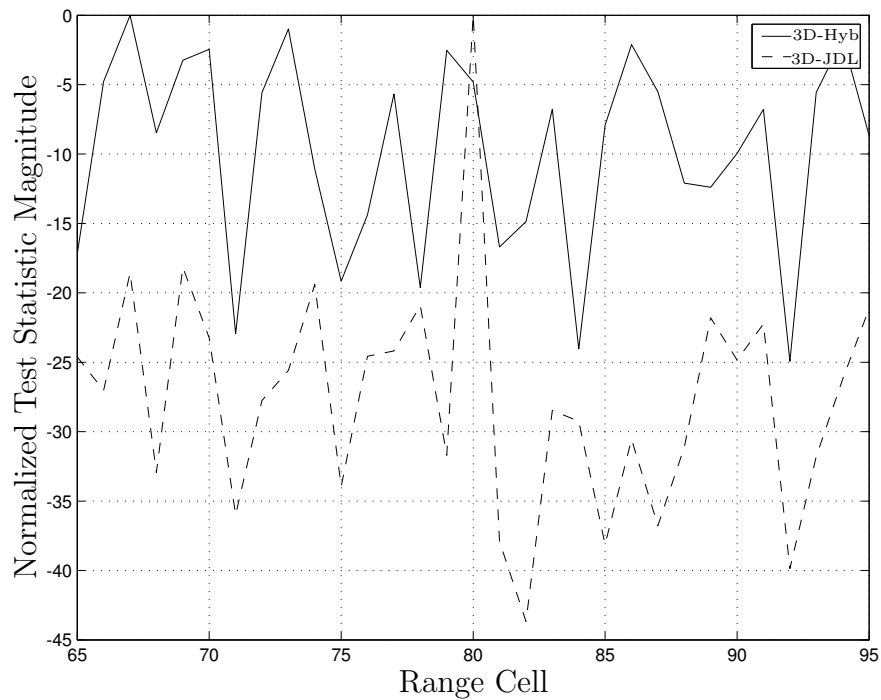


Figure 6.7: Results for the 3D inverse hybrid concept in *heterogeneous* data.

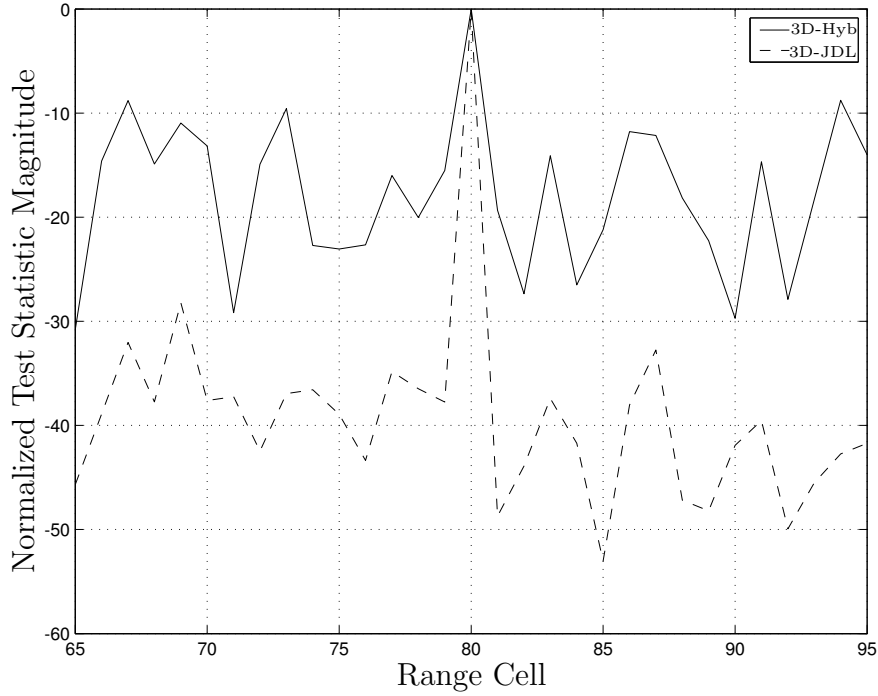


Figure 6.8: Results for the 3D inverse hybrid concept in *heterogeneous* data. Look direction is now at 45° azimuth instead of 65° .

operation equates to a two-element beamforming operation which effectively creates a virtual null in the desired signal direction. Unfortunately, a two-element beamformer produces a very wide null that not only removes the desired signal during interference estimation, but also removes a significant portion of the interference. Therefore, *as the look direction converges on the interferer location, the 3D inverse hybrid method becomes incapable of suppressing the interferer(s).*

Figure 6.8 reinforces this concept and shows the inverse 3D hybrid method applied to the same data set used for the previous two figures. The *only* exception is that the look direction is now at 45° azimuth. Since the target is located at 25° azimuth (look direction matched to target in elevation and normalized Doppler, but not azimuth), the scenario remains heterogeneous. Given the interferer is now 20° away from the look direction, there should be *no* response indicating target presence at range cell 80. Unfortunately, the initial co-phasing operation resulted in

significant interferer suppression and effectively removes it prior to interference estimation within the deterministic processing stage. The proposed 3D inverse hybrid method only produces an 8.77 dB RPSL (3D original hybrid extension produced a 6.56 dB RPSL) response at the discrete interferer range cell, falsely indicating target presence.

6.3 Known Interferer Location

The primary goal of hybrid methods is discrete interferer suppression. The previous 3D methods have shown varying degrees of success in achieving this goal. The 3D extension of the original hybrid offered acceptable performance, as long as the interferer location was sufficiently separated from the radar look direction. This condition alleviates inadvertent nulling of the interferer as a result of the co-phasing operation during interference estimation. Unfortunately, the inverse 3D hybrid formulation suffered a similar drawback.

In light of the goal, a proof-of-concept approach is introduced to shed some light on method viability. In particular, the case is considered where interferer location (azimuth, elevation, Doppler, and range) is perfectly known *a priori*. This evaluation provides performance characteristics that could be considered optimum. Furthermore, the evaluation serves as a foundation for a new 3D technique exhibiting excellent detection *and* interferer rejection characteristics. The proposed method cannot be characterized as a hybrid since it does not meld deterministic and statistical methods into a single framework. However, the proposed method *does* satisfy the goal of hybrid techniques. As such, its development is included within this chapter for appropriate comparison to the other techniques.

Given known interferer location, constructing a filter to suppress the discrete interferer is relatively simple. For example, consider elevation (\mathbf{e}_i), azimuth (\mathbf{a}_i), and Doppler (\mathbf{b}_i) steering vectors describing the known interferer's location. A filter,

based loosely on Wiener filtering concepts, can be constructed from

$$\mathbf{C} = (\mathbf{e}_i \otimes \mathbf{b}_i \otimes \mathbf{a}_i) (\mathbf{e}_i \otimes \mathbf{b}_i \otimes \mathbf{a}_i)^H \quad (6.35)$$

$$\mathbf{W} = (\mathbf{C} + \sigma^2 \mathbf{I}_{MNP})^{-1} \mathbf{T}, \quad (6.36)$$

where \mathbf{C} is an artificial covariance matrix analogous to the one used in Chapter IV, σ^2 corresponds to the noise power and \mathbf{T} is a set of space-time steering vectors corresponding to the LPC. The matrix \mathbf{T} is analogous to the LPC adaptive transformation previously described in Eqn. (6.29) where the individual components are replaced by steering vectors.

Using the transformation of Eqn. (5.33) to get to the azimuth-Doppler-elevation domain results in an LPC identical to the one used in 3D-JDL. Within this LPC, statistical adaptivity is implemented in a manner identical to 3D-JDL. Therefore, performance within homogeneous data should approach or equal 3D-JDL, a method shown to offer excellent detection probability in homogeneous data. However, the proposed technique should also result in excellent rejection of discrete interferers since a null is specifically formed in their direction.

6.3.1 “Optimum” Results. This section offers an evaluation of the proposed technique using known interferer location. The scenario is identical to the previous sections, allowing side-by-side comparison of different approaches.

Figure 6.9 is a plot for the proposed method using known interferer location and homogeneous data. As expected, performance mirrors 3D-JDL and indicates excellent detection probability with an RPSL of 43.52 dB. However, performance within heterogeneous data is of primary interest. Fig. 6.10 illustrates heterogeneous data results that are comparable with Figs. 6.3 and 6.7. Although the previous methods offered *acceptable* performance with this heterogeneous scenario, the proposed known interferer location method clearly offers improved interferer rejection with -14.08 dB RPSL at the interferer location. Previously, the 3D original hy-

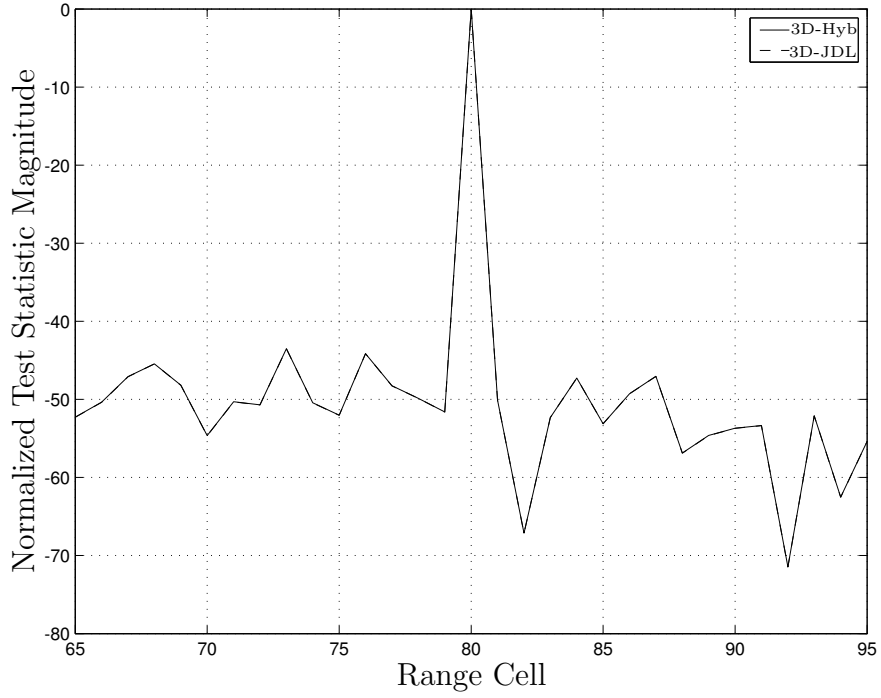


Figure 6.9: Results for proposed 3D technique assuming known interferer location, *homogeneous* data. Results are identical for the two methods.

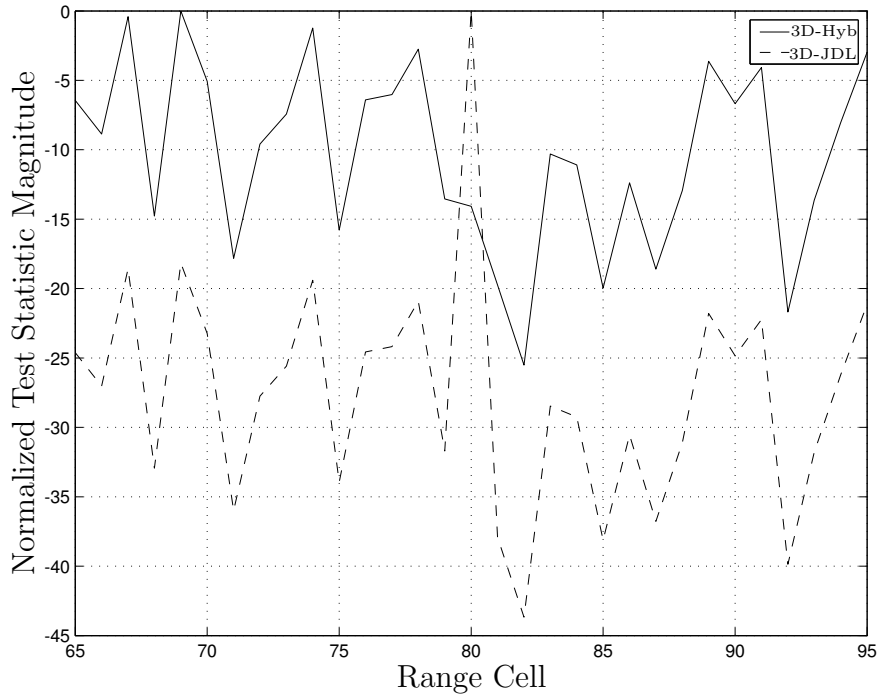


Figure 6.10: Results for proposed 3D technique assuming known interferer location, *heterogeneous* data.

brid extension illustrated -4.56 dB RPSL while the inverse hybrid method exhibited -4.81 dB.

In previous 2D and 3D hybrid approaches, the primary limitation was the beamforming null placed in the look direction used in the differencing operation. This null was necessary to remove desired signal responses from the interference estimate. As shown in Figs. 6.4 and 6.8, both techniques were unable to suppress interferers as the look direction approached the interferer location. This result is expected to a certain extent since an interferer present *at* the look direction is, by definition, a target. However, the previous figures illustrated significant output response when the look direction was 20° *removed in azimuth* from the interferer. Obviously, any output response should be considered a false alarm. Ideally, any difference between look direction and target location should result in no output response. However, real-world antenna sidelobe levels preclude performance approaching this ideal limit.

! A rather obscure but important point is that performance would *not* improve with an increase in the number of elements. The co-phasing operation involves differencing adjacent elements, essentially a two-element beam-former. The operation remains the same regardless of the total number of elements or pulses used.

Figure 6.11 contains a plot of the proposed method's output response with the interferer removed 20° (in azimuth) from the look direction. The RPSL at the interferer location is measured at -16.15 dB. Clearly, the method is unaffected by the discrete interferer being within close proximity to the radar look direction ("close" as measured by the degradation of the previous hybrid techniques). Results are drastically improved over both the 3D original hybrid extension and the inverse hybrid method.

The final figure solidifies the claims made for this technique. The previous results for each proposed technique (3D extension to the original 2D hybrid, the 3D inverse hybrid concept, and the known interferer location method of this section) illustrated inherent weaknesses in the first two proposed methods. As such, a single

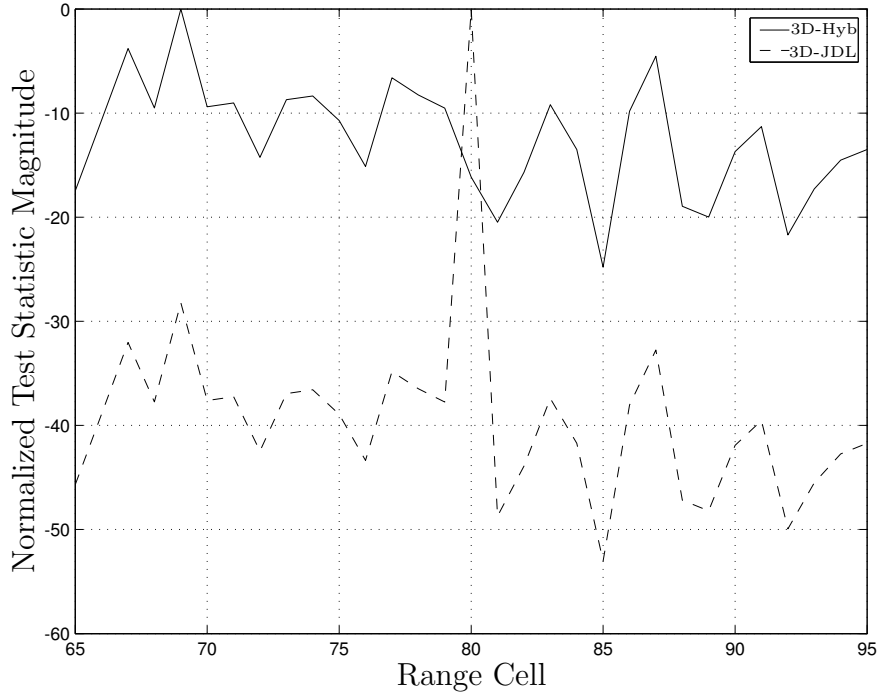


Figure 6.11: Results for proposed 3D technique assuming known interferer location, *heterogeneous* data. Look direction is now at 45° azimuth instead of 65° .

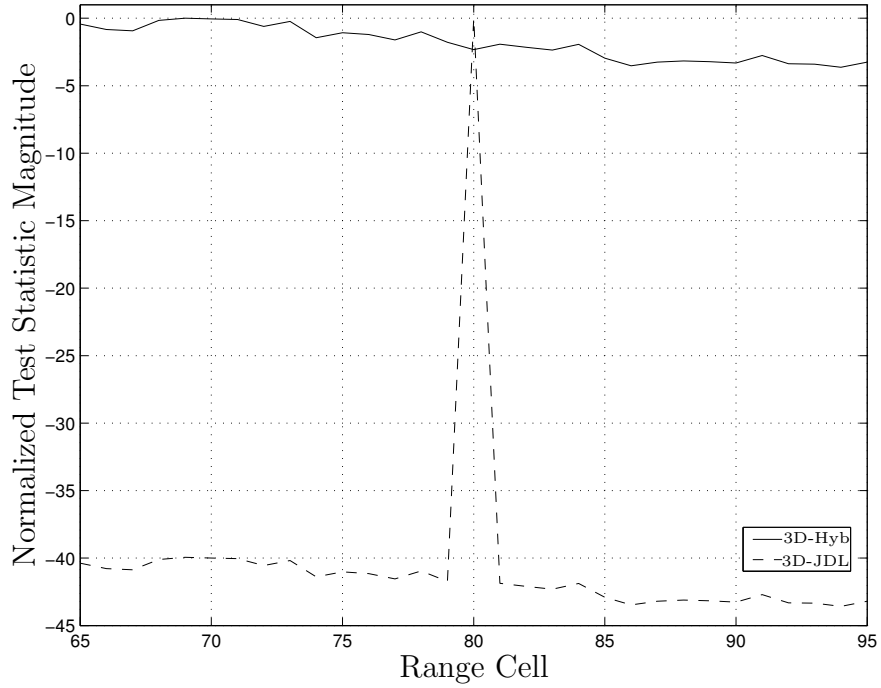


Figure 6.12: Results for proposed 3D technique assuming known interferer location, *heterogeneous* data. Look direction is now at 45° azimuth instead of 65° and curves are an average of 500 realizations.

realization offered sufficient evidence of these weaknesses. However, the claims made for the known interferer location method require more support. Figure 6.12 offers this support by presenting results averaged over 500 realizations. The scenario is identical to that of Figs. 6.11, 6.8, and 6.4 with the look direction 20° away from the discrete interferer in azimuth. Clearly, the curves illustrate the proposed known interferer location approach completely mitigates the discrete interferer effects.

Examination of the RPSL metric averaged over the 500 realizations indicates -9.71 dB with a standard deviation of 5.58 dB for the proposed known interferer location method. For comparison, the 3D-JDL approach offered an average RPSL of 32.56 dB with a standard deviation of 1.93 dB.

! The *average RPSL metric* does not equate to the *RPSL of the average* curves in Fig. 6.12. As defined in this work, the RPSL is a measure of the response in the target/interferer location relative to the next highest peak. Hence, the “next highest peak” is *not* the same from realization to realization. Therefore, average RPSL is more indicative of actual performance.

6.4 Summary

The 3D research progression of Fig. 1.2 is now completed. This chapter filled the final square by extending the current state-of-the-art in 2D hybrid techniques into three dimensions and also offered several new variants.

The 3D original hybrid extension exhibited distinct performance advantages in heterogeneous clutter. The formulation mirrored 2D results with a modest penalty incurred when operating in homogeneous data, as compared to 3D-JDL. However, a design characteristic of the method precludes acceptable performance when discrete interferers encroach upon the radar look direction. The wide null generated in the two-element co-phasing operation, as part of the deterministic adaptivity stage, effectively suppresses “close” interferers in the interference estimate. This co-phasing operation is designed to eliminate inadvertent target signal cancellation. The effec-

tive removal/suppression of interferers during interference estimation is simply an undesired byproduct.

The second proposed hybrid technique is the inverse hybrid. This method attempts to alleviate a perceived drawback in the original hybrid formulation. As discussed, deterministic techniques offer inferior correlated interference suppression when compared to statistical interference suppression methods. Therefore, discrete interferer suppression would likely be improved if the correlated interference were suppressed first. This order is the exact opposite of how the original 2D hybrid technique, and the 3D extension thereof, is constructed. The inverse 3D hybrid method first applies repetitive statistical adaptivity, thereby populating the beamspace. At this point, equivalent space-time data is recovered using an inverse three-dimensional discrete Fourier transform. Deterministic techniques are then used to suppress discrete interference sources.

Inverse hybrid results indicate performance comparable to the 3D original hybrid extension. Since the same deterministic techniques were used, the same performance penalty is incurred as a byproduct of the co-phasing operation. Hence, the perceived gains due to reversing the adaptivity order are not fully realized.

A proposed solution involves departing from the current hybrid mindset and returning to the fundamental goal of these techniques. Each method is designed to 1) offer maximum detection probability when operating within heterogeneous data environments while 2) also retaining acceptable detection probability within homogeneous environments. As Section 6.3 illustrated, the goal is realizable based on known interferer location. Given known location, there is no need for a technique melding deterministic and statistical techniques. Hence, the proposed method is not a hybrid in a strict sense. The known interferer location method is presented in this chapter since it meets the goal of hybrid techniques. Results presented within this section showed excellent performance within *both* heterogeneous and homogeneous environ-

ments. In particular, *no performance degradation occurred within homogeneous data sets.*

VII. Conclusions

The primary objective of this research effort involved the advancement of adaptive interference suppression techniques for airborne radar. The problem addressed is one of detecting targets within severe interference environments characterized by high levels of ground clutter, noise jammer infiltration, and other strong sources not of interest (termed discrete interferers). Aircraft motion further complicates the detection problem due to induced velocity and dynamic ground clutter returns, causing them to occupy a wide range of Doppler frequencies.

The work began with an examination of the current state-of-the-art in 2D techniques. Duplicated here in Fig. 7.1, Fig. 1.2 contains a block diagram representing the 2D research progression. Each facet of *more than 30 years* of research in 2D STAP is represented. This research represents a parallel to the 2D development which provided the focus for this work.

Each major research area in 2D STAP has been duplicated within a 3D framework. The overall 3D research progression is encapsulated by the righthand side of Fig. 7.1, where each major research area is detailed in a previous chapter. The 3D framework incorporates radar returns on an azimuth channel, pulse, and *elevation channel* basis. As shown previously and summarized below, significant performance gains are realized as a direct result of incorporating elevation adaptivity. Figure 7.2 graphically illustrates the links between 3D research contributions and corresponding publications resulting from each.

7.1 3D Data Model

The first step in paralleling the 2D research involved construction of an appropriate 3D data model. Based on previous 2D work, the proposed 3D model presented in Chapter III offers several extensions.

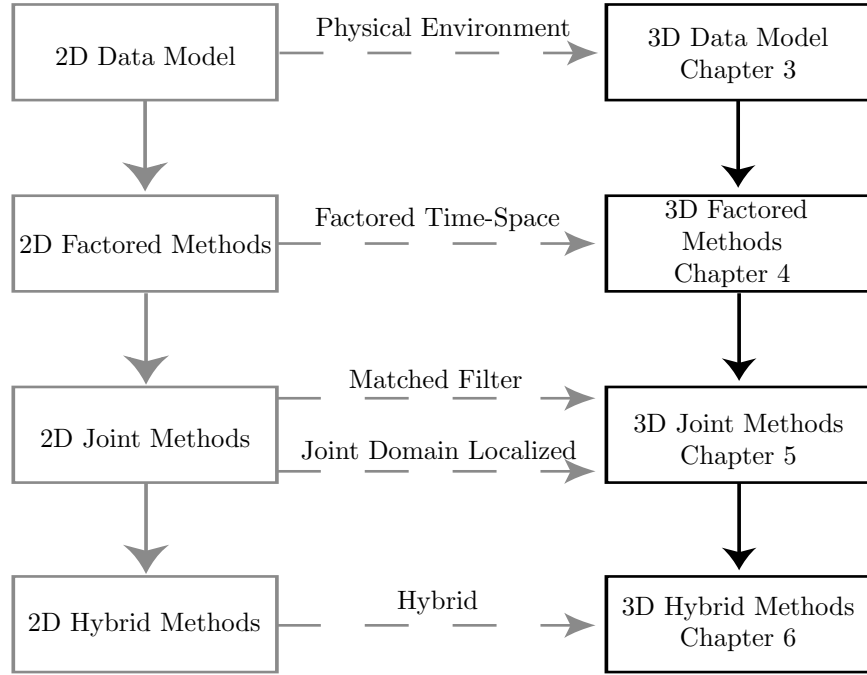


Figure 7.1: Three-dimensional research progression parallels historical two-dimensional work. Contributions have been made to each area in the three-dimensional research chain.

First, returns from elevation channels have been incorporated into the vector framework. Extension to a 2D planar array forced the use of array element patterns as a function of azimuth and elevation, now explicitly included in the model. Elevation functionality within the individual element patterns represents an important factor when attempting to compare with actual measured data.

Each facet of the airborne radar problem is addressed in detail. A coordinate system common to airborne radar platforms serves to describe returns from the entire sphere surrounding the radar. Using this coordinate system, the transmit signal is examined within a mathematical framework suitable for subsequent analysis. This mathematical foundation allows characterization of the return signal on a per pulse, per element basis. Working at the per pulse, per element level, a vectorized format was developed allowing statistical characterization of clutter, jamming, and thermal noise components present in actual airborne radar scenarios.

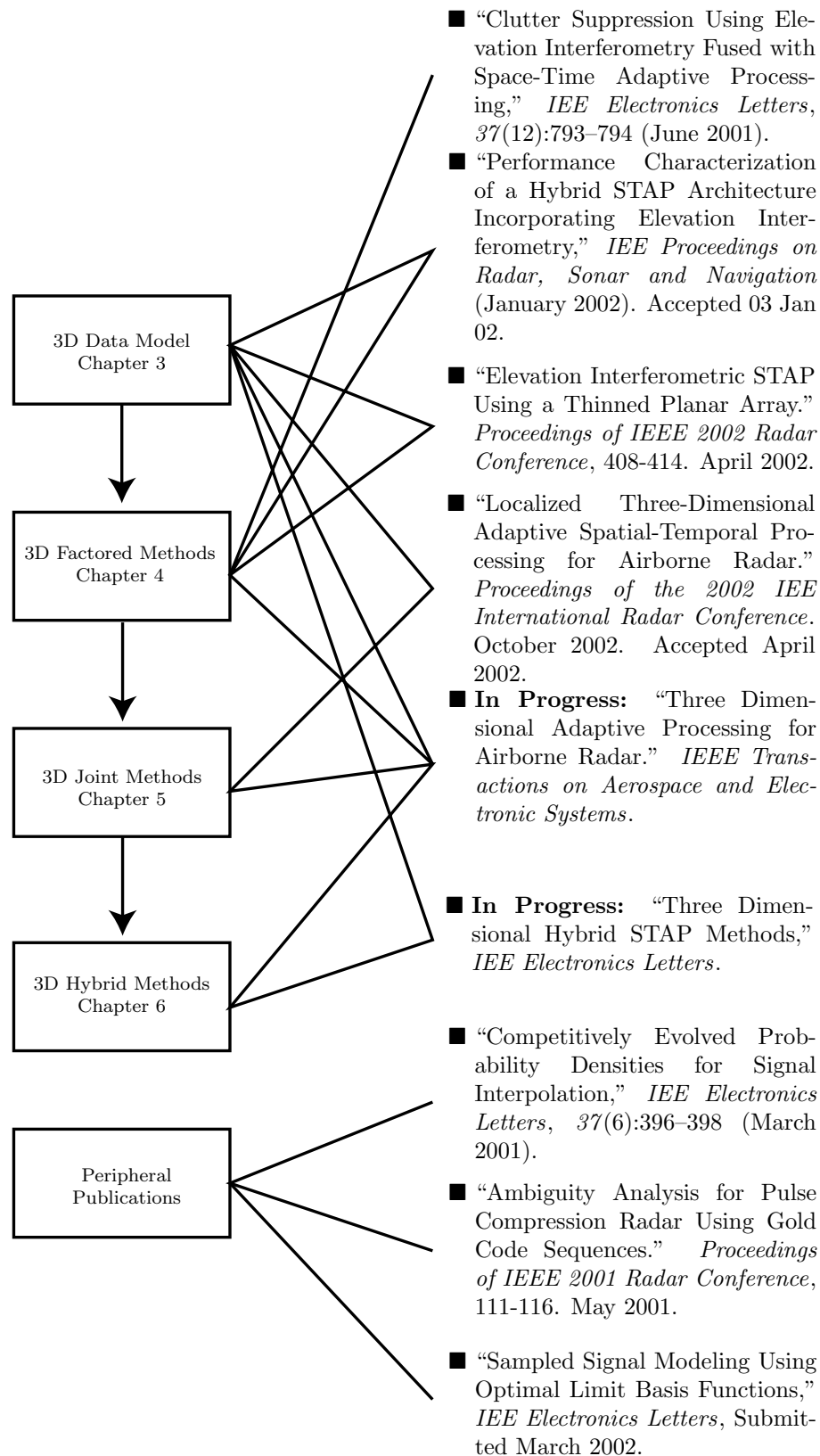


Figure 7.2: Research contributions linked to publications. Contributions have been made in each area of the three-dimensional development chain.

A fairly important aspect of the 3D data model involves range ambiguous returns. Although the original 2D model has range ambiguous return capability, *all reported results based on the model, including the original work [65], do not account for nor include range ambiguous clutter effects.* This work not only provides for these returns within the 3D model, but also presents results for cases including range ambiguous clutter. Range ambiguous clutter has a significant impact for medium and high-PRF radars as shown throughout this work. Elevation adaptivity serves to alleviate the associated performance loss.

From the 3D data model framework, expressions for the space-time steering vector, covariance matrix, and related processing elements were developed. These individual components serve as the building blocks for the subsequent 3D adaptive methods. The 3D model is purposely constructed in a manner providing generality. An in-depth discussion of the original 2D model was not provided since the 3D model effectively collapses to the 2D case.

7.2 3D Factored Approaches

The first step in developing adaptive methods for the 3D case, and the second step of 3D research identified in Fig. 7.1, involved factored approaches. A factored approach implements adaptivity in successive stages, where each stage addresses a single dimension, e.g., azimuth, normalized Doppler, or elevation.

Intuitively, beginning with factored methods made sense because of their inherent simplistic design. Chapter IV developed a series of 3D factored methods that not only illustrate the inherent advantages of 3D processing, but also served to reinforce the validity of the 3D data model provided in Chapter III.

The first factored approach involved a simplistic implementation of 3D Factored Time-Space (3D-FTS). Ground clutter is suppressed by first implementing a simple two-element beamformer. This beamforming is adaptive on a range cell ba-

sis only with clutter null placement based on the *calculated* ground clutter location according to aircraft attitude and a spherical Earth model.

The simplistic 3D-FTS approach served two primary purposes: model and concept validation. Constraining the technique to two elevation channels allowed validation with collected Multi-Channel Airborne Radar Measurement (MCARM) data. The MCARM program involved collection of actual airborne radar measurements for the purpose of adaptive radar processing research. Introduction of this rudimentary 3D-FTS approach illustrated the drastic performance gains incurred as a result of incorporating elevation adaptivity. In particular, greater than 15 dB improvement in Relative Peak Sidelobe Level (RPSL) (comparable to output Signal-to-Interference plus Noise Ratio (SINR)), relative to 2D-FTS, was demonstrated using the MCARM data. Furthermore, *only* two vertical data channels are available from the MCARM radar array. Subsequent analysis using an increased number of vertical channels showed better results, in particular approximately 30 dB *reduction* in SINR was shown for constant detection probability (P_d) (compared to 2D-FTS). The 3D-FTS performance comparisons using simulated data produced results *identical* to the MCARM tests and effectively validated the 3D data model.

The next research step involved necessary extensions to make 3D-FTS more robust. Several limitations of the simplistic approach were addressed. The two elevation channel constraint was removed (originally enforced to allow comparison with available MCARM data). Also, several approaches to ground clutter null placement were examined and evaluated. In particular, a technique capable of suppressing range ambiguous clutter returns was introduced. As shown in Chapter IV, 3D performance greatly improved over equivalent 2D counterparts. For the array and coherent processing interval sizes considered, RPSL performance improvements on the order of 23 dB were demonstrated.

The excellent 3D-FTS performance results prompted array thinning analysis. The introduction of elevation adaptivity in conjunction with the factored Doppler

and azimuth approaches, 3D-FTS in its entirety, suggested there might be minimal performance degradation as the array is thinned. The array thinning analysis served two primary purposes. First, array element failure can result in inadvertent thinning. The performance degradation associated with element failure is an important topic in radar design. Second, reducing the total number of elements reduces the total cost of fabrication. Therefore, antenna cost can be reduced with no significant performance penalty. As the array thinning analysis in Section 4.3 shows, significant reductions in the total number of elements can be realized with minimal performance degradation. Approximately 70% of the elements were selectively removed and SINR performance only degraded by 3 dB. This result is a direct consequence of the 3D extension. Placing nulls in azimuth, Doppler, *and* elevation enables the radar to more effectively separate targets from interference using a reduced number of Degrees Of Freedom (DOF).

The final factored approach considered was Elev-JDL. The robust performance of 2D-JDL prompted an exploration into a factored 3D implementation. This factored approach served as a precursor to the joint approaches subsequently presented in Chapter V. As expected, detection probability and output SINR for the Elev-JDL technique edged out 3D-FTS performance due to the robust nature of the joint domain localized processing stage.

7.3 3D Joint Approaches

By definition, factored approaches are suboptimal. Suboptimal performance stems directly from the sequential (versus combined) nature of the factored approach; effective null placement is achieved for particular locations in azimuth, Doppler, *or* elevation, but not for particular locations in azimuth, Doppler, *and* elevation. Achieving/approaching optimal performance requires extension to joint domain techniques, i.e., techniques operating jointly within the azimuth-Doppler-elevation space versus individual spaces.

The previous factored approaches greatly improve clutter suppression performance. Conversely, the next research topic focused on joint domain techniques. First, the 3D Matched Filter (3D-MF) for known interference is derived using three different approaches. As in the 2D case, the three approaches generate identical filters within a scale factor, showing equivalence.

Unfortunately, the interference encountered in actual airborne radar scenarios is unknown *a priori*. This fact forces construction of adaptive methods for estimated covariance. The most obvious approach is the 3D Adaptive Matched Filter (3D-AMF), where an estimated covariance matrix is substituted into the matched filter. This approach generated well established practical limitations consistent with the 2D case, including issues involving computational load, secondary data support sizes, and stationarity. As expected, the extension to 3D further compounds these limitations.

The desire to generate a practical 3D adaptive interference suppression method forced further research. The subject of this research, and subsequently the main goal of Chapter V, involved extension of more robust 2D STAP techniques, i.e., the Joint Domain Localized (2D-JDL) method [64]. This method is a beamspace approach whereby adaptivity is implemented in the azimuth-Doppler domain. Of particular interest is the analytic simplicity of the ideal target model when transformed to the azimuth-Doppler domain. Given ideal conditions, a target is projected into a single azimuth-Doppler bin, inherently allowing adaptivity within a small localized region. Using a small localized adaptivity region offers several benefits. First, fewer DOF are needed, directly resulting in tremendous computational efficiency (when compared to methods such as the 2D-AMF and 3D-AMF). Second, required sample support can be drastically reduced in response to fewer DOF. This reduction in sample support makes 2D-JDL performance less susceptible to adverse heterogeneous clutter effects. For these reasons, a three-dimensional variant of 2D-JDL appeared enticing as the next research step.

Chapter V implements a true 3D Joint Domain Localized (3D-JDL) adaptive processor within the azimuth-Doppler-elevation space. The proposed concepts are validated using results based on simulated *range ambiguous* airborne radar data. The 3D-JDL method demonstrated target detection improvement on the order of 10 dB and 57 dB when compared to standard 2D-JDL and 2D-FTS processing, respectively, for an 8×8 non-uniform rectangular array.

7.4 3D Hybrid Approaches

The final 3D Hybrid work identified in Fig. 7.1 extends the current state-of-the-art in 2D hybrid techniques and offers several new variants. The initial 3D hybrid extension exhibited distinct performance advantages in heterogeneous clutter. The formulation mirrored 2D results with a modest penalty incurred when operating in homogeneous data, as compared to 3D-JDL. However, design characteristics of the initial 3D hybrid extension precluded acceptable performance when discrete interferers encroach the radar look direction. Specifically, the relatively wide null generated in the two-element co-phasing operation, as part of the deterministic adaptivity stage, effectively suppresses “close” interferers *in the interference estimate*. This co-phasing operation is designed to eliminate inadvertent *target signal* cancellation and should *not* remove/suppress interferers within the interference estimate. This undesired byproduct precludes incorporation into the adaptive nulling pattern by not allowing *accurate* interference estimation.

A proposed alternate technique is the inverse 3D hybrid. This method attempts to alleviate a different perceived drawback in the original hybrid formulation. Namely, deterministic techniques offer inferior correlated interference suppression when compared to statistical interference suppression methods. Therefore, discrete interferer suppression would likely be improved if the correlated interference were suppressed first. In this case, the desired suppression order is exactly opposite of the original 2D hybrid and the initial 3D extension. The inverse hybrid method first

applies repetitive statistical adaptivity, thereby populating the beamspace. At this point, equivalent space-time data is recovered using an inverse three-dimensional discrete Fourier transform. Deterministic techniques are then applied to suppress discrete interference sources.

Inverse hybrid results indicate achievable performance is comparable to the initial 3D extension of the original 2D hybrid. Since the same deterministic techniques were used, the same performance penalty was incurred as a byproduct of the co-phasing operation. Hence, the perceived gains due to reversing the adaptivity order were not fully realized.

A potential solution would involve breaking away from the current hybrid mindset and returning to the fundamental goal of these techniques. Each method is designed to 1) offer maximum detection probability when operating within heterogeneous data environments while 2) retaining acceptable detection probability within homogeneous environments. As Section 6.3 illustrates, the goal is realizable based on known interferer location. Given known interference location, there is no need to meld deterministic and statistical techniques and the proposed method is not a hybrid in the strict sense - the method is introduced for completeness since it meets the goal of hybrid techniques. Results presented show excellent performance within *both* heterogeneous and homogeneous environments. In heterogeneous data environments, the proposed method was impervious to the discrete interferer with an RPSL of -16.15 dB (positive response indicates *false* target indication) compared to 8.77 dB for the proposed inverse 3D hybrid and 6.56 dB for the 3D extension to the original 2D hybrid. Furthermore, *no performance degradation occurred within homogeneous data sets*; the proposed inverse 3D hybrid and 3D extension suffered 25 dB and 13.5 dB degradation (compared to 3D-JDL), respectively. Identifying accurate interferer location remains a topic for future research.

7.5 *Future Work*

The comparison drawn between 2D and 3D approaches, as presented in this document, constrains the number of azimuth channels N and the number of pulses M . This constraint puts the two methods on an equal footing in terms of azimuth and Doppler resolution. The 3D approach gains the added elevation processing advantage. Reported results give an improvement due to the extension to 3D, bounded to be no *less* than $10 \log_{10} P$ (the ideal white noise limited case). A portion of any improvement could be attributed to the increase in total DOF, depending on the interference scenario. In light of this argument, future work could constrain the total DOF and offer a new analysis.

Appendix A. Kronecker Product

The Kronecker Product is simple in concept. Given two matrices \mathbf{A} and \mathbf{B} , the Kronecker Product is defined in the following manner [28],

$$\mathbf{A} \otimes \mathbf{B} \equiv \begin{bmatrix} A_{11}\mathbf{B} & A_{12}\mathbf{B} & A_{13}\mathbf{B} & \cdots & A_{1M}\mathbf{B} \\ A_{21}\mathbf{B} & A_{22}\mathbf{B} & A_{23}\mathbf{B} & \cdots & A_{2M}\mathbf{B} \\ \vdots & \vdots & \vdots & \vdots & \vdots \\ A_{N1}\mathbf{B} & A_{N2}\mathbf{B} & A_{N3}\mathbf{B} & \cdots & A_{NM}\mathbf{B} \end{bmatrix}. \quad (\text{A.1})$$

Therefore, given an $N \times M$ matrix \mathbf{A} and $P \times Q$ matrix \mathbf{B} results in an $NP \times MQ$ matrix. The following table of identities holds for Kronecker products.

Table A.1: Properties of Kronecker Products

1. $(\mathbf{A} + \mathbf{B}) \otimes \mathbf{C} = \mathbf{A} \otimes \mathbf{C} + \mathbf{B} \otimes \mathbf{C}$
2. $(\mathbf{A} \otimes \mathbf{B}) \otimes \mathbf{C} = \mathbf{A} \otimes (\mathbf{B} \otimes \mathbf{C})$
3. $\alpha(\mathbf{A} \otimes \mathbf{B}) = (\alpha\mathbf{A}) \otimes \mathbf{B} = \mathbf{A} \otimes (\alpha\mathbf{B})$
4. $(\mathbf{A} \otimes \mathbf{B})^H = \mathbf{A}^H \otimes \mathbf{B}^H$
5. $(\mathbf{A} \otimes \mathbf{B})^{-1} = \mathbf{A}^{-1} \otimes \mathbf{B}^{-1}$
6. $(\mathbf{A} \otimes \mathbf{B})(\mathbf{C} \otimes \mathbf{D}) = (\mathbf{AC}) \otimes (\mathbf{B} \otimes \mathbf{D})$
7. $(\mathbf{A} \otimes \mathbf{B}) = (\mathbf{A} \otimes \mathbf{I})(\mathbf{I} \otimes \mathbf{B})$

Corollary A.1. *The outer product of three Kronecker vector terms is given by*

$$(\mathbf{a} \otimes \mathbf{b} \otimes \mathbf{c})(\mathbf{a} \otimes \mathbf{b} \otimes \mathbf{c})^H = \mathbf{a}\mathbf{a}^H \otimes \mathbf{b}\mathbf{b}^H \otimes \mathbf{c}\mathbf{c}^H. \quad (\text{A.2})$$

Proof. The proof of the above corollary is simple using property 6 of the Kronecker product. Let $\mathbf{y} = \mathbf{b} \otimes \mathbf{c}$. Performing this substitution and using property 4 results in

$$(\mathbf{a} \otimes \mathbf{y})(\mathbf{a}^H \otimes \mathbf{y}^H), \quad (\text{A.3})$$

and after direct application of property 6 the result is

$$\mathbf{a}\mathbf{a}^H \otimes (\mathbf{y} \otimes \mathbf{y}^H). \quad (\text{A.4})$$

Substituting back in for \mathbf{y} and applying property 6 again achieves the desired result,

$$\mathbf{a}\mathbf{a}^H \otimes [(\mathbf{b} \otimes \mathbf{c})(\mathbf{b} \otimes \mathbf{c})^H] = \mathbf{a}\mathbf{a}^H \otimes (\mathbf{b}\mathbf{b}^H \otimes \mathbf{c} \otimes \mathbf{c}^H) \quad (\text{A.5})$$

$$= \mathbf{a}\mathbf{a}^H \otimes \mathbf{b}\mathbf{b}^H \otimes \mathbf{c}\mathbf{c}^H. \quad (\text{A.6})$$

The final simplification merely takes advantage of the column vector format used throughout this report. \square

Appendix B. Angular Scales

Many of the plots for radar work involve either an elevation or azimuth angular scale. Although this scaling is not difficult to generate, there are some subtle nuances that come about from its derivation. As always, the result of a Fourier transform is a normalized scale that we must convert to angle, normalized Doppler, or whatever coordinates are appropriate for the problem at hand. This appendix describes the formulation of the angle scale used throughout this work.

First, consider the Discrete Fourier Transform (DFT) given by

$$W[k] = \sum_{p=0}^{P-1} w[p] e^{-j2\pi \frac{kp}{P}}. \quad (\text{B.1})$$

In an ideal space/spatial analogy, this transform converts the spatial domain signal $w(p)$ to an angular domain signal $W(k)$ based on ideal phase delays contained in the term $e^{-j2\pi \frac{kp}{P}}$. The integer index k corresponds to a normalized spacing in the angle domain, where each k is a single angle. As a quick test of the concept, consider a signal boresight to the array or 0° . This angle corresponds to an angular integer index of $k = 0$. Substituting for k in the DFT expression, the baseband or zero angle component within the angle domain is simply the summation of all the spatial components. This result is exactly as expected since the phase front of the impinging wave on the array is perfectly aligned with the array for 0° .

Now extend the concept to incorporate the parameters within the radar and processing models. When aligning the element returns in phase to correspond to a particular angle, use a spatial steering vector (in either azimuth or elevation). However, a spatial steering vector aligns the returns for a single angle. Given this observation, a single steering vector essentially amounts to a column of the DFT matrix or single instance of the index integer k . Now apply the elevation steering vector of Eqn. (3.40) to an incoming data vector \mathbf{x} containing complex samples from

the P elements of an ideal vertical linear array to get $\mathbf{e}^H \mathbf{x}$. From simple matrix theory, this inner product can be also be represented as

$$X[k] = \sum_{p=0}^{P-1} \mathbf{e}^*[p]x[p]. \quad (\text{B.2})$$

The index integer k is introduced at this point to begin the analogy between the steering vector and DFT. The next few steps derive exactly what k corresponds to and eventually show the angular scale. Substitute for the steering vector components to get

$$X[k] = \sum_{p=0}^{P-1} x[p]e^{-j2\pi p \frac{d_z}{\lambda_o} \sin \theta_k}, \quad (\text{B.3})$$

where the k subscript on the elevation angle θ highlights the dependence. The transformation looks suspiciously like a DFT! Rearrange to make it look exactly like a DFT,

$$X[k] = \sum_{p=0}^{P-1} x[p]e^{-j2\pi \frac{p}{P} \left(\frac{Pd_z}{\lambda_o} \sin \theta_k \right)}. \quad (\text{B.4})$$

Now, simply equate the parenthetic term with k to get the transformation from the index space to the angle scale

$$k = \frac{Pd_z}{\lambda_o} \sin \theta_k. \quad (\text{B.5})$$

Unfortunately, the development is not quite where it needs to be just yet. Remember, k is an integer index scale. The idea is to convert the *normalized* angular frequency scale to pure radar elevation angle. The DFT scale extends from 0 to 2π and when normalized by π it extends $0, \dots, 2$. Since k extends $0, \dots, P-1$, k can

be converted to the normalized scale¹ by multiplying by $\frac{2}{P}$,

$$\frac{2}{P}k = \frac{2d_z}{\lambda_o} \sin \theta_k. \quad (\text{B.6})$$

The quantity $\frac{2}{P}k$ is simply a normalized axis scale from $0, \dots, 2$. After an FFT shift, it is equivalent to $\text{linspace}(-1, 1 - 1/P, P)$. Hence, the axis scale becomes

$$\boxed{\boldsymbol{\theta} = \sin^{-1} \left[\frac{\lambda_o}{2d_z} \text{linspace}(-1, 1 - 1/P, P) \right]}. \quad (\text{B.7})$$

The scale for azimuth and normalized Doppler is found using the same method.

B.1 Grating Lobes, Over Sampling, and Under Sampling

One of the most important points embedded within Eqn. (B.7) is a subtlety regarding under and over sampling. Common knowledge states inter-element spacing in the spatial domain should correspond to the half the wavelength. Substituting this knowledge into the expression shows the expression collapses to

$$\boldsymbol{\theta} = \sin^{-1} [\text{linspace}(-1, 1 - 1/P, P)]. \quad (\text{B.8})$$

This case corresponds to ideal sampling; the signal is neither over or under sampled spatially. As expected, the angular extent of the waveform is from $\pm 90^\circ$.

Now consider the case where the signal is over sampled. This case is commonly considered a “good thing”. The mindset is always that more is better. Yet, this is not always true. Use one quarter wavelength spacing and substitute into the expression,

$$\boldsymbol{\theta} = \sin^{-1} [2 \text{linspace}(-1, 1 - 1/P, P)]. \quad (\text{B.9})$$

¹Zero padding is rarely done in adaptive processing techniques. The change would only be minor in that P would be replaced by the zero padded length of the steering vector/incoming data vector.

The argument of the inverse sin expression now extends beyond ± 1 and the result is complex for the values beyond ± 1 . Only the real valued portions of the expression above are realized in the physical array. The expression is only valid from $\pm 90^\circ$ and the result of over sampling is spreading the antenna pattern in angle. The main beam is enlarged and perhaps even cut off if it is steered into the complex region.

The best explanation of this phenomenon is in view of sin-theta space as discussed in [60]. Consider Fig. B.1, where the main beam and grating lobes for the MCARM array are shown in sin-theta space. The MCARM array, oriented in the x - z plane, is under sampled in elevation (z -axis) and slightly over sampled in azimuth (x -axis). The circle corresponds to the physically realized portions of the array pattern, i.e., the real valued region. Outside the circle lies the complex valued region where grating lobes exist but are not physically realized.

The black dots in the figure correspond to a main beam steered to 0° in both elevation and azimuth. The center dot is the mainbeam, while all the other dots are grating lobes and occur at multiples of $\frac{\lambda_o}{d_x}$ along the x -axis and multiples of $\frac{\lambda_o}{d_z}$ along the z -axis. For the ideally spatially sampled array, the black dots should all be located at multiples of 2 since the interelement spacing would be half the wavelength. If this were the case, the figure shows that no matter where the mainbeam is steered within the circle, no grating lobes can exist (enter the circle), with the exception of the endfire condition when there is actually a main beam at $\pm 90^\circ$.

Given the MCARM array, we see grating lobes can exist. For example, the array is under sampled in elevation. When the beam is steered to 45° in elevation, a grating lobe enters the circle and is realized, as shown by the x's in the figure. This essentially amounts to two main beams in elevation. Conversely, the array is over sampled in azimuth (along the x -axis). No matter where the beam is steered within the circle, no grating lobes can enter and become realized. However, there is a second issue to consider. The antenna pattern is essentially stretched; only that portion lying within the circle is realized. Therefore, the physically realized pattern

is stretched and then clipped at the real-complex circle boundary. If the mainbeam is steered outside the circle, there will be no realized mainbeam.

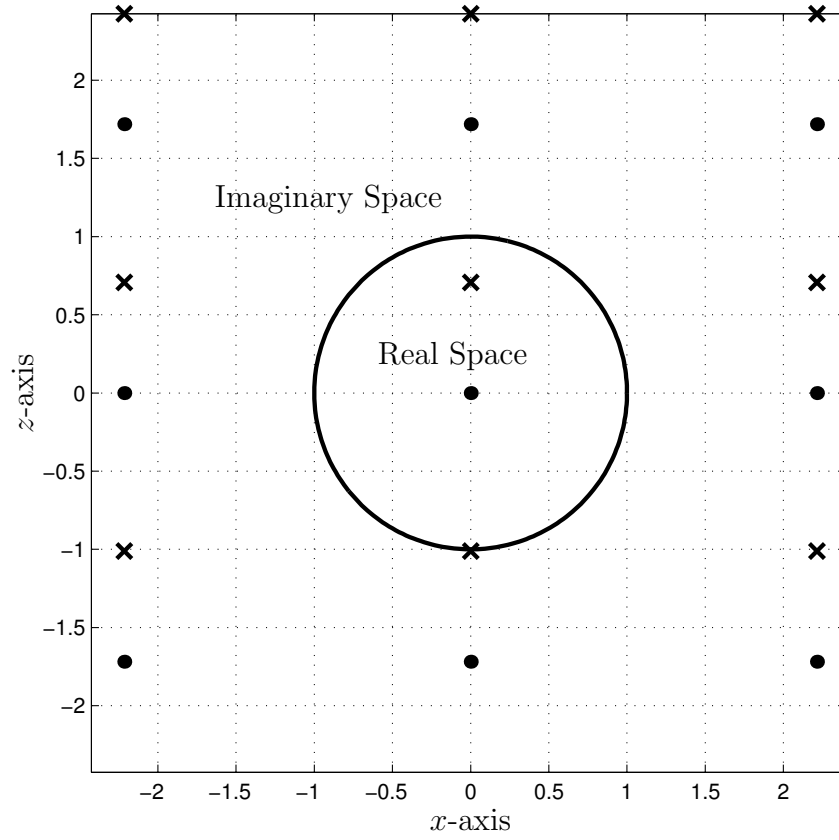


Figure B.1: Sin-theta space for the MCARM array interelement distances.

Appendix C. SNR and Power Calculations

In determining the target SNR, several definitions must be examined and related to the previous work. First, consider the receiver structure shown in Fig. C.1 for each element. The goal is to determine the target SNR on a per element, per pulse basis since the matched filtering operation is on a pulse-by-pulse basis.

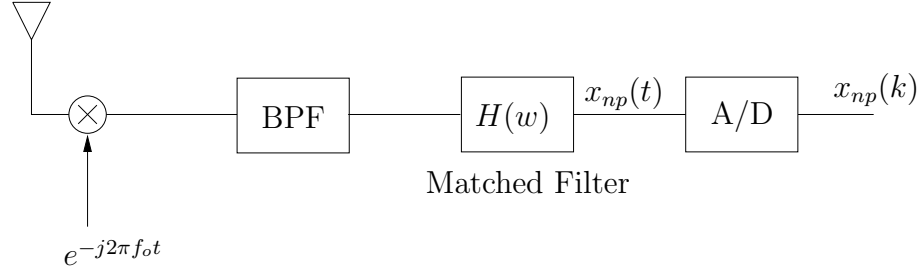


Figure C.1: The simplified receiver structure for each array element illustrates the down conversion to IF/baseband and the bandpass filter for optimum SNR. ADC is an analog to digital converter.

C.1 Target Power

The received signal on a per element basis was derived in Chapter III and shown in Eqn. (3.9),

$$\tilde{s}_{np}(t) = a_r u(t - \tau_{np}) e^{j2\pi f_o(t - \tau_{np})} e^{j2\pi f_t(t - \tau_{np})} e^{j\varphi}. \quad (\text{C.1})$$

This expression corresponds to the signal received at the element before any mixing or filtering operations. After down conversion, the received signal becomes (see Eqn. (3.28))

$$\tilde{s}_{np}(t) = a_r u(t - \tau_t) e^{j2\pi f_t t} e^{j2\pi(n\vartheta_x + p\vartheta_z)} e^{j\varphi}. \quad (\text{C.2})$$

IF is assumed baseband as before. A note is in order regarding the use of complex envelope notation in the development. The actual transmitted waveform is real valued, derived analytically from the given complex expression above by taking the

real part. This operation results in the signal becoming a cosine term which, after down conversion/mixing to baseband, leaves two components each weighted in amplitude by a factor of $\frac{1}{2}$. We have assumed a filter is in place to remove the upper frequency component and leave only the baseband portion within this development. The bandwidth of this filter is assumed large enough that all signal power passes through. However, a factor of two resulting from the trigonometric identity for a product of two cosines is omitted when using the complex envelope notation. The complex notation above is generated within the radar receiver by sampling in-phase and quadrature components of the real valued received waveform, i.e., the I and Q components.

The parameter of interest is the target signal power per element per pulse. The expression already gives the voltage waveform per element, however it still contains all the pulses. Substituting in for the pulse train,

$$\tilde{s}_{np}(t) = a_r \sum_{m=0}^{M-1} u_p(t - \tau_t - mT_r) e^{j2\pi f_t(t-mT_r)} e^{j2\pi(n\vartheta_x + p\vartheta_z)} e^{j\varphi}, \quad (\text{C.3})$$

then allows picking off a single pulse. The voltage for pulse zero ($m = 0$) is then

$$\tilde{s}_{np}(t) = a_r u_p(t - \tau_t) e^{j2\pi f_t(t-mT_r)} e^{j2\pi(n\vartheta_x + p\vartheta_z)} e^{j\varphi}. \quad (\text{C.4})$$

Notice that this is not the output of the matched filter as developed in Chapter III.

C.1.1 Instantaneous Power, Average Power, and Total Power. Essentially, there are three different forms of power that can be addressed. The development to this point generated an expression for the voltage on a per element basis, given by the previous equation. Using the common normalization of the power to a resistive value of one, the instantaneous power is simply the voltage magnitude squared or

$$p(t) = a_r^2 u_p^2(t - \tau_t). \quad (\text{C.5})$$

Interestingly, the signal of interest is classified as an energy signal. In other words, the received signal has finite non-zero energy but *zero* average power [57]. This classification is evidenced by the previous definition in Eqns. (3.5) and (3.6), where the energy in a single transmitted pulse was defined such that it was all captured in a_t^2 . Using this definition, all of the energy in the received pulse is then captured within a_r^2 ,

$$E_r = \int_{\tau_t}^{T_p + \tau_t} a_r^2 u_p^2(t - \tau_t) dt = a_r^2. \quad (\text{C.6})$$

Notice that this development assumes a deterministic, non-periodic returned target signal. For the purposes of injecting a target within the data set, this approach is sufficient for target SNR calculations based on the injected target amplitude a_r . However, an actual target signal would be random. This signal would be classified as a power signal and the power spectral density would be calculated using the Fourier transform of its autocorrelation function.

For the purpose of calculating the target power, the total power is used. The total power of the signal can be found by integrating the instantaneous power $p(t)$ across all time. However, this approach neglects the bandwidth of the receiver. More appropriate for this application is first obtaining the Fourier transform of the received signal and then integrating the squared magnitude over the receiver bandwidth. Assuming a bandwidth of $\frac{1}{T_p}$ at baseband, the total received power for the injected target is

$$P_t = \int_{-\frac{1}{T_p}}^{\frac{1}{T_p}} |\mathcal{F}\{\tilde{s}_{np}(t)\}|^2 df, \quad (\text{C.7})$$

where $\mathcal{F}\{\cdot\}$ represents the Fourier transform operator. Substituting for the Fourier transform of a rectangular pulse and simplifying gives

$$P_t = a_r^2 \int_{-\frac{1}{T_p}}^{\frac{1}{T_p}} T_p^2 \text{sinc}^2(fT_p) df. \quad (\text{C.8})$$

One approximation was applied in generating the above result. The target Doppler shift f_t merely amounts to a convolution in the frequency domain with a delta function. This convolution would result in a frequency translation/shift but, since f_t is considered small relative to the bandwidth of the signal, this frequency shift is negligible and the Doppler term is therefore ignored. The time delay τ_t (associated with the range of the target) in the unit energy pulse, $u_p(t - \tau_t)$, is just a complex exponential term after the Fourier transform. Since this term is merely a phase term, it falls out when the magnitude is taken. The integral term is approximated by [62]

$$\int_{-\frac{1}{T_p}}^{\frac{1}{T_p}} T_p \text{sinc}^2(fT_p) df \approx 0.903. \quad (\text{C.9})$$

Therefore, the total signal power per element per pulse that made it through the receiver bandwidth is

$$\boxed{P_t \approx 0.903 a_r^2 T_p.} \quad (\text{C.10})$$

C.2 Noise Power

The noise is considered a random quantity, specified by its Power Spectral Density (PSD) $\frac{N_o}{2}$. As developed in Chapter III, the receiver noise is modeled as purely white, meaning it has infinite frequency extent. Therefore, the total receiver noise power is determined as the integral over the receiver bandwidth,

$$P_n = \frac{N_o}{2} \int_{-\frac{1}{T_p}}^{\frac{1}{T_p}} df \quad (\text{C.11})$$

or simply

$$\boxed{P_n = \frac{N_o}{T_p} = N_o B.} \quad (\text{C.12})$$

C.3 Target SNR

The target SNR is simply the total target power referenced to the total noise power. Using the previously derived expressions, this ratio becomes

$$\boxed{\text{SNR} = \frac{P_t}{P_n} \approx \frac{0.903a_r^2 T_p^2}{N_o}} \quad (\text{C.13})$$

C.4 Target SINR

The target SINR includes the effects of interference and noise. For the purposes of this report, this quantity is calculated as derived in this section.

Both the clutter and jammer received amplitudes are considered random quantities. From the definitions given in the data model developed in Chapter III, the JNR and CNR on a per element per pulse basis were defined as

$$\xi_j = \frac{J_o}{N_o} \quad (\text{C.14})$$

and

$$\xi_{ik} = \frac{P_t G_t(\theta_i, \phi_k) g(\theta_i, \phi_k) \lambda_o^2 \sigma_{ik}}{(4\pi)^3 N_o B L_s R_i^4}, \quad (\text{C.15})$$

respectively (as shown in Eqns. (3.82) and (3.103)). The CNR shown above pertains to a single patch. To get the entire CNR on each element and each pulse, the quantity must be summed across all patches in the range ring (and ambiguous range rings). This requires the double summation shown in

$$\xi_c = \sum_{i=1}^{N_c} \sum_{k=1}^{N_r} \frac{P_t G_t(\theta_i, \phi_k) g(\theta_i, \phi_k) \lambda_o^2 \sigma_{ik}}{(4\pi)^3 N_o B L_s R_i^4}. \quad (\text{C.16})$$

The total clutter and jammer powers are then found by multiplying the JNR and CNR by the noise power,

$$\xi_j N_o B = J_o \quad (\text{C.17})$$

$$\xi_c N_o B = \sum_{i=1}^{N_c} \sum_{k=1}^{N_r} \frac{P_t G_t(\theta_i, \phi_k) g(\theta_i, \phi_k) \lambda_o^2 \sigma_{ik}}{(4\pi)^3 L_s R_i^4}. \quad (\text{C.18})$$

From these two quantities, the SINR definition simply becomes

$$\boxed{\text{SNR} = \frac{P_t}{P_n + J_o + \xi_c N_o B} \approx \frac{0.903 a_r^2 T_p^2}{N_o + J_o + \xi_c N_o B}}. \quad (\text{C.19})$$

Bibliography

1. Adve, R. S., Antonik, P., Baldygo, W., Capraro, C., Capraro, G., Hale, T., Schneible, R., and Wicks, M. *Knowledge-Base Application to Ground Moving Target Detection*. In-House AFRL-SN-RS-TR-2001-185, Rome Research Site, Rome, NY: Air Force Research Laboratory, September 2001.
2. Adve, R. S., Hale, T., Wicks, M., and Antonik, P. "Knowledge Based Adaptive Processing for Ground Moving Target Indication," *IEEE Transactions on AES*, VV(NN):XX–XX (August 2001). Submitted August 2001.
3. Adve, R. S., Hale, T., Wicks, M., and Genello, G. "Space-Time Adaptive Processing Techniques for Enhanced Ground Moving Target Detection." *Proceedings of the AP2000 Millenium Conference on Antennas and Propagation*. April 2000.
4. Adve, R. S., Hale, T. B., and Wicks, M. C. "Transform Domain Localized Processing Using Measured Steering Vectors and Non-Homogeneity Detection." *Proceedings of the 1999 IEEE National Radar Conference*. April 1999.
5. Adve, R. S., Hale, T. B., and Wicks, M. C. "A Two-Stage Hybrid Space-Time Adaptive Processing Algorithm." *Proceedings of the 1999 IEEE National Radar Conference*. 279–284. April 1999.
6. Adve, R. S., Hale, T. B., and Wicks, M. C. "Practical Joint Domain Localised Adaptive Processing in Homogeneous and Nonhomogeneous Environments, Part 1: Homogeneous Environments," *IEE Proceedings - Radar, Sonar, and Navigation*, 147(2):57–65 (April 2000).
7. Adve, R. S., Hale, T. B., and Wicks, M. C. "Practical Joint Domain Localised Adaptive Processing in Homogeneous and Nonhomogeneous Environments, Part 2: Nonhomogeneous Environments," *IEE Proceedings - Radar, Sonar, and Navigation*, 147(2):66–74 (April 2000).
8. Adve, R. S., Wicks, M., and Hale, T. "Effects of Mutual Coupling and Channel Mismatch on Space-Time Adaptive Processing Algorithms." *Proceedings of the AP2000 Millenium Conference on Antennas and Propagation*. April 2000.
9. Adve, R. S., Wicks, M., Hale, T., and Antonik, P. "Ground Moving Target Indication Using Knowledge Based Space-Time Adaptive Processing." *Record of the 2000 IEEE International Radar Conference*. 735–740. May 2000.
10. Adve, R. S. and Wicks, M. C. "Joint Domain Localized Processing Using Measured Spatial Steering Vectors." *Proceedings of the 1998 IEEE National Radar Conference*. May 1998.

11. Applebaum, S. P. and Chapman, D. J. "Adaptive Arrays with Main Beam Constraints," *IEEE Transactions on Antennas and Propagation*, AP-24, No. 5:650–662 (September 1976).
12. Balanis, C. *Antenna Theory* (Second Edition). New York, NY: John Wiley & Sons, Inc., 1997.
13. Barton, T. A. and Smith, S. T. "Structured Covariance Estimation for Space-Time Adaptive Processing." *Proceedings of IEEE International Conference on Acoustics, Speech, and Signal Processing* 5. 3493–3496. 1997.
14. Berger, S. *Dual Channel Matched Filtering and Space-Time Adaptive Processing*. PhD dissertation, Graduate School of Engineering, Air Force Institute of Technology (AETC), Wright-Patterson AFB OH, April 1999. AFIT/DS/ENG/99-04.
15. Boroson, D. "Sample Size Considerations for Adaptive Arrays," *IEEE Transactions on Aerospace and Electronic Systems*, AES-16(4):446–451 (July 1980).
16. Borsari, G. K. "Mitigating Effects on STAP Processing Caused by an Inclined Array." *Proceedings of the 1998 IEEE Radar Conference*. 135–140. 1998.
17. Brennan, L. and Reed, I. "Theory of Adaptive Radar," *IEEE Transactions on Aerospace and Electronic Systems*, AES-9, No. 2:237–252 (March 1973).
18. Brooks, L. S. and Reed, I. S. "Equivalence of the Likelihood Ratio Processor, the Maximum Signal-to-Noise Ratio Filter, and the Wiener Filter," *IEEE Transactions on Aerospace and Electronic Systems*, 690–692 (September 1972). Correspondence.
19. Brown, W., Temple, M., Penno, R., and Hong, L., "Interferometric Radar & Clutter Suppression." Technical Appendix to DAGSI Proposal #16 (SN-08), November 1999.
20. Carlson, B. D. "Covariance Matrix Estimation Errors and Diagonal Loading in Adaptive Arrays," *IEEE Transactions on Aerospace and Electronic Systems*, 24(4):397–401 (July 1988).
21. Chen, W. and Reed, I. S. "A New CFAR Detection Test for Radar," *Digital Signal Processing*, 4:198–214 (October 1991).
22. Cook, C. E. and Bernfeld, M. *Radar Signals, An Introduction to Theory and Application*. Orlando, FL 32887: Academic Press, Inc., 1967.
23. Dudgeon, D. E. and Mersereau, R. M. *Multidimensional Signal Processing*. Englewood Cliffs, New Jersey 07632: Prentice-Hall, Inc., 1984.
24. Gardner, W. A. *Cyclostationarity in Communications and Signal Processing*. Piscataway, NJ: IEEE Press, 1994.

25. Goldstein, J. S. and Reed, I. S. "Theory of Partially Adaptive Radar," *IEEE Transactions on Aerospace and Electronic Systems*, 33, No. 4:1309–1325 (October 1997).
26. Goldstein, J. S. and Reed, I. S. "A Tutorial on Space-Time Adaptive Processing." *Proceedings of IEEE National Radar Conference*. May 1997.
27. Golub, G. H. and Loan, C. F. V. *Matrix Computations* (3 Edition). 2715 North Charles Street, Baltimore, MD 21218-4319: The Johns Hopkins University Press, 1996. ISBN 0-8018-5413-X.
28. Graham, A. *Kronecker Products and Matrix Calculus with Applications*. Ellis Horwood: Mathematics and its Applications, Market Cross House, Cooper Street, Chichester, West Sussex, PO19 1EB, England: Ellis Horwood Limited, 1981.
29. Gustafson, S., Hale, T., and Claypoole, R. "Competitively Evolved Probability Densities for Signal Interpolation," *IEE Electronics Letters*, 37(6):396–398 (March 2001).
30. Haimovich, A. M. and Bar-Ness, Y. "An Eigenanalysis Interference Canceler," *IEEE Transactions on Signal Processing*, 39, No. 1:76–84 (January 1991).
31. Hale, T., Temple, M., and Wicks, M. "Clutter Suppression Using Elevation Interferometry Fused with Space-Time Adaptive Processing," *IEE Electronics Letters*, 37(12):793–794 (June 2001).
32. Hale, T., Temple, M., Wicks, M., Raquet, J., and Oxley, M. "Performance Characterization of a Hybrid STAP Architecture Incorporating Elevation Interferometry," *IEE Proceedings - Radar, Sonar and Navigation* (January 2002). Accepted for Publication, 03 Jan 02.
33. Hale, T. B., Adve, R. S., and Wicks, M. C., "Two-Stage Hybrid Space-Time Adaptive Processing in Radar and Communication Systems." United States Patent, June 2001. Air Force Invention No. RL10,028, U.S. Patent No. 6,252,540.
34. Hale, T. B., Temple, M. A., Wicks, M. C., Raquet, J. F., and Oxley, M. E. "Elevation Interferometric STAP Using a Thinned Planar Array." *Proceedings of IEEE 2002 Radar Conference*. 408–414. Long Beach, CA: IEEE Aerospace and Electronic Systems Society, April 2002.
35. Hale, T. B., Temple, M. A., Wicks, M. C., Raquet, J. F., and Oxley, M. E. "Localized Three-Dimensional Adaptive Spatial-Temporal Processing for Airborne Radar." *Proceedings of the 2002 IEE International Radar Conference*. October 2002. Accepted for publication, April 2002.
36. Harris, F. J. "On the Use of Windows for Harmonic Analysis with the Discrete Fourier Transform." *Proceedings of the IEEE* 66, No. 1. 51–83. January 1978.

37. Haykin, S. *Adaptive Filter Theory* (3 Edition). Information and System Sciences, Upper Saddle River, NJ 07458: Prentice-Hall, Inc., 1996.
38. Hughes, D. T. and McWhirter, J. G. "Penalty Function Method for Sidelobe Control in Least Squares Adaptive Beamforming," *SPIE-Advanced Signal Processing Algorithms*, 2563:170–181 (July 1995).
39. Jaffer, A., Baker, M., Ballance, W., and Staub, J. *Adaptive Space-Time Processing Techniques for Airborne Radars*. Contract F30602-89-D-0028, Fullerton, CA 92634: Hughes Aircraft Company, July 1991.
40. Kay, S. M. *Fundamentals of Statistical Signal Processing, Estimation Theory*. Upper Saddle River, NJ 07458: Prentice-Hall, 1993.
41. Kelly, E. "An Adaptive Detection Algorithm," *IEEE Transactions on Aerospace and Electronic Systems*, AES-22, No. 1:115–127 (March 1986).
42. Klemm, R. *Space-Time Adaptive Processing Principles and Applications*. IEE Radar, Sonar, Navigation, and Avionics Series 9, Michael Faraday House, Six Hills Way, Stevenage, Herts. SG1 2AY, United Kingdom: The Institution of Electrical Engineers, 1998. ISBN 0852969465.
43. Lancaster, P. and Tismenetsky, M. *The Theory of Matrices, With Applications* (Second Edition). Computer Science and Applied Mathematics, Orlando, FL 32887: Academic Press, Inc., 1985.
44. Liberti, J. C. and Rappaport, T. S. *Smart Antennas for Wireless Communications: IS-95 and Third Generation CDMA Applications*. Upper Saddle River, New Jersey: Prentice-Hall, Inc., 1997.
45. Melvin, W. L. and Wicks, M. C. "Improving Practical Space-Time Adaptive Radar." *Proceedings of the 1997 IEEE National Radar Conference*. May 1997.
46. Morris, G. V. *Airborne Pulsed Doppler Radar*. 685 Canton Street, Norwood, MA 02062: Artech House, Inc., 1988.
47. Park, S. and Sarkar, T. K. "A Deterministic Eigenvalue Approach to Space-Time Adaptive Processing." *Proceedings of the 1996 IEEE Antennas and Propagation Society International Symposium*. June 1996.
48. Rappaport, T. S. *Wireless Communications: Principles and Practice*. Englewood Cliffs, New Jersey 07632: Prentice-Hall, Inc., 1996.
49. Reed, I. S., Mallett, J., and Brennan, L. "Rapid Convergence Rate in Adaptive Arrays," *IEEE Transactions on Aerospace and Electronic Systems*, AES-10, No. 6:853–863 (November 1974).
50. Roberts, R. A. and Mullis, C. T. *Digital Signal Processing*. Reading, Massachusetts: Addison-Wesley Publishing Company, 1987.

51. Robey, F. C., Fuhrmann, D. R., Kelly, E. J., and Nitzberg, R. "A CFAR Adaptive Matched Filter Detector," *IEEE Transactions on Aerospace and Electronic Systems*, 28(1):208–216 (January 1992).
52. Roman, J. R. and Davis, D. W. *Multichannel System Identification and Detection Using Output Data Techniques*. Contract C-F30602-93-C-0193, RL-TR-97-5, 26 Electronic Parkway, Rome, NY 13441-4514: Rome Laboratory/OCSM, May 1997. Volume II of II.
53. Sarkar, T. K., Koh, J., Adve, R. S., Schnieble, R. A., Wicks, M. C., Choi, S., and Palma, M. S. "A Pragmatic Approach to Adaptive Antennas," *IEEE Antennas and Propagation Magazine*, 42(2):39–55 (April 2000).
54. Sarkar, T. K. and Sangruji, N. "An Adaptive Nulling System for a Narrow-band Signal with a Look-direction Constraint Utilizing the Conjugate Gradient Method," *IEEE Transactions on Antennas and Propagation*, 37:940–944 (July 1989).
55. Sarkar, T. K., Wang, H., Park, S., Adve, R. S., Koh, J., Kim, K., Zhang, Y., Wicks, M. C., and Brown, R. D. "A Deterministic Least-Squares Approach to Space-Time Adaptive Processing (STAP)," *IEEE Transactions on Antennas and Propagation*, 49(1):91–103 (January 2001).
56. Schneible, R. A. *A Least Squared Approach to Radar Array Adaptive Nulling*. PhD dissertation, Division of Electrical Engineering and Computer Science, Syracuse University, 1996.
57. Sklar, B. *Digital Communications Fundamentals and Applications*. Englewood Cliffs, NJ 07632: Prentice-Hall, Inc., 1988.
58. Skolnik, M. I. *Introduction to Radar Systems, Second Edition*. New York: McGraw-Hill, Inc., 1980.
59. Sloper, D., Fenner, D., Arntz, J., and Fogle, E. *Multi-Channel Airborne Radar Measurement (MCARM), MCARM Flight Test*. Contract F30602-92-C-0161, Box 1693, Baltimore, MD 21203: Westinghouse Electronic Systems, April 1996.
60. Stimson, G. W. *Introduction to Airborne Radar* (Second Edition). Mendham, NJ: SciTech Publishing, Inc., 1998.
61. Stutzman, W. L. and Thiele, G. A. *Antenna Theory and Design* (Second Edition). New York, NY: John Wiley & Sons, Inc., 1998.
62. Temple, M. A. "Class Notes." EENG673 Spread Spectrum Communications, June 2000.
63. Therrien, C. W. *Discrete Random Signals and Statistical Signal Processing*. Englewood Cliffs, New Jersey 07632: Prentice-Hall, Inc., 1992.

64. Wang, H. and Cai, L. "On Adaptive Spatial-Temporal Processing for Airborne Surveillance Radar Systems," *IEEE Transactions on Aerospace and Electronic Systems*, 30(3):660–669 (July 1994).
65. Ward, J. *Space-Time Adaptive Processing for Airborne Radar*. Contract F19628-95-C-0002, Lexington, Massachusetts: Lincoln Laboratory, Massachusetts Institute of Technology, December 1994.
66. Wicks, M. C., Melvin, W. L., and Chen, P. "An Efficient Architecture for Nonhomogeneity Detection in Space-Time Adaptive Processing Airborne Early Warning Radar." *Proceedings of the 1997 International Radar Conference*. October 1997. Edinburgh, UK.
67. Wilson, K. S. *Effects of Clutter Height Discrimination on Adaptive Clutter Erasure Performance*. PhD dissertation, Graduate School of Engineering, Air Force Institute of Technology (AETC), Wright-Patterson AFB OH, June 1998. AFIT/DS/ENG/98-05.
68. Woodward, P. M. *Probability and Information Theory, With Applications to Radar*. 330 West 42nd Street, New York 36, NY: McGraw-Hill Book Co., Inc., 1953.
69. Zatman, M. "Circular Array STAP." *Proceedings of the 1999 IEEE Radar Conference*. 108–112. April 1999.
70. Zatman, M. "Circular Array STAP," *IEEE Transactions on Aerospace and Electronic Systems*, 36(2):510–516 (April 2000).

Index

The index is conceptual and does not designate every occurrence of a keyword. Page numbers in bold represent concept definition or introduction.

Symbols _____	A 177
B 80, 83	B 110
E_p 61	E 110, 178
E_t 62	T 179
E_u 61	X 21
G 181	a 21, 70 , 99, 110
I 181	b 22, 70 , 110
K 100, 115, 120	e 70 , 110
L 25	v 22
L_r 82	\mathbf{v}_a 19, 87
M 17, 20, 61 , 69	\mathbf{w}_a 110
N 17, 69	\mathbf{x}_m 21
N_c 25, 85	ω_o 60
N_o 80, 82, 83	\otimes 22, 70, 110
P 69, 98	ϕ 19, 58
P_d 17, 115, 120, 128	ϕ_t 16
P_{fa} 17, 128	ψ 20
R_c 84	ψ_c 84
R_t 63	σ^2 80, 113
R_u 86	τ_t 63
S_j 82	τ_{np} 62
T_r 17, 20	θ 19, 58
α_t 21	$\tilde{\mathbf{A}}$ 180
$\bar{\omega}$ 17, 21, 63	$\tilde{\mathbf{E}}$ 181
χ 22, 71 , 109	$\tilde{\mathbf{T}}$ 181
$\hat{\mathbf{R}}_N$ 114	φ 60, 69
$\hat{\mathbf{k}}(\phi, \theta)$ 19	ϑ 21, 65, 72
	a_e 85

a_r	21, 62, 69
a_t	20, 60, 61
c	64
d	18
d_x	57, 65
d_z	57, 65
$f(\theta, \phi)$	71
f_o	20
f_r	17, 62
f_t	17, 20, 62
$g(\theta, \phi)$	71
$h(t)$	67
h_a	85
$u(t)$	20, 60
$u_p(t)$	20
v_t	20, 62
x_{nm}	21
z_a	180
z_b	181
\mathbf{C}_e	112, 142
2D-AMF.....	38, 120
2D-FTS.....	7, 35, 96, 98
2D-JDL.....	8, 40–42, 50, 135
2D-MF.....	132
3D-FTS.....	5, 6, 36, 48, 94–135
3D-JDL.....	6, 162–165
3D-MF.....	134

A

A/D convertor.....	66, 223
abstract.....	xvii
ACE.....	49, 96, 98, 106
adaptive clutter erasure.....	<i>see</i> ACE
adaptive dwell time.....	20, 28, 31, 32
adaptive MF.....	<i>see</i> AMF
adaptive transform.....	50

adaptive weights.....	16
AFRL.....	9
aliasing.....	1, 62
altitude.....	85, 90
ambiguity function.....	68
AMF.....	8
angle scale.....	218–222
antenna array.....	58
antenna geometry.....	59
applications.....	9
array.....	44
factor.....	74
linear.....	16, 64
orientation.....	19, 57
pattern.....	72–77
planar.....	57
azimuth-Doppler-elevation hypercube.....	2,
8, 211	
azimuth-Doppler plane.....	2, 34
azimuth angle.....	19, 58
azimuth steering vector.....	21, 22, 70

B

backlobe attenuation.....	72
bandwidth.....	80, 113
barrage noise jamming.....	24, 81
Baye's criterion.....	156
beamspace.....	40
beam sharpening.....	99
boresight.....	58

C

carrier.....	20, 60
cartesian coordinate system.....	19, 58
CDMA.....	11

CFAR 39, 99
 clutter 24–27, 83–90
 Doppler 87
 patch 25, **85**
 power *see* power
 RCS density 88
 reflectivity 85, 88
 ridge 1, 127
 ring 25, **85**, 112, 124
 clutter-to-noise ratio *see* CNR
 clutter covariance . *see* covariance matrix
 CNR 26, **89**, 227
 co-phasing 49
 coherent integration 69
 coherent integration time 61
 coherent processing interval *see* CPI
 comments 9, 14, 15, 23, 27, 37,
 41, 46, 81, 88, 90, 105, 107, 109,
 113, 130, 135, 156, 164, 167, 178,
 181, 182, 186, 188, 201, 203
 complex envelope notation 20
 constant gamma model 85
 constrained difference maximization . 181
 contributions 4
 coordinate system 18–19, 57–60
 covariance, known 156, 164
 covariance matrix 28, 33, 35, 99
 artificial 112, 142, 199
 clutter 26, **90**
 jammer 24, **83**
 noise 23, **81**
 CPI 20, 28, 31, **61**, 69
 crab angle 57, 87

D

datacube 32, 33

data matrix
 azimuth 177
 elevation 178
 temporal 179
 data model 57–91
 2D 17–27
 degrees of freedom *see* DOF
 detection probability .. 17, 100, 115, 120,
 128
 deterministic method 33
 discrete interferer **29**, 44, 52, 93, 198
 document organization 4
 document standardization 9
 DOF **32**, 35
 lost in deterministic approach 48,
 182, 184
 Doppler 20, **62**, 87
 filtering 35, 114
 foldover 62
 normalized **17**, 21, **63**, 68
 tolerance 68
 down conversion 21, 67

E

earth
 actual radius 85
 effective radius 84, 85
 spherical model 84, 124
 element pattern 71–72, 89
 element spacing 57
 Elev-JDL 135–138
 elevation angle 19, **58**
 elevation steering vector **70**
 energy signal 225
 envelope function 20, 60
 equivalence of 2D & 3D 13

Euclidean norm 159

F

factored method 7
factored time space *see* FTS
false alarm probability .. 17, 36, 100, 128
FFT 50
Fourier transform 225
 multidimensional discrete 193
frequency 60, 80
 IF 67
 spatial *see* spatial frequency
Frobenius norm 159, 181
fundamental pulse 20, 61

G

Gaussian interference 156
geometric series 74
GLRT 39
GMTI 43
grating lobes 71, 77, 124, 220–222
grazing angle 84, 85
ground clutter 25, 84
guard cell *see* secondary data

H

height discrimination 2
height interferometry 96–105
heterogeneity 8, 27–30, 44
homogeneity 27–30
horizon range 86
hybridization 3
hybrid method, original 42–51
 3D extension 175–190
hybrid method, purpose 8

hypothesis test 156

I

i.i.d. data 28
ICE 48, 98
IF *see* frequency
improvement surface 103
impulse response 67
independent and identically distributed data
 see i.i.d. data
interelement spacing 18, 57
interference covariance *see*
 covariance matrix
interference matrix
 azimuth 180
 elevation 181
 temporal 181
interferogram 49
interferometric clutter erasure... *see* ICE
interferometry 97, 106
inverse hybrid concept 191–198
invertibility 23, 81

J

jammer-to-noise ratio *see* JNR
jammers 24
jammer power *see* power
jammer power spectral density 82
jamming model 81–83
JNR 24, 82, 227
joint domain 8, 34, 211

K

Kronecker delta 80

Kronecker product...22, 70, 110, 216–217

L

L'Hôpital rule 75
Lagrange multiplier method...47, 160, 182
likelihood ratio 157
Likelihood Ratio Processor 37, 155
literature review 13–56
LPC 163
LPC adaptive transform 184
LPR 41, 163

M

mainbeam 16
matched filter 158
maximum SINR filter 37, 158
 hybrid 182
MCARM 84, 94, 96
MF 8, 21
MLE 38, 164, 187
Monte Carlo analysis 122, 128
multidimensional processing 1–4
multiplier 17

N

Neyman-Pearson test 156
NHD 29–30, 44
noise covariance... *see* covariance matrix
noise jammer 1, 24
noise model 23, 80–81
noise power 23, 80, 226
noise power spectral density... 80, 83, 113
noise snapshot 23
normalized Doppler *see* Doppler
notation 9

null hypothesis 156

O

optimality... 7, 34, 36, 38, 109, 122, 136,
211

P

PD 19, 57, 60
performance bound 132
permute operator 178
physical environment 3, 18
platform geometry 19
power
 average 225
 clutter 228
 instantaneous 224
 jammer 228
 total 225
power gain 46, 181
power signal 225
power spectral density *see* PSD
PRF 1, 17, 62
PRI 17, 20, 60, 61
primary range cell *see* range cell
probability density function 156
probability of false alarm *see* detec-
 tion probability, false alarm prob-
 ability
problem statement 1–4
propagation velocity... *see* speed of light
PSD 226
pulse energy 61
 transmitted 61, 225
pulse repetition frequency *see* PRF
pulse repetition interval *see* PRI

pulse train 60

R

radar geometry 59

radar coordinate system *see*
coordinate system

radar cross section *see* RCS

radar geometry 57

random phase 60, 69

range ambiguities ... 27, 72, **86**, 113, 116,
120, 141

range cell 33, **84**
under test **29**, 33

range resolution 88

RASL **100**, 117

RCS 62, 85

received signal 21, 66

received waveform 62–69

receiver 19, 60, 65, 80
matched filter 67

receiver losses 82

Reed's rule 29, 36, **38**, 115

relative average sidelobe level . *see* RASL

relative peak sidelobe level *see* RPSL

relative velocity 62, 87

research chain **4**, 13, 31, 57, 94

research goal 13

reshape operator 177

residual interference power 46, 181

round trip time 63

RPSL **100**, 117

S

sample matrix inversion *see* SMI

secondary data 33, 35

guard cell 29

symmetric window 28

sigma zero 88

signal-to-interference plus noise ratio . *see*

SINR

signal energy 62

signal power 226

sin-theta space 71, **221**

SINR 37, 100, 115, 227, **228**

SINR, output 166

sky clutter 84

SNR 223, **227**

Space-Time Adaptive Processing *see*

STAP

space-time product 39

space-time snapshot .. 22, 26, **71**, 99, 109

space-time steering vector **22**, **71**

spatial frequency ... 21, 22, **64**, 66, 71, 86

spatial phase progression 46

spatial steering vector *see* azimuth or ele-
vation steering vector

speed of light 64

spherical coordinate system 60

sponsorship 12

STAP **16**

overview 16

statistical methods **31**

stealth technology 2

sub-clutter visibility 49

surgical warfare 2

symmetric window ... *see* secondary data

T

target 116

target SNR 227

temporal phase progression 47

temporal steering vector 22, **70**
test range cell *see* range cell
test statistic 99
TFACF 67, 68
thermal noise 23, 80
thinned array 126–135
threshold 17, 36
time-frequency autocorrelation function *see*
 TFACF
transformation matrix 40
transmitted waveform 19–20, 60–62
transmit beam 72

U

ULA 64
unambiguous range 86
uniformly spaced linear array... *see* ULA
uniform sampling 194
unit vectors 19, **60**

V

$\text{vec}(\cdot)$ 23, 48
velocity vector 19, 57
virtual null 188, 197

W

weight vector
 3D-FTS 110
 3D-JDL 164
 3D-MF 158, 160, 161
 3D original hybrid extension 183
 azimuth 114, 177, 182, 183
 Elev-JDL 137
 elevation 98, 112, 183
 LPC 186
 temporal 183
whitening filter 158
Wiener filter 35, 37, 160
Wienr-Hopf equations 160
windowing 99
Wishart distribution 100, 116

Author Index

The author index gives pages numbers for each author citation. All authors on a paper appear in the index.

A

Adve11, 31, 34, 40, 42–44, 46, 48, 50, 51,
173, 176, 191
Antonik 43
Applebaum.....32
Arntz 18, 25, 27, 84, 96, 129

B

Baker 17, 32, 51, 57
Balanis.....74
Baldygo 43
Ballance.....17, 32, 51, 57
Bar-Ness 32
Barton 39
Berger.....32
Bernfeld.....67
Boroson 29, 39
Borsari.....127, 151
Brennan 29, 32, 36–38, 42, 115, 162, 165,
169
Brooks.....37, 155, 158, 159
Brown.....44, 48, 49, 176

C

Cai...8, 32, 40, 42, 50–52, 135, 154, 162,
163, 173, 212
Capraro 43

Carlson.....32, 39
Chapman.....32
Chen30, 32, 39, 44, 99, 100, 115, 116, 161
Choi 31
Claypoole 7
Cook.....67

D

Davis.....51
Dudgeon 193

F

Fenner 18, 25, 27, 84, 96, 129
Fogle 18, 25, 27, 84, 96, 129
Fuhrmann 32, 39, 99, 115, 161

G

Gardner.....31
Genello.....43
Goldstein.....32
Golub 159
Graham 216
Gustafson 7

H

Haimovich.....32

Hale 5–7, 11, 18, 25, 34, 40, 42,
43, 46, 51, 96, 106, 116, 126, 128,
130, 137, 141, 150, 155, 173, 191

Harris 99

Haykin 156, 158, 160

Hong 49

Hughes 32

J

Jaffer 17, 32, 51, 57

K

Kay 157

Kelly 32, 38, 39, 99, 115, 161

Kim 44, 48, 176

Klemm 5, 105, 120, 127

Koh 31, 44, 48, 176

L

Lancaster 23, 48

Liberti 11, 28

Loan 159

M

Mallett 32, 36, 38, 42, 115, 162, 165, 169

McWhirter 32

Melvin 30, 44

Mersereau 193

Morris 67

Mullis 74

N

Nitzberg 32, 39, 99, 115, 161

O

Oxley 5, 6, 18, 25, 96, 126, 128, 130, 137,
141, 150, 155

P

Palma 31

Park 44, 48, 176

Penno 49

R

Rappaport 11, 28

Raquet 5, 6, 18, 25, 96, 126, 128, 130,
137, 141, 150, 155

Reed 29, 32, 36–39, 42, 99, 100, 115, 116,
155, 158, 159, 161, 162, 165, 169

Roberts 74

Robey 32, 39, 99, 115, 161

Roman 51

S

Sangruji 44, 47, 176, 182

Sarkar 31, 44, 47, 48, 176, 182

Schneible 43, 48

Schnieble 31

Sklar 225

Skolnik 68, 88

Sloper 18, 25, 27, 84, 96, 129

Smith 39

Staub 17, 32, 51, 57

Stimson 221

Stutzman 74

T _____
 Temple 5, 6, 18, 25, 49, 96, 106, 116, 126,
 128, 130, 137, 141, 150, 155, 226
 Therrien 160
 Thiele 74
 Tismenetsky 23, 48

W _____
 Wang ... 8, 32, 40, 42, 44, 48, 50–52, 135,
 154, 162, 163, 173, 176, 212
 Ward ... 3, 7, 14, 17–19, 27, 32, 34, 36, 51,
 57, 58, 71, 72, 82, 84, 88, 92, 99,
 115, 165, 166, 209

Wicks 5, 6, 11, 18, 25, 30, 31,
 34, 40, 42–44, 46, 48, 50, 51, 96,
 106, 116, 126, 128, 130, 137, 141,
 150, 155, 173, 176, 191
 Wilson 48, 49, 96, 106
 Woodward 67

Z _____
 Zatman 127, 151
 Zhang 44, 48, 176

REPORT DOCUMENTATION PAGE

Form Approved
OMB No. 0704-0188

Public reporting burden for this collection of information is estimated to average 1 hour per response, including the time for reviewing instructions, searching existing data sources, gathering and maintaining the data needed, and completing and reviewing the collection of information. Send comments regarding this burden estimate or any other aspect of this collection of information, including suggestions for reducing this burden to Washington Headquarters Services, Directorate for Information Operations and Reports, 1215 Jefferson Davis Highway, Suite 1204, Arlington, VA 22202-4302, and to the Office of Management and Budget, Paperwork Reduction Project (0704-0188), Washington, DC 20503.

PLEASE DO NOT RETURN YOUR FORM TO THE ABOVE ADDRESS.

1. REPORT DATE (DD-MM-YYYY) June 2002		2. REPORT TYPE Doctoral Dissertation		3. DATES COVERED November 2000-June 2002	
4. TITLE AND SUBTITLE AIRBORNE RADAR INTERFERENCE SUPPRESSION USING ADAPTIVE THREE-DIMENSIONAL TECHNIQUES				5a. CONTRACT NUMBER	
				5b. GRANT NUMBER	
				5c. PROGRAM ELEMENT NUMBER	
6. AUTHOR(S) Hale, Todd B., Captain, USAF				5d. PROJECT NUMBER	
				5e. TASK NUMBER	
				5f. WORK UNIT NUMBER	
7. PERFORMING ORGANIZATION NAME(S) AND ADDRESS(ES) Air Force Institute of Technology Graduate School of Engineering and Management (AFIT/EN) 2950 P Street, Building 640 WPAFB OH 45433-7765				8. PERFORMING ORGANIZATION REPORT NUMBER AFIT/DS/ENG/02-02	
9. SPONSORING/MONITORING AGENCY NAME(S) AND ADDRESS(ES) AFRL/SNRT Attn: Michael C. Wicks Rome Research Site Rome, NY 13440 DSN587-2556, (315)330-2556				10. SPONSOR/MONITOR'S ACRONYM(S)	
				11. SPONSOR/MONITOR'S REPORT NUMBER(S)	
12. DISTRIBUTION/AVAILABILITY STATEMENT Approved for public release; distribution unlimited.					
13. SUPPLEMENTARY NOTES					
14. ABSTRACT This research advances adaptive interference suppression techniques for airborne radar, addressing the problem of target detection within severe interference environments characterized by high ground clutter levels, noise jammer infiltration, and strong discrete interferers. Two-dimensional (2D) Space-Time Adaptive Processing (STAP) concepts are extended into three-dimensions (3D) by casting each major 2D STAP research area into a 3D framework. The work first develops an appropriate 3D data model with provisions for range ambiguous clutter returns. Adaptive 3D development begins with two factored approaches, 3D Factored Time-Space (3D-FTS) and Elevation-Joint Domain Localized (Elev-JDL). The 3D adaptive development continues with optimal techniques, i.e., joint domain methods. First, the 3D Matched Filter (3D-MF) is derived followed by a 3D Adaptive Matched Filter (3D-AMF) discussion focusing on well established practical limitations consistent with the 2D case. Finally, a 3D-JDL method is introduced. Proposed 3D Hybrid methods extend current state-of-the-art 2D hybrid methods. The initial 3D hybrid, a functional extension of the 2D technique, exhibits distinct performance advantages in heterogeneous clutter. The final 3D hybrid method is <u>virtually impervious to discrete interference.</u>					
15. SUBJECT TERMS radar, radar clutter, radar interference, adaptive filters, search radar					
16. SECURITY CLASSIFICATION OF:			17. LIMITATION OF ABSTRACT	18. NUMBER OF PAGES	19a. NAME OF RESPONSIBLE PERSON
a. REPORT	b. ABSTRACT	c. THIS PAGE			19b. TELEPHONE NUMBER (include area code)
UU	UU	UU	SAR	263	Michael A. Temple, AFIT/ENG 937-255-3636x4703